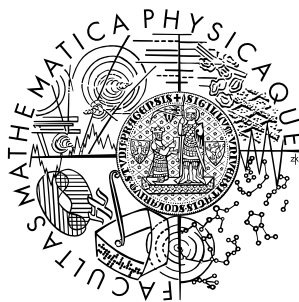Charles University in Prague
Faculty of Mathematics and Physics

DOCTORAL THESIS

Richard Řezníček

Hyperfine interactions and electronic structure of magnetite

Department of Low Temperature Physics

Supervisor of the doctoral thesis:
prof. RNDr. Helena Štěpánková, CSc.

Study program:
Physics

Specialization:
Physics of Condensed Matter and Materials Research

Prague 2015

I declare that I carried out this doctoral thesis independently, and only with the cited sources, literature and other professional sources.

I understand that my work relates to the rights and obligations under the Act No. 121/2000 Coll., the Copyright Act, as amended, in particular the fact that the Charles University in Prague has the right to conclude a license agreement on the use of this work as a school work pursuant to Section 60 paragraph 1 of the Copyright Act.

In Prague   date 15th July 2015   signature

Název práce: Hyperjemné interakce a elektronová struktura magnetitu
Autor: Richard Řezníček
Katedra: Katedra fyziky nízkých teplot
Vedoucí doktorské práce: prof. RNDr. Helena Štěpánková, CSc.

Abstrakt: Předložená práce se zaměřuje na analýzy experimentálních dat jaderné magnetické rezonance ^{57}Fe a výsledků ab initio výpočtů pro získání hlubšího vhledu do hyperjemné a elektronové struktury magnetitu pod i nad Verweyovým fázovým přechodem. Parametry hyperjemných interakcí a údaje o elektronové struktuře Cc fáze magnetitu byly extrahovány z výsledků ab initio výpočtů založených na nedávno publikované krystalové struktuře. Publikované experimentální závislosti frekvencí jaderné magnetické rezonance ^{57}Fe na směru vnějšího magnetického pole byly kvantitativně reanalyzovány, což poskytlo údaje o hyperjemné anizotropii, které byly porovnány s analogickými parametry hyperjemného pole z ab initio výpočtů. Zjištění byla interpretována v kontextu soudobých modelů nábojového uspořádání magnetitu. Pozornost byla věnována také dopadu různých kationtových substitucí a defektů na elektronovou strukturu a hyperjemné interakce v magnetitu projevující se ve spektrech jaderné magnetické rezonance ^{57}Fe: pod Verweovým přechodem byly analyzovány posuny intenzity signálu; nad Verweyovým přechodem byl pro analýzu teplotní závislosti frekvencí satelitních signálů přizpůsoben model středního pole a anomální teplotní vývoj šířek hlavních čar byl studován ve vztahu k elektrické vodivosti.

Klíčová slova: NMR, hypejemná interakce, magnetit, elektronová struktura

Title: Hyperfine interactions and electronic structure of magnetite
Author: Richard Řezníček
Department: Department of Low Temperature Physics
Supervisor of the doctoral thesis: prof. RNDr. Helena Štěpánková, CSc.

Abstract: The present work focuses on analyses of the experimental ^{57}Fe nuclear magnetic resonance data and the results of ab initio calculations in order to achieve deeper insight into the hyperfine and electronic structure of magnetite both below and above the Verwey phase transition. Parameters of hyperfine interactions and electronic structure data of the Cc phase of magnetite were extracted from the results of ab initio calculations based on the recently reported crystal structure. Published experimental dependences of the ^{57}Fe nuclear magnetic resonance frequencies on the external magnetic field direction were quantitatively reanalyzed, yielding hyperfine anisotropy data, which were compared to the analogous hyperfine field parameters from the ab initio calculations. The findings were interpreted in the context of up-to-date charge ordering models for magnetite. Attention was also paid to the impact of various cationic substitutions and defects on the electronic structure and hyperfine interactions in magnetite manifested in the ^{57}Fe nuclear magnetic resonance spectra: below the Verwey transition, signal intensity shifts in the spectra were analyzed; above the Verwey transition, the mean field model was adapted for an analysis of temperature dependence of satellite signal frequencies, while the anomalous temperature evolution of main line widths was studied in relation to electrical conductivity.

Keywords: NMR, hyperfine interaction, magnetite, electronic structure

Contents

Chapter 1

Introduction

Magnetite (Fe_3O_4) is an interesting compound due to its unusual physical properties as well as a wide range of technical applications of magnetite-derived ferrites. The characteristic behaviour of magnetite is still not entirely understood despite a long-lasting research, but at the same time, its properties make magnetite a promising candidate for emerging fields of applications ranging from spintronics to hyperthermia therapy. The most typical feature of magnetite is the Verwey phase transition accompanied by significant change of electrical conductivity and other physical quantities. The main open questions are thus related to the mechanism of the Verwey transition as well as to the charge ordering and electronic structure in general, both below and above the transition.

A recent major advance in magnetite research is presented by the determination of the precise crystallographic structure below the Verwey transition accompanied by a suggested model of trimerons [1]. The present thesis takes advantage of this progress while experimental data obtained by nuclear magnetic resonance (NMR) are analyzed in conjunction with results of ab initio calculations using the precise crystal structure. The ^{57}Fe NMR spectra reflect hyperfine field distribution in a sample since resonating nuclei serve as local hyperfine field probes. If limitations of ab initio calculations of electronic structure are properly treated, they make accessible physical quantities and qualities which might be hardly extracted directly from experiments. Suitable combination of these two well-established complementary data sources thus provides reliable deeper insight into the hyperfine interactions and the underlying electronic structure of magnetite below the Verwey transition.

Local sensitivity of NMR qualifies this method also for a study of the impact of substitution defects on the electronic structure of magnetite. This comprises investigations of signal intensity shifts in spectra of the low-temperature phase of magnetite as well as temperature evolution of satellite signal frequencies and anomalous temperature dependence of main line widths above the Verwey transition. Observations of these effects were already reported, but no substantial analyses were available.

The thesis is structured into 9 chapters. The current knowledge about magnetite is summarized in Chapter 2. The objectives of this work are specified in Chapter 3 together with the strategies for their achievement. Chapter 4 covers the theory of the hyperfine interactions as well as the principles of the hyperfine (NMR and Mössbauer) spectroscopies. The density functional theory is explained

in Chapter 5. The employed methods are described in Chapter 6. The results of the work and their discussion related to the low- and high-temperature phase of magnetite are contained in Chapters 7 and 8, respectively. Chapter 9 recapitulates all the findings. Supplementary figures and tables are provided in Appendices A and B, respectively.

Chapter 2

Properties of Magnetite – the State of the Art

Magnetite is a prototype mixed valence iron oxide with strongly correlated charge carriers, which has been fascinating researchers for decades. Large amount of relevant data has been collected during that time and many theoretical models have been conceived. However, despite such a thorough study, the knowledge about the physics of magnetite is still far from complete. This chapter summarizes the most important properties of magnetite together with up-to-date models and interpretations of underlying structure and processes.

2.1 Crystal and Magnetic Structure

Chemical formula of magnetite can be written as $[Fe]_A[Fe_2]_B O_4$, where two different types of iron sites are explicitly denoted – the iron ions at the A sites are inside tetrahedra formed by the nearest oxygen ions, while the B site iron ions are surrounded by oxygen ions forming octahedra. The most known phenomenon connected with magnetite is the Verwey transition occurring at temperature $T_V \approx 120$ K. A broader overview is provided in several reviews, e. g. Refs. [2], [3], [4] and [5].
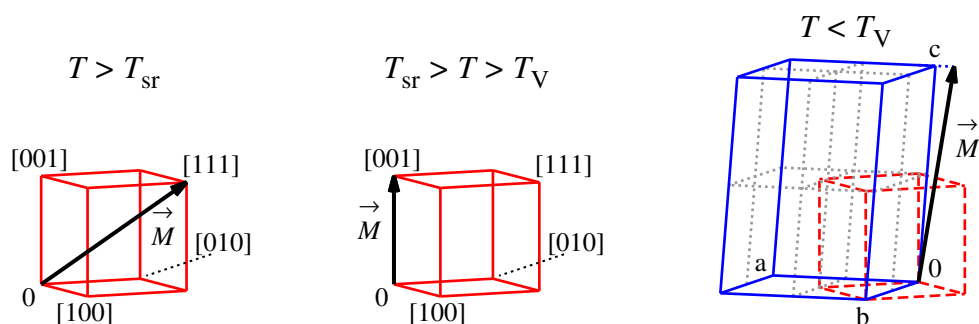
Figure 2.1: Elementary cell of magnetite above (cubic; in red) and below (monoclinic; in blue) the Verwey transition. The black arrows indicate the easy magnetization direction. The illustration exaggerates the tilt of the monoclinic axis as well as of the magnetization direction below the Verwey transition.

Magnetic moments of Fe(A) ions are anti-parallel to the moments of Fe(B) ions [6], resulting total magnetic moment is in a direction of Fe(B) moments. Thus magnetite presents a ferrimagnetic material with Curie temperature $T_C \approx 860$ K. Magnetic ordering of magnetite is caused by double exchange and superexchange interactions [7]. Fig. 2.2 shows temperature dependence of magnetization of both A and B sublattices obtained from experiment [8] and from calculations [7] based on Kubo-Ohata mean field theory [9].
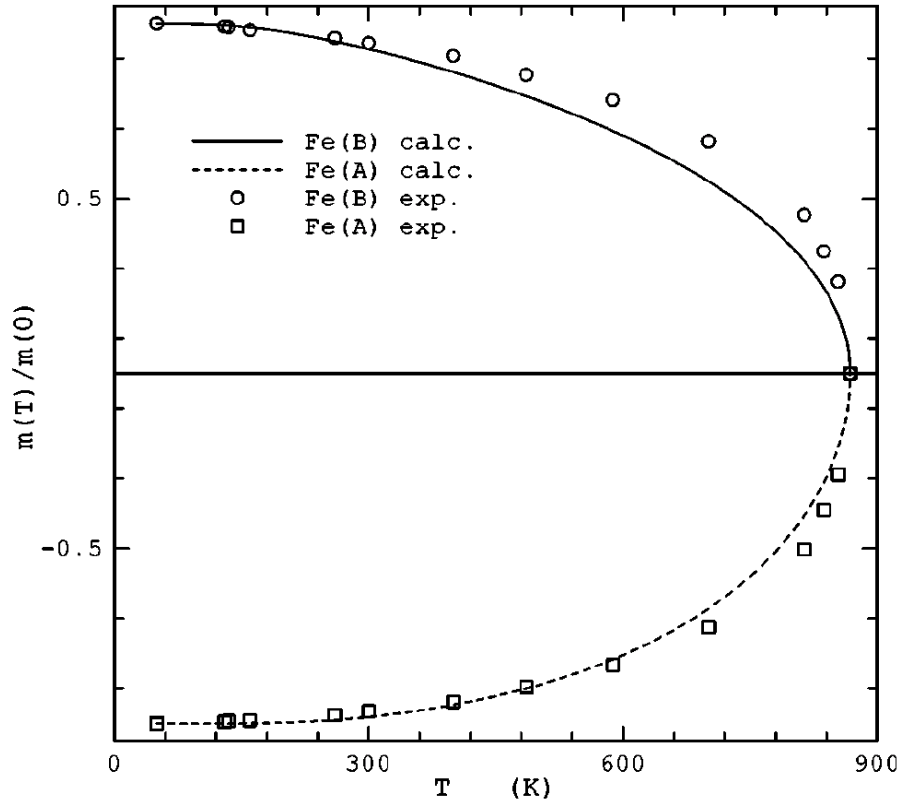
Figure 2.2: Reduced magnetizations of the A and B sublattices in magnetite – experimental and calculated data after Ref. [7]

2.1.1 Structure Above the Verwey Transition

The cubic inverse spinel structure of magnetite above the Verwey transition belongs to a space group $Fd\bar{3}m$ (O_h^7). Lattice parameter is $a_c = 8.3939\,(2)$ Å (at 130 K) [10]. There are 32 O^{2-} ions in an elementary cell forming a face centred cubic lattice with 64 tetrahedral and 32 octahedral interstitial sites between the oxygen ions. Eight Fe^{3+} ions are located at the tetrahedral A sites and sixteen mixed valence $Fe^{2.5+}$ ions occupy the octahedral B sites. The elementary cell consists of eight octants with two different iron ion arrangements as illustrated in Fig. 2.3 – details can be found in Refs. [11], [6]. Local symmetry and other crystallographic parameters of occupied sites are listed in Table 2.1 [12] while Table 2.2 summarizes the nearest neighbour distances.
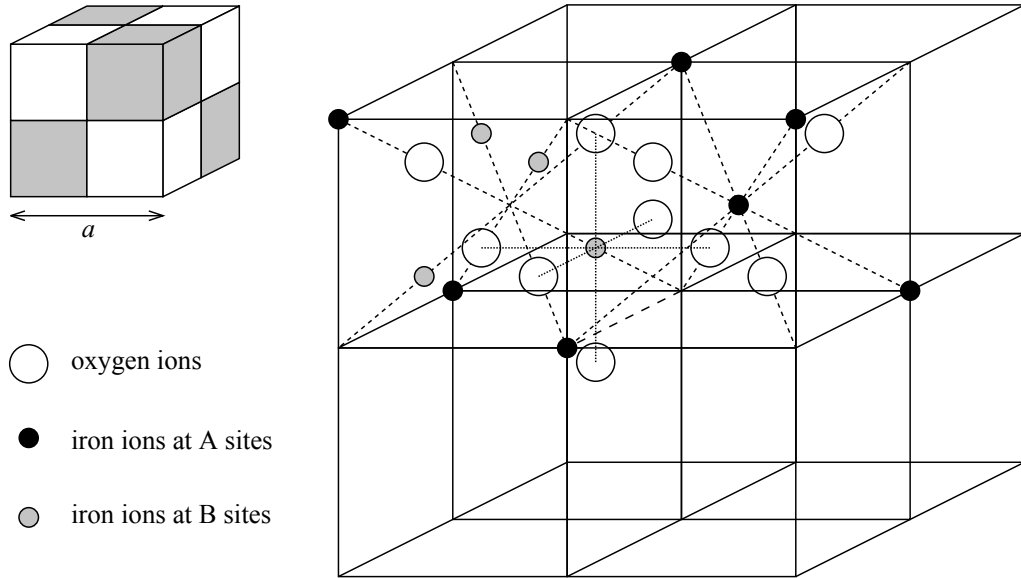
Figure 2.3: Arrangement of ions in an elementary cell of magnetite above the Verwey transition

Table 2.1: Occupied crystallographic sites in cubic magnetite structure (origin at tetrahedral site) [12]; $\mu = 3/8 + 0.0049\,(5)$[10]. Additional positions are generated by (0, 1/2, 1/2), (1/2, 0, 1/2) and (1/2, 1/2, 0) translations.

Occupied positions	Multiplicity	Wyckoff symbol	Symmetry	Fractional coordinates	
Fe^{3+} ion A sites	8	a	$\bar{4}3m$	0, 0, 0	1/4, 1/4, 1/4
$Fe^{2.5+}$ ion B sites	16	d	$\bar{3}m$	5/8, 5/8, 5/8	7/8, 5/8, 7/8
				5/8, 7/8, 7/8	7/8, 7/8, 5/8
O^{2-} ion sites	32	e	3m	$\mu, -\mu, -\mu$	$1/4 - \mu, 1/4 - \mu, 1/4 - \mu$
				$-\mu, \mu, -\mu$	$1/4 - \mu, 1/4 + \mu, 1/4 + \mu$
				$-\mu, -\mu, \mu$	$1/4 + \mu, 1/4 - \mu, 1/4 + \mu$
				μ, μ, μ	$1/4 + \mu, 1/4 + \mu, 1/4 - \mu$

Table 2.2: Nearest neighbour distances in the cubic phase of magnetite – based on Refs. [1] and [10].

sites	distance (nm)
Fe(A) - Fe(A)	0.36347(1)
Fe(A) - Fe(B)	0.34799(1)
Fe(B) - Fe(B)	0.29677(1)
Fe(A) - O	0.18885(2)
Fe(B) - O	0.20582(1)

If the temperature is between the Verwey transition and the spin reorientation transition, which occurs at $T_{sr} \approx 125 - 130$ K, the easy magnetization direction corresponds to [001] direction in the cubic lattice. All Fe(A) ions are then magnetically equivalent and the same applies for the Fe(B) ions.

Above the spin reorientation transition, the easy magnetization direction becomes the cube diagonal [111]. While the Fe(A) sites all remain magnetically equivalent, the Fe(B) sites split into 2 groups of magnetically equivalent sites in a ratio of 1:3.

2.1.2 Structure Below the Verwey Transition

When the temperature drops below the Verwey transition temperature, the symmetry of magnetite structure is lowered from cubic to monoclinic Cc symmetry. Lattice parameters of the Cc cell at 10 K are $a = 11.88881\,(3)$ Å, $b = 11.84940\,(3)$ Å, $c = 16.77515\,(14)$ Å and the monoclinic angle has a value of $\beta = 90.2363\,(2)°$ [10]. Since the angle β is very close to right angle, the dominant deformation is orthorhombic with orthogonal system of axes $\vec{a}$, $\vec{b}$, $\vec{c}_0$. The $\vec{c}_0$ axis is usually chosen parallel to cubic [001] direction, $\vec{a} \parallel [\bar{1}10]$ and $\vec{b} \parallel [1\bar{1}0]$. The elementary cell now contains 32 Fe(A) sites and 64 Fe(B) sites which are grouped in quartets of crystallographically equivalent sites due to centration and ac-glide symmetry. Fractional coordinates of the atoms in the magnetite Cc cell were published by Senn et al. [1]

Orthorhombic Twinning

Cooling of magnetite through the Verwey transition is generally accompanied by orthorhombic twinning as the cubic $\rightarrow$ orthorhombic symmetry lowering provides six types of orthorhombic domains (the indices refer to cubic cell):

$$O_1 \equiv \vec{a} \parallel [\bar{1}\bar{1}0], \ \vec{b} \parallel [1\bar{1}0], \ \vec{c}_0 \parallel [001] \tag{2.1}$$
$$O_2 \equiv \vec{a} \parallel [1\bar{1}0], \ \vec{b} \parallel [110], \ \vec{c}_0 \parallel [001]$$
$$O_3 \equiv \vec{a} \parallel [0\bar{1}\bar{1}], \ \vec{b} \parallel [0\bar{1}1], \ \vec{c}_0 \parallel [100]$$
$$O_4 \equiv \vec{a} \parallel [01\bar{1}], \ \vec{b} \parallel [011], \ \vec{c}_0 \parallel [100]$$
$$O_5 \equiv \vec{a} \parallel [\bar{1}0\bar{1}], \ \vec{b} \parallel [\bar{1}01], \ \vec{c}_0 \parallel [010]$$
$$O_6 \equiv \vec{a} \parallel [\bar{1}0\bar{1}], \ \vec{b} \parallel [\bar{1}01], \ \vec{c}_0 \parallel [010]$$

However, the orthorhombic twinning can be avoided if the cooling happens in an external magnetic field, because the crystallographic axes correspond to the

hard, intermediate and easy magnetization directions. For example, Mizoguchi applied $B_{ext} = 1.5$ T parallel to [113] or [$\bar{1}$23] [13] and $\vec{B}_{ext} \| [\bar{1}12]$ [14], while Abe et al. [15] employed a field forming an angle of 40° with [001] in $(1\bar{1}0)$ plane to suppress orthorhombic twinning (the indices refer to cubic cell). As a result, the $\vec{c}_0$ axis was set parallel to [001] and $\vec{a}$, $\vec{b}$ were unambiguously defined.

Monoclinic Twinning

Orthorhombic deformation is accompanied by tiny monoclinic deformation – the monoclinic $\vec{c}$ axis is tilted by an angle of $\approx 0.23°$ from the orthorhombic $\vec{c}_0$ axis towards the $-\vec{a}$ axis. However, impact of this small tilt on magnetic anisotropy is significant – the magnetization easy axis is neither the $\vec{c}_0$ nor the $\vec{c}$ axis, but it is canted by $\approx 2°$ towards $-\vec{a}$ direction [16]. For this magnetization direction, the number of magnetically non-equivalent sites is the same as the number of crystallographically non-equivalent sites – i. e. there are 8 magnetically non-equivalent Fe(A) sites and 16 magnetically non-equivalent Fe(B) sites.

Two equivalent cantings exist and thus a monoclinic twinning occurs. The monoclinic twinning cannot be prevented by an external magnetic field. Nevertheless, a proper combination of a pressure and the field may eliminate the both the orthorhombic and monoclinic twinning – e. g. Abe et al. [16] applied $B_{ext} = 1.35$ T parallel to cubic [001] axis and simultaneously squeezed magnetite crystal in the cubic [111] direction. Unless the monoclinic twining is removed, equal probability of the two possible monoclinic twins is usually assumed [13], [14], [16].

2.2 The Verwey Transition and the Charge Ordering

The typical anomaly connected with the Verwey transition concerns a rather sharp step in temperature dependence of DC electrical conductivity – see Fig. 2.4 [17]. Other anomalies at T_V can be observed e. g. in the AC susceptibility, specific heat or magnetization measurements. The original hypothesis of the Verwey transition origin comprised a charge ordering of Fe^{2+} and Fe^{3+} B site cations in alternating (001) layers below T_V [18]. The process of the ordering is facilitated by electron hopping between the cation sites, while the thermal excitations above T_V break the ordering. However, this concept was found inadequate by later works.

Several experiments [19], [20], [21] suggested that the transition is driven probably by the Coulomb interaction rather than by the magnetic interaction. Taking into account the strength of the nearest neighbour Coulomb interaction, Anderson [22] interpreted the Verwey transition as a transition between the long range ordered (LRO) (below T_V) and short range ordered (SRO) (above T_V) states. The SRO is described by the Anderson condition: the sum of the charges of the 4 nearest neighbour Fe(B) ions forming a tetrahedron (see Fig. 2.3) is constant – i. e. each tetrahedron contains 2 Fe^{2+}(B) and 2 Fe^{3+}(B) ions. The LRO order below the Verwey transition shall be caused by the next nearest neighbour Coulomb interaction or some other additional interaction.
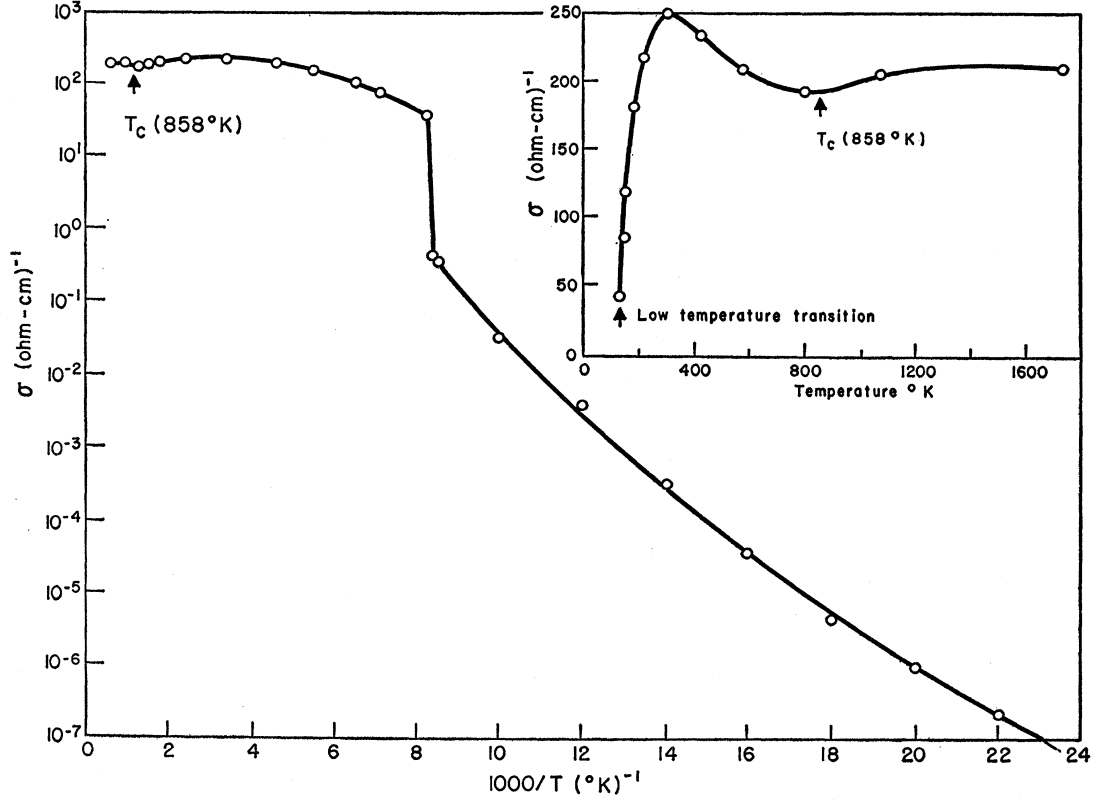
Figure 2.4: Temperature dependence of DC electrical conductivity of magnetite. [17]

Various other detailed concepts were proposed to explain the experimental data. Several polaron (i. e. considering electron-phonon interaction) models were derived in order to understand the temperature dependence of electrical conductivity. The small polaron model developed by Ihle and Lorenz [23], [24] describes the data in terms of polaron hopping and band conductivity while achieving a good agreement with experiments [25].

The anomaly in magnetization at T_V as well as the very low mobility of charge carriers above T_V are treated in the magneto-electronic model of Belov [26] by considering the Vonsovskii exchange interaction. Below T_V, the Vonsovskii interaction causes localization and ordering of the hopping electrons into a sublattice antiferromagnetically coupled to the B sublattice. Whereas above T_V, this ordering is broken but the electron mobility is still impacted.

Various models of charge ordering in the low-temperature LRO phase based on experimental data (e. g. Refs. [10], [13], [20], [27], [28], [29]) or ab initio calculations (e. g. Refs. [30], [31], [32], [33], [34], [35], [36]) were published. The ^{57}Fe NMR measurements [37] indicated the charge carrier localization (at least at the characteristic timescale of the experiment) but also dismissed the sharp categorization of Fe(B) ions as Fe^{2+} and Fe^{3+} due to a strong mixing of the iron ion states. Based on his NMR data, Mizoguchi [14] proposed the charge ordering below T_V as a frozen charge density wave. However, a lack of knowledge of the precise crystal structure of the low-temperature phase presented a major impediment in the search for the real charge ordering.

This was changed recently by Senn et al. [1] – they reported the crystal

structure of the Cc phase of magnetite, as well as the information of Fe(B) charges in the form of bond valence sums, which allowed them to conceive a model of trimerons. The trimeron consists of three nearest-neighbour Fe(B) ions in a line. The distances between these ions are typically shorter compared to the average Fe(B)-Fe(B) bonds. A part of the minority-spin t_{2g} electron of the Fe^{2+}-like ion in the trimeron centre is transferred to the two Fe^{3+}-like ions at the ends. The trimerons are connected together through the end ions (with one exception) and thus compose a complex network. There are two Fe(B) ions which are not parts of any trimeron. The work in Ref. [1] was followed by ab initio calculations of electronic structure [38].

C. H. Patterson in his recent work [39] carried out another ab initio calculation (employing the hybrid Becke, three-parameter, Lee-Yang-Parr (B3LYP) exchange-correlation potential) of electronic structure of the low-temperature phase of magnetite based on the crystal structure data from Ref. [1]. The results of the calculation were accompanied by an alternative concept of the charge ordering of Fe(B) ions. According to Patterson, six from the ten shortest Fe(B)-Fe(B) bonds from bimodal Fe(B)-Fe(B) distance distribution compose a branched broken zig-zag chain with delocalized minority-spin $3d$ electrons, whereas the remaining four bonds are one-electron bonds between Fe(B) ion pairs. (Within the trimeron model, these ten shortest Fe(B)-Fe(B) bonds are contained in the trimeron network.)

The work of Senn et al. [1] indicate that from a crystallographic point of view, a cooling through the Verwey transition can be described as a freezing of a large set of phonon modes. The mechanism and dynamics of the Verwey transition was studied in the context of trimeron model by S. de Jong et al. [40] by means of pump–probe X-ray diffraction and optical reflectivity methods. They found that femtosecond laser excitation applied on a magnetite sample below T_V induces charge transfer resulting within 300 fs into a creation of holes in the trimeron lattice. When the laser pulse fluence was high enough, this was followed on 1.5 ± 0.2 ps timescale by a phase separation.

The question of SRO state above the Verwey transition was investigated in many experiments comprising namely photoemission spectroscopy [41], [42], [43], [44], various scattering methods [45], [46], [47], [48], [49], extended x-ray absorption fine structure measurements [50], optical conductivity spectroscopy [51] and acoustical measurements [52], [53]. The experiments indicate a presence of correlated SRO state, probably of the polaronic character (see Refs. [23], [24]). On the other hand, the ^{57}Fe NMR measurements [37] found no SRO above T_V at the NMR experiment timescale. That means that the possible SRO state above T_V is expected to be fast fluctuating. This might be related to the idea of trimerons existing above the Verwey transition as quasiparticles [1]. The recent work of A. Bosak et al. [54] based on the temperature evolution of x-ray diffuse scattering in magnetite revealed that the SRO state pattern is inherited from the structure below T_V and the Verwey transition is connected with a loss of commensurability. Their observation of characteristic length varying from ≈ 2 unit cells at a temperature slightly above T_V to ≈ 1 unit cell at room temperature implies that the ordering pattern is related more likely to trimeron complexes than to individual trimerons.

2.3 Substitution Defects in Magnetite

If structural defects like cationic substitutions or vacancies are present in magnetite lattice, they can significantly influence physical properties of studied sample. The most representative manifestation of this influence is a decrease of the Verwey transition temperature when a concentration of substitution or vacancies in the sample increases [55], [56], [57], which is illustrated in Fig. 2.5 [58]. If the concentration exceeds a critical limit (denoted in figure 2.5 by vertical line), the Verwey transition is no longer the first order transition – see Refs. [3], [58]. Beside the changes of T_V, the temperature dependences of electrical resistivity [57], [59] as well as Mössbauer spectra [8], [60], [61], [62] were measured for various concentrations and types of substitution. Due to the impact of the charged defects on electronic structure of the B sublattice, a deeper investigation of substituted or vacancy-containing samples may shed a light on the related questions.
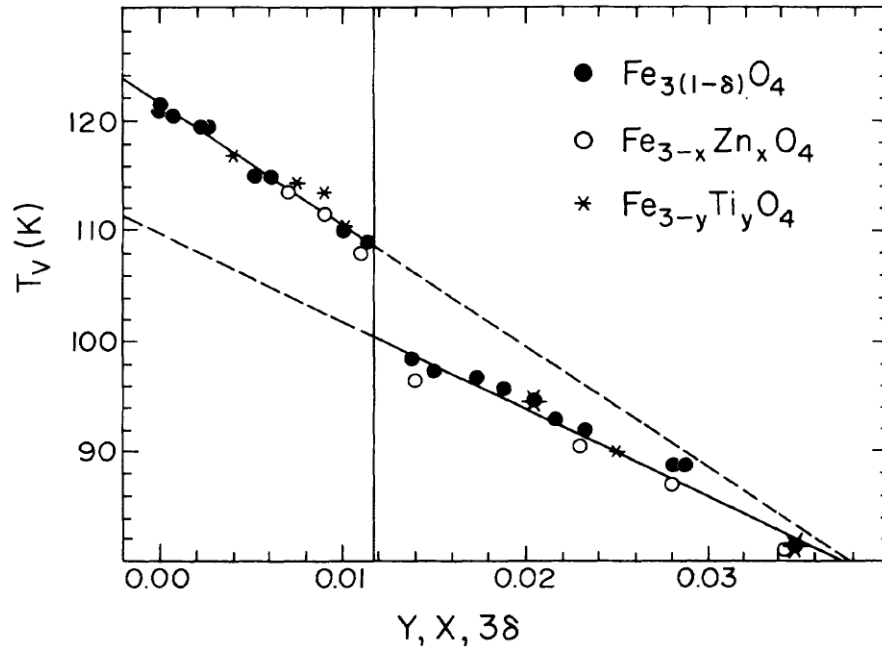
Figure 2.5: Dependence of the Verwey transition temperature on sample composition. The range on the left from the vertical line corresponds to the first order transition. [58]

Chapter 3

Objectives and Strategies

This study shall contribute to the answers to the questions concerning the charge ordering in the long range ordered state below the Verwey transition and the electronic ordering and processes in the high-temperature phase. The focus will be placed on the hyperfine interactions and the underlying electronic structure. The data obtained for pure magnetite will be complemented by the results for magnetite with various substitution defects. The results of new experiments and calculations as well as already available data will be analyzed and interpreted in the context of the current knowledge about magnetite.

Below the Verwey transition, the investigation will be based on a thorough analysis of ab initio calculations of the electronic structure and hyperfine fields (taking advantage of the precise crystal structure published by Senn et al. [1]) in combination with a rigorous quantitative reanalysis of the experimental ^{57}Fe NMR data of Mizoguchi [14]. The results shall allow for an assessment of the validity of the trimeron concept and the Patterson's model [39] and for a deeper understanding of the charge-ordered structure and properties of these models. A reliable detailed assignment of NMR signals below the Verwey transition to corresponding crystallographic sites is not known yet, thus a comparison of the hyperfine parameters extracted from the ab initio calculations and from the experimental data shall not only corroborate the calculation results but also seek links between particular NMR signals and crystallographic sites. Employing the acquired knowledge, an improvement of the current insight into the impact of substitution defects on electronic structure is expected from an analysis of ^{57}Fe NMR spectra of magnetite samples with various types and concentrations of the defects. Further, the link between the ab initio calculation results and another experimental hyperfine method will be created by a simulation of Mössbauer spectrum, which will allow for a comparison with corresponding experimental data.

Above the Verwey transition, the work will focus on an analysis of manifestations of cationic defect presence in ^{57}Fe NMR spectra, which comprise namely satellite signals and line broadening. Temperature evolution of both effects will be studied for various types of substitution defects. The dependences of satellite signal frequencies will be analyzed in comparison with an adapted mean field model. The line broadening will be studied in a broader context of anomalous temperature dependence of linewidths exhibited by magnetite above the Verwey transition and a search for a relation to electronic processes will be attempted.

Chapter 4

Hyperfine Interactions

Hyperfine interactions are very sensitive to the crystal and magnetic, as well as electronic structure of the sample in a neighbourhood of a particular nucleus. This renders the study of hyperfine interactions a very suitable tool for investigation of magnetically ordered materials – both unperturbed and defect-containing systems.

4.1 Magnetic Hyperfine Interaction

4.1.1 Nuclear Magnetic Moment

Nuclear spin $\vec{I}$ is a vector sum of spin and orbital angular momenta of nucleons. Magnitude of nuclear spin $|\vec{I}|$ is related to a nuclear spin quantum number I (0, 1/2, 1, 3/2, ...):

$$|\vec{I}| = \hbar\sqrt{I(I+1)}. \tag{4.1}$$

The z-component of the nuclear spin is determined by nuclear spin magnetic quantum number m ($-I$, $-I+1$, ..., $I-1$, I)

$$I_z = \hbar m. \tag{4.2}$$

Nuclear magnetic moment is given by a product of the nuclear spin and gyromagnetic ratio γ or it can be expressed equivalently using nuclear g factor (μ_N is nuclear magneton)

$$\hat{\vec{\mu}} = \gamma\hat{\vec{I}} = \frac{g\mu_\mathrm{N}}{\hbar}\hat{\vec{I}}, \tag{4.3}$$

while the following holds for z-component:

$$\hat{\mu}_z = \gamma\hat{I}_z = \frac{g\mu_\mathrm{N}}{\hbar}\hat{I}_z. \tag{4.4}$$

4.1.2 Hamiltonian of Magnetic Hyperfine Interaction

Assuming that the nuclear magnetic moment $\vec{\mu}$ is placed in a (static) magnetic field $\vec{B}_0$, the interaction can be described by Hamiltonian

$$\hat{H}_0 = -\hat{\vec{\mu}} \cdot \vec{B}_0. \tag{4.5}$$

Choosing $\vec{B}_0 = (0, 0, B_0)$ allows to rewrite the Hamiltonian as

$$\hat{H}_0 = -\gamma \hat{I}_z B_0 = -\frac{g\mu_{\mathrm{N}}}{\hbar} \hat{I}_z B_0. \tag{4.6}$$

The values of magnetic quantum number m (see (4.2)) determine energy eigenvalues:

$$E_m = -\gamma \hbar m B_0 = -g\mu_{\mathrm{N}} m B_0. \tag{4.7}$$

The set of $2I + 1$ energy eigenvalues represents Zeeman multiplet. Equidistant energy levels of the multiplet are linked with particular orientations of the nuclear magnetic moment with respect to $\vec{B}_0$ direction.

4.1.3 Hyperfine Field

In magnetically ordered matters, a dominant contribution to a local magnetic field at nuclei is the hyperfine field, which arise from magnetic moments of electrons:

$$\hat{\vec{B}}_{\mathrm{hf}} = -\frac{\mu_0 \mu_B}{2\pi} \sum_i \left(\frac{\hat{\vec{l}}_i}{r_i^3} + \frac{\hat{\vec{s}}_i}{r_i^3} - \frac{3\left(\hat{\vec{s}}_i \cdot \vec{r}_i\right)\vec{r}_i}{r_i^5} + \frac{8\pi}{3}\hat{\vec{s}}_i \delta\left(\vec{r}_i\right) \right), \tag{4.8}$$

where the index i ranges over all electrons in the material, μ_0 stands for vacuum permeability, μ_B for Bohr magneton, $\hat{\vec{l}}_i$ for orbital moments and $\hat{\vec{s}}_i$ for spins of particular electrons, while $\vec{r}_i$ denotes their positions (with respect to nucleus). The first term of this formula describes magnetic field originating from electron orbital moments, the next two terms represent dipolar interaction between nucleus and electron spins, whereas the last term denotes Fermi contact interaction – the equation can be thus schematically rewritten as

$$\hat{\vec{B}}_{\mathrm{hf}} = \hat{\vec{B}}'_{\mathrm{orb}} + \hat{\vec{B}}'_{\mathrm{dip}} + \hat{\vec{B}}'_{\mathrm{cont}}. \tag{4.9}$$

In the case of a calculation of hyperfine field, it is convenient to split the summation in equation (4.8) to a summation over on-site electrons and to a contribution of electron magnetic moments at other sites of crystal lattice. Therefore, the relation (4.9) changes to

$$\hat{\vec{B}}_{\mathrm{hf}} = \hat{\vec{B}}_{\mathrm{orb}} + \hat{\vec{B}}_{\mathrm{dip}} + \hat{\vec{B}}_{\mathrm{cont}} + \hat{\vec{B}}_{\mathrm{lat}}. \tag{4.10}$$

Hyperfine Field Anisotropy

Due to the anisotropic nature of crystal lattice environment, the hyperfine field B_{hf} at a particular site in a crystal in general significantly varies depending on the direction of magnetization $\vec{M}$. Assuming that 4th and higher order terms in direction cosines ϑ_α, $\alpha = a, b, c$ (with respect to orthogonal axes[1]) of $\vec{M}$ may be neglected, magnitude of the hyperfine field at a particular site in a crystal can be expressed as

---

[1]such as orthorhombic axes $\vec{a}$, $\vec{b}$, $\vec{c}_0$ common for an approximate description of low-temperature phase of magnetite

$$B_{\text{hf}} = B_{\text{iso}} + B_{aa}\vartheta_a^2 + B_{bb}\vartheta_b^2 + B_{cc}\vartheta_c^2 + 2(B_{ab}\vartheta_a\vartheta_b + B_{ac}\vartheta_a\vartheta_c + B_{bc}\vartheta_b\vartheta_c) =$$

$$= B_{\text{iso}} + \begin{pmatrix} \vartheta_a \\ \vartheta_b \\ \vartheta_c \end{pmatrix} \cdot \begin{pmatrix} B_{aa} & B_{ab} & B_{ac} \\ B_{ab} & B_{bb} & B_{bc} \\ B_{ac} & B_{bc} & B_{cc} \end{pmatrix} \cdot \begin{pmatrix} \vartheta_a \\ \vartheta_b \\ \vartheta_c \end{pmatrix} = B_{\text{iso}} + \begin{pmatrix} \vartheta_a \\ \vartheta_b \\ \vartheta_c \end{pmatrix} \cdot \hat{B}_{\text{ani}} \cdot \begin{pmatrix} \vartheta_a \\ \vartheta_b \\ \vartheta_c \end{pmatrix},$$

$$(4.11)$$

where the isotropic field B_{iso} and anisotropy tensor $\hat{B}_{\text{ani}}$ $(\text{Tr}\left[\hat{B}_{\text{ani}}\right] = 0)$ are separated. The tensor of anisotropy can be transformed into a canonical form

$$\hat{B}'_{\text{ani}} = \begin{pmatrix} B'_a & 0 & 0 \\ 0 & B'_b & 0 \\ 0 & 0 & B'_c \end{pmatrix} \tag{4.12}$$

while principal axes $\vec{p}_a$, $\vec{p}_b$ and $\vec{p}_c$ of the tensor are obtained. A simple parameter serving as a measure of hyperfine field anisotropy can be defined:

$$B_{\text{ani}} = \sqrt{\frac{1}{3}((B'_a - B'_b)^2 + (B'_b - B'_c)^2 + (B'_c - B'_a)^2)} = \sqrt{B_a'^2 + B_b'^2 + B_c'^2}. \tag{4.13}$$

4.2 Electric Hyperfine Interaction

4.2.1 Charge of Nucleus

A description of electric potential $\varphi_{\text{N}}\left(\vec{r}\right)$ produced by a charge of nucleus usually employs multipole expansion

$$\varphi_{\text{N}}\left(\vec{r}\right) = \frac{1}{4\pi\epsilon_0}\left[\frac{q}{r} + \frac{\vec{p}\cdot\vec{r}}{r^3} + \frac{1}{2}\sum_{i,j}Q_{ij}\frac{x_ix_j}{r^5} + ...\right], \tag{4.14}$$

where q is a total charge, $\vec{p}$ is a dipole moment and Q_{ij} represents a quadrupole moment, which can be expressed using a volume charge density $\rho_{\text{N}}\left(\vec{r}\right)$:

$$q = \int_{V'}\rho_{\text{N}}\left(\vec{r'}\right)dV' \tag{4.15}$$

$$\vec{p} = \int_{V'}\vec{r'}\,\rho_{\text{N}}\left(\vec{r'}\right)dV' \tag{4.16}$$

$$Q_{ij} = \int_{V'}\left(3x_i'x_j' - \delta_{ij}r'^2\right)\rho_{\text{N}}\left(\vec{r'}\right)dV' \tag{4.17}$$

Quantum mechanics yields the following relation for the charge density

$$\rho_{\text{N}}\left(\vec{r'}\right) = \sum_{i=1}^{Z}eP_i\left(\vec{r'}\right), \tag{4.18}$$

where e is an elementary charge and

$$P_i\left(\vec{r}'\right) = \int |\psi\left(\vec{r}^{(1)},...\vec{r}^{(i-1)},\vec{r}',\vec{r}^{(i+1)},...\vec{r}^{(A)}\right)| d\vec{r}^{(1)}...d\vec{r}^{(i-1)} d\vec{r}^{(i+1)}...d\vec{r}^{(A)} \tag{4.19}$$

(i. e. $P_i\left(\vec{r}'\right)dV'$ is a probability of nucleon i being located in a volume element dV' containing the point $\vec{r}'$). Thus, the expressions (4.15), (4.16) and (4.17) can be written in the following form where $d\tau = d\vec{r}^{(1)}...d\vec{r}^{(A)}$:

$$q = \sum_{k=1}^{Z} \int e|\psi|^2 d\tau = Ze \tag{4.20}$$

$$\vec{p} = \sum_{k=1}^{Z} \int e\vec{r}'^{(k)}|\psi|^2 d\tau \tag{4.21}$$

$$Q_{ij} = \sum_{k=1}^{Z} \int e\left(3x_i'^{(k)}x_j'^{(k)} - \delta_{ij}\left(r'^{(k)}\right)^2\right)|\psi|^2 d\tau. \tag{4.22}$$

Considering the defined parity of wave function of a nucleus in a stationary state, the expression (4.21) implies that the dipole moment, as well as higher even-order moments, are zero.

Nuclear Electric Monopole

The first term in the multipole expansion (4.14) is called a monopole. When focusing solely on this term, the charge of nucleus is often approximated by a point charge, which yields electric potential

$$\varphi_{\mathrm{Nm}}\left(\vec{r}\right) = \frac{1}{4\pi\epsilon_0}\frac{Ze}{r} \tag{4.23}$$

for $r > 0$.

If the finite size of nucleus is taken into account, a better approximation shall be used [63]: the potential (4.23) applies outside of the nuclear charge radius R, whereas a homogeneously charged sphere of radius R is usually assumed in place of the nucleus, i. e.

$$\varphi_{\mathrm{Nm}}\left(\vec{r}\right) = \frac{1}{4\pi\epsilon_0}\frac{Ze}{R}\left(\frac{3}{2} - \frac{1}{2}\left(\frac{r}{R}\right)^2\right) \tag{4.24}$$

for $r \le R$.

The nuclear charge radius R can be derived from nuclear mean square radius $\langle r_{\mathrm{N}}^2 \rangle$ [64] as

$$R = \sqrt{\frac{5}{3}\langle r_{\mathrm{N}}^2 \rangle}. \tag{4.25}$$

Nuclear Electric Quadrupole

Quadrupole moment Q_{ij} is a symmetric second-order tensor. Transformation of the tensor into a system of its principal axes eliminates non-diagonal elements. Taking into account zero trace of the tensor (see equations (4.17) or (4.22)) and axial symmetry of nuclear charge distribution, only the Q_{zz} element appears to be independent.

Using the Wigner-Eckart theorem, the quadrupole moment can be expressed in terms of nuclear spin

$$Q_{ii} = eQ\frac{3I_i^2 - \vec{I}^2}{I(2I-1)}, \tag{4.26}$$

where the quantity Q is called nuclear quadrupole moment. In the case of nuclei with the spin $I < 1$, the Q is zero. The spin of ^{57}Fe nuclei in the ground state is $1/2$ so there is no interaction comprising nuclear quadrupole moment observable by ^{57}Fe NMR. However, the first excited state of ^{57}Fe nucleus has the spin $3/2$, thus the nuclear quadrupole interaction with electric field gradient plays a role in Mössbauer spectra (see part 4.5.4).

4.2.2   Monopole Interaction

The interaction of electrons with the potential generated by nuclear monopole can be based on the point charge approximation (potential (4.23)) while the effect of finite size of nucleus is treated as a perturbation. The perturbation potential [65]

$$\Delta\varphi(r) = \frac{1}{4\pi\epsilon_0}Z\frac{e}{R}\left[\left(\frac{3}{2} - \frac{1}{2}\left(\frac{r}{R}\right)^2\right) - \frac{R}{r}\right] \tag{4.27}$$

for $r \leq R$ and $\Delta\varphi(r) = 0$ for $r > R$ allows to express the perturbation energy

$$\Delta E = \frac{1}{4\pi\epsilon_0}\frac{2}{5}\pi ZeR^2\rho_0, \tag{4.28}$$

where ρ_0 is electron charge density at nucleus (assumed to be constant within the nuclear charge radius R).

For constant values of R and ρ which is the case of ^{57}Fe NMR experiments, ΔE presents only a shift of energy levels of the electrons-nuclei system without any observable effect on NMR transition energies. Nevertheless, the first excited state of ^{57}Fe nucleus has different R than the ground state, which gives a rise to isomer shifts in spectra (see part 4.5.3).

4.2.3   Quadrupole Interaction

Electric Field Gradient Tensor

A charge distribution in crystal lattice determines an electrostatic potential $\varphi\left(\vec{r}\right)$. While the first derivative of the potential corresponds to a negative of the electric field, the second derivative is gradient of the electric field:

$$\varphi_{ij}\left(\vec{r}\right) = \frac{\partial^2\varphi\left(\vec{r}\right)}{\partial x_i \partial x_j} \tag{4.29}$$

This expression evaluated at the position of a particular nucleus and brought into a traceless form

$$V_{ij} = \varphi_{ij} - \frac{1}{3}\delta_{ij}\sum_k \varphi_{kk} \qquad (4.30)$$

is referred to as the electric field gradient (EFG) tensor. The EFG tensor

$$V = \begin{pmatrix} V_{aa} & V_{ab} & V_{ac} \\ V_{ba} & V_{bb} & V_{bc} \\ V_{ca} & V_{cb} & V_{cc} \end{pmatrix} \qquad (4.31)$$

can be diagonalized, which yields

$$V' = \begin{pmatrix} V_{xx} & 0 & 0 \\ 0 & V_{yy} & 0 \\ 0 & 0 & V_{zz} \end{pmatrix} \qquad (4.32)$$

and principal axes $\vec{v}_{xx}$, $\vec{v}_{yy}$ and $\vec{v}_{zz}$. The traceless form implies that only two elements are independent. By convention, the component of the largest magnitude is denoted as V_{zz} and the remaining components are characterized by the asymmetry parameter

$$\eta = \frac{V_{xx} - V_{yy}}{V_{zz}}, \qquad (4.33)$$

while $|V_{zz}| \geq |V_{yy}| \geq |V_{xx}|$.

Hamiltonian of Nuclear Electric Quadrupole Interaction

Based on the relations characterizing nuclear electric quadrupole moment and electric field gradient, their interaction can be described (in a frame of reference defined by the principal axes of the EFG tensor) by the following Hamiltonian:

$$\hat{H}_Q = \frac{eQV_{zz}}{4I(2I-1)}\left[\left(3\hat{I}_z^2 - |\hat{\vec{I}}|^2\right) + \eta\left(\hat{I}_x^2 - \hat{I}_y^2\right)\right] \qquad (4.34)$$

Corresponding eigen energies for $I = 3/2$ (excited state of ^{57}Fe in Mössbauer spectroscopy) are given by expression

$$E_{Q,m} = \frac{eQV_{zz}}{4I(2I-1)}\left(3m^2 - I(I+1)\right)\sqrt{1 + \frac{\eta^2}{3}}. \qquad (4.35)$$

4.3 Combined Magnetic and Electric Hyperfine Interaction

In the case of a simultaneous presence of magnetic and electric hyperfine interaction, an analysis of eigen energy levels becomes more complex. While the monopole interaction can be treated separately, the magnetic and quadrupole interactions have to be solved en bloc. Combined Hamiltonian

$$H_{0,Q} = H_0 + H_Q = -\gamma\hat{I}_{z'}B_0 + \frac{eQV_{zz}}{4I(2I-1)}\left[\left(3\hat{I}_z^2 - |\hat{\vec{I}}|^2\right) + \eta\left(\hat{I}_x^2 - \hat{I}_y^2\right)\right] \qquad (4.36)$$

(where the quantization axis z' of the magnetic interaction is generally independent of the principal axes of the EFG tensor used as a frame of reference in the quadrupole interaction term) can be solved exactly only in special cases. If one of the interactions is considerably weaker than the other one, analytical solutions based on perturbation theory can be used – see e. g. Ref. [66]. Otherwise, numerical methods have to be applied in order to find the solution of Hamiltonian (4.36) as well as the intensities of possible transitions – note that even transitions forbidden for a pure (or weakly perturbed) magnetic interaction may occur in such a case.

4.4   Nuclear Magnetic Resonance Spectroscopy

4.4.1   NMR Principles

Effect of RF Field

Let us assume a nucleus with a magnetic moment $\hat{\vec{\mu}}$ placed in a static magnetic field B_0 – such a system is described by Hamiltonian (4.5). Now we apply also an external radio-frequency (RF) magnetic field $\vec{B}_1 = (B_1 \cos \omega_z t, B_1 \sin \omega_z t, 0)$ (ω_z is angular frequency) beside the static magnetic field $\vec{B}_0$. Hamiltonian of the interaction of the nuclear magnetic moment with the magnetic field reads

$$\hat{H} = \hat{H}_0 + \hat{H}_1 \left(t \right), \tag{4.37}$$

where

$$\hat{H}_1 = -\hat{\vec{\mu}} \cdot \vec{B}_1 = -\gamma B_1 \left(\hat{I}_x \cos \omega_z t + \hat{I}_y \sin \omega_z t \right) = -\frac{\gamma B_1}{2} \left(\hat{I}^- e^{i\omega_z t} + \hat{I}^+ e^{-i\omega_z t} \right) \tag{4.38}$$

($\hat{I}^-$ and $\hat{I}^+$ are ladder operators).

Transitions between the Zeeman multiplet levels induced by the RF field present the nuclear magnetic resonance (NMR). Perturbation theory approximation (valid for $B_1 << B_0$) yields the probability of transition between states with quantum numbers m and m' proportional to perturbation matrix element

$$P_{m',m} \sim |\langle m'|\hat{H}_1|m\rangle|^2. \tag{4.39}$$

The form of Hamiltonian (4.38) together with the properties of ladder operators allow only transitions between neighbouring levels (i. e. $m' = m \pm 1$).

These allowed transitions are connected with an absorption or an emission of energy quantum $|\Delta E| = \gamma \hbar B_0$ (see equation (4.7)). This energy can be rewritten into a form of $\Delta E = \hbar \omega_0$, thus yielding the resonance condition [67]

$$\omega_0 = \gamma B_0, \tag{4.40}$$

where ω_0 is named Larmor frequency.

Nuclear Magnetization

A sum of magnetic moments $\vec{\mu}_i$ of nuclei in volume V form macroscopic nuclear magnetization $\vec{M}$

$$\vec{M} = \sum_{i=1}^{N} \frac{\vec{\mu}_i}{V}, \tag{4.41}$$

where N denotes the number of nuclei in the volume V.

In thermal equilibrium with lattice at temperature T, the Boltzmann distribution determines occupation probability p_m for level E_m (corresponding to magnetic quantum number m) of the Zeeman multiplet

$$p_m = \frac{e^{-\frac{E_m}{k_B T}}}{\sum_{m'=-I}^{I} e^{-\frac{E_{m'}}{k_B T}}} \tag{4.42}$$

(k_B stands for the Boltzmann constant). The equilibrium nuclear magnetization $\vec{M}_0 = (0, 0, M_0)$ in the external magnetic field $\vec{B}_0$ can be calculated using relations (4.2) and (4.4):

$$M_0 = \sum_{i=1}^{N} \frac{\gamma \hbar}{V} \sum_{m=-I}^{I} m p_m = \frac{N \gamma \hbar}{V} \frac{\sum_{m=-I}^{I} m e^{-\frac{E_m}{k_B T}}}{\sum_{m=-I}^{I} e^{-\frac{E_m}{k_B T}}} = \frac{N \gamma \hbar}{V} I B_I \left(\frac{I \gamma \hbar B_0}{k_B T} \right), \tag{4.43}$$

where $B_I(x)$ denotes the Brillouin function. Assuming $\frac{I \gamma \hbar B_0}{k_B T} << 1$, the equation transforms into the Curie law

$$M_0 = \frac{N \gamma^2 \hbar^2}{V} \frac{I(I+1) B_0}{3 k_B T}. \tag{4.44}$$

Bloch Equations

The motion of nuclear magnetization $\vec{M}$ in a condensed matter in an external magnetic field $\vec{B} = \vec{B}_0 + \vec{B}_1(t)$ (assuming $|B_1| << |B_0|$) can be phenomenologically described by the Bloch equations:

$$\frac{dM_x}{dt} = \gamma \left(\vec{M} \times \vec{B} \right)_x - \frac{M_x}{T_2} \tag{4.45}$$

$$\frac{dM_y}{dt} = \gamma \left(\vec{M} \times \vec{B} \right)_y - \frac{M_y}{T_2} \tag{4.46}$$

$$\frac{dM_z}{dt} = \gamma \left(\vec{M} \times \vec{B} \right)_z - \frac{M_z - M_0}{T_1} \tag{4.47}$$

where T_1 is named spin-lattice (longitudinal) relaxation time, T_2 is called spin-spin (transverse) relaxation time and $\vec{M}_0 = (0, 0, M_0)$ presents equilibrium magnetization in the field $\vec{B}_0$.

The first term at the right side of the Bloch equations characterizes the impact of torsional moment of the external field on the nuclear magnetization.

Without the RF field (i. e. $B_1 = 0$), nuclear magnetization exhibits the Larmor precession about the static field $\vec{B}_0$ direction at the Larmor frequency

$$\vec{\omega}_0 = -\gamma \vec{B}_0. \tag{4.48}$$

In the presence of the RF field, transformation of relations (4.45), (4.46) and (4.47) into a frame of reference rotating with the RF field replaces the time-dependent field $\vec{B}$ in the equations by a time-independent effective field

$$\vec{B}_{\text{ef}} = \left(B_1, 0, B_0 + \frac{\omega_z}{\gamma} \right). \tag{4.49}$$

In the rotating coordinate system, nuclear magnetization exercises a precession at a frequency $\vec{\omega}_1 = -\gamma \vec{B}_{\text{ef}}$ about the effective field $\vec{B}_{\text{ef}}$.

Let us consider now the RF field having a form of a single pulse of length τ. At start, $B_1 = 0$ and $\vec{M} \parallel \vec{B}_0$. Next, the RF pulse is applied. Right after the pulse, the nuclear magnetization is tilted to an angle (with respect to z-axis)

$$\theta = \gamma B_1 \tau. \tag{4.50}$$

This simple sequence thus allows for precession angle adjustment.

The second term at the right side of the Bloch equations provides a description of a return of the nuclear magnetization into equilibrium. The last term at the right side of equation (4.47) characterizes the interaction between nuclear spins and a lattice. The speed of energy transfer from spin system to the lattice after tilting nuclear magnetization from equilibrium is described by spin-lattice relaxation time T_1. The second terms at the right side of equations (4.45) and (4.46) determines the decay of transverse components of nuclear magnetization also due to fluctuations of Larmor precession frequencies of individual nuclear magnetic moments. If the field $\vec{B}_0$ were absolutely homogeneous, the decay rate would be given by spin-spin relaxation time T_2. However, in a real experiment, Larmor frequencies of particular nuclear magnetic moments vary because of local inhomogeneities of the field $\vec{B}_0$. This leads to a faster decay approximately described by time $T_2^\star$ due to out-of-phase motion of individual moments.

4.4.2 Pulse Sequences

Nowadays, pulse methods definitely prevail in NMR spectroscopy. These methods apply the excitation RF field $\vec{B}_1(t)$ as short pulses, whereas the response of nuclear magnetization is recorded after or between the pulses. The pulse length is supposed to be very short compared to T_1 and T_2 relaxation times. This part briefly describes two simple pulse sequences (FID (free induction decay) and spin echo) and the CPMG sequence, which is often used for NMR experiments in magnetically ordered materials.

Free Induction Decay

Free induction decay (FID) pulse sequence (see Fig. 4.1) comprises a single RF pulse at Larmor frequency of length nuclear magnetization by $\pi/2$ (see equation

(4.50)) – this pulse is called $\pi/2$-pulse. Signal induced by transverse component of preceding nuclear magnetization can be observed after the end of the pulse as the FID signal. Assuming absolutely homogeneous field $\vec{B}_0$, the decay of signal amplitude A in time t ($t = 0$ corresponds to the start of pulse) would obey this dependence

$$A\left(t\right) \sim \exp\left(-\frac{t}{T_2}\right). \tag{4.51}$$

However, absolutely homogeneous field is not the case of a real experiment, thus local inhomogeneities of the magnetic field $\vec{B}_0$ result in significantly faster decay

$$A\left(t\right) \sim \exp\left(-\frac{t}{T_2^\star}\right). \tag{4.52}$$
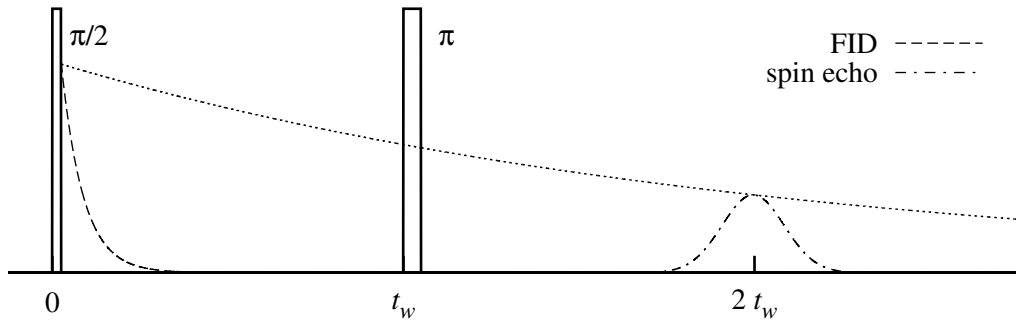
Figure 4.1: The FID and spin echo sequences

Spin Echo

By attaching another RF pulse (at Larmor frequency) length of which provides π tilt of nuclear magnetization (see relation (4.50)) at time t_w after the $\pi/2$-pulse, the FID sequence changes into the spin echo pulse sequence. The π-pulse turns over the transverse component of nuclear magnetization by π angle about the $\vec{B}_1$ direction. Therefore, the local magnetization vectors aligns in the time $2t_w$ and a precession of the transverse component of nuclear magnetization gives a rise to a spin echo signal (provided that the time t_w is not significantly longer than spin-spin relaxation time T_2). Spin echo amplitude is determined by equation (4.51) (set $t = t_w$).

The CPMG Sequence

Appending more π-pulses in $2t_w$ intervals to the spin echo sequence is the concept of the Carr-Purcell pulse sequence illustrated in Fig. 4.2. This sequence allows for a detection of spin echo in every interval between the π-pulses (as well as after the last pulse), while amplitude of these echoes follows equation (4.51). A drawback of the Carr-Purcell sequence is its high sensitivity to improper adjustment of length and intensity of the RF pulses as even a small deviation deflects nuclear magnetization slightly out of the transverse plane and this error further builds up

during the pulse sequence. A solution for this cumulative error issue comprises $\pi/2$ phase shift of $\pi/2$-pulse with respect to a phase of the π-pulses' – the result is called the Carr–Purcell–Meiboom–Gill (CPMG) pulse sequence. [68]

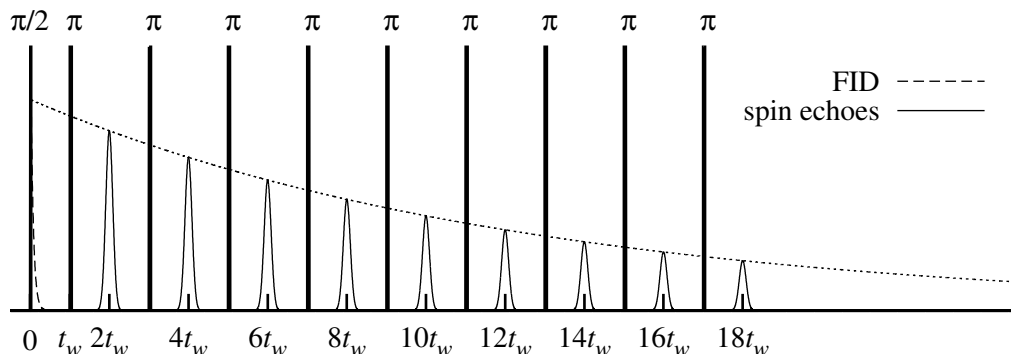**Figure 4.2:** The Carr-Purcell/CPMG pulse sequence

4.4.3 NMR Spectrum

The NMR spectrum presents a distribution of resonance (Larmor) frequencies of nuclei in the sample which pulse sequence excited. Time domain record of the NMR signal obtained in the pulse experiments has to be converted to a frequency domain by the Fourier transform. It is generally possible to transform the signal of FID or spin echo directly. On the other hand, it is better to average signals of individual detected echoes in the CPMG sequence at first – this provides a waveform similar to a signal of a single spin echo with considerably higher signal-to-noise ratio (SNR). Nevertheless, a care must be taken if the averaged echoes come from a time window comparable to spin-spin relaxation time as relative intensities of spectral lines can be affected by a frequency dependence of this relaxation rate.

   In the case of broad spectrum, it is usually not technically feasible to excite the whole spectral range at once. Therefore, a wide spectrum has to be measured step-by-step with a suitable frequency steps considering spectral line width and pulse lengths. The whole spectrum shall be created as an envelope of subspectra (Fourier transform modules) acquired in particular steps – see Fig. 4.3. Sometimes, especially if the spectral lines are very broad, the spectra can be constructed simply from Fourier transform modules at the excitation frequency of particular steps.

4.4.4 NMR in Magnetics

In magnetically ordered materials, the local magnetic field at nuclei consists mainly from the hyperfine field – see part 4.1.3. Time average of the hyperfine field in such matter is high even without an external magnetic field. Thus the NMR experiments on these substances can be carried out even in a zero external static magnetic field.

   Since the hyperfine field reflects the crystal, electronic and magnetic structure in proximity of resonating nuclei, the NMR frequencies of nuclei at crys-
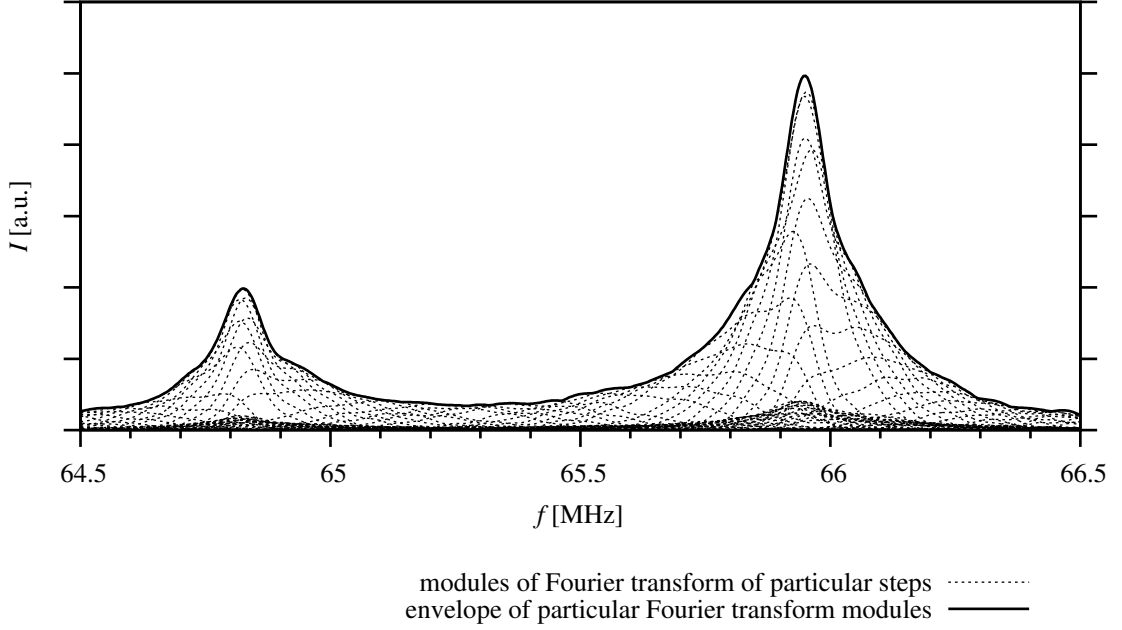
Figure 4.3: Illustration how the spectrum is constructed from particular steps

tallographically or magnetically non-equivalent sites are different. Similarly, any perturbation in the vicinity of a resonating nucleus is able to shift its Larmor frequency. Thus the resonating nuclei serve as local hyperfine field probes and the resulting NMR spectrum provides information on hyperfine field distribution. Every group of magnetically equivalent sites of resonating nuclei yields one spectral signal, while the intensity of this signal is proportional to a number of the nuclei in this group. Relatively broad distribution of the hyperfine field is the reason why NMR spectra of magnetics often span over a wide frequency range.

Beside the interaction of nuclear magnetic moments with an external RF field explained in previous parts, there is also an interaction between the external RF field and electron magnetic moments, which gives a rise to an oscillating component of the hyperfine field. As a result, total RF field which interacts with nuclear moments is in magnetically ordered materials often much stronger compared to the external RF field. This amplification effect is characterized by the enhancement factor defined as a ratio of the total RF field amplitude B_2 and the external RF field amplitude B_1

$$\eta_{\mathrm{enh}} = \frac{B_2}{B_1}.\tag{4.53}$$

The enhancement factor typically ranges from 1 to 10^4 depending on material and magnetic ordering. The value of η_{enh} for nuclei in magnetic walls usually differs from the one for nuclei in magnetic domains, because the amplification effect in the walls originates from wall motion, whereas the enhancement in the domains is due to a rotation of electron magnetization.

There is also a similar mechanism based on nucleus - electron coupling which causes an amplification of magnetic field produced by preceding nuclear moments and thus increases the intensity of detected NMR signal.

4.4.5 NMR in Magnetite

The ability of NMR to resolve signals originating from nuclei in different groups of magnetically equivalent crystallographic sites due to the different hyperfine field makes it a suitable tool for investigation of crystal, magnetic and electronic structure of magnetite. Spectral structure thus reflects changes of crystal and magnetic structure of magnetite during the Verwey and spin reorientation transition – see Fig. 4.4 [69]. Below the Verwey transition, the ^{57}Fe NMR spectrum consists of 8 lines (two of them accidentally overlapping) from Fe(A) nuclei and 16 lines from Fe(B) nuclei (one of them overlapped by Fe(A) lines). Between the Verwey and the spin reorientation transitions, there are only one Fe(A) line and one Fe(B) line in the spectrum. Above the spin reorientation transitions, the spectrum contains still a single Fe(A) line while the Fe(B) signal splits into 2 lines in an intensity ratio of 1:3.
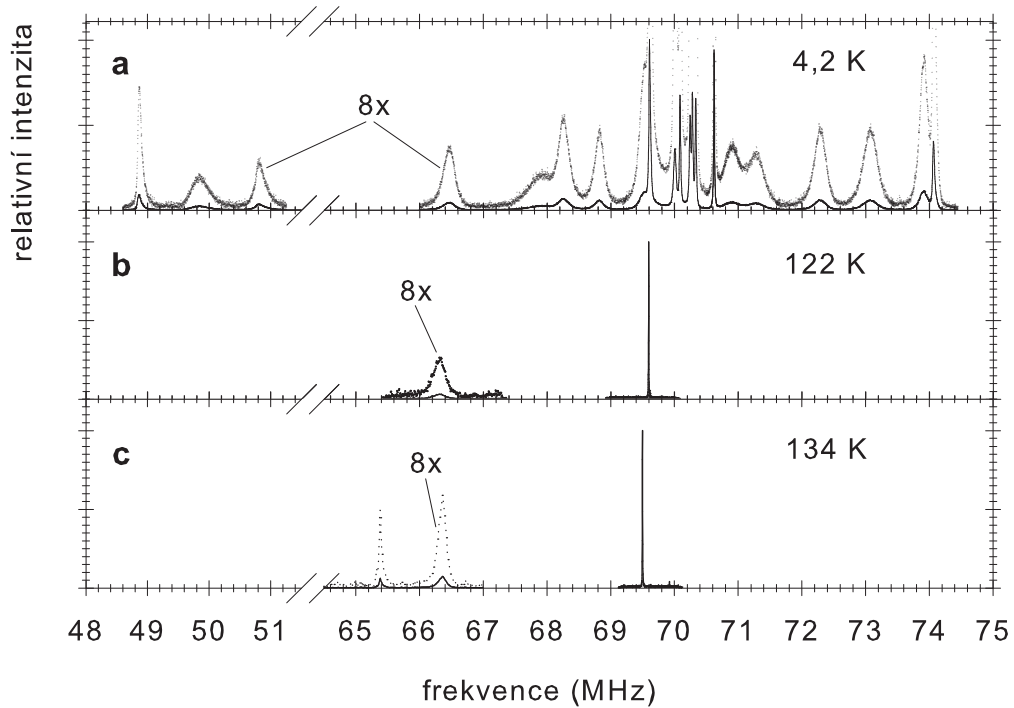
Figure 4.4: The ^{57}Fe NMR spectra of pure magnetite acquired below the Verwey transitions (a), between the Verwey and the spin reorientation transition (b) and above the spin reorientation transition (c) [69]

Individual ^{57}Fe NMR signals in magnetite spectra were resolved in Refs. [37] and [14]. Nevertheless, assignment of particular lines in Cc phase of magnetite to corresponding crystallographic sites remains an open question despite a recent attempt in Ref. [39]. The work of Mizoguchi [14] provides also valuable data of angular dependences of spectral signal frequencies in an external magnetic field – see Figs. 4.5 and 4.6. Variation of spectral line frequencies with temperature from 4.2 K to 135 K were also published in Ref. [37], whereas the variation from the Verwey temperature to 320 K for both Fe(A) and Fe(B) resonances (and up to 400 K for Fe(A) signal only) were reported in Ref. [70] for pure and aluminium-substituted magnetite and in Ref. [71] for pure magnetite and non-stoichiometric magnetite.
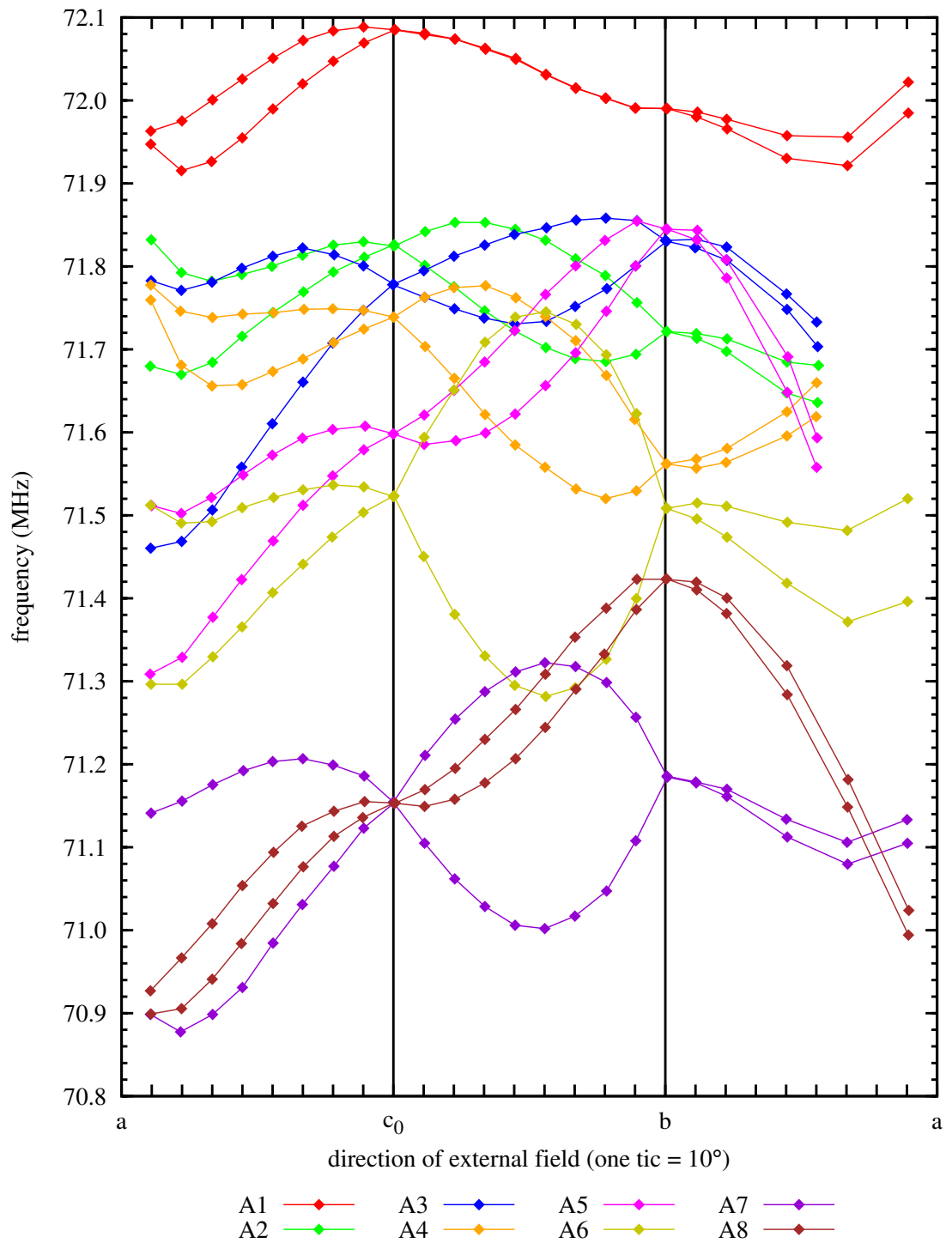
Figure 4.5: Dependences of frequencies of ^{57}Fe NMR signals from the A sublattice on the direction of the external magnetic field $B_{ext} = 1.3$ T in the *ac-*, *bc-*, and *ab*-planes after Ref. [14]. The lines are guides for the eye only.

Figure 4.6: Dependences of frequencies of ^{57}Fe NMR signals from the B sublattice on the direction of the external magnetic field $B_{\text{ext}} = 1.3$ T in the *ac*-, *bc*-, and *ab*-planes after Ref. [14]. The lines are guides for the eye only.

Results of measurements of relaxation times in pure magnetite at 4.2 K are presented in Ref. [37]. While the differences between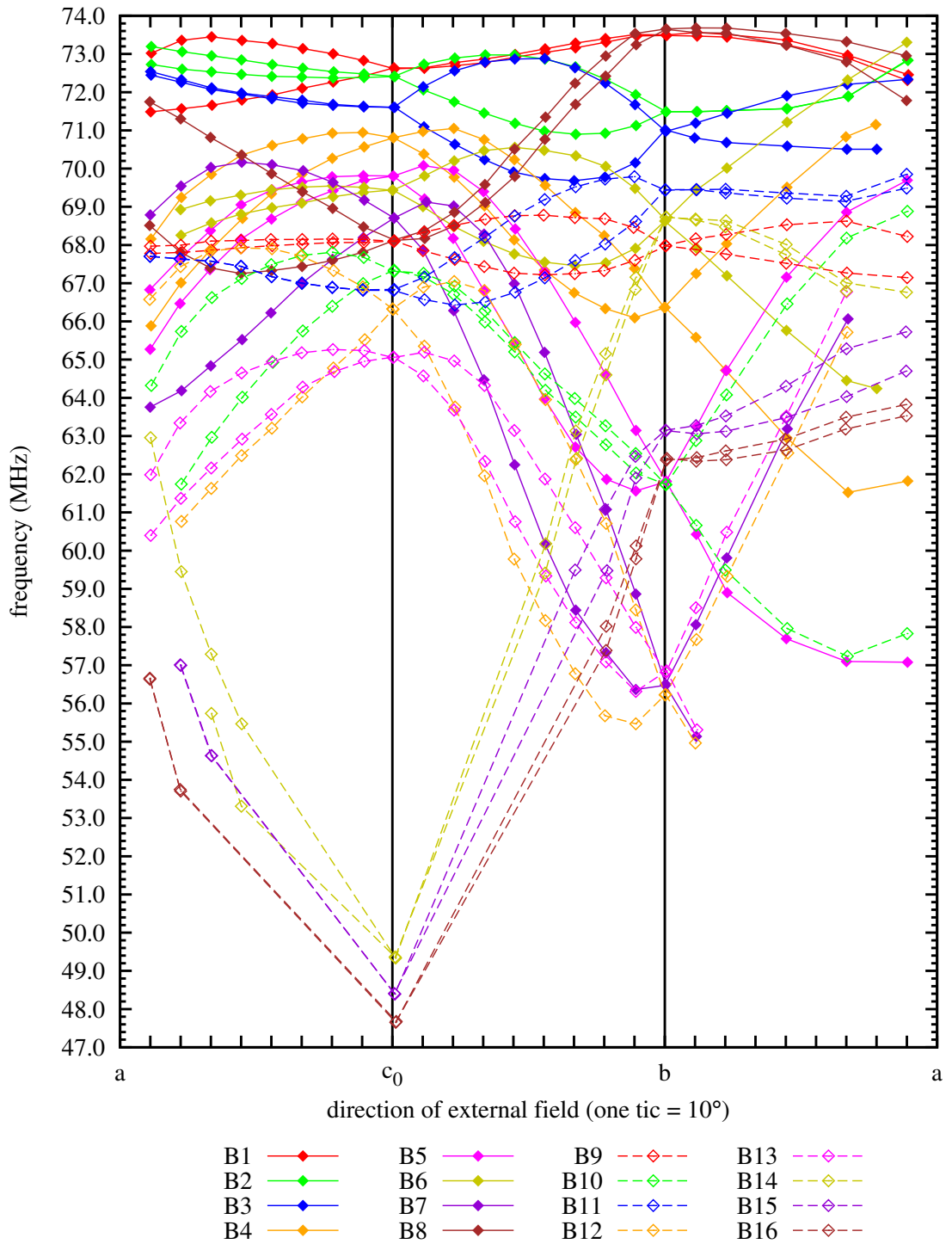 T_1 time of particular spectral signals are relatively modest, the T_2 parameters significantly vary. Variation of relaxation rates of individual lines in magnetite spectra below the Verwey temperature were reported in Ref. [72] – relaxation times of all Fe(A) signals exhibit similar temperature dependences and the Fe(B) relaxations can be described by the same words. Relaxation data for zinc-substituted magnetite acquired at 4.2 K, 198 K and 273 K can be found in Ref. [73].

4.5 Mössbauer Spectroscopy

4.5.1 Basic Principle

Mössbauer spectroscopy is based on recoilless emission and absorption of γ radiation [74]. Nuclei in radiation source and in absorbing sample are embedded in a crystal lattice and provided that the γ transition energy is below a certain limit ($\approx$ 100 keV), a significant portion of transitions is recoilless thus allowing for observation of the Mössbauer effect [75]. For the purposes of Mössbauer spectroscopy, the γ transitions between the ground and the first excited state of given isotope are usually used. These two states typically differ in various nuclear parameters – see Table 4.1 for data on a common Mössbauer nuclei ^{57}Fe.

Table 4.1: Physical parameters of ^{57}Fe nuclei relevant to Mössbauer spectroscopy ($\mu_N \approx 5.051 \cdot 10^{-27}$ J·T^{-1} stands for nuclear magneton and b = 10^{-28} m^2 for barn unit)

quantity	ground state value	excited state value
excitation energy	–	$E_0 = 14.412497(3)$ keV [76]
half life	stable	$\tau_{1/2} = 98.3(3)$ ns [77]
spin	$I = 1/2$	$I^\star = 3/2$
magnetic moment	$\mu_{z,\text{max}} = +0.09062300(9)\ \mu_N$ [78]	$\mu^\star_{z,\text{max}} = -0.1549(2)\ \mu_N$ [79]
quadrupole moment	$Q = 0$ b	$Q^\star = +0.15(2)$ b [80]

Precise values of γ transition energy are affected by hyperfine interactions which turns the Mössbauer effect into a useful tool for a study of magnetic and electronic structure of various materials. However, this implies a necessity for a variation of the γ ray energy in order to cover the range of energy shifts caused by the hyperfine interactions. This range is very narrow compared to the transition energy, thus the desired energy modulation ΔE_D can be achieved by a Doppler shift of the source mounted on a velocity transducer:

$$\Delta E_D = E_0 \frac{v}{c} \tag{4.54}$$

(v is the source velocity, c is a speed of light). The velocity v expressed in the units of mm·s^{-1} is commonly used in Mössbauer spectra as the energy scale, while equation (4.54) serves as a conversion relation.

4.5.2 Lineshape

If there were no line broadening caused for instance by a distribution of hyperfine parameters or by a thickness of a sample, the absorption lines in Mössbauer spectra would have a Lorentzian profile

$$I\left(\Delta E_{\mathrm{D}}\right) = \frac{1}{\pi} \frac{\Gamma}{\left(\Delta E_{\mathrm{D}} - \Delta E_{\mathrm{D},c}\right)^2 + \Gamma^2}, \tag{4.55}$$

where I is absorption intensity, $\Delta E_{\mathrm{D},c}$ is line centre position and Γ (determining half-width at half-maximum intensity (HWHM)) is Heisenberg natural linewidth related to excited state half life $\tau_{1/2}$:

$$\Gamma = \hbar \frac{\ln\left(2\right)}{\tau_{1/2}} \tag{4.56}$$

4.5.3 Isomer Shift

The difference ΔR between nuclear charge radius R of ^{57}Fe nucleus in the ground state compared to $R^\star$ in the first excited state implies a difference ΔE' in monopole interaction energy. This difference is determined by perturbation energy (4.28) corresponding to effect of finite size nucleus [65], [63]:

$$\Delta E\text{'} = \Delta E^\star - \Delta E = \frac{1}{4\pi\epsilon_0} \frac{2}{5} \pi Z e \left((R^\star)^2 - R^2\right) \rho_0 \approx \frac{1}{4\pi\epsilon_0} \frac{4}{5} \pi e Z R^2 \frac{\Delta R}{R} \rho_0. \tag{4.57}$$

As a result, energy shifts of Mössbauer transitions in both source and absorber give rise to isomer shift (expressed as a velocity) observable in spectra:

$$\delta\text{'} = \frac{c}{E_0} \frac{1}{10\epsilon_0} Z e \left((R^\star)^2 - R^2\right) \left(\rho_0 - \rho_{0,src}\right) \tag{4.58}$$

(ρ_0 and $\rho_{0,src}$ are electron charge densities at nuclei in absorber and in source, respectively). In the case of ^{57}Fe Mössbauer spectroscopy, the isomer shift δ is usually expressed with respect to isomer shift $\delta\text{'}_{Fe}$ of α-Fe metal standard:

$$\delta = \delta\text{'} - \delta\text{'}_{Fe} = \frac{c}{E_0} \frac{1}{10\epsilon_0} Z e \left((R^\star)^2 - R^2\right) \left(\rho_0 - \rho_{0,Fe}\right) \tag{4.59}$$

($\rho_{0,Fe}$ is electron charge density at nuclei in α-Fe).

4.5.4 Quadrupole Splitting

Excited state of ^{57}Fe nuclei in a zero magnetic field and a non-zero EFG is split into two (degenerate) energy levels (expressed relative to energy level of the excited state without any hyperfine interaction) by quadrupole interaction (4.35):

$$E_{Q,-\frac{1}{2}} = E_{Q,+\frac{1}{2}} = -\frac{1}{4} e Q V_{zz} \sqrt{1 + \frac{\eta^2}{3}} \tag{4.60}$$

$$E_{Q,-\frac{3}{2}} = E_{Q,+\frac{3}{2}} = +\frac{1}{4} e Q V_{zz} \sqrt{1 + \frac{\eta^2}{3}} \tag{4.61}$$

This is manifested in Mössbauer spectrum by two resonance signals of equal intensity separated by quadrupole splitting energy

$$\Delta E_Q = |E_{Q,-\frac{1}{2}} - E_{Q,-\frac{3}{2}}| = |E_{Q,+\frac{1}{2}} - E_{Q,+\frac{3}{2}}| = |\frac{1}{2} e Q V_{zz} \sqrt{1 + \frac{\eta^2}{3}}|. \tag{4.62}$$

4.5.5 Magnetic Dipole Splitting

Magnetic dipole interaction is responsible for a splitting of energy levels of both ground and excited state of nuclei (provided that the spin is non-zero) into Zeeman multiplets (4.7). If there is no quadrupole interaction, energy levels in each of these multiplets are equidistant. Mössbauer transition occurring between excited and ground state are affected by the Zeeman splitting and they are subject to selection rules (unless there is a strong quadrupole interaction present) allowing for a change of m during the transition by only -1, 0 or 1. For ^{57}Fe, this results in a sextet of spectral lines, relative intensity of which is in a ratio

$$3\left(1+\cos^2\theta\right) : 4\sin^2\theta : \left(1+\cos^2\theta\right) : \left(1+\cos^2\theta\right) : 4\sin^2\theta : 3\left(1+\cos^2\theta\right) \quad (4.63)$$

(θ denotes the angle between the γ ray and magnetic moment of the nucleus) as determined by Clebsch-Gordan coefficients. Averaging in the case of a powder sample yields intensity ratio of 3:2:1:1:2:3.

4.5.6 Combined Quadrupole And Magnetic Dipole Splitting

Combination of quadrupole and magnetic dipole interactions is described by Hamiltonian (4.36). If the quadrupole interaction is weak compared to the magnetic one, the corresponding ^{57}Fe spectrum consists of a sextet of lines which are shifted due to the quadrupole splitting. When the quadrupole interaction gets stronger, it cannot be treated as a perturbation of magnetic interaction any longer, spectral line positions and also their intensities become significantly affected and forbidden transitions appear.

Chapter 5

Density Functional Theory

The density functional theory (DFT) in a combination with the adiabatic approximation opens a way for a solution of the many-electron problem linked with crystals. Within this theory, the total energy E_{tot} of the ground state is expressed as a functional of electron density $\rho\left(\vec{r}\right)$:

$$E_{\text{tot}}\left[\rho\right] = T_{\text{s}}\left[\rho\right] + E_{\text{ee}}\left[\rho\right] + E_{\text{Ne}}\left[\rho\right] + E_{\text{xc}}\left[\rho\right] + E_{\text{NN}}, \tag{5.1}$$

where T_{s} presents kinetic energy of (non-interacting) electrons, E_{ee} corresponds to the electron-electron repulsion, E_{Ne} is Coulomb attraction between nuclei and electrons, E_{xc} denotes the exchange-correlation energy and E_{NN} stands for electrostatic repulsion between nuclei. According to Kohn and Hohenberg [81], this functional is minimal for the true ground state electron density.

Unlike to the other terms in (5.1), which can be treated in exact form, the exchange-correlation energy has to be described by a suitable approximation. The local spin density approximation (LSDA) expresses E_{xc} using a local exchange-correlation energy density $\mu_{\text{xc}}\left(\rho\left(\vec{r}\right)\right)$ of some particular form :

$$E_{\text{xc}} = \int \mu_{\text{xc}}\left(\rho\left(\vec{r}\right)\right)\rho\left(\vec{r}\right)d\,\vec{r} \tag{5.2}$$

The generalized gradient approximation (GGA) improves the LSDA by an addition of gradient terms of the electron density to the exchange-correlation energy. In the case of transitional metal oxides, a self-interaction corrected GGA in a combination with the Hubbard model (GGA+U(SIC)) [82] presents a suitable approach achieving a reasonable agreement with experimental data. The GGA+U method is controlled by the parameter U_{eff} corresponding to a difference between on-site repulsion and exchange [83].

Variational principle applied on (5.1) provides Kohn-Sham equations [84]

$$\left(-\Delta + V_{\text{ee}} + V_{\text{Ne}} + V_{\text{xc}}\right)\psi_i\left(\vec{r}\right) = \epsilon_i\psi_i\left(\vec{r}\right), \tag{5.3}$$

which shall be solved iteratively while keeping a self-consistency – the potentials (on the left side) depend on electron density which in turn depends on the Kohn-Sham wave functions $\psi\left(\vec{r}\right)$ and their populations n_i:

$$\rho\left(\vec{r}\right) = \sum_i n_i|\psi_i\left(\vec{r}\right)|^2 \tag{5.4}$$

The solution of equations (5.3) shall be found in a suitable basis of functions $\phi_{\vec{k}_n}\left(\vec{r}\right)$:

$$\psi_{\vec{k}}\left(\vec{r}\right) = \sum_n c_n \phi_{\vec{k}_n}\left(\vec{r}\right) \tag{5.5}$$

Within the muffin tin approach common for this type of problem, the crystal volume is divided into non-overlapping atomic spheres, where the basis functions are expressed in terms of atomic-like wave functions $u_l\left(r, E_l\right)$, and an interstitial region, in which the plane waves are used. The popular linearized augmented plane wave (LAPW) method employs the following form of the basis functions inside the atomic spheres:

$$\phi_{\vec{k}_n}\left(\vec{r}\right) = \sum_{lm} \left(A_{lm,\vec{k}_n} u_l\left(r, E_l\right) + B_{lm,\vec{k}_n} \dot{u}_l\left(r, E_l\right)\right) Y_{lm}\left(\vec{r}\right) \tag{5.6}$$

($Y_{lm}\left(\vec{r}\right)$ are spherical harmonics and the $A_{lm,\vec{k}_n}$ and $B_{lm,\vec{k}_n}$ coefficients are set to match the value and slope of the function at the atomic sphere boundary with the plane wave) and the following one in the interstitial area:

$$\phi_{\vec{k}_n}\left(\vec{r}\right) = \frac{1}{\sqrt{\omega}} e^{i\vec{k}_n \cdot \vec{r}} \tag{5.7}$$

($\vec{k}_n = \vec{k} + \vec{K}_n$, where $\vec{k}$ is a wave vector in the first Brillouin zone and $\vec{K}_n$ is a vector of the reciprocal lattice). The size of the basis set (in both methods) is usually controlled by the parameter $R_{\mathrm{MT}} K_{\max}$ – a product of the smallest atomic sphere radius R_{MT} and the length $K_{\max}$ of the largest $\vec{K}$ vector used.

The LAPW basis can be extended by local orbitals (LO) [85]

$$\phi_{lm}^{\mathrm{LO}}\left(\vec{r}\right) = \sum_{lm} \left(A_{lm} u_l\left(r, E_{1,l}\right) + B_{lm}\dot{u}_l\left(r, E_{1,l}\right) + C_{lm} u_l\left(r, E_{2,l}\right)\right) Y_{lm}\left(\vec{r}\right), \tag{5.8}$$

each presenting a linear combination of 2 radial functions at different energies and one energy derivative, which improves the linearization and allows for a consistent handling of semicore and valence states within the same energy range. The values of the coefficients A_{lm}, B_{lm} and C_{lm} are chosen to ensure zero value and slope of $\phi_{lm}^{\mathrm{LO}}\left(\vec{r}\right)$ at the atomic sphere radius.

Higher computation efficiency can be achieved using a standard augmented plane wave (APW) basis with $u_l\left(r, E_l\right)$ at a fixed value of energy E_l

$$\phi_{\vec{k}_n}\left(\vec{r}\right) = \sum_{lm} \left(A_{lm,\vec{k}_n} u_l\left(r, E_l\right)\right) Y_{lm}\left(\vec{r}\right) \tag{5.9}$$

combined with another local orbital (lo) function

$$\phi_{lm}^{\mathrm{lo}}\left(\vec{r}\right) = \left(A_{lm} u_l\left(r, E_{1,l}\right) + B_{lm}\dot{u}_l\left(r, E_{1,l}\right)\right) Y_{lm}\left(\vec{r}\right), \tag{5.10}$$

in which the A_{lm} and B_{lm} coefficients (ensuring normalization and zero value of $\phi_{lm}^{\mathrm{lo}}\left(\vec{r}\right)$ at the atomic sphere boundary) do not depend on $\vec{k}_n$ unlike to (5.6) [86]. This approach allows for a significant reduction of the set of the basis functions and thus also for a faster calculation.

Chapter 6

Methods

6.1 Sample Preparation

The single crystal samples of magnetite investigated in this work are listed in Table 6.1. The notation $[Fe_{1-x}X_x]_A[Fe_{2-x'}X'_{x'}]_B O_4$, where x and x' denote concentrations of substitution defects X and X', respectively, explicitly indicates the sublattice occupied by the particular defect. The sample dimensions were typically in the order of millimetres. Two methods were employed for a preparation of the samples: a growth in a cold crucible and a floating zone melting. The samples were kindly provided by prof. J. M. Honig from Purdue University, USA and prof. V. A. M. Brabers from Eindhoven University of Technology, Netherlands.

Table 6.1: Studied single crystal magnetite samples and their spin reorientation and Verwey transition temperatures. The three dots (...) denote vacancies.

compound	T_{sr} (K)	T_V (K)	preparation method
$[Fe]_A[Fe_2]_B O_4$	132.7	122.2	floating zone
$[Fe_{0.96}Ga^{3+}_{0.04}]_A[Fe_{1.99}Ga^{3+}_{0.01}]_B O_4$	126.7	117.5	floating zone
$[Fe_{0.993}Zn^{2+}_{0.007}]_A[Fe_2]_B O_4$	124.0	113.2	cold crucible
$[Fe_{0.991}Zn^{2+}_{0.009}]_A[Fe_2]_B O_4$	122.5	110.0	cold crucible
$[Fe_{0.983}Zn^{2+}_{0.017}]_A[Fe_2]_B O_4$	121.0	104.3	cold crucible
$[Fe_{0.97}Zn^{2+}_{0.03}]_A[Fe_2]_B O_4$		91	cold crucible
$[Fe]_A[Fe_{1.994}...^0_{0.006}]_B O_4$	128.0	114.1	cold crucible
$[Fe]_A[Fe_{1.9895}...^0_{0.0105}]_B O_4$			cold crucible
$[Fe]_A[Fe_{1.973}...^0_{0.027}]_B O_4$	124.0	101.0	cold crucible
$[Fe]_A[Fe_{1.992}Ti^{4+}_{0.008}]_B O_4$	128.0	116.4	floating zone
$[Fe]_A[Fe_{1.992}Ti^{4+}_{0.008}]_B O_4$	126.0	119.0	cold crucible
$[Fe]_A[Fe_{1.98}Ti^{4+}_{0.02}]_B O_4$	110.0	77.0	cold crucible
$[Fe]_A[Fe_{1.9}Ti^{4+}_{0.1}]_B O_4$			floating zone
$[Fe]_A[Fe_{1.995}Al^{3+}_{0.005}]_B O_4$	128.3	119.7	floating zone
$[Fe]_A[Fe_{1.99}Al^{3+}_{0.01}]_B O_4$			floating zone
$[Fe]_A[Fe_{1.97}Al^{3+}_{0.03}]_B O_4$	126.5	97.3	floating zone

The cold crucible method of growth from melt (also known as a skull melter) [87] was carried out in the laboratory of prof. J. M. Honig at Purdue University, USA. The grown single crystals underwent subsolidus annealing in mixtures of CO/CO_2 gas to achieve the desired oxygen stoichiometry. After the anneal-

ing, the samples were rapidly quenched to room temperature in order to freeze in the high temperature thermodynamic equilibrium. Although this procedure creates defects connected with the high temperature disorder, most of the low-temperature electronic properties are not impacted, which is evidenced by the sharpness and high temperature of the Verwey transition.

The floating zone method of sample preparation [88] was employed in the laboratory of prof. V. A. M. Brabers at Eindhoven University of Technology, Netherlands. Initially, ceramic techniques were used to obtain polycrystalline rods of appropriate stoichiometric composition. Afterwards, these rods placed in a N_2 atmosphere were exposed to a melting in a floating zone apparatus based on an arc-image furnace. Subsequent annealing in an O_2 atmosphere was intended for an improvement of the mechanical quality of the samples.

The AC susceptibility measurements performed by prof. A. Kozłowski at the AGH University of Science and Technology, Krakow and Ing. M. Maryško, CSc. at the Institute of Physics of the Czech Academy of Sciences, Prague yielded the Verwey and spin reorientation transition temperatures. The Verwey temperatures were also used for a verification of the defect concentration based on their general mutual dependence shown in Fig. 2.5.

6.2 Nuclear Magnetic Resonance Experiments

A basic block diagram of a pulse NMR spectrometer is drawn in Fig. 6.1. The purpose of the spectrometer is to apply the appropriate RF pulse sequence to an investigated sample and to record the response of preceding nuclear magnetization.

A pulse generator controls the timing and length of excitation pulses and triggers signal acquisition. A frequency synthesizer generates an RF signal of requested frequency and phase, which is then led into an input of a modulator – a device which creates RF pulses from this signal. The pulses are passed through an attenuator and a power amplifier in order to obtain desired pulse intensity. Throughout the excitation, an output pulse is send from the power amplifier through the receive/transmit (RX/TX) switch to an LC resonance circuit (sample is placed in the coil) contained in the probe, while the input of a preamplifier is isolated to avoid its saturation or damage. The motion of transverse component of nuclear magnetization induces a signal in the LC resonance circuit, which is led to the preamplifier input during the detection period. In this period, the power amplifier is isolated from the probe to eliminate it as one of noise sources (and to simply fulfill impedance matching requirements at the same time). Amplified NMR signal is mixed with the local oscillator RF signal generated also by the synthesizer at a frequency shifted by intermediate frequency (IF) from the excitation frequency. The mixer output is again amplified in an IF amplifier and then passed in an in-phase/quadrature (I/Q) detector. The analog-to-digital (A/D) converter digitizes the in-phase and quadrature signals from the detector outputs and stores the data in a memory. (Modern NMR spectrometers often implement an alternative detection method – the A/D converter digitizes directly the IF amplifier output signal and the subsequent I/Q detection is performed digitally.) Coherence of the whole setup, which is ensured by a stable frequency reference, is crucial for a coherent summation of the signal – i.e. the pulse sequence is re-

peated for many times and the data records from all scans are summed to increase the SNR, which is proportional to a square root of a number of scans. Acquired signal records are transferred into a control computer for further processing.
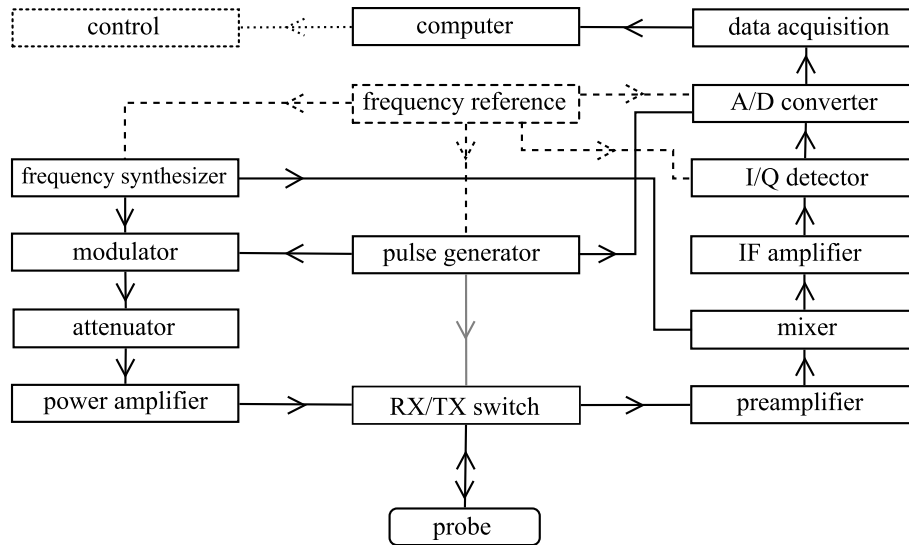

Figure 6.1: Basic block diagram of pulse NMR spectrometer

The NMR experiments performed in this work employed the Bruker Avance spectrometer in a custom configuration suitable for broadband measurements of magnetically ordered materials. Typically, the CPMG pulse sequence was used with $\pi/2$-pulse length $1-2$ μs and the number of π-pulses of the order of 10 or 100 (limited by a spin-spin relaxation rate and by a π-pulse time spacing set in the order of 10 or 100 μs to accommodate the whole echo signal). The repetition time of the pulse sequence (i. e. time between successive scans), which had to be long enough with respect to a spin-lattice relaxation rate, ranged from 5 ms to several seconds and the number of scans was set to values of the order from 10 to 10,000 (according to the SNR). The amplitude of RF pulses was adjusted for an appropriate excitation of the nuclei in magnetic domains. Receiver gain allowing for a suitable utilization of the A/D converter input range was chosen. The detected signal was sampled at either 0.7 or 2 MSps rate and the recorded data encompassed the whole length of the pulse sequence. A postprocessing of the data carried out carefully in order to achieve a good SNR of the resulting spectra, while minimizing the impact of frequency-dependent spin-spin relaxation rates on a shape of the spectra.

The spectra at 4.2 K were measured with the probe with the sample submersed in liquid helium in a Dewar vessel. Higher temperatures were provided by Oxford Instruments helium continuous flow cryostat with the Lakeshore temperature controller. The measurements which required external magnetic field were carried out in a water-cooled $0-0.7$ T electromagnet connected to the PCE A2800 power supply operating in a current limitation mode.

6.3 Mössbauer Spectroscopy Experiment

The measurement of the ^{57}Fe Mössbauer spectrum was carried out by dr Jan Żukrowski at AGH University of Kraków, Poland. The experiment employed a

constant acceleration spectrometer in transmission geometry with a ^{57}Co in Rh source at ambient temperature. The absorber was kept at 4 K in a closed cycle refrigeration system. The spectrometer was calibrated using an α-Fe foil of a thickness of 10 μm. The sample of pure magnetite single crystal was in a form of a $\approx$ 100 μm thick plate. The area of the sample exposed to the γ-ray was of a diameter of $\approx$ 3 mm. No external magnetic field was applied during the measurement and cooling of the sample.

6.4 Calculations Based on the Density Functional Theory

The ab initio calculations based on the density functional theory, which are presented in this work, were carried out using the WIEN2k software [89]. This software allows for a convenient combination of both the LAPW and APW+lo methods in the same calculation. The number of the basis functions amounted to 9500 ($R_{\mathrm{MT}}K_{\mathrm{max}} = 6.0$) and there were 9 k-points in irreducible part of Brillouin zone. The density of charge was Fourier expanded to G_{max}=16 Ry$^{\frac{1}{2}}$.

The parameters of the low-temperature crystal structure published by Senn *et al.* [1] were used for the calculations. For a general magnetization direction, the Cc elementary cell contained 112 non-equivalent ions. Contrary to the work of Patterson [39], the structure optimization was not employed as the structure is complicated and many crystal structure parameters would change during the optimization procedure. Apparently multiple minima of total energy exist and it is not certain that the correct energy minimum would be reached. The situation is further complicated by a presence of magnetostriction, which is not taken into account in the optimization process. Thus the unoptimized experimental structure was used – average of force acting on the ions was 9.8 mRy $\cdot$ a.u.$^{-1}$, while the maximum force was 19.3 mRy $\cdot$ a.u.$^{-1}$.

There are four sources contributing to total hyperfine field: Fermi contact interaction (B_{cont}), dipolar on-site interaction with electron spin (B_{dip}), on-site interaction with orbital momentum (B_{orb}) and interaction with other electron magnetic moments in the lattice (B_{lat}). In the case of the contact contribution, a semi-empirical approach [90] was used. This method is better than the one used by Patterson [39] because the corresponding relation (3) in Ref. [39] approximates the contact field poorly [91]. The necessary values of spin magnetic moments of the 3d and 4s electrons of iron ions were calculated using R_{MT}(Fe)= 2 a.u. and the GGA+U method with $U_{\mathrm{eff}} = 4.5$ eV. Contrary to the work in Ref. [38], spin-orbit coupling was included in the calculations.

The oxidation states and spin magnetic moments of Fe ions were not determined in the usual way which takes a sum and a difference, respectively, of spin-up and spin-down electron density in the atomic spheres around the particular ions. Instead, the atoms in molecules approach (AIM) [92] was applied. This method considers atom as a generalized volume around the nucleus and thus takes into account also the electron density in the interstitial region.

Chapter 7

Electronic Structure and Hyperfine Interactions in Magnetite Below the Verwey Transition – Results and Discussion

This chapter presents the results of the investigation of the electronic ordering and hyperfine field anisotropy in low-temperature phase of magnetite in a context of the trimeron model proposed by Senn et al. [1]. An important piece of information was gained by an analysis of the results of ab initio calculations. Further, the experimental data from the ^{57}Fe NMR measurements published by Mizoguchi [14] were rigorously reanalyzed, thus providing a counterpart of the data based on the ab initio calculations. The hyperfine anisotropy results of both approaches were then compared and significant correlations were found. A comparison with the work of Patterson [39] on a similar topic, which was published at the time when results presented here in parts 7.2.1, 7.2.2 and 7.3 were finished and our related manuscript of Ref. [93] had been finalized, is provided in the corresponding parts.

Moreover, the data obtained from the ab initio calculations allowed for a simulation of Mössbauer spectrum of magnetite which was compared to the spectrum from the experiment [94]. Finally, the impact of substitution defects introduced into magnetite was analyzed from differences in the ^{57}Fe NMR spectra of single crystal samples of magnetite with various substitutions.

7.1 Site Numbering Convention

Currently, there is no reliable unique assignment of the ^{57}Fe NMR resonance signals to corresponding crystallographic positions available. Mizoguchi [14] numbered the signals originating from the A and B site nuclei according to the decreasing nuclear magnetic resonance frequency for magnetization in the easy direction – see Figs. and . This convention labelling the experimental NMR resonances A1 through A8 and B1 through B16 is followed in this work. On the other hand, the ab initio calculations are based on the crystal structure published by Senn et

al. [1]. The crystallographic sites <u>A</u>1 through <u>A</u>8 and <u>B</u>1 through <u>B</u>16 referred to in this chapter are distinguished from the experimental NMR signal labels by the underlined <u>A</u> and <u>B</u> letters and they are numbered in the same order as they are listed in Ref. [1] – see Table 7.1. The results presented here revealed a grouping of the B sites (and of the corresponding NMR signals), thus in some figures and tables, the sites are arranged or have their labels coloured to make their grouping (discussed in part 7.3.3) apparent.

Table 7.1: Assignment of the site labels used in this work for ab initio calculations to the crystallographic sites defined by fractional coordinates (x, y, z) as reported by Senn et al. [1]

Site label	Site notation in Ref. [1]	x	y	z
<u>A</u>1	A11	0.87509(2)	0.75133(2)	0.065377(13)
<u>A</u>2	A12	0.87814(2)	0.25204(2)	0.065046(13)
<u>A</u>3	A13	0.62475(2)	0.75276(2)	0.437877(13)
<u>A</u>4	A14	0.62660(2)	0.25398(2)	0.437830(13)
<u>A</u>5	A21	0.874607(18)	0.50477(2)	0.190290(11)
<u>A</u>6	A22	0.880722(18)	0.00074(2)	0.188506(11)
<u>A</u>7	A23	0.625263(19)	0.50162(2)	0.31109(1)
<u>A</u>8	A24	0.629229(18)	0.005024(19)	0.312775(11)
<u>B</u>1	B1A1	0.75057(3)	-0.00212(3)	0.002273(14)
<u>B</u>2	B1A2	0.75116(3)	0.49865(3)	0.001114(14)
<u>B</u>3	B1B1	0.00187(3)	0.50050(3)	0.501700(15)
<u>B</u>4	B1B2	-0.00257(2)	0.00076(2)	0.496931(13)
<u>B</u>5	B2A1	0.74758(2)	0.756391(15)	0.252602(14)
<u>B</u>6	B2A2	0.75929(2)	0.252197(16)	0.253673(13)
<u>B</u>7	B2B1	0.00255(3)	0.74372(1)	0.751877(18)
<u>B</u>8	B2B2	0.00214(3)	0.24588(1)	0.751910(17)
<u>B</u>9	B31	0.87694(2)	0.879450(17)	0.379805(13)
<u>B</u>10	B32	0.87644(2)	0.387473(16)	0.380749(13)
<u>B</u>11	B33	0.62663(2)	0.886624(15)	0.121776(12)
<u>B</u>12	B34	0.62878(2)	0.374621(18)	0.123112(13)
<u>B</u>13	B41	0.87599(2)	0.62482(2)	0.376706(14)
<u>B</u>14	B42	0.87543(2)	0.13087(2)	0.374365(15)
<u>B</u>15	B43	0.62566(2)	0.62776(2)	0.125840(15)
<u>B</u>16	B44	0.62788(3)	0.12601(3)	0.126517(16)

7.2 Electronic Structure

7.2.1 Valence Electron Density in Trimeron Planes

One of the most illustrative representations of electronic structure is a map of electron density. In this case, the density of minority spin valence electrons in selected planes of the trimerons was plotted in Fig. 7.1. (An analogous plot limited to minority spin iron $3d$ valence electrons can be found in Appendix as Fig. A.1.) The electron density was calculated with magnetization in $\vec{c}$ axis. The maps were

averaged with the sites connected by the *ac*-glide symmetry operation in order to suppress possible (although minor) artifacts originating from switching off this symmetry operation for consistency with the calculations of angular dependences of the hyperfine field (see part 7.3).

The most apparent feature is that the electron cloud encompassing the central Fe^{2+}-like ion of each trimeron is significantly elongated in the trimeron axis direction. Further, the asymmetry of electron distribution around the end ions of trimerons is lower (and even negligible in some cases).

These findings align well with the concept of trimerons – a considerable fraction of minority spin $3d$ electron is found in central ion's t_{2g} orbital corresponding to the trimeron axis, while the remainder of the electron is transferred into the same orbitals of the end ions. The electron density in the vicinity of the central ion is thus significantly anisotropic. On the other hand, electron clouds around the end ions are much more symmetric even when the ion participates in multiple trimerons because the fractional charges are transferred into different orbitals in this situation.

The results allow for a comparison with the concept recently proposed by Patterson [39]. Although the picture presented here may be in accordance with the expectations for inner ions in the zig-zag chain in Patterson's model, electron cloud moved towards the chain would be intuitively expected for the chain end and branch ions (e. g. B1, B13) but this was not found in the electron density maps. In case of the iron ion pairs not included in the chain (e. g. B5'–B7), one-electron bonds between such ions would impose similar charge configuration of the ions which also has not been observed.

7.2.2 Electron Populations and Valence States of Iron

The trimeron model provided in the work of Senn *et al.* [1] describes distribution of electrons in the trimeron: if maximum donor-to-acceptor transfer is assumed, 0.6 e (e denotes elementary charge) is located in the central ion's t_{2g} orbital corresponding to the trimeron axis direction, whereas 0.2 e is transferred to the same orbital of each of the end ions. Thus the populations of the iron minority spin $3d$ states can be qualitatively determined and compared to the data from the ab initio calculations – see Table 7.2. (Note that these populations are expressed in orthogonal coordinates respecting local (pseudo)symmetry of the B sites: $\vec{z}$ axis is parallel to $\vec{c}$, $\vec{x}$ axis points in the [110] Cc direction. Thus appropriate transformation of a raw output of the DFT calculations had to be applied.)

Visualization of the t_{2g} populations obtained from the ab initio calculations is provided in Fig. 7.2. Similar plot including also the e_g populations (Fig. A.2) can be found in Appendix as well as a visualization of the populations deduced from the trimeron model (Fig. A.3).[1] The correlation between Fig. 7.2 and populations derived from the trimeron concept is apparent.

For comparison purposes, net charge and Mulliken populations of minority spin $3d$ electrons taken from Ref. [39] were included in Table 7.2 (contrary to

---

[1]In order to avoid confusion, Figs 7.2, 7.3, 7.6, 7.13, A.2 and A.3 in this thesis depict the same trimerons which are shown in Fig. 4d in Ref. [1] and the positions of iron ions are also the same. However, should a comparison be made with Fig. 3 in Ref. [38], offset (e. g. B1B2 (= B4) is not in the centre of the cell) and a partially different set of plotted trimerons have to be taken into account.

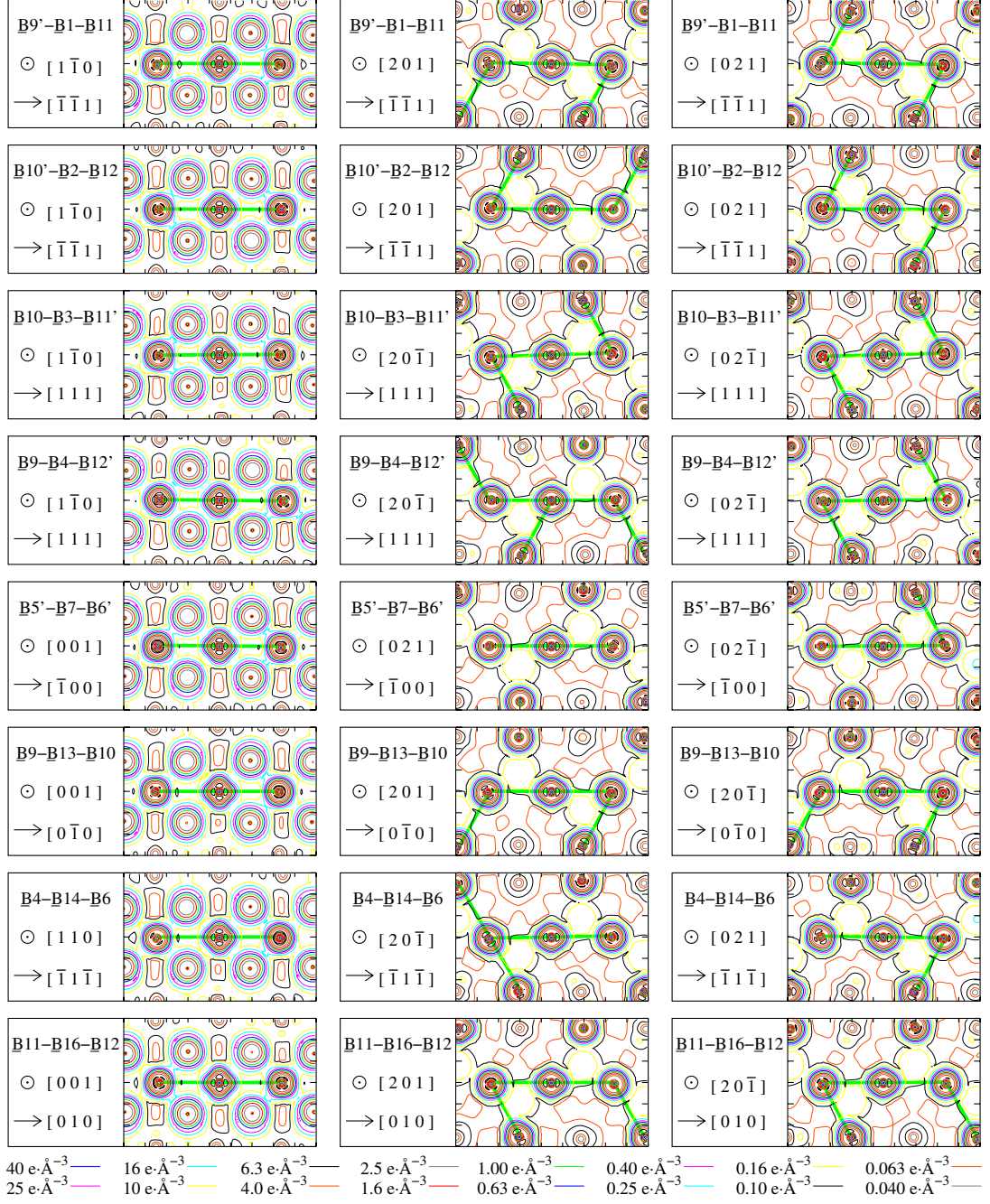**Figure 7.1:** Maps of minority spin valence electron density in trimeron planes. Each map has 9 Å × 6 Å dimensions. Green lines denote trimerons [1]. Sites of iron ions participating in the trimeron located on a horizontal axis of a particular map are indicated next to the map; the centre of the image plane is placed in the location of the trimeron's central ion. The monoclinic tilt of $\vec{c}$ axis makes the standard crystallographic plane notation inconvenient for selected planes, thus orientation of the planes is specified by normal vector of the plane (which points out of the page) shown at the $\odot$ symbol in combination with an in-plane vector indicated by an arrow (indices of these vectors are taken with respect to Cc coordinates). In each row, the plane of the first map forms with the planes of the other two maps an angle of $\approx 55°$, whereas the angle between the planes of the last two maps is $\approx 70.5°$. Site numbering follows the convention introduced in part 7.1; primes indicate the ac-glide symmetry generated sites.

other population data in Table 7.2, the Mulliken populations are limited to 16 bands right under the valence band maximum) – they correlate very well with the data presented here and also with expectations based on the trimeron model. The valence of the iron ions at the B sites can be examined in column $n_{t_{2g}} + n_{e_g}$ of Table 7.2 – the values are not far from 1 for Fe^{2+}-like ions, while in the case of Fe^{3+}-like ions, they are systematically lower, though still apparently exceeding 0. The sum of this column for the 16 B sites is 13.25 electrons, while only 8.00 electrons are expected assuming formally 8 Fe^{2+} and 8 Fe^{3+} ions occupying these sites. The situation at the A sites is also interesting as there are no minority spin $3d$ electrons expected at all at the Fe^{3+} ions, but actually $n_{t_{2g}} + n_{e_g} = 0.72$. This effect is caused by a transfer (asymmetric in spin) of electrons from oxygen ligands to the A and B sites which results in the described excess charge. Therefore, the AIM method was employed to obtain the valence states more reliably and also to determine spin magnetic moments. The valence charges yielded by AIM were scaled by factor 1.6 which brings average valence charge of oxygen to -2, thus the oxidation states were obtained. The resulting B iron oxidation states are in good agreement with the values of bond valence sum (BVS) published in [1] – see the 14th and 15th column of Table 7.2.

Table 7.2: Populations of iron minority spin electrons expressed with respect to Fe^{3+} state – derived from the DFT calculations (even lines) and from Ref. [1] (odd lines) together with valence and oxidation states (in units of elementary charge) and magnetic moments (in Bohr magnetons) obtained by the AIM method, as well as bond valence sums from Ref. [1]. The Mulliken n'_{3d} populations (after Ref. [39] are restricted to 16 bands right under the valence band maximum, whereas there is no such limitation for the net charge populations n_{3d} [39] or for any other data in the table. Populations were taken in local coordinates with $\vec{x}$ axis set to the [110] Cc direction and $\vec{z}$ axis parallel to the $\vec{c}$ axis of the Cc system. Variation of the parameters of different A site ions is very low, thus only an average is presented. Site numbering follows the convention introduced in part 7.1.

DFT site	nominal valence state	n_{xy}	n_{xz}	n_{yz}	$n_{t_{2g}}$	n_{z^2}	$n_{x^2-y^2}$	n_{e_g}	$n_{t_{2g}} + n_{e_g}$	n_{3d} [39]	n'_{3d} [39]	AIM valence	AIM oxidation state	Bond valence sum [1]	AIM spin magnetic moment
A average	3+	0.00	0.00	0.00	0.00	0.00	0.00	0.00	0.00						
		0.17	0.18	0.17	0.52	0.10	0.10	0.20	0.72			1.77	2.82		-4.083
B1	2+	0.00	0.60	0.00	0.60	0.00	0.00	0.00	0.60						
		0.03	0.73	0.04	0.80	0.10	0.11	0.21	1.01	1.14	0.63	1.47	2.34	2.48	3.691
B2	2+	0.00	0.60	0.00	0.60	0.00	0.00	0.00	0.60						
		0.03	0.74	0.04	0.80	0.09	0.11	0.20	1.01	1.12	0.61	1.46	2.33	2.44	3.696
B3	2+	0.00	0.60	0.00	0.60	0.00	0.00	0.00	0.60						
		0.03	0.70	0.05	0.78	0.10	0.11	0.21	0.99	1.16	0.65	1.47	2.35	2.47	3.708
B4	2+	0.00	0.60	0.20	0.80	0.00	0.00	0.00	0.80						
		0.03	0.55	0.05	0.63	0.12	0.13	0.25	0.88	1.06	0.48	1.57	2.51	2.56	3.858
B5	3+	0.20	0.00	0.00	0.20	0.00	0.00	0.00	0.20						
		0.12	0.07	0.06	0.25	0.21	0.19	0.40	0.65	0.95	0.29	1.79	2.85	2.77	4.153
B6	3+	0.20	0.00	0.20	0.40	0.00	0.00	0.00	0.40						
		0.09	0.05	0.19	0.33	0.18	0.18	0.36	0.69	1.01	0.39	1.74	2.78	2.67	4.095
B7	2+	0.60	0.00	0.00	0.60	0.00	0.00	0.00	0.60						
		0.72	0.03	0.03	0.78	0.12	0.09	0.21	0.99	1.07	0.53	1.48	2.36	2.48	3.722

Table continues on next page.

Table 7.2 – continues from previous page.

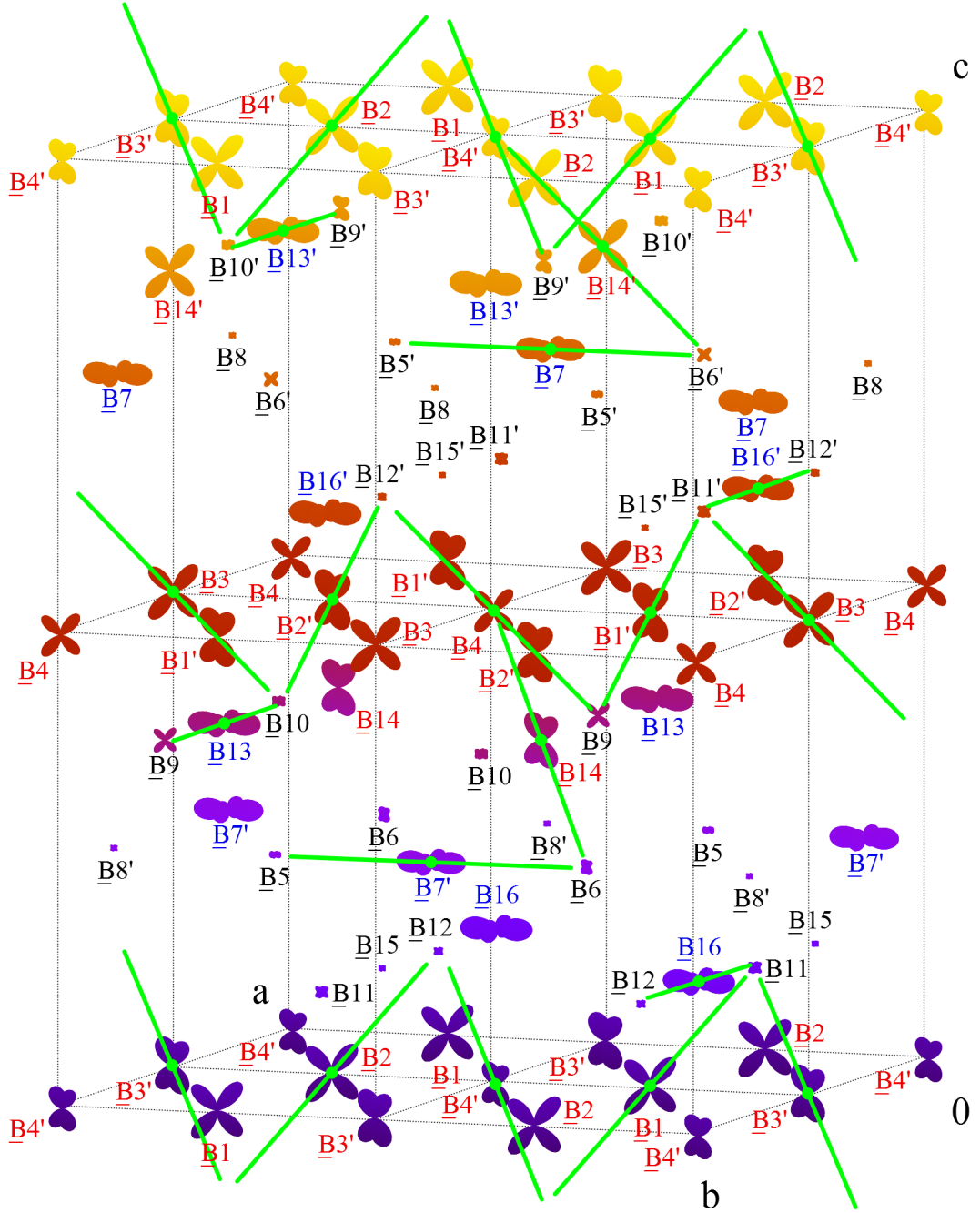| DFT site	nominal valence state	n_{xy}	n_{xz}	n_{yz}	$n_{t_{2g}}$	n_{z^2}	$n_{x^2-y^2}$	n_{e_g}	$n_{t_{2g}}+n_{e_g}$	n_{3d} [39]	n'_{3d} [39]	AIM valence	AIM oxidation state	Bond valence sum [1]	AIM spin magnetic moment
B8	3+	0.00	0.00	0.00	0.00	0.00	0.00	0.00	0.00						
		0.07	0.06	0.06	0.20	0.22	0.21	0.43	0.62	0.85	0.07	1.83	2.92	2.96	4.192
B9	3+	0.20	0.20	0.20	0.60	0.00	0.00	0.00	0.60						
		0.05	0.31	0.07	0.43	0.15	0.17	0.32	0.75	1.04	0.44	1.68	2.68	2.58	4.021
B10	3+	0.20	0.20	0.20	0.60	0.00	0.00	0.00	0.60						
		0.13	0.11	0.11	0.34	0.18	0.18	0.36	0.70	1.06	0.45	1.73	2.76	2.61	4.081
B11	3+	0.20	0.20	0.20	0.60	0.00	0.00	0.00	0.60						
		0.11	0.13	0.12	0.36	0.18	0.18	0.35	0.71	1.06	0.45	1.72	2.74	2.64	4.066
B12	3+	0.20	0.20	0.20	0.60	0.00	0.00	0.00	0.60						
		0.08	0.09	0.07	0.25	0.20	0.20	0.41	0.65	0.94	0.26	1.79	2.86	2.81	4.146
B13	2+	0.60	0.00	0.00	0.60	0.00	0.00	0.00	0.60						
		0.76	0.03	0.03	0.81	0.12	0.09	0.20	1.01	1.12	0.60	1.46	2.33	2.44	3.692
B14	2+	0.00	0.60	0.60	0.60	0.00	0.00	0.00	0.60						
		0.03	0.03	0.69	0.76	0.10	0.12	0.22	0.97	1.07	0.52	1.50	2.39	2.54	3.736
B15	3+	0.00	0.00	0.00	0.00	0.00	0.00	0.00	0.00						
		0.07	0.06	0.06	0.19	0.21	0.21	0.42	0.62	0.85	0.07	1.83	2.92	2.93	4.195
B16	2+	0.60	0.00	0.00	0.60	0.00	0.00	0.00	0.60						
		0.75	0.03	0.03	0.80	0.12	0.08	0.20	1.00	1.13	0.64	1.46	2.32	2.38	3.703

Figure 7.2: Populations of minority spin t_{2g} electrons of the B site iron ions from the DFT calculations visualized as an angular variation of the electron density, i.e. the distance of the surface from a given site denotes the density at the corresponding angle scaled by 3 Å·e⁻¹ coefficient. Green lines highlight trimerons [1]. Site numbering and label colours follow the convention introduced in part 7.1; primes indicate the *ac*-glide symmetry generated sites. (Surface colour indicating *z*-coordinate is intended just to improve clarity.)

7.2.3   EFG Tensors

Another important property characterizing the electronic structure is represented by electric field gradients (EFG) at particular crystallographic sites. Here we

focus on EFG tensor at the iron sites. Although these data are not experimentally accessible by means of ^{57}Fe NMR (the spin of ^{57}Fe nuclei in ground state is 1/2, thus the nuclei exhibit no quadrupole moment), they manifest themselves e. g. in Mössbauer spectra.

The EFG tensors at the A and B sites extracted from the ab initio calculations are listed in Table B.1 in Appendix with respect to the orthorhombic coordinate system (see definition (4.31)) as well as in a canonical form (see definition (4.32)) accompanied by the asymmetry parameters (see relation (4.33)) and principal axes of the tensors. The tensors are visualized in Fig. 7.3 for the B sites and in Fig. A.4 in Appendix for the A sites as objects drawn in magnetite elementary cell – the following formula defines the distance r of object surface from the particular iron position

$$r = C \cdot [V_{aa}\vartheta_a^2 + V_{bb}\vartheta_b^2 + V_{cc}\vartheta_c^2 + 2(V_{ab}\vartheta_a\vartheta_b + V_{ac}\vartheta_a\vartheta_c + V_{bc}\vartheta_b\vartheta_c)], \qquad (7.1)$$

where ϑ_α, $\alpha = a$, b, c are direction cosines with respect to the orthorhombic axes and C is a suitable scaling coefficient (common for all sites in the plot).

The figures provide an overall picture of size of EFG at particular sites and of orientation of principal axes of the tensors. In comparison with the B sites, the EFG at the Fe^{3+} ions at the A sites is small due to nearly spherical symmetry of their electronic configuration. On the other hand, Fig. 7.3 shows a more complex situation which shall be interpreted in the context of trimerons. Apparently, the EFG at the trimeron central ions is significantly larger than at the end ions, while the principal axis linked with the smallest eigenvalue of corresponding EFG tensor of central ion is approximately parallel to the trimeron axis. This finding is in alignment with the expectations derived from the electronic structure of trimerons: The minority spin charge density around the central Fe^{2+}-like ions is considerably anisotropic because the charge is located in t_{2g} orbital corresponding to the trimeron axis. In case of Fe^{3+}-like end ions, the roughly spherically symmetric electron density is affected only by the partial charge transferred from the central ions. (If the end ion participates in multiple trimerons, the central ions donate the charge into different orbitals so the impact on the symmetry of end ion is still small.) The EFG at Fe^{3+}-like ions B8 and B15, which are not a part of trimeron network, is the smallest from the B sites because the symmetry of their electronic configuration is not perturbed by transferred charge. (An overview graph comparing the V_{zz} parameters with the Fe(B) ion valences is provided in Fig. 7.11 in part 7.3.3.) The discrepancy between these results and Patterson's model [39] can be demonstrated on Fe(B) pairs which are not in the zig-zag chain (e. g. B5'–B7): the one-electron bond would imply relatively similar charge configuration of the ions but the disparity of EFG at these sites is apparent.

7.2.4   Charge Density at Iron Nuclei

The DFT calculations were also used to determine charge density at iron nuclei – a quantity which is experimentally accessible by Mössbauer spectroscopy in the form of isomer shift relative to metallic bcc α-Fe. In the calculations, the charge density at iron nuclei was obtained as the density at the radial grid point R_0
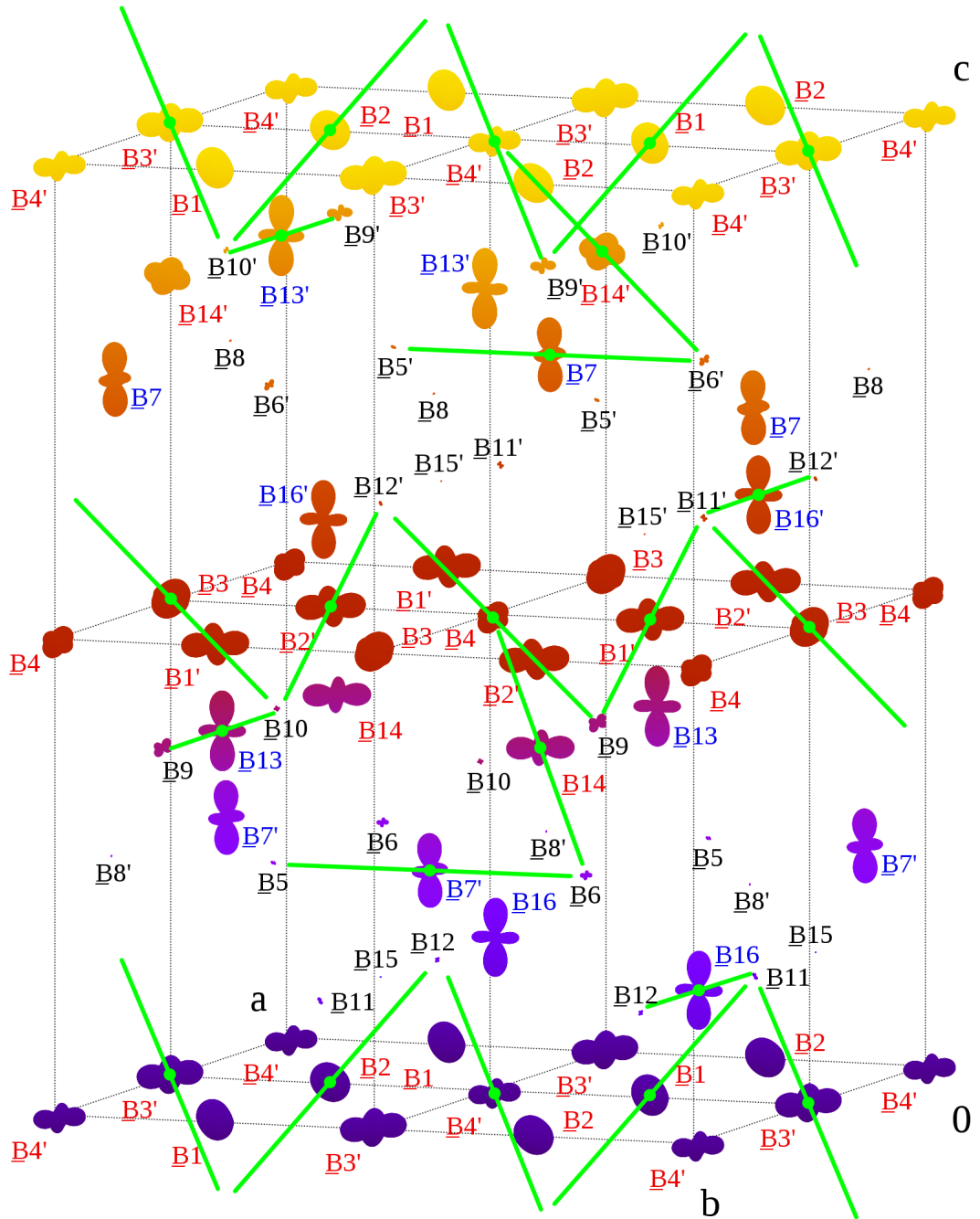
Figure 7.3: EFG tensors at iron B sites obtained from the DFT calculations visualized in the elementary cell (scaling coefficient $C = 0.05 \text{ Å} \cdot 10^{-21} \text{ V}^{-1} \cdot \text{m}^2$). Green lines highlight trimerons [1]. Site numbering and label colours follow the convention introduced in part 7.1; primes indicate the ac-glide symmetry generated sites. (Surface colour indicating z-coordinate is intended just to improve clarity.)

nearest to the nucleus position assumed constant over a sphere with radius R_0. The value $R_0 = 5 \cdot 10^{-5} a_0$ ($a_0 \approx 5.292 \cdot 10^{-11}$ m is the Bohr radius) was used, so the R_0 was comparable to the nuclear radius. The resulting charge densities at iron nuclei ρ_0 are listed in Table 7.3.

Table 7.3: Calculated charge density ρ_0 at iron nuclei in magnetite and corresponding isomer shift δ determined using equation (7.2) (the isomer shift error is determined by the fit error of α – see text; $a_0 \approx 5.292 \cdot 10^{-11}$ m is the Bohr radius)

DFT site	nominal valence state [1]	ρ_0 $(e \cdot a_0^{-3})$	$\rho_0 - \rho_{0,Fe}$ $(e \cdot a_0^{-3})$	$\delta \pm 4\%$ (mm·s^{-1})
A1	3+	15308.964	-1.233	0.350
A2	3+	15308.964	-1.233	0.350
A3	3+	15308.951	-1.245	0.354
A4	3+	15308.982	-1.215	0.345
A5	3+	15308.975	-1.222	0.347
A6	3+	15308.991	-1.206	0.342
A7	3+	15308.994	-1.202	0.341
A8	3+	15308.985	-1.211	0.344
B1	2+	15306.875	-3.322	0.943
B2	2+	15306.844	-3.352	0.952
B3	2+	15306.924	-3.273	0.929
B4	2+	15307.382	-2.815	0.799
B5	3+	15308.316	-1.880	0.534
B6	3+	15308.095	-2.101	0.597
B7	2+	15306.885	-3.311	0.940
B8	3+	15308.513	-1.684	0.478
B9	3+	15307.812	-2.385	0.677
B10	3+	15308.095	-2.101	0.597
B11	3+	15308.063	-2.133	0.606
B12	3+	15308.347	-1.849	0.525
B13	2+	15306.805	-3.392	0.963
B14	2+	15307.029	-3.167	0.899
B15	3+	15308.499	-1.697	0.482
B16	2+	15306.790	-3.406	0.967

Isomer shift δ is related to the charge density at nucleus by expression (4.59). However, the uncertainty of nuclear charge radius $R^\star$ in the excited state prevents a direct application of equation (4.59) to obtain isomer shift from calculated charge densities [65]. Instead, the following relation shall be used

$$\delta = \alpha \left(\rho_0 - \rho_{0,Fe} \right), \tag{7.2}$$

where α is a coefficient determined by a calibration procedure described e. g. in Ref. [95]. The procedure comprised a calculation of charge density at iron nuclei in various materials (including iron oxides) in the same way as for the data in Table 7.3. These charge densities were paired with published experimentally observed values of isomer shift (see Table 7.4) and used for fitting

the dependence (7.2) (see Fig. 7.4). The fit yielded the coefficient value of $\alpha = -0.284 \pm 0.011$ mm·s^{-1}·e^{-1}·a_0^3 ($a_0 \approx 5.292 \cdot 10^{-11}$ m is the Bohr radius), which is close to the value obtained in Ref. [95] ($\alpha = -0.291 \pm 0.014$ mm·s^{-1}·e^{-1}·a_0^3 for halides and TiFe using the full-potential linearized augmented plane-wave and augmented plane wave plus local orbitals methods implemented in the WIEN2k software) or [96] ($\alpha = -0.278 \pm 0.028$ mm·s^{-1}·e^{-1}·a_0^3 for iron complexes using quasi-relativistic DFT within the zero-order regular approximation). Note that despite the good agreement with these published results, it was crucial to carry out the calibration with the particular DFT calculation method (including its specific parameter settings) instead of just using some of published α values because the resulting α coefficient significantly varies depending on the employed DFT calculation method [97], [98].

Table 7.4: Charge density ρ_0 at iron nuclei from DFT calculations and experimental isomer shift δ_{exp} for various iron compounds ($a_0 \approx 5.292 \cdot 10^{-11}$ m is the Bohr radius)

compound	$\rho_0\ (e \cdot a_0^{-3})$	$\rho_0 - \rho_{0,Fe}\ (e \cdot a_0^{-3})$	$\delta_{\mathrm{exp}}\ (\mathrm{mm \cdot s^{-1}})$
TiFe	15310.829	0.632	-0.145 ± 0.007 [99]
Fe	15310.196	0	0
FeAl	15309.133	-1.064	0.272 ± 0.015 [100]
Fe_2O_3	15308.139	-2.058	0.47 ± 0.03 [101]
FeF_3	15307.628	-2.568	0.489 [102]
YIG a	15308.219	-1.978	0.57 ± 0.05 [103]
YIG d	15308.996	-1.200	0.26 ± 0.05 [103]
Fe_3O_4 A	15308.866	-1.330	0.36 [104]
(above T_{V})			0.34 [105]
			0.27 ± 0.03 [106]
Fe_3O_4 B	15307.608	-2.589	0.78 [104]
(above T_{V})			0.66 [105]
			0.67 ± 0.03 [106]
FeS	15307.176	-3.020	1.1 ± 0.1 [103]
FeF_2	15305.414	-4.783	1.467 [107]
			1.40 ± 0.05 [103]

The isomer shift values determined by equation (7.2) for particular iron sites in magnetite were added to Table 7.3. The sensitivity of isomer shift to the configuration of 3d electrons [103] is apparent: $\delta = 0.34 - 0.35$ mm·s^{-1} for Fe^{3+} ions at the A sites, while at the B sites $\delta = 0.48 - 0.68$ mm·s^{-1} for Fe^{3+}-like ions and $\delta = 0.80 - 0.97$ mm·s^{-1} for Fe^{2+}-like ions. Although in general, the dependence of charge density at iron nucleus (and thus of isomer shift) on the iron ion charge is not monotonic [108] due to different effects of 3d and 4s orbital populations [109], the nominal iron valence in magnetite is confined to a narrow range from 2+ to 3+ where more or less proportional behaviour can be expected. Thus the systematic correlation between the 3d populations and the calculated isomer shift is not surprising.
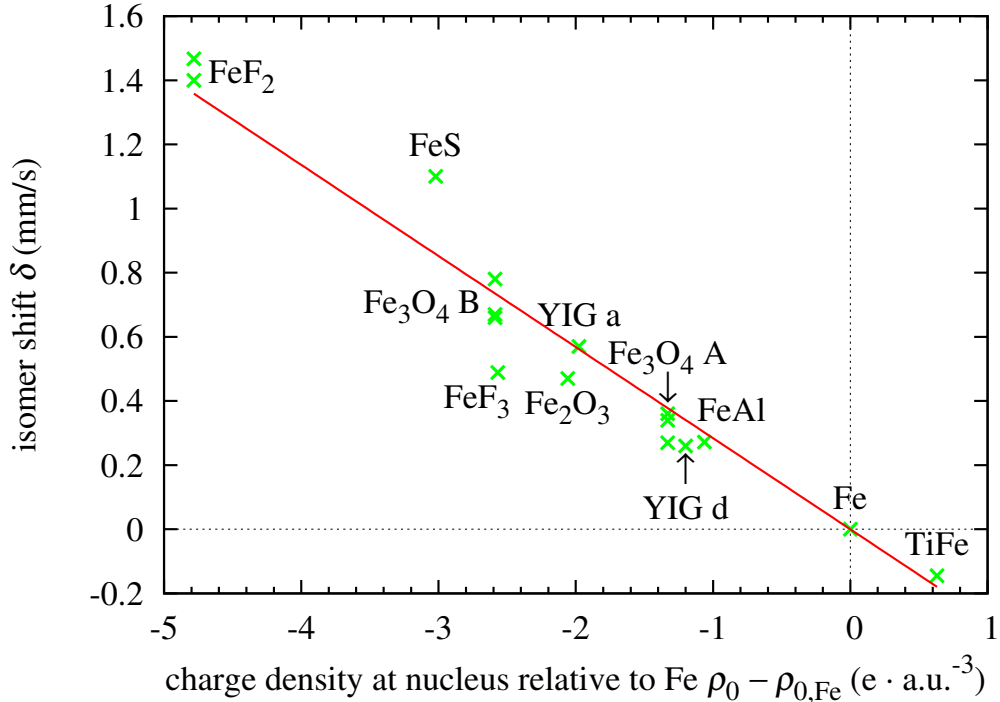
Figure 7.4: Calibration of isomer shift – points represent the values from Table 7.4, the line is a fit of equation (7.2). ($a_0 \approx 5.292 \cdot 10^{-11}$ m is the Bohr radius)

7.3 Hyperfine Field Anisotropy

7.3.1 Analysis of Hyperfine Parameters from the DFT Calculations

In order to obtain hyperfine field anisotropy tensors and isotropic parts, the ab initio calculations of the hyperfine field were performed for multiple directions of magnetization in the *ac-*, *cb-* and *ab-*planes. (This approach can be understood as a parallel to the experiment of Mizoguchi [14], although there are several important differences.) The dominant part of the hyperfine field is presented by the isotropic contact term B_{cont} ($|B_{cont}|$ reaches up to 53.8 T for the A sites and up to 54.9 T for the B sites). The role played by the other hyperfine field contributions can be judged by their magnitude – for the iron ions at the B sites, $|B_{dip}|$ ranges up to 13.7 T, $|B_{orb}|$ to 4.6 T and $|B_{lat}|$ to 1.1 T. Note that anisotropy of all of these terms is significant. (In Ref. [39], the terms B_{orb} and B_{lat} were omitted.)

Processing of the output data had to be done with caution: One has to take into account a tendency of the spin and orbital magnetization to incline towards the easy magnetization axis caused by spin-orbit coupling if a general magnetization direction is specified. In this case, the resulting direction of total magnetization (which was later passed in the fit) differed from the specified direction by at most 10° and the magnetic moments of individual iron ions were collinear as supposed (deviations from the direction of the total magnetization direction were below 0.5°). Another caveat concerns the complex dependence of the total energy on the direction of magnetization which presumably possesses

multiple local minima. The self-consistent iteration procedure started for close (or even the same) magnetization directions may be susceptible to converging to unrelated minima depending on the initial population matrices. Independently repeated calculation for the specified magnetization direction $[30\bar{1}]$ yielded an estimate of error of the hyperfine field up to 0.3 T (i. e. 0.4 MHz error of the ^{57}Fe NMR frequency) caused by this effect.

Fit of Hyperfine Anisotropy Tensors

The dependences of hyperfine fields on magnetization direction are determined by hyperfine field anisotropy – see part 4.1.3. In order to simplify a comparison of the results with the ^{57}Fe NMR data of Mizoguchi [14], the calculated hyperfine fields at iron nuclei were expressed as ^{57}Fe NMR resonance frequencies by considering their direct proportionality characterized by gyromagnetic factor $\gamma = 1.38156$ MHz·T^{-1} [110]. Thus, the equations from part 4.1.3 can be written in terms of frequency:

The dependence of resonance frequency f on magnetization direction denoted by direction cosines ϑ_α, $\alpha = a$, b, c (taken with respect to orthorhombic axes $\vec{a}$, $\vec{b}$, $\vec{c}_0$) can be expressed as

$$
f = f_{\text{iso}} + f_{aa}\vartheta_a^2 + f_{bb}\vartheta_b^2 + f_{cc}\vartheta_c^2 + 2(f_{ab}\vartheta_a\vartheta_b + f_{ac}\vartheta_a\vartheta_c + f_{bc}\vartheta_b\vartheta_c) =
$$
$$
= f_{\text{iso}} + \begin{pmatrix} \vartheta_a \\ \vartheta_b \\ \vartheta_c \end{pmatrix} \cdot \begin{pmatrix} f_{aa} & f_{ab} & f_{ac} \\ f_{ab} & f_{bb} & f_{bc} \\ f_{ac} & f_{bc} & f_{cc} \end{pmatrix} \cdot \begin{pmatrix} \vartheta_a \\ \vartheta_b \\ \vartheta_c \end{pmatrix} = f_{\text{iso}} + \begin{pmatrix} \vartheta_a \\ \vartheta_b \\ \vartheta_c \end{pmatrix} \cdot \hat{F}_{\text{ani}} \cdot \begin{pmatrix} \vartheta_a \\ \vartheta_b \\ \vartheta_c \end{pmatrix}, \quad (7.3)
$$

where the isotropic term f_{iso} and anisotropy tensor $\hat{F}_{\text{ani}}$ ($\text{Tr}\left[\hat{F}_{\text{ani}}\right] = 0$) are explicitly separated as in equation (4.11). The transformation of the anisotropy tensor into a canonical form

$$
\hat{F}'_{\text{ani}} = \begin{pmatrix} f'_a & 0 & 0 \\ 0 & f'_b & 0 \\ 0 & 0 & f'_c \end{pmatrix} \quad (7.4)
$$

yields the same principal axes $\vec{p}_a$, $\vec{p}_b$ and $\vec{p}_c$ of the tensor as in the case of expression (4.12). Similarly to relation (4.13), a parameter characterizing the magnitude of hyperfine anisotropy can be introduced

$$
f_{\text{ani}} = \sqrt{\frac{1}{3}((f'_a - f'_b)^2 + (f'_b - f'_c)^2 + (f'_c - f'_a)^2)} = \sqrt{f'^2_a + f'^2_b + f'^2_c}. \quad (7.5)
$$

In the elementary Cc cell of magnetite, the glide along the $\vec{c}$ axis with the ac-glide plane creates 8 different pairs of crystallographically equivalent sites from 16 Fe(A) and 16 different pairs of crystallographically equivalent sites from 32 Fe(B).[2] However, the sites in these pairs are not magnetically equivalent for a general direction of magnetization. Taking into account the nature of the glide

---

[2]Centration, which is not considered here, just doubles the numbers of sites in the elementary cell belonging to each group of crystallographically and magnetically equivalent sites.

symmetry operation, the f_{ac} parameter in equation (7.3) is the same for the two crystallographically equivalent sites in each pair, whereas the parameters f_{ab}, f_{bc} have opposite signs. This is the reason of splitting of the angular dependences of ^{57}Fe NMR frequencies for magnetization in the bc- and ab-planes observed in the results of the DFT calculations as well as in the results of Mizoguchi [14].

The calculated dependences of the hyperfine field on magnetization direction were fitted with equation (7.3) and subsequently the canonical form of $\hat{F}_{ani}$ tensors was found (see Table B.2 in Appendix). Uncertainty of the fitted parameters was typically below 0.03 MHz for the A sites and 0.03 – 0.6 MHz for the B sites. Fitted dependences are plotted in Fig. 7.5 – the splitting of the curves for magnetic field in ac-plane mimics monoclinic twinning in Mizoguchi's experiment.

The tensors of hyperfine field anisotropy $\hat{F}_{ani}$ were visualized in Fig. 7.6 (the B sites) and in Fig. A.5 in Appendix (the A sites) in a similar fashion as the EFG tensors – only the formula (7.1) determining the distance r of object surface from the position of iron ion in question was modified:

$$ r = C \cdot [f_{aa}\vartheta_a^2 + f_{bb}\vartheta_b^2 + f_{cc}\vartheta_c^2 + 2(f_{ab}\vartheta_a\vartheta_b + f_{ac}\vartheta_a\vartheta_c + f_{bc}\vartheta_b\vartheta_c)] \qquad (7.6) $$

(ϑ_α, $\alpha = a$, b, c are direction cosines with respect to the orthorhombic axes and C is a scaling coefficient). Interpretation of the figures is also closely related to electronic configuration of particular iron ions. In case of the B sites, the anisotropy of trimeron central ions is significantly larger compared to the end ions and the principal axis connected with the smallest eigenvalue of anisotropy tensor of central ion is the closest to the axis of the trimeron. This observation reflects that the minority spin electron density around the central Fe^{2+}-like ions is considerably anisotropic because the charge is situated in a t_{2g} orbital corresponding to the trimeron axis. In contrast, the roughly spherical symmetry of the Fe^{3+}-like end ions is perturbed only by the partial charge transferred from the central ions. (In many cases, the end ion participates in multiple trimerons. Then the charges transferred from the central ions enter different orbitals and the impact on the symmetry of the end ion is still low.) The anisotropy of Fe^{3+}-like ions B8 and B15, which are not members of trimeron network, is small because the symmetry of their charge configuration is not considerably affected. The difference between the results and the model of Patterson [39] can be shown on Fe(B) pairs that are not parts of the zig-zag chain (e. g. B5'–B7): relatively similar electronic configuration of the ions would result from the one-electron bond, but the anisotropies of these ions are incomparable. In case of the Fe^{3+} ions at the A sites, the small anisotropy is the result of nearly spherical symmetry of their charge configuration.
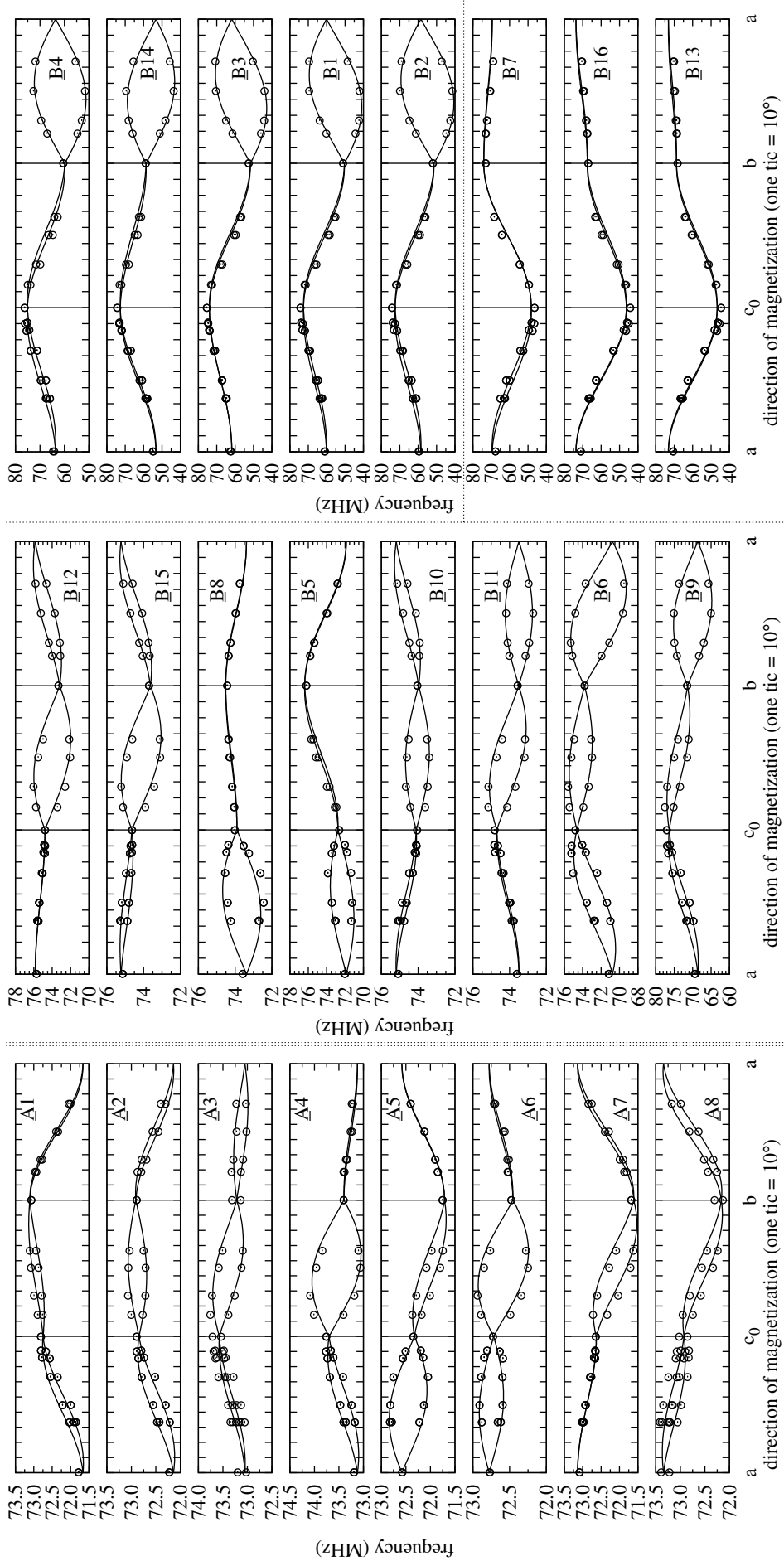
Figure 7.5: Dependence of calculated ^{57}Fe NMR frequencies on direction of magnetization in the ac-, bc-, and ab-planes – the data from the DFT calculations are represented by circles, while curves correspond to the best fit of equation (7.3) to these data. Site numbering and arrangement follow the convention introduced in part 7.1.
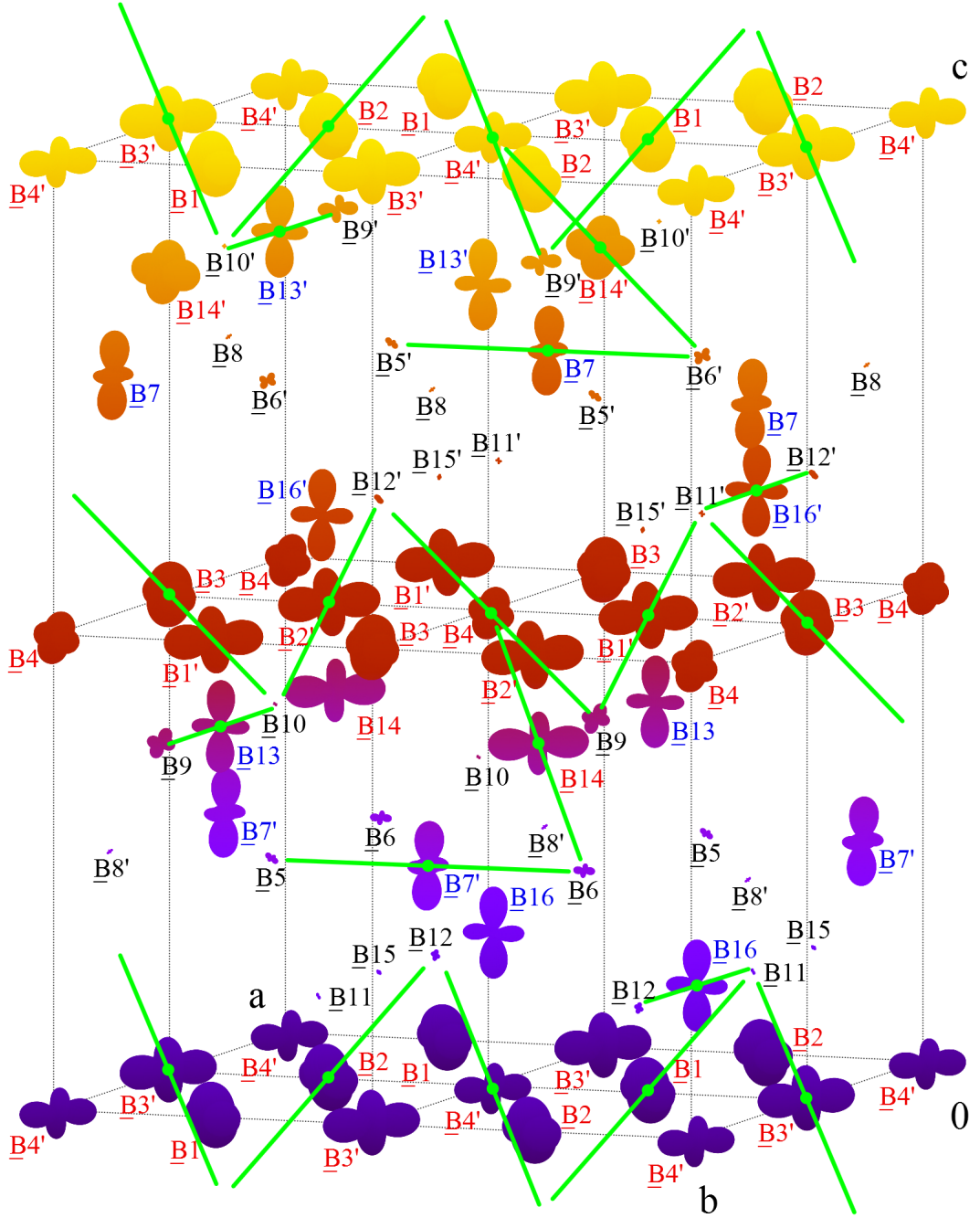
54

Figure 7.6: Hyperfine field anisotropy tensors of iron B sites extracted from the DFT calculations visualized in the elementary cell (scaling coefficient $C = 0.05 \text{ Å} \cdot \text{MHz}^{-1}$). Green lines highlight trimerons [1]. Site numbering and label colours follow the convention introduced in part 7.1; primes indicate the *ac*-glide symmetry generated sites. (Surface colour indicating *z*-coordinate is intended just to improve clarity.)

7.3.2   Reanalysis of the NMR Data of Mizoguchi

In his article [14], Mizoguchi published dependences of the ^{57}Fe NMR frequency on external magnetic field direction for all A and B sites. The experiment was performed at 4.2 K on a spherical single crystal sample with orthorhombic twin-

ning prevented during cooling. The external field $B_{\text{ext}} = 1.3$ T was rotated in the ac-, bc- and ab-planes (assuming orthorhombic coordinates) by 10° steps. For each of the A and B sites, there are two branches of the frequency dependence – monoclinic twinning (not incorporated in analysis in Ref. [39]) present in the sample is a cause of splitting of the curves for the magnetic field in *the ac*-plane, whereas the splitting for magnetic field in the ab- and bc-planes occurs because the sites connected by the ac-glide symmetry are not magnetically equivalent for magnetization lying in a general direction in these planes.

Calculation of Magnetization Direction

One has to point out that Mizoguchi rotated the external magnetic field, whereas the magnetization was rotated directly in the ab initio calculations described in the previous part. In general, magnetization direction is different from the direction of the external field due to magnetocrystalline anisotropy. Therefore, the directions of magnetization $\vec{M}$ had to be determined for given directions of the external field in order to process Mizoguchi's data properly. A numerical method similar to a procedure used by Mizoguchi [13] was implemented (unlike to Ref. [39], where the non-collinearity of the magnetization and the external magnetic field was neglected in analysis and it was only discussed).

The problem can be formulated as a minimization of energy

$$E = -\vec{B}_{\text{ext}} \cdot \vec{M} + E_{\text{an}}, \tag{7.7}$$

where E_{an} stands for the magnetocrystalline anisotropy, which can be expressed as

$$E_{\text{an}} = K_a \vartheta_a^2 + K_b \vartheta_b^2 + K_{aa} \vartheta_a^4 + K_{bb} \vartheta_b^4 + K_{ab} \vartheta_a^2 \vartheta_b^2 - K_u \vartheta_{111}^2. \tag{7.8}$$

in direction cosines (ϑ_a, ϑ_b and ϑ_{111} are direction cosines of magnetization taken with respect to the monoclinic $\vec{a}$, $\vec{b}$ axes and cubic [111] direction (6$^{\text{th}}$ and higher order terms neglected)). [16] The anisotropy constants of magnetite at 4.2 K were determined by Abe et al. [16] (in units of 10^4 J$\cdot$m^{-3}):

$$
\begin{aligned}
K_a = 25.5, \ K_b = 3.7, \ K_{aa} = 1.8, \\
K_{bb} = 2.4, \ K_{ab} = 7.0, \ K_u = 2.1.
\end{aligned}
\tag{7.9}
$$

In his works, Mizoguchi [13], [14] employed more precise values:

$$
\begin{aligned}
K_a = 25.52, \ K_b = 3.66, \ K_{aa} = 1.76, \\
K_{bb} = 2.42, \ K_{ab} = 7.0, \ K_u = 2.13.
\end{aligned}
\tag{7.10}
$$

Using the values (7.10) and $M = 5.09 \cdot 10^5$ A$\cdot$m^{-1} [14], [13], a numerical calculation of the $\vec{M}(\vec{B}_{\text{ext}})$ dependence was carried out for $B_{\text{ext}} = 1.3$ T – the result is plotted in Fig. 7.7. Apparently, if $\vec{B}_{\text{ext}}$ is in the ac- and bc-planes, $\vec{M}$ lies almost perfectly in these planes. On the other hand, this does not apply if $\vec{B}_{\text{ext}}$ is in the ab-plane. Thus, even a small misorientation of the external field close to the hard $\vec{a}$ direction may result in a non-negligible error of the magnetization direction.
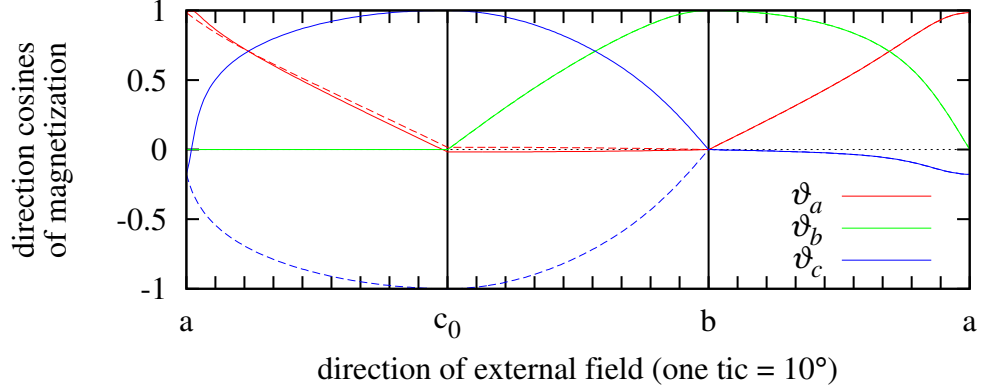
Figure 7.7: Calculated dependence of magnetization direction on the direction of the external magnetic field B_{ext} = 1.3 T. Dashed curves indicates magnetization trajectory in the monoclinic twin. The dependence was calculated in orthorhombic coordinates (which do not contain $\vec{c}$ axis tilt).

The situation is slightly complicated by monoclinic twins present in the sample as a demagnetizing field of one of the monoclinic domains adds to the magnetic field in the other domain(s) (and vice versa). It seems impossible to find out the actual configuration of monoclinic domains in the magnetite sphere when Mizoguchi performed his experiment. Therefore, only a primitive model supposing a homogeneous distribution of both types of domains (in a ratio of 1:1) in the sample volume was tested. The model yielded slightly different $\vec{M}(\vec{B}_{ext})$ dependences which in turn led to small changes of fitted values of f_{iso} and $\hat{F}_{ani}$. Nevertheless, the quality of the fit was almost the same as in the case when this model was not used. Considering that the model is too simple to characterize reality, the demagnetizing field of the domains was not included in the analysis.

Fit of Hyperfine Anisotropy Tensors

Before fitting the dependence (7.3), the frequency shift caused by the external field was compensated for by a subtraction of a projection of $\vec{B}_{ext}$ on magnetization direction (multiplied by the gyromagnetic factor γ) from the NMR frequencies. The fit reflected the splitting of the curves for each iron site – i. e. fits of all combinations of assignments of individual branches to monoclinic twins (for $\vec{M}$ in the ac-plane) and to particular ac-glade symmetry connected sites (for $\vec{M}$ in the bc- and ab-plane) were tried and the best one was chosen. The signs of f_{ab}, f_{bc} and of b-component of principal axes are arbitrary (but the sign of $f_{ab} \cdot f_{bc}$ is known) since the iron positions connected by the ac-glide symmetry cannot be distinguished by the experiment. Errors of the fitted parameters were typically lower than or close to 0.01 MHz in case of the A sites and 0.02 – 0.7 MHz for the B sites. Subsequently, the anisotropy tensors $\hat{F}_{ani}$ were brought to their canonical form $\hat{F}'_{ani}$. The results are provided in Table B.3 in Appendix, while fitted curves are shown in Fig. 7.8.
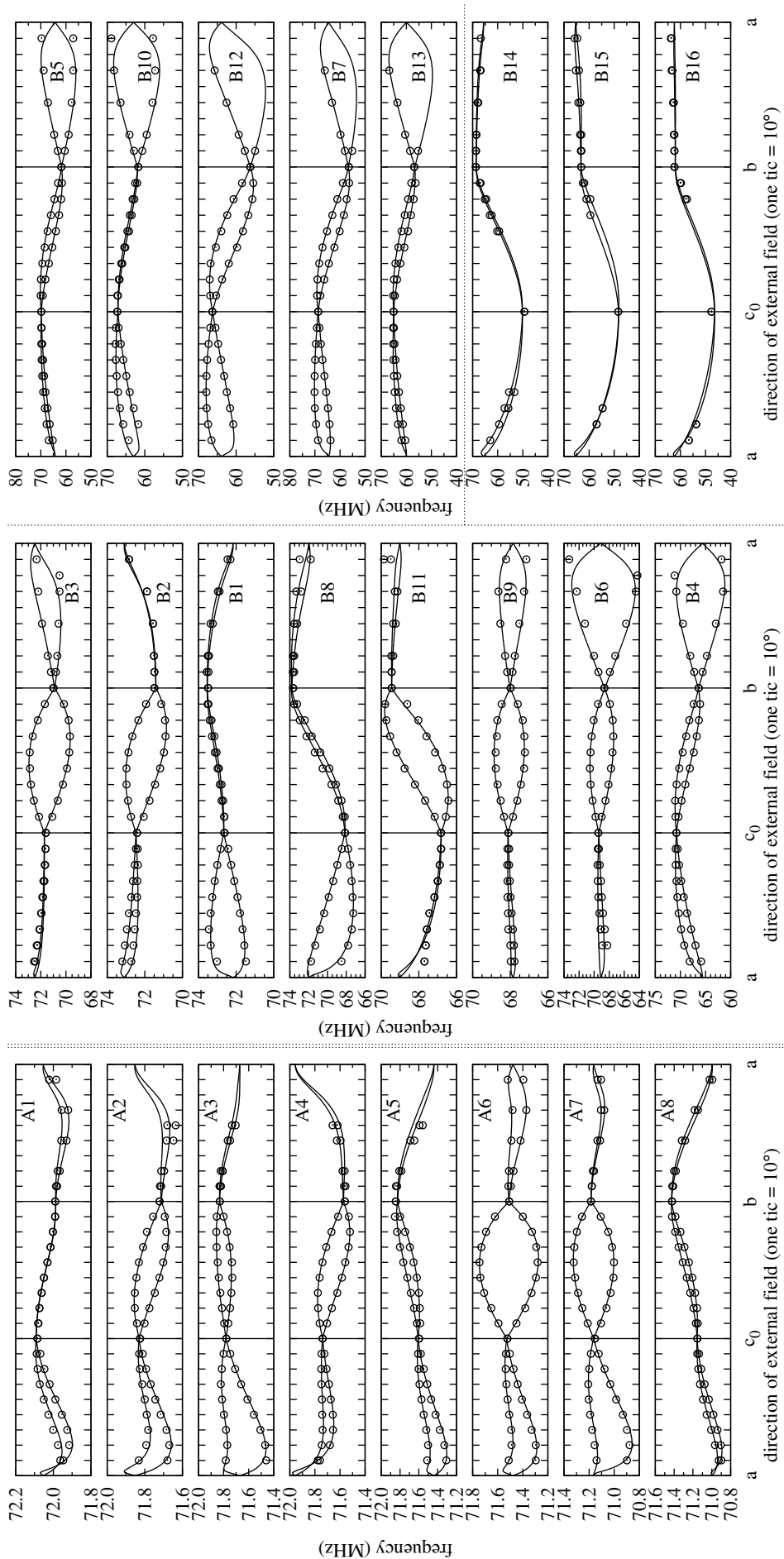
Figure 7.8: Dependence of experimental ^{57}Fe NMR frequencies on the direction of the external field $B_{\text{ext}} = 1.3$ T in the ac-, bc-, and ab-planes – the experimental data [14] are represented by circles, while curves correspond to the best fit of equation (7.3) to these data. Site numbering and arrangement follow the convention introduced in part 7.1.

58

7.3.3 Comparison of the Hyperfine Parameters Extracted from the NMR Data and from the DFT Calculations

Figs. 7.9 and 7.10 present a useful, though simple, comparison of calculated and experimental ^{57}Fe NMR frequencies: the iron sites are ordered by their decreasing isotropic part f_{iso}. The situation depicted in Fig. 7.9 is fairly simple – the Fe^{3+} state of the A site ions is associated with high spin moment and low orbital moment, thus isotropic part f_{iso} is high and anisotropy f_{ani} is low. Variation of f_{iso} and f_{ani} of the A site ions is small as differences of their electronic configurations are tiny. A different picture is found in Fig. 7.10 displaying the B site parameters – apparently, both calculated and experimental data can be separated into two groups. Iron ions in the left part of the graph exhibit higher isotropic part f_{iso} and smaller anisotropy f_{ani} in comparison with the ions in the right part. This indicates that the iron ions in the left part are Fe^{3+}-like (see Table 7.2) because the occupation of their minority spin $3d$ states is low, resulting in higher spin moment, and thus also higher f_{iso}. Simultaneously, orbital moments of these ions are low, leading to a small anisotropy. An opposite description would apply to the Fe^{2+}-like ions in the right part of Fig. 7.10. A more direct comparison of the f_{iso} and f_{ani} (as well as V_{zz}) parameters from the DFT calculations with the Fe(B) ion valence is provided in Fig. 7.11, confirming these deductions.
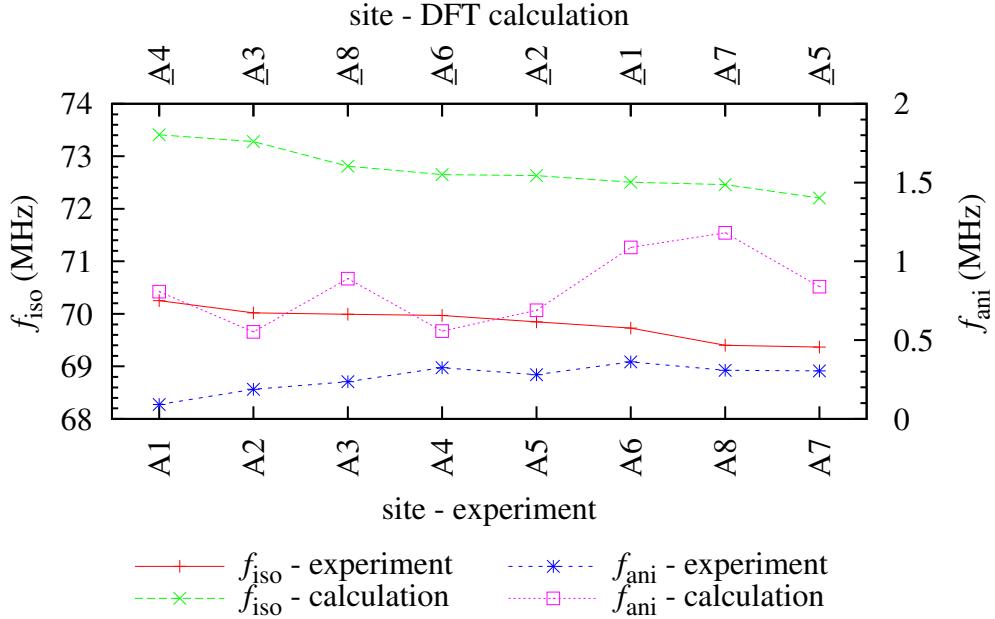
Figure 7.9: Comparison of isotropic and anisotropic parts of the ^{57}Fe NMR frequencies of the A site ions obtained from the experiment of Mizoguchi and from the DFT calculations. The sites are arranged by decreasing f_{iso}. In the case of the experimental data, site labels respect the convention of Ref. [14]. For the data from the DFT calculations, the site numbering follows the convention introduced in part 7.1. The lines are guides for the eye only.

Since the hyperfine data are now divided into groups of Fe^{3+}-like and Fe^{2+}-like ions, one would be able to interpret the experimental hyperfine parameters in relation to the electronic configuration of trimerons – the argumentation would be
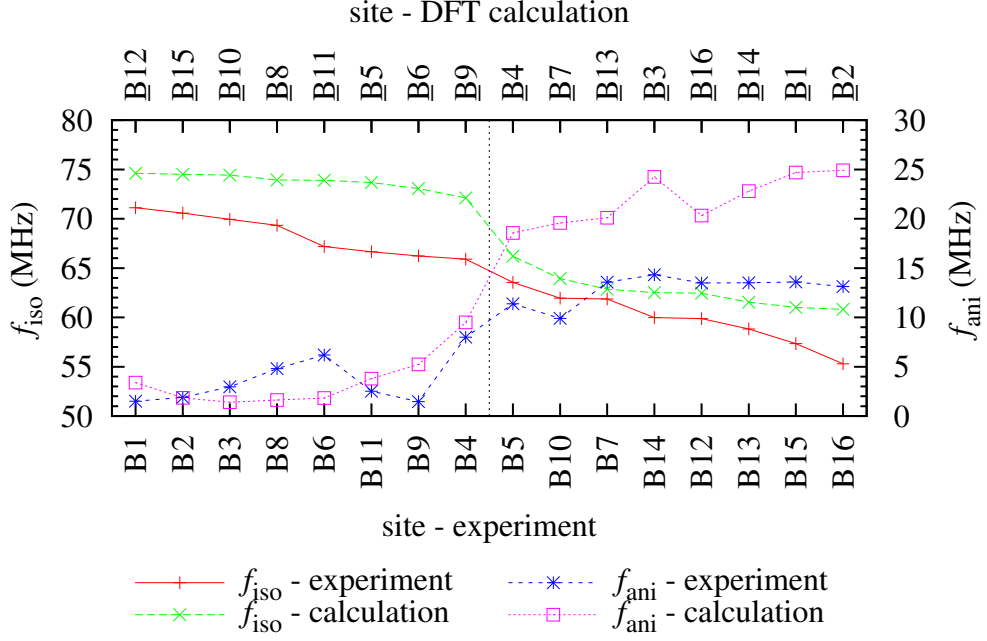
Figure 7.10: Comparison of isotropic and anisotropic parts of the ^{57}Fe NMR frequencies of the B site ions obtained from the experiment of Mizoguchi and from the DFT calculations. The sites are arranged by decreasing f_{iso}. In the case of the experimental data, site labels respect the convention of Ref. [14]. For the data from the DFT calculations, the site numbering follows the convention introduced in part 7.1. The lines are guides for the eye only.

essentially the same as in the case of the parameters from the DFT calculations, but a unique link between the hyperfine data and particular crystallographic positions would be missing.

However, the hyperfine field anisotropy tensors contain much more information than the f_{ani} parameter, thus allowing for a deeper search for the connection between the calculated and experimental data. Experimental angular dependences of NMR frequencies can be correlated with the ones from the DFT calculations by evaluating mean square deviation $\sigma(i,j)$:

$$
\sigma(i,j) = [\sum_{\alpha=aa,bb,cc} ((f_{\mathrm{iso}}^{\mathrm{calc}}(i) + f_{\alpha}^{\mathrm{calc}}(i)) - (f_{\mathrm{iso}}^{\mathrm{exp}}(j) + f_{\alpha}^{\mathrm{exp}}(j)))^2
$$

$$
+ 2 \sum_{\alpha=ab,ac,bc} (f_{\alpha}^{\mathrm{calc}}(i) - f_{\alpha}^{\mathrm{exp}}(j))^2]^{1/2}. \tag{7.11}
$$

The index i of the calculated data indicates a particular B site in the Cc cell, whereas the index j of the experimental data relates to a specific pair of branches of the frequency dependence. (Considering arbitrary sign of f_{ab}^{exp} and f_{bc}^{exp} and the known sign of their product, the combinations of the signs resulting in the lowest $\sigma(i,j)$ were chosen for the evaluation.) The values of $\sigma(i,j)$ are listed in Table B.4 in Appendix and graphically presented in Fig. 7.12. They facilitate association of the B sites with the hyperfine field parameters obtained from the experiment. Each possible assignment of experimental and calculated data can be characterized by a total mean square deviation
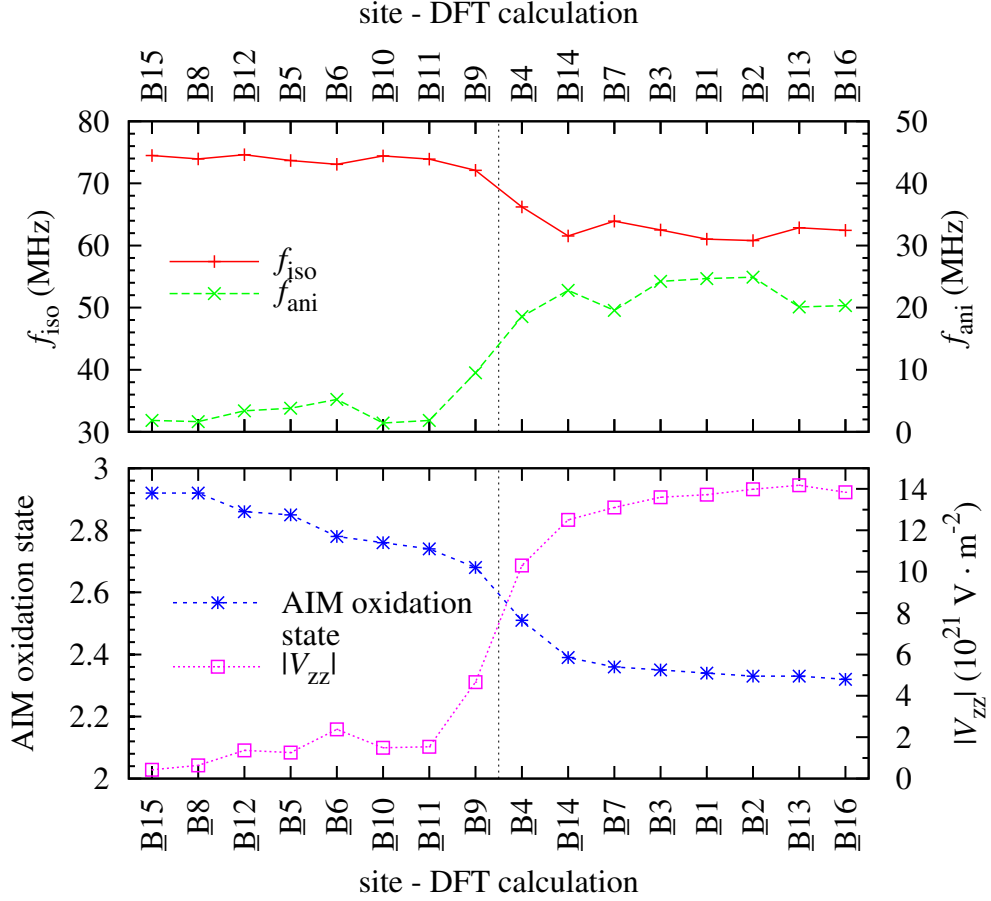
Figure 7.11: Isotropic and anisotropic parts of the ^{57}Fe NMR frequencies of the B site ions and V_{zz} parameter of EFG obtained from the DFT calculations in comparison with the Fe(B) ion valence from the AIM method. The sites are ordered by the decreasing valence. The site numbering follows the convention introduced in part 7.1. The lines are guides for the eye only.

$$\sigma = \frac{1}{16} \sum_{K=1}^{16} \sigma(i_K, j_K). \tag{7.12}$$

The assignment determines the sixteen pairs (i_K, j_K) of indices. Minimal value of the total mean square deviation was found to be $\sigma_{\min} = 11$ MHz. The association corresponding to a diagonal of Fig. 7.12, which presents one of the best assignments, is visualized in Fig. 7.13 in the same style as Fig. 7.6. Nevertheless, note that multiple assignments with total mean square deviation close to the value of $\sigma_{\min}$ exist.

By examination of $\sigma(i, j)$ values, three groups of the B sites with correlated hyperfine parameters from experimental and DFT data were found. The members of these groups are denoted by a colour of the labels in Figs 7.2, 7.3, 7.6, 7.13, A.2 and A.3. The first group consists of eight Fe^{3+}-like ions with smaller anisotropy – this corroborates the finding based on Fig. 7.10. Further, the examination successfully matched a group of three crystallographic sites with three NMR lines which appear in a zero field spectrum [37], [72] at low frequencies separated from other spectral signals. The ions in this group exhibit similar hyperfine anisotropy

61
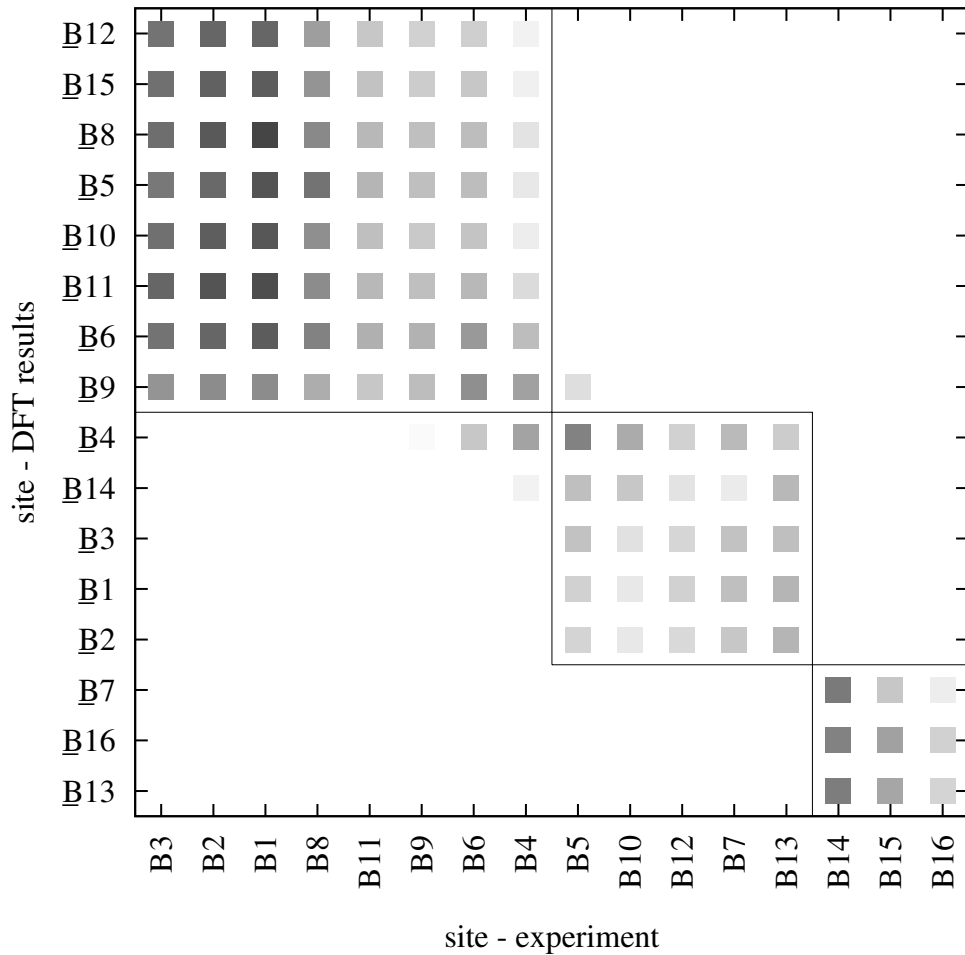
Figure 7.12: Visualization of mean square deviation $\sigma(i,j)$ calculated using equation (7.11) for all combinations of the B site data extracted from the DFT results and from the experiment. Brightness of each mark is proportional to $\sigma(i,j)$ magnitude (black for $\sigma(i,j) = 0$ MHz; white for $\sigma(i,j) \geq 18$ MHz) – darker field means better match. The site numbering follows the convention introduced in part 7.1. The sites are arranged to make their grouping (see text) apparent.
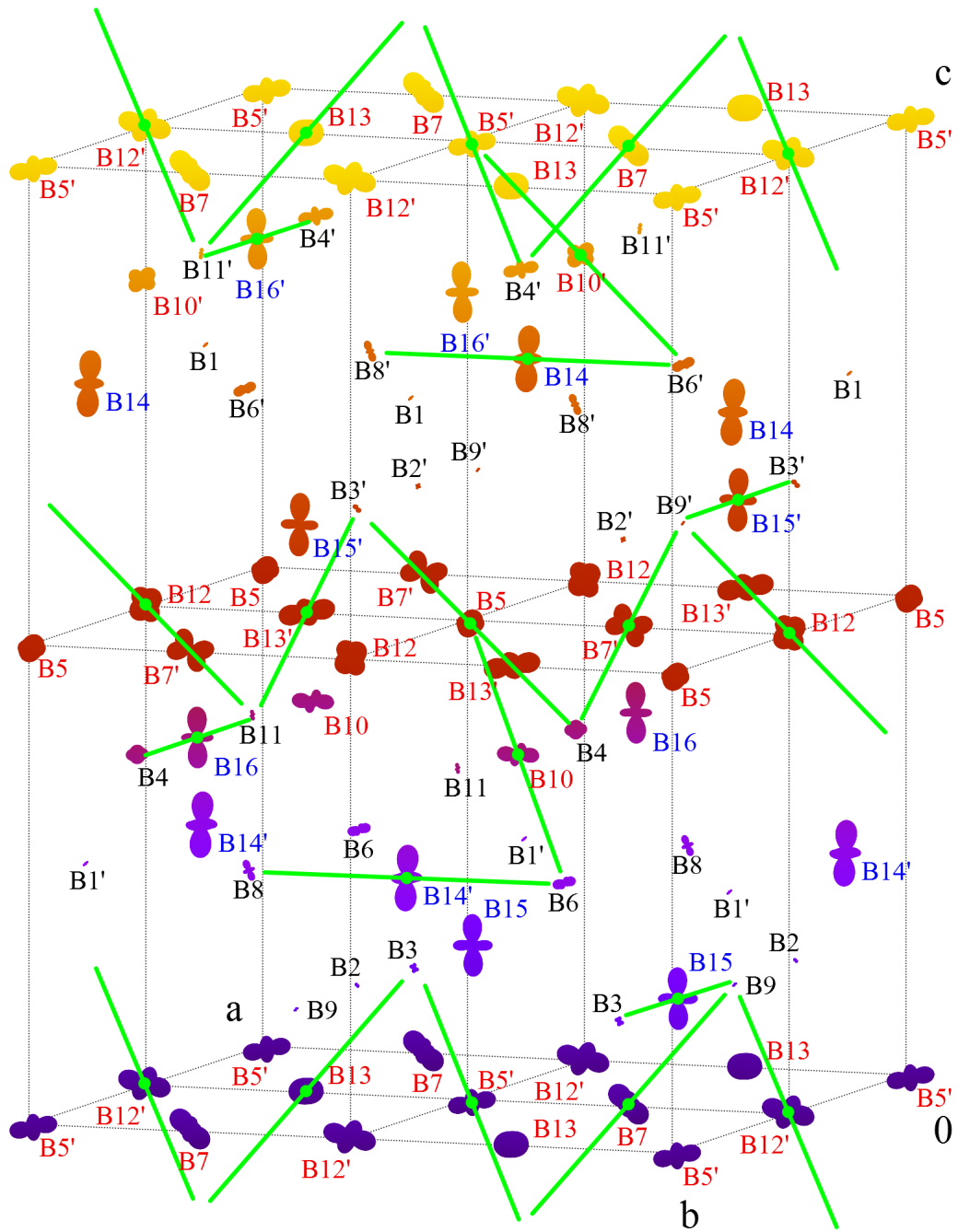
Figure 7.13: Hyperfine field anisotropy tensors of the B sites extracted from the NMR data visualized in the elementary cell (scaling coefficient $C = 0.05 \, \text{Å} \cdot \text{MHz}^{-1}$). Assignment with one of the minimal total mean square deviations σ (7.12) was used for the plot. Green lines highlight trimerons [1]. Site numbering follows the convention introduced in part 7.1; primes indicate the ac-glide symmetry generated sites. Sites belonging to the same group in Fig. 7.12 have the same label colour. (Surface colour indicating z-coordinate is intended just to improve clarity.)

tensors – their longest principal axis is parallel to the $\vec{c}_0$ direction and the other two principal axes point approximately along the $\vec{a}$ and $\vec{b}$ axes. Finally, the last group contains five Fe^{2+}-like ions situated in {002} planes of elementary Cc cell (with the exception of the ion at $\underline{B}14$ site) with the principal axes of their anisotropy tensors belonging to the highest (in absolute value) eigenvalues being close to either $[1\bar{1}0]$ or $[110]$ Cc direction.

The described correlation procedure based on equation (7.11) can be improved by taking into account that the DFT calculations yielded both isotropic parts and anisotropy tensors systematically overestimated. Therefore, a renormalization of these data in order to match their average with the average of experimental data may suppress this effect:

$$\sigma'(i,j) = [\sum_{\alpha=aa,bb,cc} ((c_{\text{iso}} f_{\text{iso}}^{\text{calc}}(i) + c_{\text{ani}} f_{\alpha}^{\text{calc}}(i)) - (f_{\text{iso}}^{\text{exp}}(j) + f_{\alpha}^{\text{exp}}(j)))^2$$
$$+ 2 \sum_{\alpha=ab,ac,bc} (c_{\text{ani}} f_{\alpha}^{\text{calc}}(i) - f_{\alpha}^{\text{exp}}(j))^2]^{1/2}. \tag{7.13}$$

$$c_{\text{iso}} = \frac{\sum_{\substack{j=1..8 \text{ (A sites)} \\ j=1..16 \text{ (B sites)}}} f_{\text{iso}}^{\text{exp}}(j)}{\sum_{\substack{i=1..8 \text{ (A sites)} \\ i=1..16 \text{ (B sites)}}} f_{\text{iso}}^{\text{calc}}(i)}$$

$$c_{\text{ani}} = \frac{\sum_{\substack{j=1..8 \text{ (A sites)} \\ j=1..16 \text{ (B sites)}}} f_{\text{ani}}^{\text{exp}}(j)}{\sum_{\substack{i=1..8 \text{ (A sites)} \\ i=1..16 \text{ (B sites)}}} f_{\text{ani}}^{\text{calc}}(i)}$$

Values of renormalization coefficients follow: $c_{\text{iso}} = 0.96$ and $c_{\text{ani}} = 0.32$ for the A sites; $c_{\text{iso}} = 0.94$ and $c_{\text{ani}} = 0.65$ in the case of the B sites. The mean square deviations $\sigma'(i,j)$ for the B sites listed in Table B.6 in Appendix thus provide more reliable measure of match of particular experimental and calculated hyperfine parameters not affected by the systematic overestimation of hyperfine field from the DFT calculations. The structure of graphical representation of $\sigma'(i,j)$ in Fig. 7.14 is the same as in Fig. 7.12, thus it corroborates the interpretation provided above. Minimal value of a total mean square deviation calculated from these values using equation (7.12) is $\sigma'_{\text{min}} = 5.2$ MHz. Again, there are multiple assignments with total mean square deviation close to σ'_{min} and the assignment plotted in Fig. 7.13 is one of them.

In the case of the Fe^{3+} ions at the A sites, the hyperfine field anisotropy is low and the isotropic terms vary only a little. Thus neither the correlation of the hyperfine parameters obtained from the experiment and from the DFT calculations based on equation (7.11) (see Table B.5 and Fig. A.6 in Appendix) nor the improved one using renormalization defined by equation (7.13) (see Table B.7 and Fig. A.7 in Appendix) allow for any attempt to assign ^{57}Fe NMR signals to particular crystallographic sites.
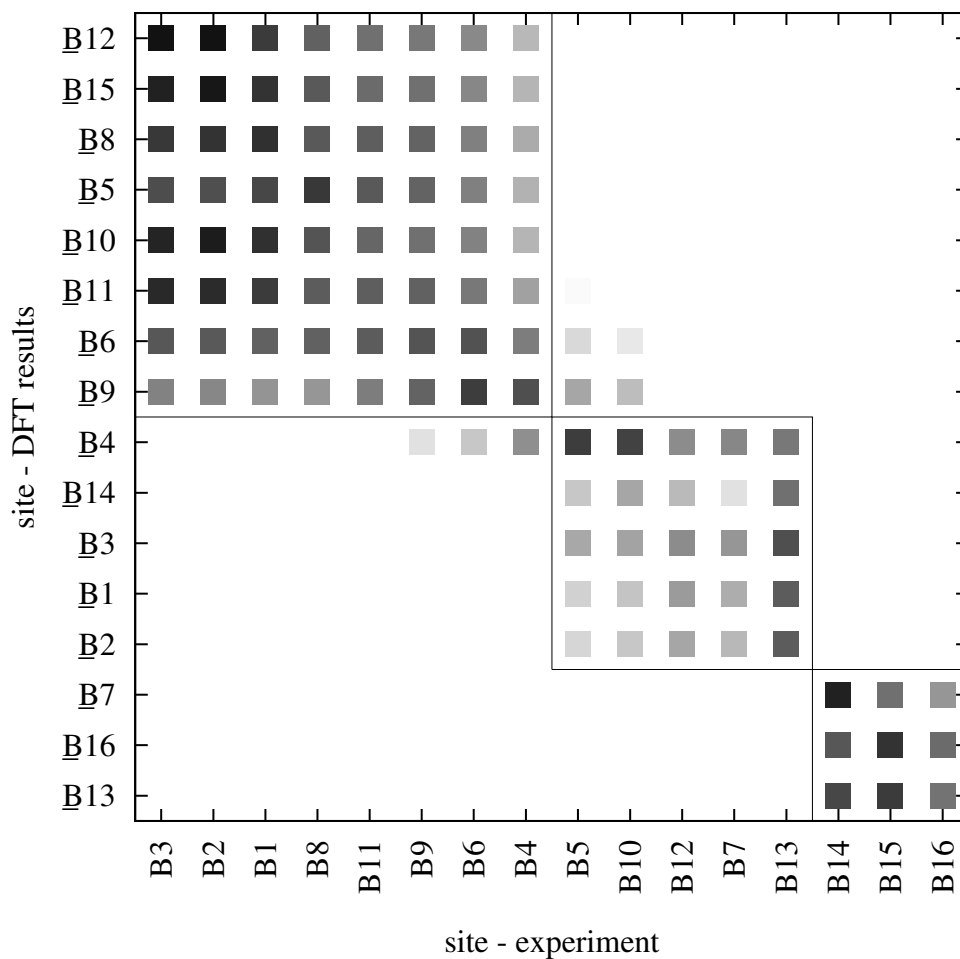
Figure 7.14: Visualization of mean square deviation $\sigma'(i,j)$ calculated using equation (7.13) for all combinations of the B site data extracted from the DFT results and from the experiment. Brightness of each mark is proportional to $\sigma'(i,j)$ magnitude (black for $\sigma'(i,j) = 0$ MHz; white for $\sigma'(i,j) \geq 15$ MHz) – darker field means better match. The site numbering follows the convention introduced in part 7.1. The sites are arranged to make their grouping (see text) apparent.

7.4 Mössbauer Spectra Simulation

The information on hyperfine fields (isotropic parts and anisotropy tensors) and electronic structure (EFG tensors and charge density at nuclei) at the iron ions in magnetite extracted from the DFT calculations in the previous parts allows for a simulation of corresponding ^{57}Fe Mössbauer spectrum of the low-temperature phase of magnetite in a zero external magnetic field.

The isomer shifts of particular iron sites determined by the charge density at the iron nuclei are listed in Table 7.3. Similarly, the EFG tensors can be easily found in Table B.1. The hyperfine fields shall be calculated using the equation (4.11), where the parameters B_{iso} and $\hat{B}_{\text{ani}}$ can be obtained from f_{iso} and $\hat{F}_{\text{ani}}$ in Table B.2 by dividing by the ^{57}Fe gyromagnetic ratio γ. Since there is no external magnetic field assumed, the magnetization lies in the easy direction.

Comparable strength of magnetic and quadrupole interaction (together with general EFG tensors) requires a numerical solution of equation (4.36) as no analytical approximations based on the perturbation theory are valid in this case. Therefore, the FitSuite 1.0.4 program [111] was employed for the simulation. For a convenient comparison with the experimental data, the HWHM linewidth was set to 2Γ and two types of samples were considered: a single-domain single crystal oriented in [201] direction towards the γ-ray and a powder sample. The resulting simulated spectra are presented in Figs. 7.15 and 7.16 together with the experimental data [94].[3] (Contributions of individual iron sites to the spectra are shown in Figs. A.8 and A.9 in Appendix.) The experimental spectrum was acquired at 4 K from a thin plate (cca 0.1 mm) single crystal sample with [001] direction parallel to γ-ray.[4] The sample was grown in a skull melter [114] and subsequently underwent a subsolidus annealing in CO/CO_2 gas mixtures to establish appropriate stoichiometry [115], [116].

Larger splitting of the outer lines in the simulated spectra in Figs. 7.15 and 7.16 than in the experimental data can be attributed to the systematic overestimation of the hyperfine fields by the DFT calculations. This can be corrected by incorporating renormalization coefficients (7.13) (introduced in part 7.3.3) into equation (4.11):

$$
\begin{aligned}
B_{\text{hf}} = c_{\text{iso}}B_{\text{iso}} + c_{\text{ani}}(B_{aa}\vartheta_a^2 + B_{bb}\vartheta_b^2 + B_{cc}\vartheta_c^2 \\
+ 2(B_{ab}\vartheta_a\vartheta_b + B_{ac}\vartheta_a\vartheta_c + B_{bc}\vartheta_b\vartheta_c)) =
\end{aligned}
\tag{7.14}
$$

$$
= c_{\text{iso}}B_{\text{iso}} + c_{\text{ani}} \begin{pmatrix} \vartheta_a \\ \vartheta_b \\ \vartheta_c \end{pmatrix} \cdot \begin{pmatrix} B_{aa} & B_{ab} & B_{ac} \\ B_{ab} & B_{bb} & B_{bc} \\ B_{ac} & B_{bc} & B_{cc} \end{pmatrix} \cdot \begin{pmatrix} \vartheta_a \\ \vartheta_b \\ \vartheta_c \end{pmatrix} =
$$

$$
= c_{\text{iso}}B_{\text{iso}} + c_{\text{ani}} \begin{pmatrix} \vartheta_a \\ \vartheta_b \\ \vartheta_c \end{pmatrix} \cdot \hat{B}_{\text{ani}} \cdot \begin{pmatrix} \vartheta_a \\ \vartheta_b \\ \vartheta_c \end{pmatrix}
$$

---

[3]The simulation can be compared also with other published experimental Mössbauer spectra of magnetite – see e. g. Refs. [104], [105], [106], [112], [113].

[4]No magnetic field was applied, thus all possible domains produced by the orthorhombic and monoclinic twinning formed in the sample. Consideration of the magnetization directions in these domains (with respect to the γ-ray direction) reveals for particular sextets total line intensities in a ratio corresponding to the one expected in the simulations.
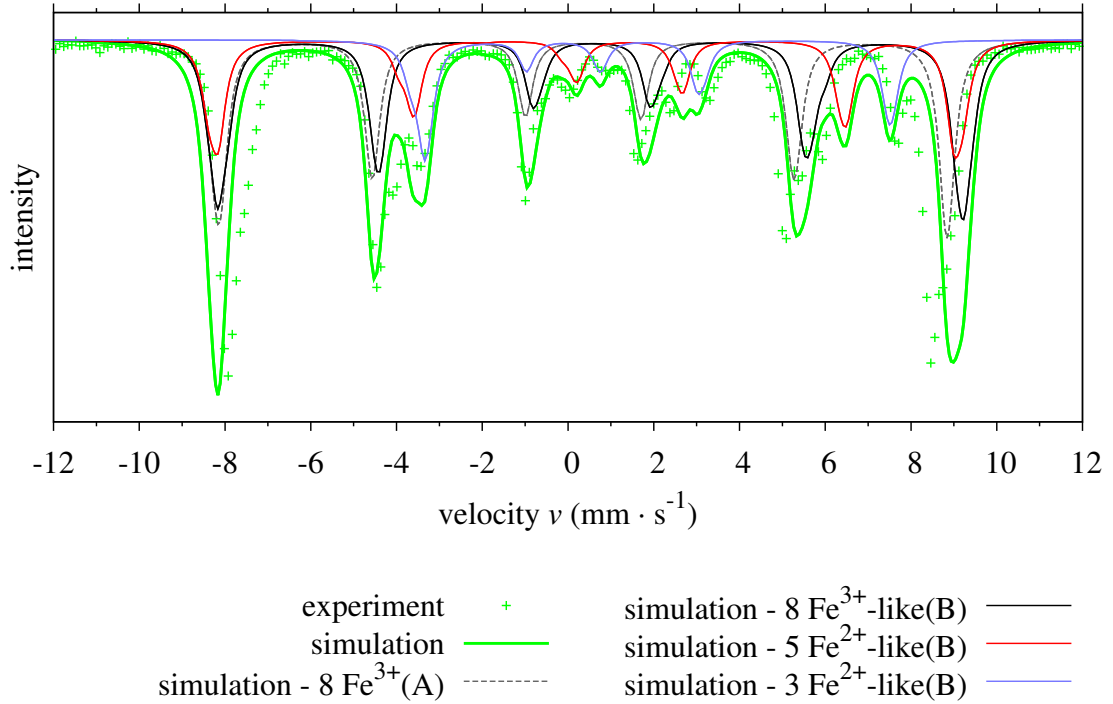
Figure 7.15: Simulated zero-field ^{57}Fe Mössbauer spectrum of a single-domain single crystal of (Cc phase) magnetite oriented in [201] direction towards the γ-ray in comparison with experimental data [94]. The three groups of Fe(B) components correspond to the three groups of Fe(B) ions in Fig. 7.12.
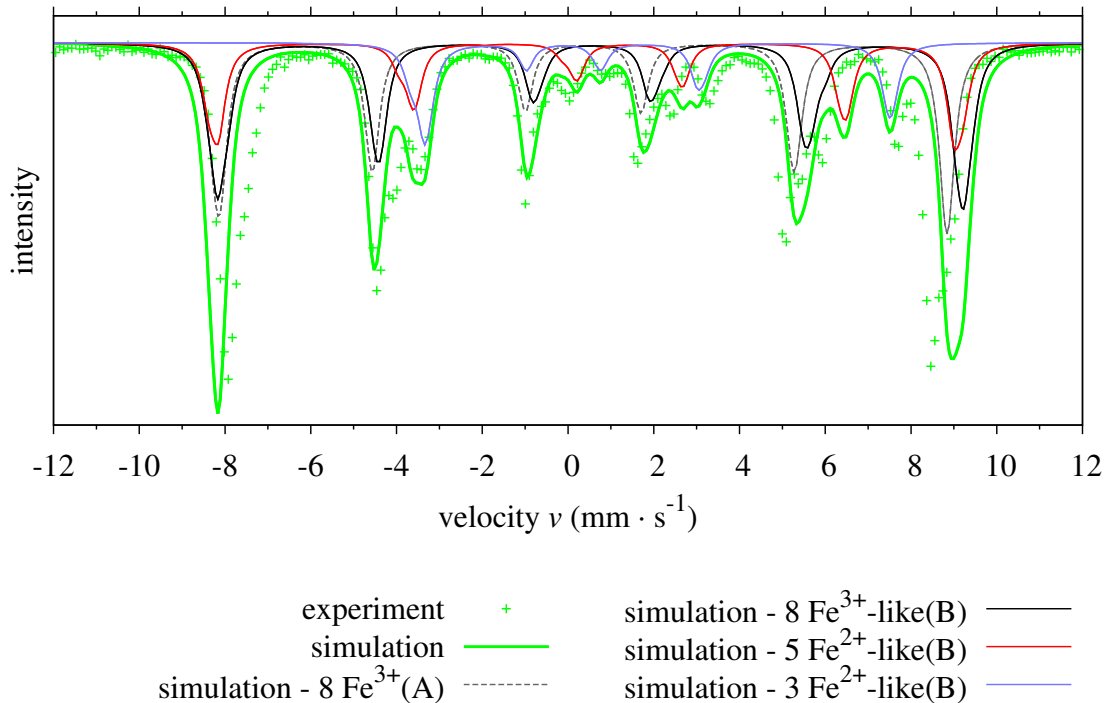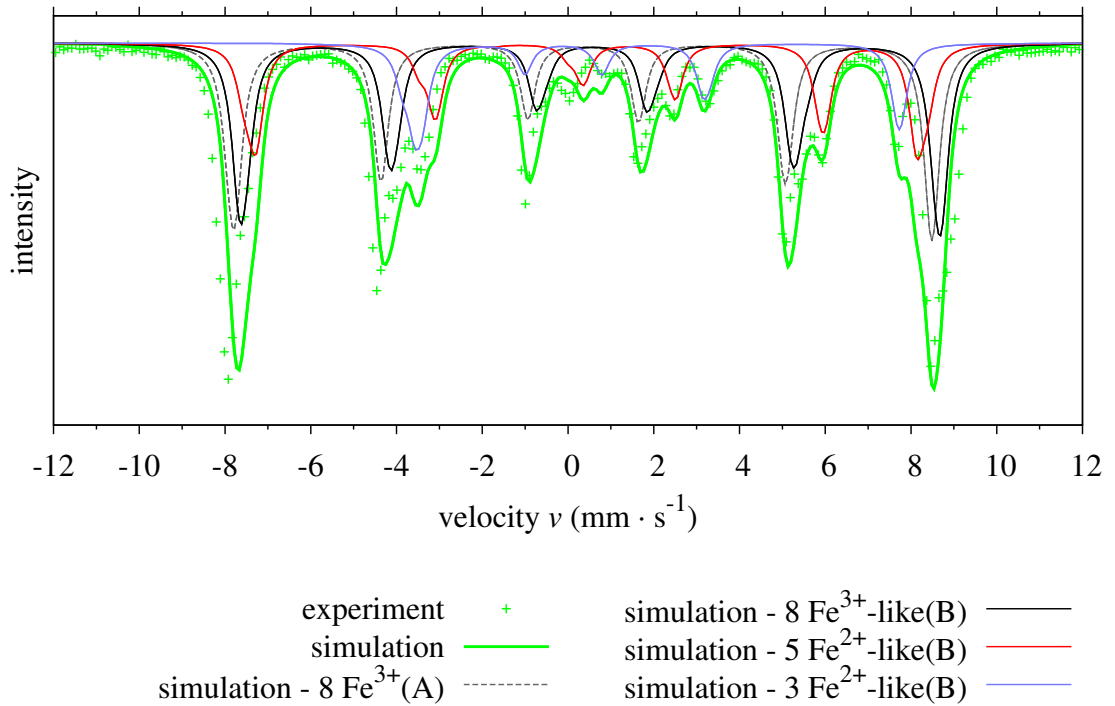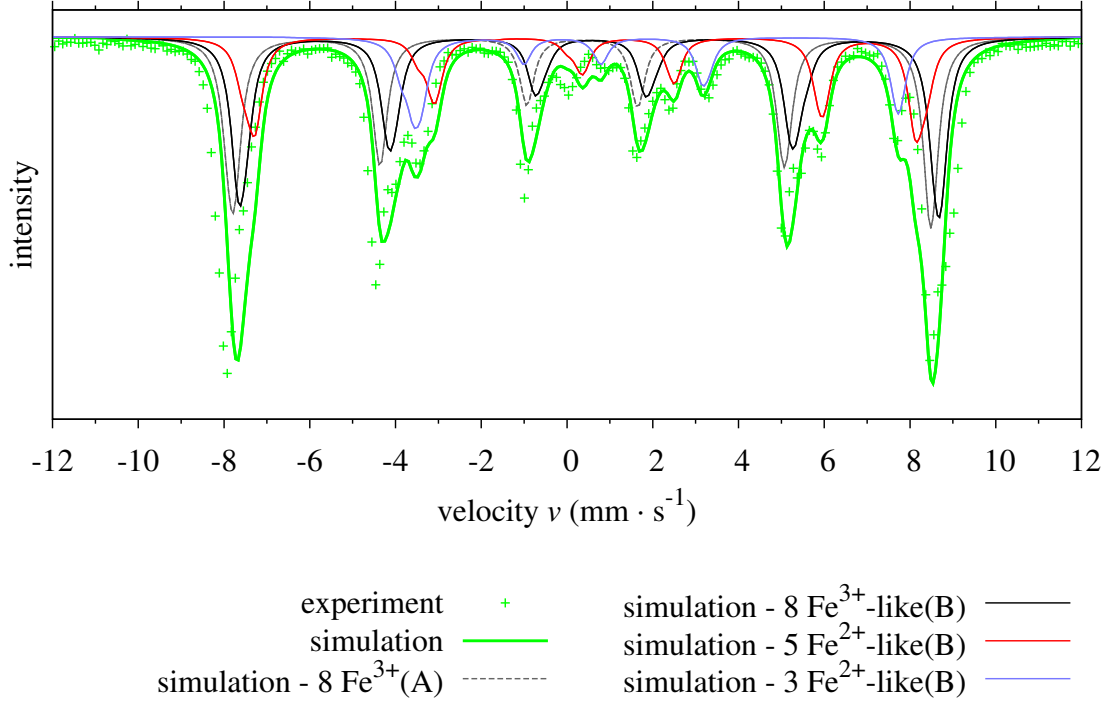

Figure 7.16: Simulated zero-field ^{57}Fe Mössbauer spectrum of a powder sample of (Cc phase) magnetite in comparison with experimental data [94]. The three groups of Fe(B) components correspond to the three groups of Fe(B) ions in Fig. 7.12.

The corresponding simulation outputs are plotted in Figs. 7.17 and 7.18. (See also Figs. A.10 and A.11 in Appendix showing contributions of individual iron sites to the spectra.) Although there are still some differences between the simulation and experiment remaining, they are more evenly distributed in the spectrum. Thus the simulation can be considered as an appropriate counterpart to the experimental data and the information how the particular groups of iron sites contribute to the spectrum can be extracted as indicated in the figures. Notably the peak at around 3 mm·s^{-1} understood by Pasternak et al. [105] as a characteristic feature distinguishing the Mössbauer spectra of the Cc phase from the cubic phase spectra can be clearly assigned to the group of $\underline{B}7$, $\underline{B}13$ and $\underline{B}16$ Fe^{2+}-like sites. The similarity of spectral contributions of individual Fe(B) ions belonging to the same group of the B sites implies that a decomposition of experimental Mössbauer spectra into four sextets ($8\times$ Fe^{3+}(A), $8\times$ Fe^{3+}-like(B), $5\times$ Fe^{5+}-like(B), $3\times$ Fe^{5+}-like(B)) is an appropriate approach whereas an identification of individual iron sites in the spectra is barely feasible.

Figure 7.17: Simulated zero-field ^{57}Fe Mössbauer spectrum of a single-domain single crystal of (Cc phase) magnetite oriented in [201] direction towards the γ-ray in comparison with experimental data [94]. This simulation is based on renormalized hyperfine fields (see text). The three groups of Fe(B) components correspond to the three groups of Fe(B) ions in Fig. 7.12.

Figure 7.18: Simulated zero-field ^{57}Fe Mössbauer spectrum of a powder sample of (Cc phase) magnetite in comparison with experimental data [94]. This simulation is based on renormalized hyperfine fields (see text). The three groups of Fe(B) components correspond to the three groups of Fe(B) ions in Fig. 7.12.

7.5   The Impact of Substitution Defects

The knowledge about the electronic structure of low-temperature phase of magnetite gained in the previous parts allows also for a better understanding of the impact of a presence of substitution defects on electronic ordering and thus also on hyperfine interactions. Chemical formula of defect-containing magnetite can be formally written as $[\text{Fe}_{1-x}\text{X}_x]_\text{A}[\text{Fe}_{2-x'}\text{X}'_{x'}]_\text{B}\text{O}_4$, where x and x' denote concentrations of defects X and X', respectively. The defects affect electronic structure in two ways: by their charge and by a local deformation of the crystal structure. In the first approximation, the former shall be in focus as it is expected to result in more significant changes. Only if the deformation induced by the defect is large (due to different ion radius), the latter becomes important as well.

The defects entering the A sites primarily affect the 12 iron ions at the B sites which are the nearest cationic neighbours. In the case of the B site defects, the nearest cationic neighbours consist of 6 B site ions and 6 A site ions, while the former are closer than the latter (see Table 2.2). If the substitution entering a particular site releases more electrons than the original iron ion at the site, the other iron ions tend to shift their valence towards lower oxidation numbers, i. e. the B site ions incline to become more Fe^{2+}-like and the valence of the A site ions might be also slightly affected. In the opposite case when the substitution disengages fewer electrons, the other iron ions tend to increase their valence so the B site ions incline to Fe^{3+}-like states, while there is not much space for a change of the A site iron ion valence. Thus the B sites are expected to be more

sensitive to the presence of the defects in the structure than the A sites. The resulting impact on the iron ion electronic ordering is also affected by a change in the valence of oxygen ions, which present links between the A and B sublattices.

Considering the situation when the Fe^{2+}-like B site ions are inclined to increase their oxidation numbers, the populations of their minority spin electrons decrease. Thus their spin moments increase, leading to higher magnitude of isotropic contact field B_{cont} and of B_{dip} arising from dipolar on-site interaction with electron spin. At the same time, their orbital moments drop, resulting in smaller B_{orb} and thus also lower hyperfine field anisotropy. On the other hand, if the Fe^{3+}-like ions at the B sites tend to decrease their valence, the consequences are opposite.

The range of the impact of a single defect is determined by two counteracting aspects. First, the insulating character of the Cc phase does not allow for a uniform dynamic distribution of the surplus or deficit charge throughout the whole crystal, thus the perturbation cannot be easily screened. Second, even though the trimerons will be broken only locally, the interconnected nature of the trimeron network (or of the zig-zag chain in the Patterson's model [39]) implies that its electronic structure will be partially affected in broader surroundings.

These considerations together with the grouping of the B sites finally allow us to understand the zero field ^{57}Fe NMR spectra of magnetite containing various defects, which may thus serve as a descriptive illustration of the situation. Examples of the spectra accompanied by a spectrum of pure magnetite are presented in Figs. 7.19 and 7.20. In the spectrum of pure magnetite, the resonances of the A site Fe^{3+} ions can be found in a fairly narrow region around 70 MHz. Concerning the B sites, there are three signals at low frequencies originating from a group of Fe^{2+}-like ions, five lines from another group of Fe^{2+}-like ions and eight resonances of Fe^{3+}-like ions in the third group. The last two sets of signals are separated from the first one but not from each other. Nevertheless, the centre of gravity of the signal from the group of 5 Fe^{2+}-like ions is lower than that of the group of Fe^{3+}-like ions.

The spectra of samples with very low concentration of defects plotted in the upper parts of the figures exhibit only a broadening of spectral lines. It seems that the broadening of the B lines is larger compared to the A lines. Manifestation of the expected changes described above becomes apparent for slightly higher defect concentrations, which can be observed in the lower parts of the plots. (For clarity, the spectra of pure magnetite convoluted with the Gaussian function are provided in Figs 7.19 and 7.20 as a reference to allow for an easier distinction between a plain broadening and a systematic shift of spectral lines.) However, even in this case, the impact of the defects concerns dominantly the B sites as the A site signals are only broadened to some expected extent, but there are no significant shifts or merging into wide bands apparent.

In the case of zinc substituted magnetite $[Fe_{1-x}Zn_x^{2+}]_A[Fe_2]_BO_4$ and magnetite with vacancies $[Fe]_A[Fe_{2-x'}...^0_{x'}]_BO_4$, the valence of the B site ions affected by the defects in their vicinity tends to increase and thus the resonance frequencies of Fe^{2+}-like ions also increase – this can be observed namely at the separated low-frequency B lines, which transform into a wide band extending to significantly higher frequencies (in the case of non-stoichiometric magnetite, this band reaches even up to the high-frequency part of the spectrum, thus illustrating the profound
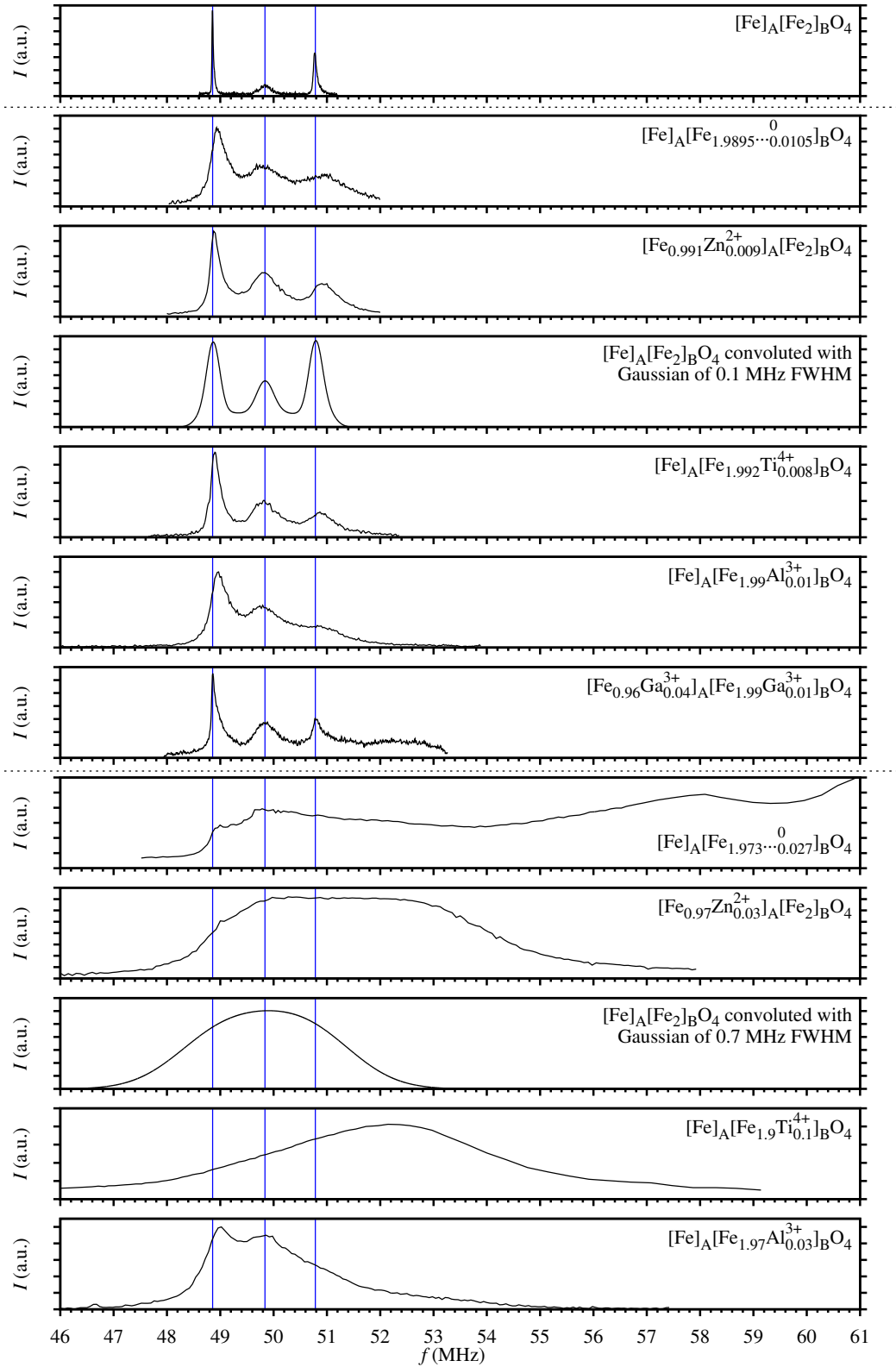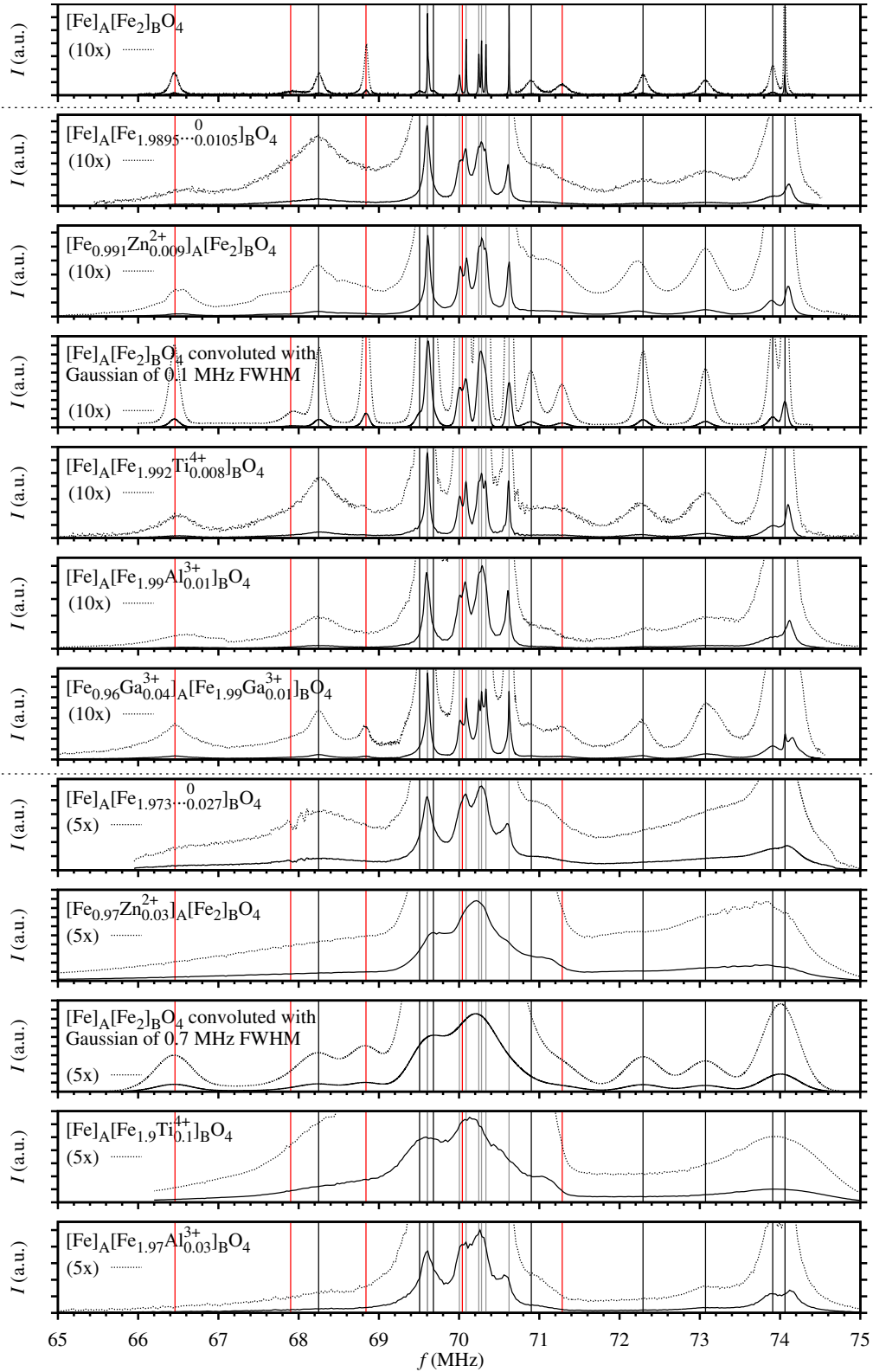
Figure 7.19: Low-frequency part of zero-field ^{57}Fe NMR spectra of magnetite at 4.2 K with various types of defects ($[Fe_{0.991}Zn^{2+}_{0.009}]_A[Fe_2]_BO_4$, $[Fe_{0.97}Zn^{2+}_{0.03}]_A[Fe_2]_BO_4$ [73]; $[Fe]_A[Fe_{1.9895}...^{0}_{0.0105}]_BO_4$ [117]; $[Fe]_A[Fe_{1.992}Ti^{4+}_{0.008}]_BO_4$ [118]; $[Fe]_A[Fe_{1.99}Al^{3+}_{0.01}]_BO_4$, $[Fe]_A[Fe_{1.97}Al^{3+}_{0.03}]_BO_4$, $[Fe_{0.96}Ga^{3+}_{0.04}]_A[Fe_{1.99}Ga^{3+}_{0.01}]_BO_4$ [119], [120], [121]) in comparison with a spectrum of pure magnetite [73]. The colour of the vertical lines in this figure and in Fig. 7.20 indicating frequencies of resonance lines of pure magnetite distinguishes between the A lines (grey) and different groups of the B lines (blue, red, black).

Figure 7.20: High-frequency part of zero-field ^{57}Fe NMR spectra of magnetite at 4.2 K with various types of defects ($[Fe_{0.991}Zn^{2+}_{0.009}]_A[Fe_2]_BO_4$, $[Fe_{0.97}Zn^{2+}_{0.03}]_A[Fe_2]_BO_4$ [73]; $[Fe]_A[Fe_{1.9895}...^0_{0.0105}]_BO_4$, $[Fe]_A[Fe_{1.973}...^0_{0.027}]_BO_4$ [117]; $[Fe]_A[Fe_{1.992}Ti^{4+}_{0.008}]_BO_4$, $[Fe]_A[Fe_{1.9}Ti^{4+}_{0.1}]_BO_4$ [118]; $[Fe]_A[Fe_{1.99}Al^{3+}_{0.01}]_BO_4$, $[Fe]_A[Fe_{1.97}Al^{3+}_{0.03}]_BO_4$, $[Fe_{0.96}Ga^{3+}_{0.04}]_A[Fe_{1.99}Ga^{3+}_{0.01}]_BO_4$ [119], [120], [121]) in comparison with a spectrum of pure magnetite [73]. The colour of the vertical lines in this figure and in Fig. 7.19 indicating frequencies of resonance lines of pure magnetite distinguishes between the A lines (grey) and different groups of the B lines (blue, red, black).

impact of the vacancies on the electronic structure of magnetite). Another change can be noticed in the 71.5 - 75 MHz range: the intensity increase in the spectral range of 71.5 - 73.5 MHz caused by a shift of resonances from lower original frequencies results in a merge of the signals in the 71.5 - 75 MHz range into a broad resonance band of heightened intensity.

Opposite situation arises in titanium substituted magnetite $[\text{Fe}]_A[\text{Fe}_{2-x'}\text{Ti}_{x'}^{4+}]_B\text{O}_4$ – the oxidation state of the B site ions in the range of the substitution impact tends to decrease. Therefore the resonance of Fe^{3+}-like ions tends to move towards lower frequencies, which is apparent especially in the spectral range of 67.5 - 69.5 MHz , where the intensity is considerably higher. Contrary to zinc-substituted and non-stoichiometric magnetite, the intensity in the range 71.5 - 73.5 MHz does not increase but rather the resonances around 74 MHz are slightly reduced. On the other hand, the three B site signals at low frequencies broaden into a single wide resonance signal and shift higher. This resembles the effects observed in the low-frequency part of the spectra of $[\text{Fe}_{1-x}\text{Zn}_x^{2+}]_A[\text{Fe}_2]_B\text{O}_4$ and $[\text{Fe}]_A[\text{Fe}_{2-x'}...{}_{x'}^0]_B\text{O}_4$, but the cause is different: The decrease of the valence of Fe(B) ions results in a decrease of their resonance frequency, thus a part of the signal is moved from the high-frequency spectral region to the low-frequency one, leading to a shift of the intensity maximum in the low-frequency part of the spectrum towards higher frequencies. Although the same effects are expected in the spectra of magnetite with aluminium substitution (which enters the B sites if the concentration is not high [60]) $[\text{Fe}]_A[\text{Fe}_{2-x'}\text{Al}_{x'}^{3+}]_B\text{O}_4$, the actual impact of the defects is lower due to a small charge difference between Al^{3+} ions and substituted B site ions. Even more specific example is presented by gallium substituted magnetite $[\text{Fe}_{1-x}\text{Ga}_x^{3+}]_A[\text{Fe}_{2-x'}\text{Ga}_{x'}^{3+}]_B\text{O}_4$ because the Ga^{3+} ions preferentially substitute Fe^{3+} ions at the A sites (thus their impact is minimal due to the same valence) but a small fraction (about 20%) of them enter the B sublattice [122], [123], inducing electronic structure changes comparable to the case of aluminium substituted magnetite. Therefore, the corresponding spectra of gallium substituted sample are placed in the upper parts of Figs. 7.19 and 7.20, even though they would fit into the lower parts if only a nominal defect concentration was taken into account.

A common feature of all of these types of defects in magnetite is the fact that the manifestation of defect impact in the spectra is limited only to line broadening if the defect concentration is very low, while it starts to be more apparent for slightly higher defect concentrations. This implies an existence of a critical defect concentration at which the crystal areas affected by individual defects start to overlap, thus turning the locally impacted structure into a globally perturbed system of the trimeron network. Studying the concentration dependences of ^{57}Fe NMR spectra published in Refs [73], [119], [117], the critical limit can be roughly estimated at about 1% of iron ions replaced by the defects with different charge. This means that the characteristic size of a region impacted by a single defect is comparable to the size of the elementary cell.

Chapter 8

Electronic Structure and Hyperfine Interactions in Magnetite Above the Verwey Transition – Results and Discussion

In the case of pure magnetite above the Verwey temperature, the hyperfine interactions observed by means of the ^{57}Fe NMR spectroscopy exhibit relatively simple behaviour as shown in part 4.4.5. However, there are still several open questions concerning linewidths and satellite signals which arise when substituted samples of magnetite are examined and when the temperature dependence of NMR spectra is closely studied.

8.1 Impact of Substitution on Electronic Structure and Hyperfine Interactions

Above the Verwey transition, pure magnetite has half-metallic character. In the B sublattice, there is one minority spin $3d$ electron per two Fe(B) sites. This is often formally expressed in the chemical formula $[Fe^{3+}]_A[Fe^{2+}Fe^{3+}]_2O_4$ as a 1:1 mixture of Fe^{2+}(B) and Fe^{3+}(B) sites, although the distribution of these 2 Fe(B) states is definitely not static. Instead, the minority-spin electrons are travelling across the B sublattice, thus being responsible for electrical conductivity. An insight into this system with strongly correlated charge carriers can be obtained by a study of consequences of an introduction of substitution defects.

Substitution valence different from the one of replaced iron ions implies that the valence of the other ions in magnetite has to change in order to maintain the whole crystal electrically neutral. Assuming the valence of Fe(A)$^{3+}$ and O^{2-} ions constant (at least to some extent), the dominant valence changes happen at the Fe(B) sublattice, which is prone to such changes due to its mixed-valence nature. Writing the general chemical formula of defect-containing magnetite as $[Fe^{3+}_{1-x}X^{v_X}_x]_A[Fe^{v_B}_{2-x'}X'^{v_X'}_{x'}]_BO_4$, where x and x' denote concentrations of defects X and X', respectively, the nominal Fe(B) valence can be calculated using the defect

concentrations x, x' and valences v_X, $v_{X'}$ by the following relation:

$$v_B = \frac{5 - (v_X - 3)\, x - v_{X'} x'}{2 - x'} \qquad (8.1)$$

A deviation of v_B from 2.5+ shall be understood as a slight prevalence of either $Fe^{2+}(B)$ or $Fe^{3+}(B)$ states. However, a distribution of time-averaged valence over the individual Fe(B) ions is not known – some form of screening of the charged defects can be expected, but the character of such screening and the role of charge carrier mobility present open questions.

Local impact of various cationic defects on crystal, electronic and magnetic structure was studied by means of the DFT calculations in Refs. [124] and [125]. The most apparent mechanism through which a non-magnetic cationic substitution affects local magnetic structure is a breaking of exchange couplings between the defect site and the iron ions in the vicinity. Further, the previously discussed change of Fe(B) valence results in a modification of magnetic moments of the B site iron ions. Finally, the difference between ionic radii of the original iron ion and of the defect ion causes a local distortion of the crystal lattice – this is also accompanied by changes in electronic configurations, magnetic moments and exchange interactions among iron ions in proximity. All these factors lead to a shift of the hyperfine field at nuclei in the vicinity of substitution defects.

8.2   Information in NMR Spectra

The ability of NMR to resolve signals originating from various crystallographic sites (and thus to study hyperfine field in different magnetic sublattices separately), together with its local sensitivity makes it a suitable tool for an investigation of hyperfine field in both pure and defect-containing magnetite samples. While the presence of substitution defects results mainly in a line broadening and changes of the shape of the spectra below the Verwey transition, the higher crystal symmetry above the Verwey transition simplifies the spectra and allows us to observe satellite signal patterns – resonating nuclei in the vicinity of a defect have their Larmor frequency shifted. Symmetry considerations determine the number and relative intensities of the satellite lines [119]: From the resonating nuclei in the first neighbourhood of the substitution ions or vacancies, there are 2 satellite signals in a ratio of 1:2 (for substitution at either A or B site) if the temperature is between the Verwey and spin-reorientation transition, while there are 3 satellite signals in a ratio of 1:1:2 for a temperature above the spin-reorientation transition. The defect concentration determines total satellite signal intensity (with respect to the main lines) as well as linewidth of the main resonances. On the other hand, frequencies of satellite lines do not depend on the concentration.

Temperature dependences of ^{57}Fe NMR spectra of single crystal magnetite with various types of substitution defects can be found in Refs. [70], [71], [118], [119], [120], [121], [123]. The spectra thus provide a useful data source for an analysis of hyperfine interactions in magnetite and impact of the substitution on them. Examples of the spectra are plotted in Figs. 8.1 and 8.2. Satellite pattern arising from the resonating iron nuclei at the A sites in the first neighbourhood of the substitution ions can be identified in spectra of titanium and aluminium substituted and vacancy-containing magnetite, while the pattern can be reliably

distinguished from satellite lines originating from resonating nuclei in a larger distance, which appear close to the main line (not indicated in the plots). However, only a single satellite resonance coming from iron nuclei at the B sites in the first substitution neighbourhood was found in spectra of gallium substituted magnetite. In the case of magnetite with zinc substitution, solely a satellite signal with the highest splitting between this line and the B lines can be reliably recognized to arise out of the ^{57}Fe nuclei in the first neighbourhood of the substitution – this signal and the satellite line in the spectra of gallium substituted magnetite have similar origin.
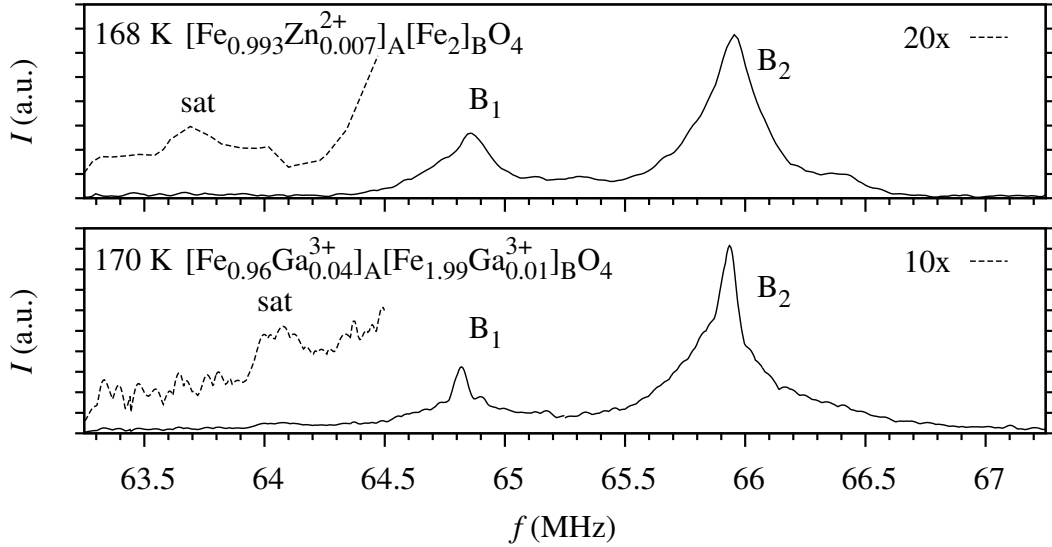
Figure 8.1: The ^{57}Fe NMR spectra of substituted magnetite well above the spin reorientation transition showing the B lines and the satellite signals (labelled "sat") from the resonating nuclei in the first neighbourhood of the substitution ions at the A sites. ($[Fe_{0.993}Zn^{2+}_{0.007}]_A[Fe_2]_BO_4$ [118])
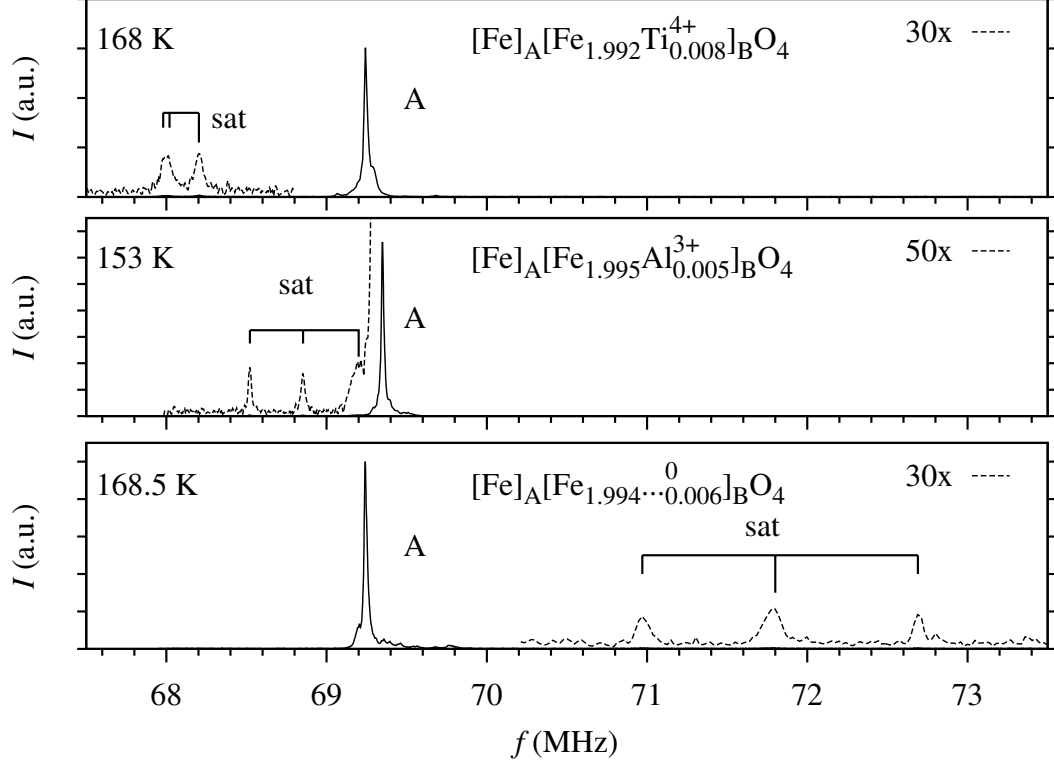
Figure 8.2: The ^{57}Fe NMR spectra of substituted magnetite well above the spin reorientation transition showing the A lines and the satellite signals (labelled "sat") from the resonating nuclei in the first neighbourhood of the substitution ions at the B sites. (Two of the three satellite lines in the spectrum of the titanium substituted sample are merged together due to their relative proximity.) ($[Fe]_A[Fe_{1.995}Al^{3+}_{0.005}]_BO_4$ [119], $[Fe]_A[Fe_{1.992}Ti^{4+}_{0.008}]_BO_4$ [118])

8.3 Temperature Dependence of Satellite NMR Signal Frequencies

Temperature dependences of frequencies of satellite signals arising from the iron nuclei in the first neighbourhood of the substitution ions are provided in Fig. 8.3, alongside with temperature dependences of the frequency of the A line and a centre of gravity of the B lines in the spectra of pure magnetite [37], [70]. In the cases of the titanium and aluminium substituted samples and magnetite with vacancies, centres of gravity of the satellite lines are plotted. Experimental data in Fig. 8.3 were fitted with dependences based on the spin wave theory: for temperature T much lower than Curie temperature, the resonance frequency f obeys

$$f\left(T\right) = f\left(0\right) - c_1 T^{\frac{3}{2}} - c_2 T^{\frac{5}{2}} \tag{8.2}$$

where c_1, c_2 denote parameters and $f\left(0\right)$ stands for the frequency at $T = 0$ K.

Since the resonance frequency of a particular site is assumed to be proportional to the magnetization of the corresponding sublattice (unless a phase transition is crossed), an analysis of the experimental data is based on the mean field method described in Ref. [7]. In this approach, magnetization m_A and m_B at the A and
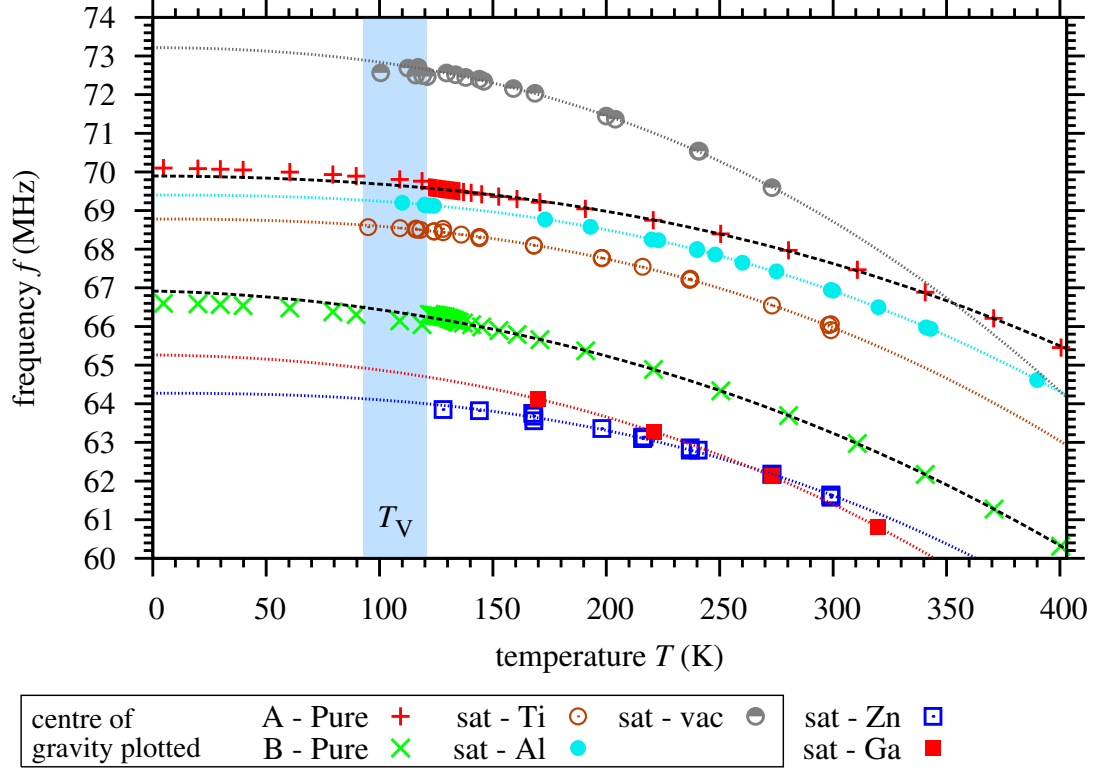
Figure 8.3: Temperature dependences of ^{57}Fe NMR frequencies of selected signals plotted together with spin wave approximation fit. (vac data [71], Al data [70], Ti and Zn data [118])

B sites, respectively, in pure magnetite is determined by relations

$$
\begin{aligned}
m_{\mathrm{A}} &= S_{\mathrm{A}} B_{S_{\mathrm{A}}}(\lambda_{\mathrm{AA}} m_{\mathrm{A}} + \lambda_{\mathrm{AB}} m_{\mathrm{B}}), \\
m_{\mathrm{B}} &= S_{\mathrm{B}} B_{S_{\mathrm{B}}}(\lambda_{\mathrm{BA}} m_{\mathrm{A}} + \lambda_{\mathrm{BB}} m_{\mathrm{B}}),
\end{aligned}
\tag{8.3}
$$

where $S_{\mathrm{A}} = 2.5$ and $S_{\mathrm{B}} = 2.25$ represent spins of the corresponding sublattices, while B_S stands for the Brillouin function. The $\lambda_{\alpha\gamma}$ coefficient definition (with α, γ equal to A, B) follows:

$$
\lambda_{\alpha\gamma} = \beta S_{\alpha} J_{\alpha\gamma} z_{\gamma}(\alpha),
\tag{8.4}
$$

where $\beta = 1/k_{\mathrm{B}}T$, superexchange constants $J_{\alpha\gamma}$ (symmetrical in α, γ) values are $J_{\mathrm{AA}} = $ -22 K, $J_{\mathrm{AB}} = J_{\mathrm{BA}} = $ -46 K, $J_{\mathrm{BB}} = $ -11 K [7] and $z_{\gamma}(\alpha)$ denotes the number of the nearest neighbour α ions to the γ ion.

The magnetization m'_{A} and m'_{B} at the A and B sites, respectively, in the nearest neighbourhood of the non-magnetic substitution ion or vacancy in defect-containing magnetite is given by relations analogous to equations (8.3)

$$
\begin{aligned}
m'_{\mathrm{A}} &= S_{\mathrm{A}} B_{S_{\mathrm{A}}}(\lambda_{\mathrm{AA}} m_{\mathrm{A}} + \lambda'_{\mathrm{AB}} m_{\mathrm{B}}), \\
m'_{\mathrm{B}} &= S_{\mathrm{B}} B_{S_{\mathrm{B}}}(\lambda'_{\mathrm{BA}} m_{\mathrm{A}} + \lambda_{\mathrm{BB}} m_{\mathrm{B}}),
\end{aligned}
\tag{8.5}
$$

where the $\lambda'_{\alpha\gamma}$ coefficients are defined similarly to (8.4) with the number of magnetic ions in the first neighbourhood decremented by one

$$
\lambda'_{\alpha\gamma} = \beta S_{\alpha} J_{\alpha\gamma}(z_{\gamma}(\alpha) - 1),
\tag{8.6}
$$

Set of the equations (8.3) together with the equations (8.5) was solved itera-
tively yielding the temperature dependences of the magnetizations m_A, m_B, m'_A,
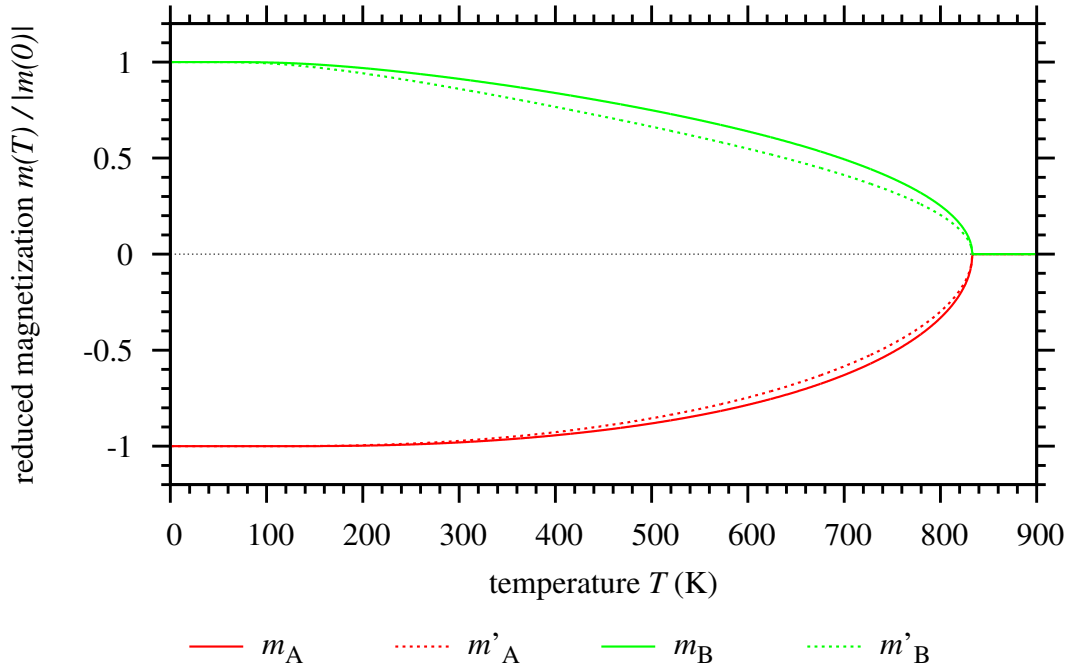and m'_B – see Fig. 8.4.

Figure 8.4: Temperature dependences of reduced magnetizations of A and B
sites obtained from the mean field calculations (see text).

Comparison of the calculation results with the experimental data is provided
in Figs. 8.5 and 8.6. Apparently, the mean field model output is closer to the
experiment for the B site defect - Fe(A) satellite resonance combination. Taking
into account that the mean field model performs better for higher number of
neighbours and considering that the J_{AB} superexchange constant has the largest
absolute value, the better result on the A site magnetism is expected as there
are 12 nearest B neighbours of the A site, whereas there are only 6 nearest A
neighbours of the B site.

Notable differences between the temperature dependences of reduced fre-
quency splitting of satellite signals caused by different substitutions entering the
same site are distinct from the behaviour of common substituted magnetic iron
oxides like substituted yttrium iron garnet (YIG) [126], where the reduced split-
ting is determined mainly by the crystallographic site of the substitution. The
mean field model treats the presence of the defects as a breaking of particular
exchange couplings, but it does not take into account changes in electronic struc-
ture caused by the valence of the defect and a local lattice distortion depending
on the ion radius of the defect. Analysis of the results thus indicates that these
changes play considerably more significant role in substituted magnetite than in
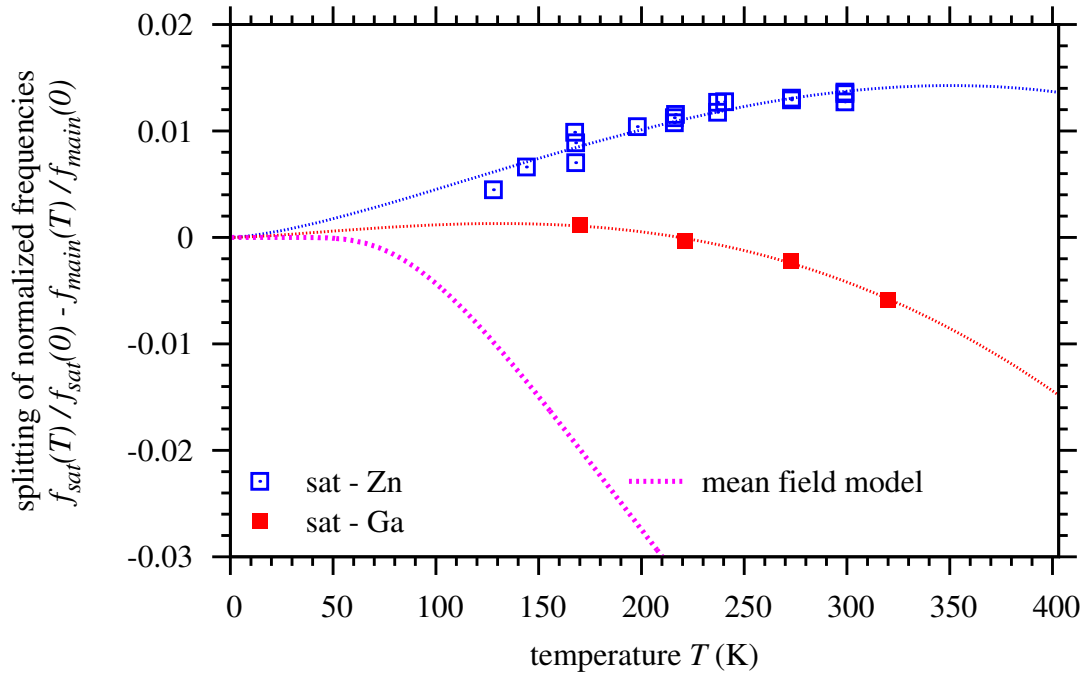other substituted magnetic iron oxides.

Figure 8.5: Splitting of temperature dependences of satellite and main line ^{57}Fe NMR frequencies normalized to their values at $T = 0$ K plotted for the A site substitution in comparison with the result of mean field calculations.
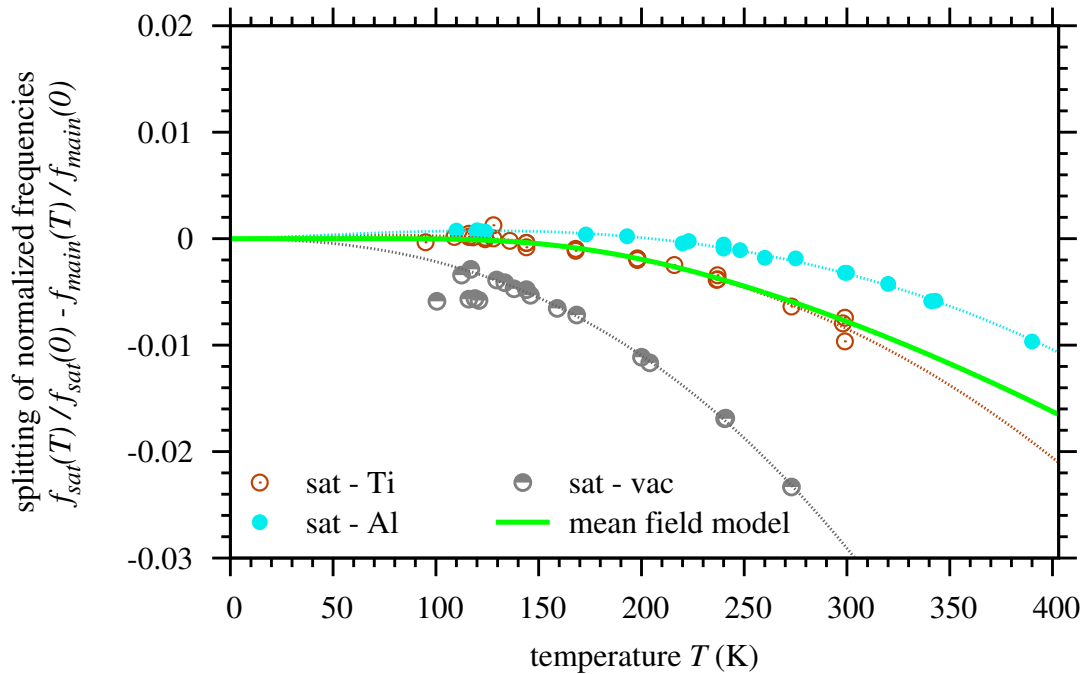

Figure 8.6: Splitting of temperature dependences of satellite and main line ^{57}Fe NMR frequencies normalized to their values at $T = 0$ K plotted for the B site substitution in comparison with the result of mean field calculations.

8.4 Temperature Dependence of Linewidth of Main NMR Signals

In general, resonance lines in solids exhibit inhomogeneous broadening. In the case of magnetic iron oxides, the main factors influencing ^{57}Fe NMR linewidths comprise a distribution of demagnetizing fields and a hyperfine field distribution related to the real sample structure (i. e. defects, substitutions or impurities in the crystal). Experiments focused on a temperature evolution of resonance lines usually reveal (beside changes of resonance frequencies or relaxation rates) line broadening with increasing temperature (see e. g. Ref. [127]). The observed broadening is a consequence of (slightly) different temperature dependences of particular resonance signal contributions, which correspond to different hyperfine fields in their aforementioned distribution.

Contrary to common magnetic iron oxide compounds exhibiting the ^{57}Fe NMR line broadening with increasing temperature, an anomalous opposite behaviour is observed in magnetite – above the spin reorientation transition, the linewidths of resonance signals decrease with rising temperature, arriving at minimal value in the range from 250 K to 350 K (depending on sample composition). This effect can be observed both in pure magnetite as well as in samples with cationic substitutions or vacancies. The data for the A lines (reproduced in Fig. 8.7) were accompanied in Ref. [118] by a brief, rather general analysis. The B line widths are presented here in Fig. 8.8 (below T_{sr}, the width of the B_2 line is taken).

Apparently, the spin reorientation transition causes a line broadening at least within a narrow temperature region around this transition – see the pure magnetite data in Figs. 8.7 and 8.8. This is caused by magnetic moment fluctuation occurring at temperatures close to T_{sr}. In order to check that the spin reorientation transition is not responsible for the line broadening in a wider temperature interval (up to room temperature), the following experiment was performed: A cylinder-shaped (diameter $\approx$ 4.5 mm, height $\approx$ 5.5 mm; cylinder axis in [110] cubic direction) single crystal $[Fe]_A[Fe_{1.97}Al_{0.03}]_BO_4$ sample ($T_V = 97.3$ K, $T_{sr} = 126.5$ K) was placed in $\approx$ 0.2 T external magnetic field along [111] cubic direction and the temperature dependence of the A line width and frequency was acquired. The same parameters were measured also without the external magnetic field. The results are shown in Fig. 8.9. The presence of the external field suppressed the spin reorientation transition by keeping magnetization in [111] direction even below T_{sr} [1], but it also resulted in additional line broadening dominantly due to induced inhomogeneous demagnetizing field, which is an expected side effect. Considering the A line spectrum as a convolution of two profiles (resonance line broadened due to the studied microscopic behaviour and inhomogeneous broadening profile) and assuming the impact of the spin-reorientation transition negligible at room temperature, the field-induced broadening can be compensated for using the following equation:

$$w_{\mathrm{f,comp}}(T) = \sqrt{w_{\mathrm{f}}^2(T) - (w_{\mathrm{f}}^2(305K) - w_0^2(305K))} \tag{8.7}$$

---

[1]This was checked on a similar sample $[Fe]_A[Fe_{1.995}Al_{0.005}]_BO_4$ ($T_V = 119.7$ K, $T_{sr} = 128.3$ K) with lower substitution concentration (and thus lower linewidths) which allowed to observe split B lines (B_1, B_2) in a spectrum at 125 K even in a slightly lower field.
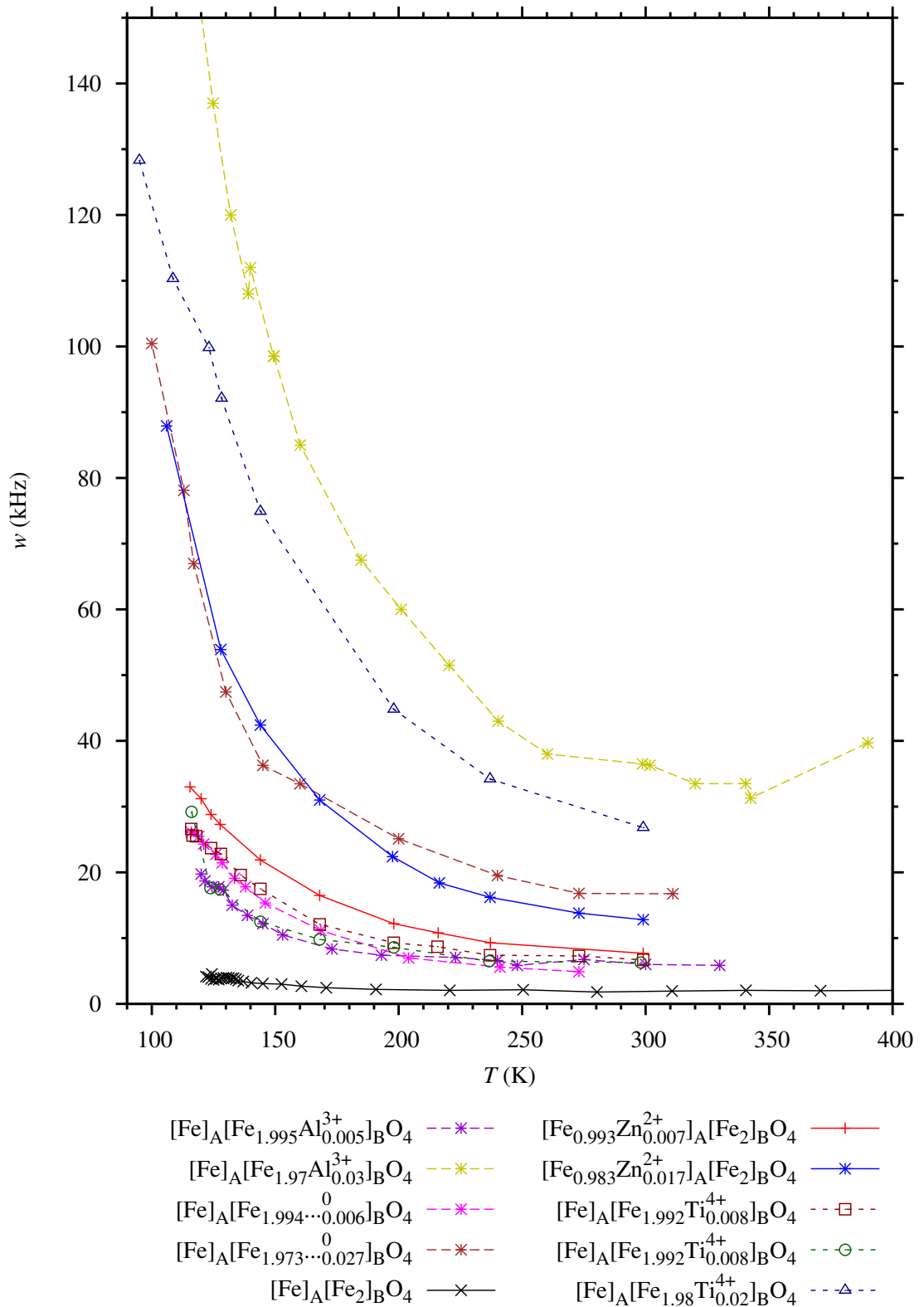
Figure 8.7: Temperature dependences of HWHM of the A lines in the spectra of pure and substituted magnetite (pure magnetite [70], [72], aluminium substituted magnetite [70]) after Ref. [118]. The lines are guides for the eye only.
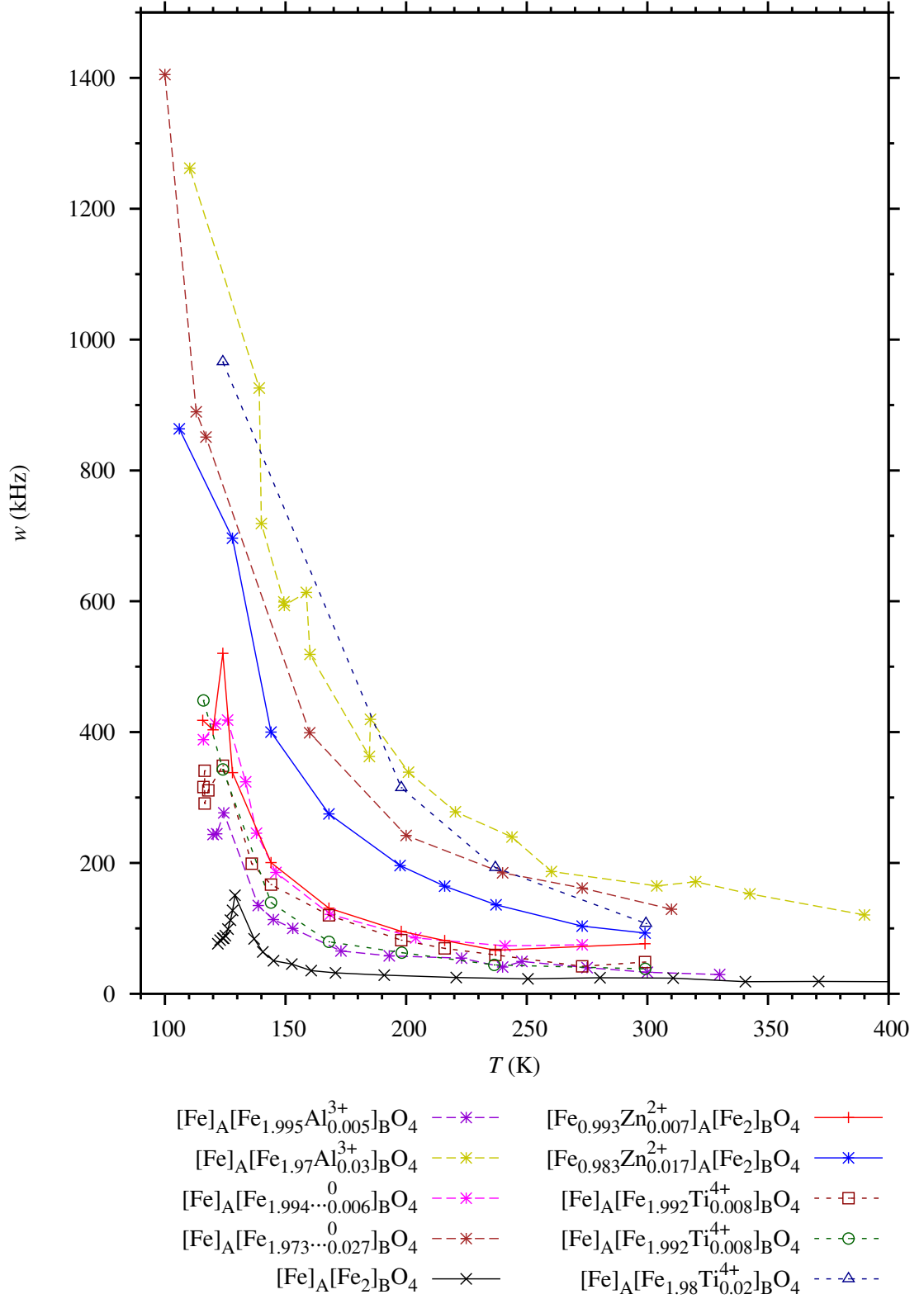
Figure 8.8: Temperature dependences of HWHM of the B lines in the spectra of pure and substituted magnetite (pure magnetite [70], [72], aluminium substituted magnetite [70]). Below T_{sr}, the width of B_2 line is taken. The lines are guides for the eye only.

where w_f is the HWHM measured in field, w_0 stands for the HWHM measured without the field and $w_{f,comp}$ represents the HWHM measured in the field corrected for the demagnetizing field broadening. The $w_{f,comp}(T)$ dependence is included in Fig. 8.9. Obviously, the compensated temperature dependence of HWHM measured in the field (i. e. with suppressed spin reorientation transition) does not significantly differ from the zero-field dependence. Thus the spin reorientation transition affects only the narrow temperature interval and is not a cause of the overall anomalous temperature evolution of linewidths above T_V.

Therefore, the linewidth narrowing with increasing temperature shall be interpreted in the context of other electronic structure properties varying in the whole investigated temperature range. To this end, electron transport (electrical conductivity) seems to be the most relevant property. The DC electrical conductivity above the Verwey transition increases with rising temperature, achieves a maximum about or above room temperature and then slightly decreases as illustrated in Fig. 8.10. In a limited range, experimental data of temperature evolution of conductivity are usually fitted by an exponential

$$\sigma(T) = \sigma_0 \exp\left(-\frac{E_a}{kT}\right) \qquad (8.8)$$

(E_a is an activation energy or energy gap, σ_0 is a constant parameter, k is the Boltzmann constant) (see e. g. Refs.[128], [129]), which is related to either Arrhenius law, Mott relation, energy gap or to a simplification of a formula from the following model.

The electron hopping model formulated by J. M. Honig [130] can describe how the charge carriers (represented in magnetite by minority-spin valence electrons (and corresponding holes) at the B sites) migrate between $Fe^{2+}(B)$ and $Fe^{3+}(B)$ sites in magnetite and yields the following relation for DC conductivity σ

$$\sigma(T) = \frac{c_0 s (1-s) e^2 \delta_2}{\tau a k T} \exp\left(-\frac{\Delta G}{kT}\right) \qquad (8.9)$$

where ΔG is an activation energy of charge hopping, e represents elementary charge, τ is a time factor, δ_2 is a dimensionless parameter, a is a lattice parameter, s is a probability that a given site is occupied by the charge carrier, c_0 is a density of sites for charge carriers. This model can be applied also for substituted magnetite – see e. g. Ref. [128]. More elaborate applicable models describe charge carriers as polarons (i. e. electron-phonon coupling is taken into account) – for instance a complex small polaron (i. e. localized charge carriers) model developed by Ihle and Lorenz [131], [24] describes the electrical conductivity of magnetite as a combination of small polaron band and hopping conductivity and achieves a reasonable agreement with experimental DC and optical conductivity data [25] (see Fig. 8.10).

A more general work [132] of Ciuchi and Fratini concerning charge ordering transitions employs the following relation for DC polaronic conductivity above the charge ordering transition:

$$\sigma_{dc}^{norm}(T) = \frac{\sigma_0}{32\sqrt{2\pi E_p} T^{3/2}} \exp\left(-\frac{E_p}{2kT}\right) \qquad (8.10)$$
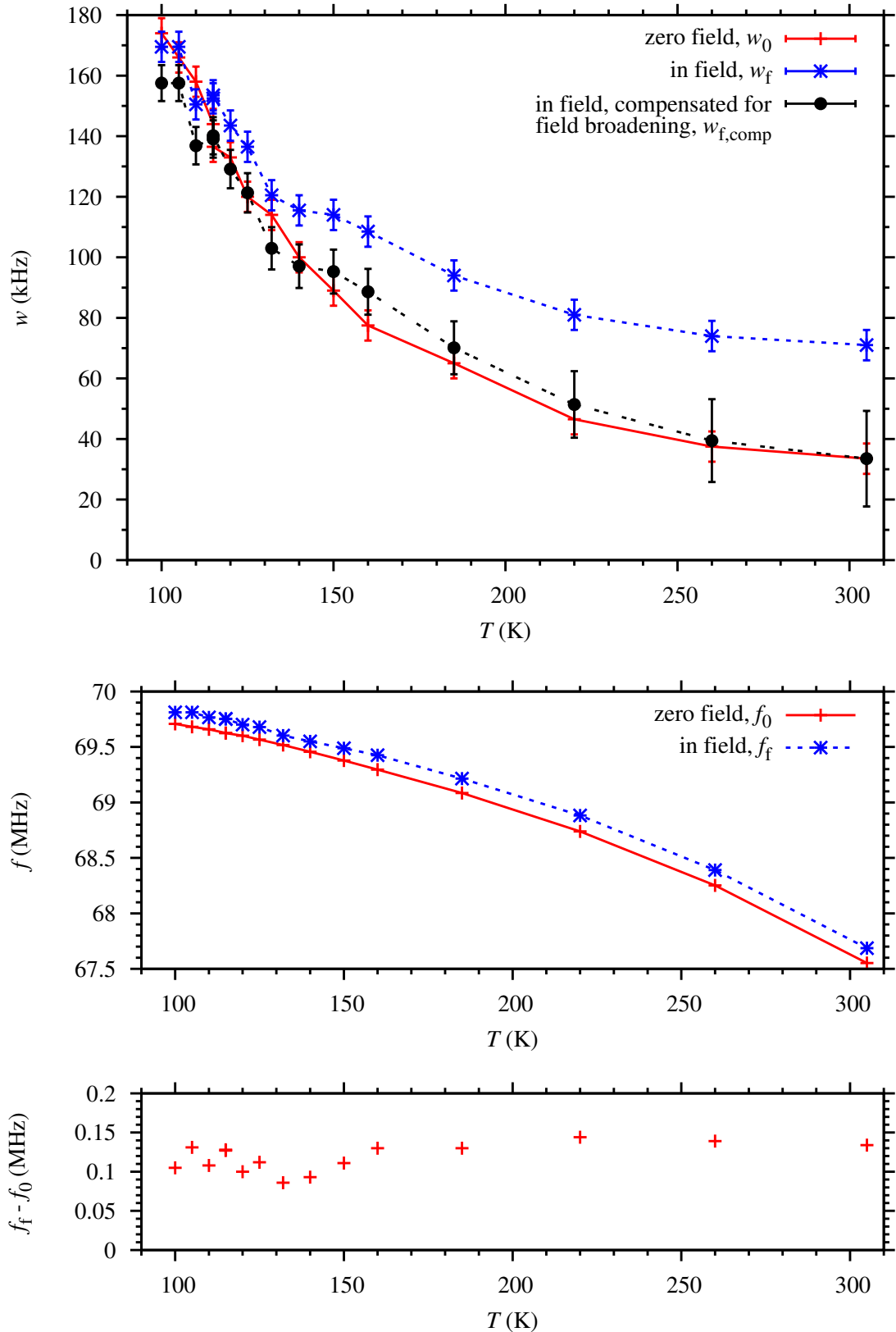
Figure 8.9: Temperature dependence of HWHM (upper plot) and frequency (middle plot) of the A line of $[Fe]_A[Fe_{1.97}Al_{0.03}]_BO_4$ sample above the Verwey transition measured with and without ≈ 0.2 T external magnetic field in [111] cubic direction. The frequency difference of the A line frequency in the field and in a zero field is plotted at the bottom – the slight dip and scatter around T_{sr} is related to anisotropy constants crossing zero in that temperature region. The lines are guides for the eye only.

(E_p is a polaron energy). A decrease of electron-phonon coupling strength with increasing temperature was observed in magnetite above the Verwey transition by M. Kimura et al. [44] – a gradual change from a small polaron to a large polaron (i. e. delocalized charge carriers) was found in the range from 250 K to 330 K.

Experimental data in Fig. 8.10 were fitted in the range from T_V to 300 K by relations (8.8), (8.9) and (8.10) (yielding $E_\mathrm{a} = 255 \pm 5$ K, $\Delta G = 460 \pm 2$ K and $E_\mathrm{p}/2 = 563.5 \pm 0.9$ K) and compared with the results of Ihle and Lorenz [131], [24] – apparently, these relations reasonably match the data in the given limited temperature range while keeping the number of fit parameters low.
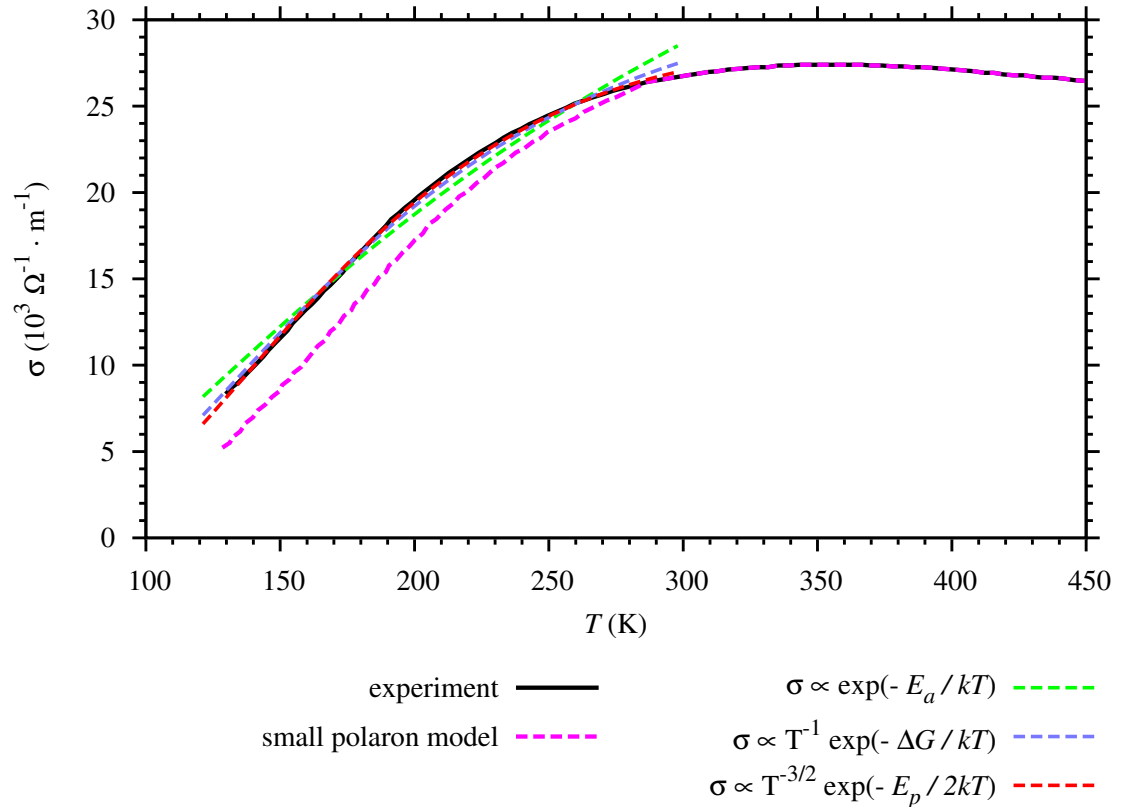
Figure 8.10: Temperature dependence of DC electrical conductivity of magnetite above the Verwey transition. The experimental data [25] are compared to the small polaron model [131], [24], as well as to relations (8.8), (8.9) and (8.10) (in a limited range).

The details of the link between electrical conductivity and ^{57}Fe NMR signal linewidth shall be explained considering the B sublattice as a 1:1 mixture of Fe^{2+} and Fe^{3+} ions. The site distribution of these ions is changing all the time as the minority-spin valence electrons hop between the B sites. Instantaneous hyperfine field at each ^{57}Fe nucleus is determined by the momentary electron configuration in its vicinity. Resonance frequency of such a nucleus is then given by an average of the hyperfine field over a characteristic time of the NMR experiment. Thus the faster the electron hopping is, the closer to spectral line centre the average is and the narrower line the whole ensemble of resonating nuclei produces in a spectrum.

The situation in substituted magnetite is more complex. For a particular

substitution, the spectra of such samples exhibit main lines broadening with increasing substitution concentration and satellite signals becoming more intense for higher concentration of the substitution. However, no dependence of satellite line frequencies on substitution concentration was observed. The electronic structure is significantly perturbed in the close vicinity of a substitution defect while a screening effect can be expected in broader surroundings. The hyperfine field is dominantly determined by the local electron configuration. Thus the resonating nuclei in the first neighbourhood of the defect have their resonating frequency substantially shifted, giving rise to satellite signals, whereas the resonance frequencies of ^{57}Fe in the second neighbourhood of the defect are much closer to the main line frequency so these signals often merge with the main line. Unless there are two or more defects in close proximity of resonating nuclei (which happens rarely, provided the substitution concentration is not too high), there is no reason for a dependence of satellite line frequencies on substitution concentration. The screening in broader surroundings manifests itself at a particular Fe(B) site as an increase of occupation probability for either Fe^{2+} or Fe^{3+} state and a simultaneous decrease for the other one. Compared to pure magnetite, the hyperfine field at iron nuclei in this region is thus affected by different preferred configurations of Fe^{2+} and Fe^{3+} ions and also by a slightly affected dynamics of electron hopping. However, similarly to the situation in pure magnetite, increased hopping rate implies a more uniform charge carrier distribution within the averaging time and the resonance frequencies of ^{57}Fe nuclei in such surroundings closer to the spectral line centre frequency.

Based on these considerations, the NMR linewidths above the Verwey transition can be expected to be inversely proportional to the DC electrical conductivity. The low number of parameters in relations (8.8), (8.9) and (8.10) makes them a suitable base for fitting the experimental temperature dependences of NMR line HWHM in the following forms:

$$w\left(T\right) = C_{\{A,B\}1} \exp\left(\frac{E_{\{A,B\}1}}{kT}\right) \tag{8.11}$$

$$w\left(T\right) = C_{\{A,B\}2}T \exp\left(\frac{E_{\{A,B\}2}}{kT}\right) \tag{8.12}$$

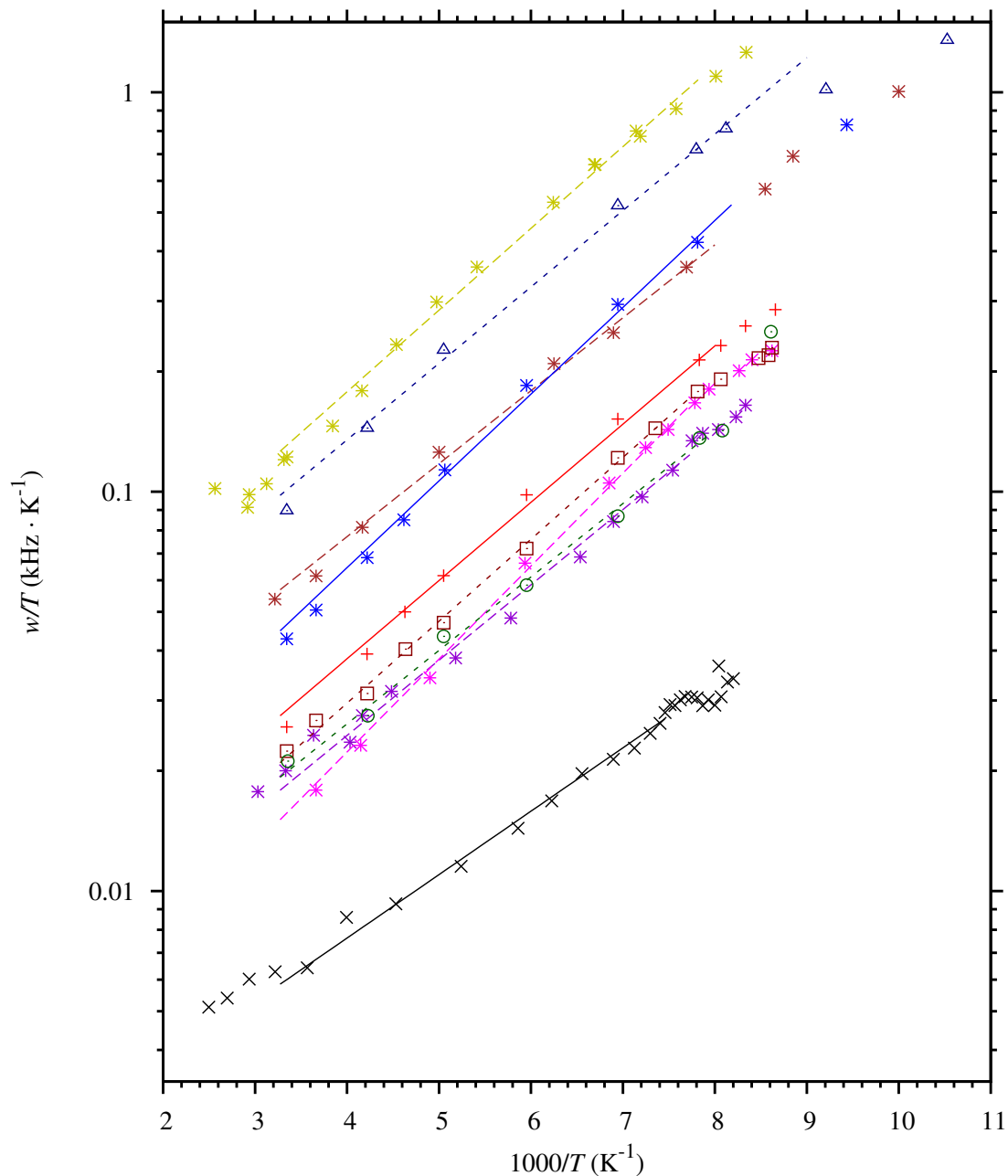$$w\left(T\right) = C_{\{A,B\}3}T^{\frac{3}{2}} \exp\left(\frac{E_{\{A,B\}3}}{kT}\right) \tag{8.13}$$

Each of these relations contains only two fitted parameters $C_{\{A,B\}\{1,2,3\}}$ and $E_{\{A,B\}\{1,2,3\}}$. The fits of dependence (8.12) in the range between T_{sr} and 310 K are presented in Figs. 8.11 and 8.12, while the other – similarly looking – fits (also between T_{sr} and 310 K) can be found in Figs. A.12, A.13, A.14 and A.15 in Appendix. The resulting fitted parameters $C_{\{A,B\}2}$ and $E_{\{A,B\}2}$ are listed in Table 8.1. The values of $C_{\{A,B\}\{1,3\}}$ and $E_{\{A,B\}\{1,3\}}$ in Tables B.8 and B.9 numerically differ, yet they provide qualitatively the same picture, thus they were placed in Appendix and the following discussion focuses on the parameters of relation (8.12). Visualization of the parameters with respect to the nominal Fe(B) valence v_B, which differs from 2.5+ due to the substitution, is shown in Fig. 8.13 and in Figs. A.16 and A.17 in Appendix.

The plots in Fig. 8.13 show that the E_{A2} and E_{B2} values of defect-containing samples are scattered around constant values of ≈ 450 K and ≈ 600 K, respectively, while the values for stoichiometric magnetite are noticeably lower. The value of $E_{B2} = 447 \pm 31$ K for pure magnetite is in agreement with the value of $\Delta G = 460 \pm 2$ K obtained by a fit of temperature dependence of the DC conductivity in Fig. 8.10 (similarly, $E_{B1} \approx E_a$ and $E_{B3} \approx E_p/2$), which confirms the connection of the electrical conductivity with the NMR linewidths. Higher values for substituted samples compared to pure magnetite can be understood as a consequence of a perturbation potential introduced by the defects, while the lack of any apparent systematic dependence on nominal Fe(B) valence can be ascribed to the screening effect and a relatively narrow range of v_B. The $C_{\{A,B\}2}$ vs. v_B plots display datapoints corresponding to v_B close to 2.5+ placed within a limited range up to 10 Hz $\cdot$ K^{-1} and 40 Hz $\cdot$ K^{-1} for C_{A2} and C_{B2}, respectively, whereas slightly higher deviations of v_B from 2.5+ result in considerably larger values of the $C_{\{A,B\}2}$ parameters. A tempting interpretation would be based on the $s(1-s)$ factor in equation (8.9) equal to $(v_B - 2)(3 - v_B)$, which affects electrical conductivity as experimentally evidenced by Tannhauser in Ref. [133] in a wider context including other magnetite-related iron oxide phases. However, a variation of the $s(1-s)$ factor for the studied set of samples is negligible, which explains limited $C_{\{A,B\}2}$ values for v_B not far from 2.5+. Therefore, the reason for the notably elevated $C_{\{A,B\}2}$ parameters in the case of samples with higher substitution concentration must be different – most likely, it is caused by the overlapping of the crystal areas affected by individual defects, which starts at some critical concentration. Based on the composition of the studied samples, the critical defect concentration can be roughly estimated at about 0.5% of iron ions replaced by the charged defects. The ratios E_{B2}/E_{A2} varying around ≈ 1.25 together with ratios C_{B2}/C_{A2} oscillating around ≈ 4 (for substituted samples) indicate a fundamental difference between the A and B sites: the electron shell of resonating nuclei at the B sites is alternating between the Fe^{2+} and Fe^{3+} state, resulting in much broader NMR lines, whereas the electron shell of resonating nuclei at the A sites is polarized by the changes in the B sublattice but does not undergo such dynamic changes of valence.

Table 8.1: Parameters of temperature dependences of NMR line width (8.12) obtained from experimental data by a fit. The uncertainties correspond to the errors from the fit.

sample composition	nominal Fe(B) valence v_B	C_{A2} (Hz $\cdot$ K^{-1})	E_{A2} (K)	C_{B2} (Hz $\cdot$ K^{-1})	E_{B2} (K)
$[Fe]_A[Fe_2]_BO_4$	2.500	1.77 ± 0.14	366 ± 12	15.2 ± 2.9	447 ± 31
$[Fe_{0.993}Zn^{2+}_{0.007}]_A[Fe_2]_BO_4$	2.504	6.28 ± 0.55	451 ± 12	22.8 ± 5.0	604 ± 31
$[Fe_{0.983}Zn^{2+}_{0.017}]_A[Fe_2]_BO_4$	2.509	8.72 ± 0.82	500 ± 14	37.6 ± 5.3	633 ± 20
$[Fe]_A[Fe_{1.994}...^{0}_{0.006}]_BO_4$	2.508	2.61 ± 0.20	536 ± 11	17.4 ± 7.8	646 ± 63
$[Fe]_A[Fe_{1.973}...^{0}_{0.027}]_BO_4$	2.534	14.3 ± 1.6	421 ± 16	69.8 ± 4.2	572 ± 11
$[Fe]_A[Fe_{1.992}Ti^{4+}_{0.008}]_BO_4$	2.494	4.47 ± 0.19	472 ± 6	23.8 ± 2.1	561 ± 13
$[Fe]_A[Fe_{1.992}Ti^{4+}_{0.008}]_BO_4$	2.494	4.82 ± 0.48	424 ± 15	15.5 ± 3.3	592 ± 34
$[Fe]_A[Fe_{1.98}Ti^{4+}_{0.02}]_BO_4$	2.485	23.1 ± 2.5	441 ± 15	73 ± 20	580 ± 36
$[Fe]_A[Fe_{1.995}Al^{3+}_{0.005}]_BO_4$	2.499	4.32 ± 0.43	434 ± 15	19.4 ± 2.5	539 ± 20
$[Fe]_A[Fe_{1.97}Al^{3+}_{0.03}]_BO_4$	2.492	27.0 ± 2.2	471 ± 12	85 ± 19	588 ± 35

Figure 8.11: Temperature dependences of HWHM of the A lines in the spectra of pure and substituted magnetite (pure magnetite [70], [72], aluminium substituted magnetite [70], zinc and titanium substituted magnetite [118]) fitted in the range between T_{sr} and 310 K with (8.12) expression.
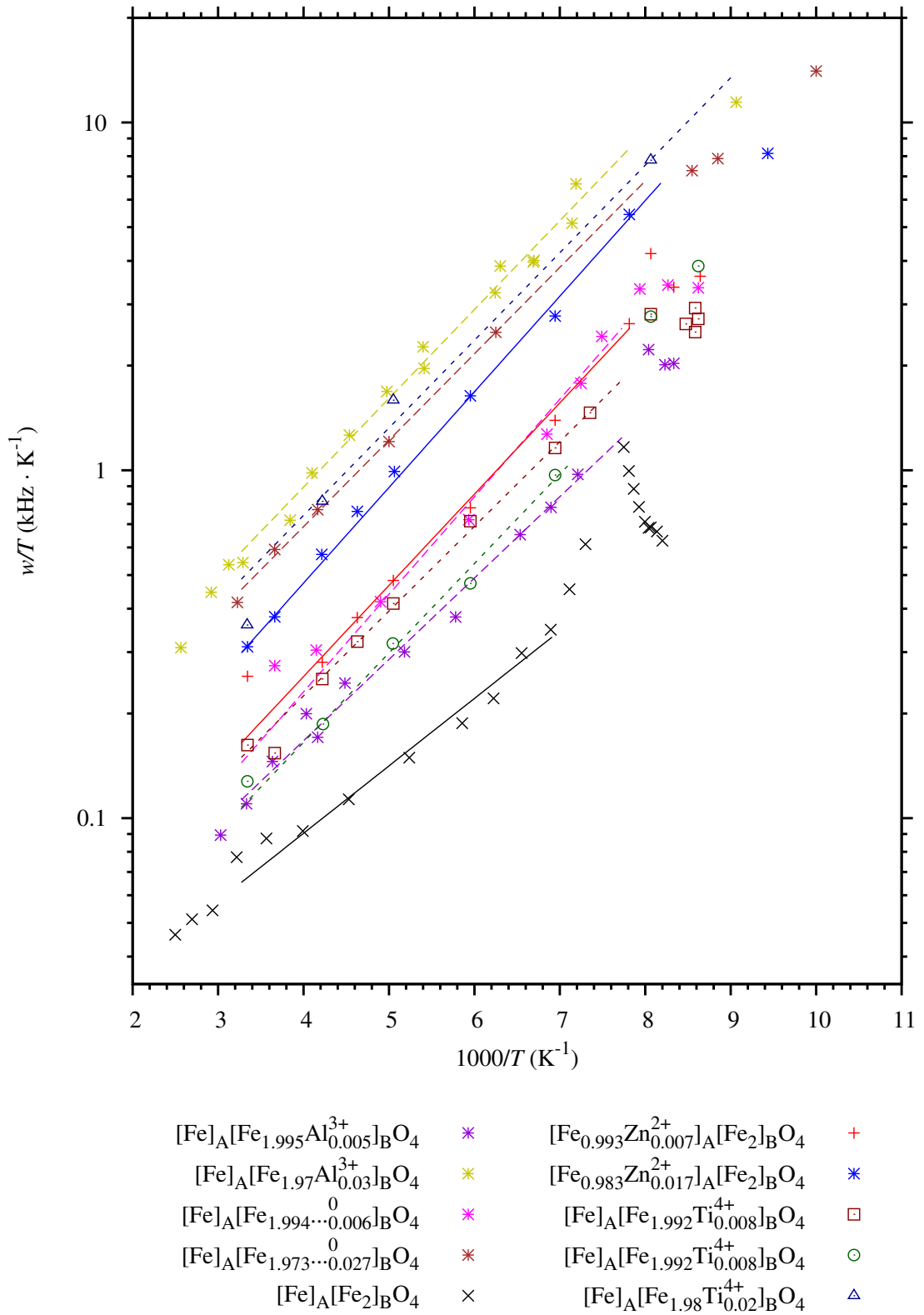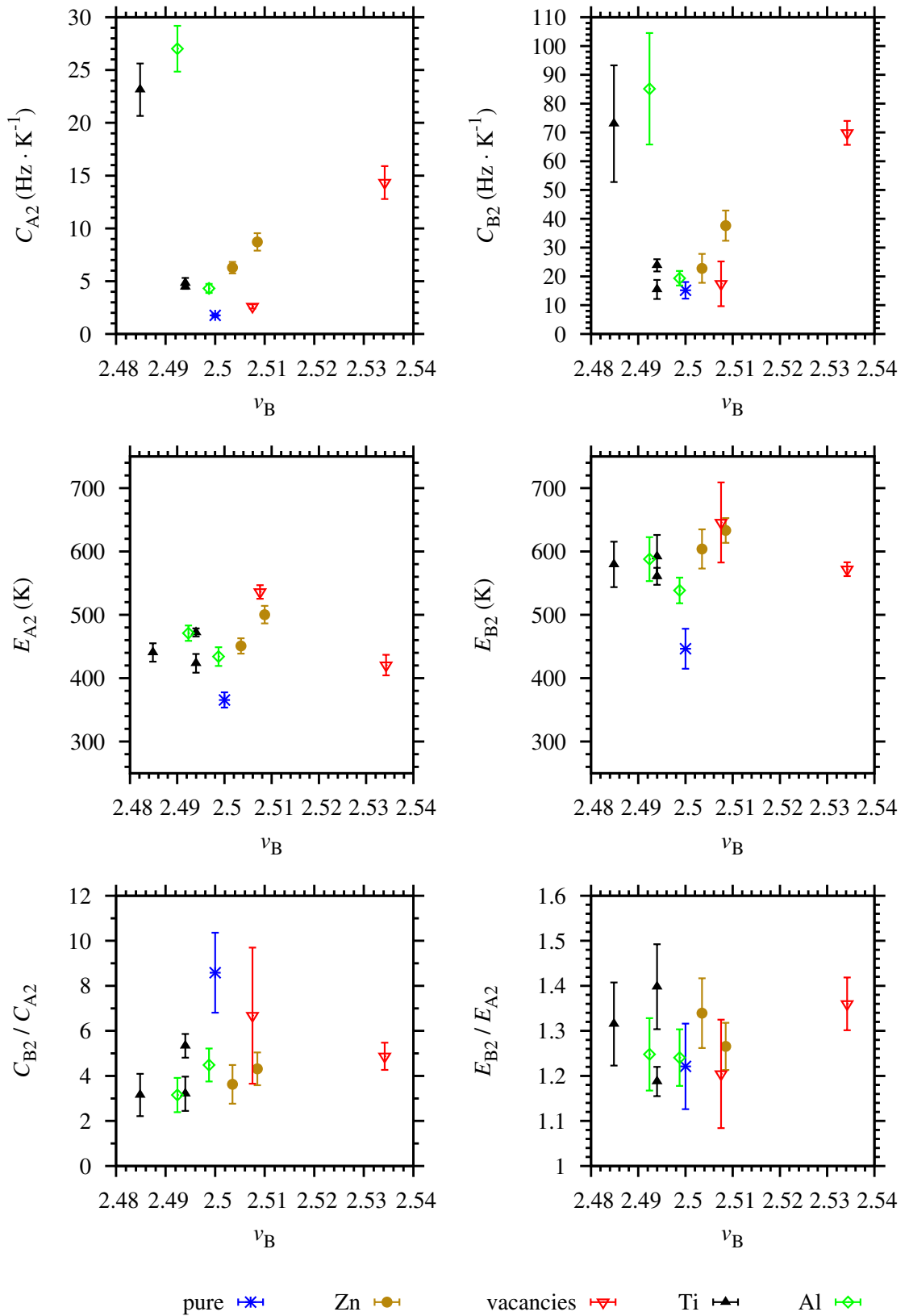
Figure 8.12: Temperature dependences of HWHM of the B lines in the spectra of pure and substituted magnetite (pure magnetite [70], [72], aluminium substituted magnetite [70]) fitted in the range between T_{sr} and 310 K with (8.12) expression.

The legend for the figure:

$[Fe]_A[Fe_{1.995}Al^{3+}_{0.005}]_BO_4$ ✳
$[Fe]_A[Fe_{1.97}Al^{3+}_{0.03}]_BO_4$ ✳
$[Fe]_A[Fe_{1.994}\cdots^0_{0.006}]_BO_4$ ✳
$[Fe]_A[Fe_{1.973}\cdots^0_{0.027}]_BO_4$ ✳
$[Fe]_A[Fe_2]_BO_4$ ×

$[Fe_{0.993}Zn^{2+}_{0.007}]_A[Fe_2]_BO_4$ +
$[Fe_{0.983}Zn^{2+}_{0.017}]_A[Fe_2]_BO_4$ ✳
$[Fe]_A[Fe_{1.992}Ti^{4+}_{0.008}]_BO_4$ □
$[Fe]_A[Fe_{1.992}Ti^{4+}_{0.008}]_BO_4$ ○
$[Fe]_A[Fe_{1.98}Ti^{4+}_{0.02}]_BO_4$ △

Figure 8.13: Visualization of the parameters of temperature dependences of NMR line width (8.12) with respect to the nominal Fe(B) valence v_B. Substitution types are distinguished by different symbols.

Chapter 9

Conclusions

The experimental ^{57}Fe NMR data and DFT calculation results were employed in the analyses of the hyperfine interactions and electronic structure of magnetite. This approach utilizing the relevant up-to-date information on magnetite turned out to be successful in extending the knowledge about magnetite by quantitative data as well as by interpretations of the observations.

Concerning **the low-temperature phase of magnetite**, the following was achieved:

- The information on the electronic structure was extracted from the ab initio calculation results in a form of valence electron density maps showing the charge distribution within trimerons, electron populations and valence states of iron suitable for a comparison with the charge transfer description from the trimeron model, the EFG tensors and the charge density at iron nuclei.

- The hyperfine fields were calculated for various magnetization directions and the resulting data sets were subsequently processed in order to extract hyperfine parameters of all 24 iron sites consisting of isotropic part of the hyperfine field and tensors of hyperfine field anisotropy.

- The quantitative reanalysis of experimental ^{57}Fe NMR data published by Mizoguchi [14] in 2001 yielded analogous hyperfine field parameters which were correlated with the parameters from the DFT calculations. The correlation revealed three mutually matching groups of the B sites in 8:5:3 ratio. The first group contains the Fe^{3+}-like ions, while the other groups are formed by the Fe^{2+}-like ions. This grouping narrows down the set of B sites a particular NMR signal comes from and corroborates the validity of the DFT calculations and the crystal structure as the sets of the B site parameters from the ab initio calculations exhibit the same grouping ratio as the sets from the experimental data.

- The results of the DFT calculations support trimeron model as the charge distribution and its impact on hyperfine parameters meets the expectations based on the model: the Fe^{3+}-like B site ions (end ions of trimerons or ions not in the trimeron network) exhibit more symmetrical charge distribution and higher electron spin magnetic moment compared to the Fe^{2+}-like ions

(central ions of trimerons), thus the Fe^{3+}-like ions feature higher isotropic part of the hyperfine field, lower hyperfine field anisotropy, lower EFG and lower isomer shift in comparison with the Fe^{2+}-like ions. Although several discrepancies between the presented results and the model of Patterson [39] were found, the trimeron model and the Patterson's concept can be understood as alternative interpretations of the same physical reality: Patterson's model comprising the broken branched zig-zag chain and pairs of Fe(B) ions with one electron bonds corresponds to the trimeron network with longer bonds omitted. Both models are derived from the nearest-neighbour Fe(B)-Fe(B) distance distribution, but the strict limit on the length of the Fe(B)-Fe(B) bond to qualify for a charge transfer imposed in the model of Patterson does not seem adequate since the distribution of the bond lengths is not broad, thus the t_{2g} orbitals of neighbouring Fe(B) ions significantly overlap even if the distance between these ions is not so small. The trimeron concept therefore describes the electronic structure of magnetite more precisely, which was demonstrated by the results presented in this work.

- The calculated EFG tensors and the charge density at iron nuclei together with calculated hyperfine fields allowed for a simulation of the Mössbauer spectra, which were compared with the experimental spectrum and allowed for a better understanding of the experimental Mössbauer spectroscopy data.

- The information about ion valence of the three groups of the B sites turned out to be the key for understanding the changes in the ^{57}Fe NMR spectra induced by a presence of substitution defects in magnetite. The tendency of Fe(B) ion valence to increase or decrease depending on a particular type of defects results in shifts of corresponding resonance signals due to the implied changes of hyperfine fields, which was successfully explained using experimental spectra of magnetite with several types of the defects in various concentrations. The analysis also revealed the characteristic size of crystal volume impacted by a single defect being comparable with the elementary cell size.

The ^{57}Fe NMR data on substituted magnetite presented an important information source also for the investigation of **the high-temperature phase of magnetite**:

- The analysis of the temperature dependence of satellite NMR signal frequencies based on a comparison with the mean field model modified for a description of structures containing non-magnetic defects revealed that substituted magnetite is considerably more sensitive to the changes in electronic structure induced by the valence of the defect and the local lattice distortion determined by the ion radius of the defect than other substituted magnetic iron oxides.

- The anomalous temperature dependences of the widths of the main lines in the ^{57}Fe NMR spectra above the Verwey transition were studied for magnetite with various types of defects as well as for pure magnetite. The spin

93

reorientation transition was experimentally found to affect only a narrow temperature interval, while the origin of the overall anomalous temperature evolution of linewidths is different. The anomaly was then interpreted in relation to the electrical conductivity mechanism and the dependences were quantitatively evaluated for both the A and B lines in order to verify this interpretation.

These results present contributions to the fundamental research of magnetite which clarify several aspects of electronic structure and hyperfine interactions in this compound and, at the same time, create a base for investigation of other magnetite-related questions (e. g. on the dynamics of the Verwey transition or on the anomalous temperature dependences of magnetocrystalline anisotropy constants above the Verwey transition) beyond the scope of this thesis.

Appendix A

Supplementary Figures

A.1 Electronic Structure and Hyperfine Interactions in Magnetite Below the Verwey Transition

A.1.1 Electronic Structure
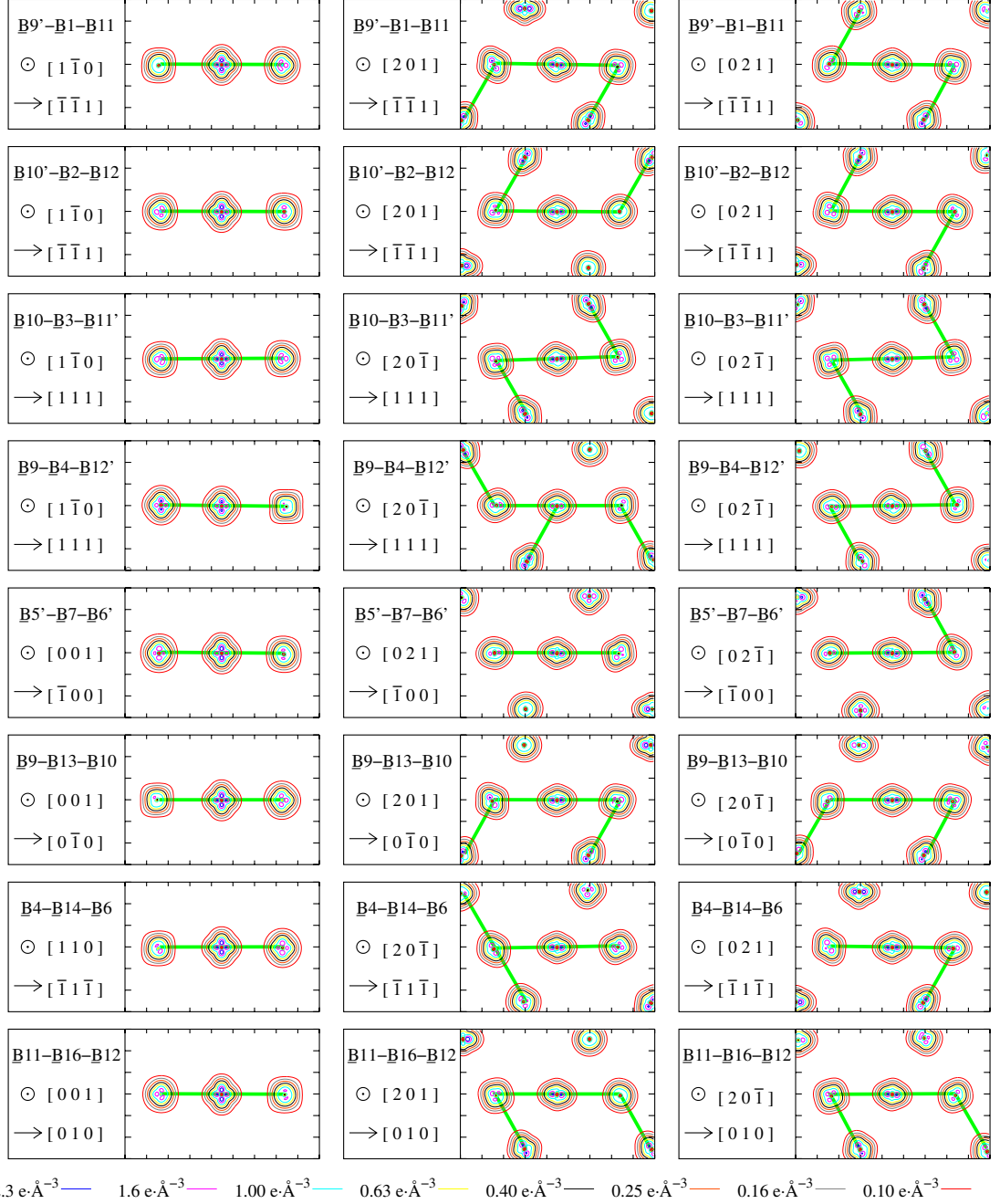
Figure A.1: Maps of minority spin iron $3d$ valence electron density in trimeron planes. Each map has 9 Å × 6 Å dimensions. Green lines denote trimerons [1]. Sites of iron ions participating in the trimeron located on a horizontal axis of a particular map are indicated next to the map; the centre of the image plane is placed in the location of the trimeron's central ion. The monoclinic tilt of $\vec{c}$ axis makes the standard crystallographic plane notation inconvenient for selected planes, thus orientation of the planes is specified by normal vector of the plane (which points out of the page) shown at the $\odot$ symbol in combination with an in-plane vector indicated by an arrow (indices of these vectors are taken with respect to Cc coordinates). In each row, the plane of the first map forms with the planes of the other two maps an angle of $\approx 55°$, whereas the angle between the planes of the last two maps is $\approx 70.5°$. Site numbering follows the convention introduced in part 7.1; primes indicate the ac-glide symmetry generated sites.

Figure A.2: Populations of minority spin $3d$ electrons of the B site iron ions from the DFT calculations visualized as an angular variation of the electron density, i.e. the distance of the surface from a given site denotes the density at the corresponding angle scaled by $3 \text{ Å} \cdot \text{e}^{-1}$ coefficient. Green lines highlight trimerons [1]. Site numbering and label colours follow the convention introduced in part 7.1; primes indicate the *ac*-glide symmetry generated sites. (Surface colour indicating *z*-coordinate is intended just to improve clarity.)
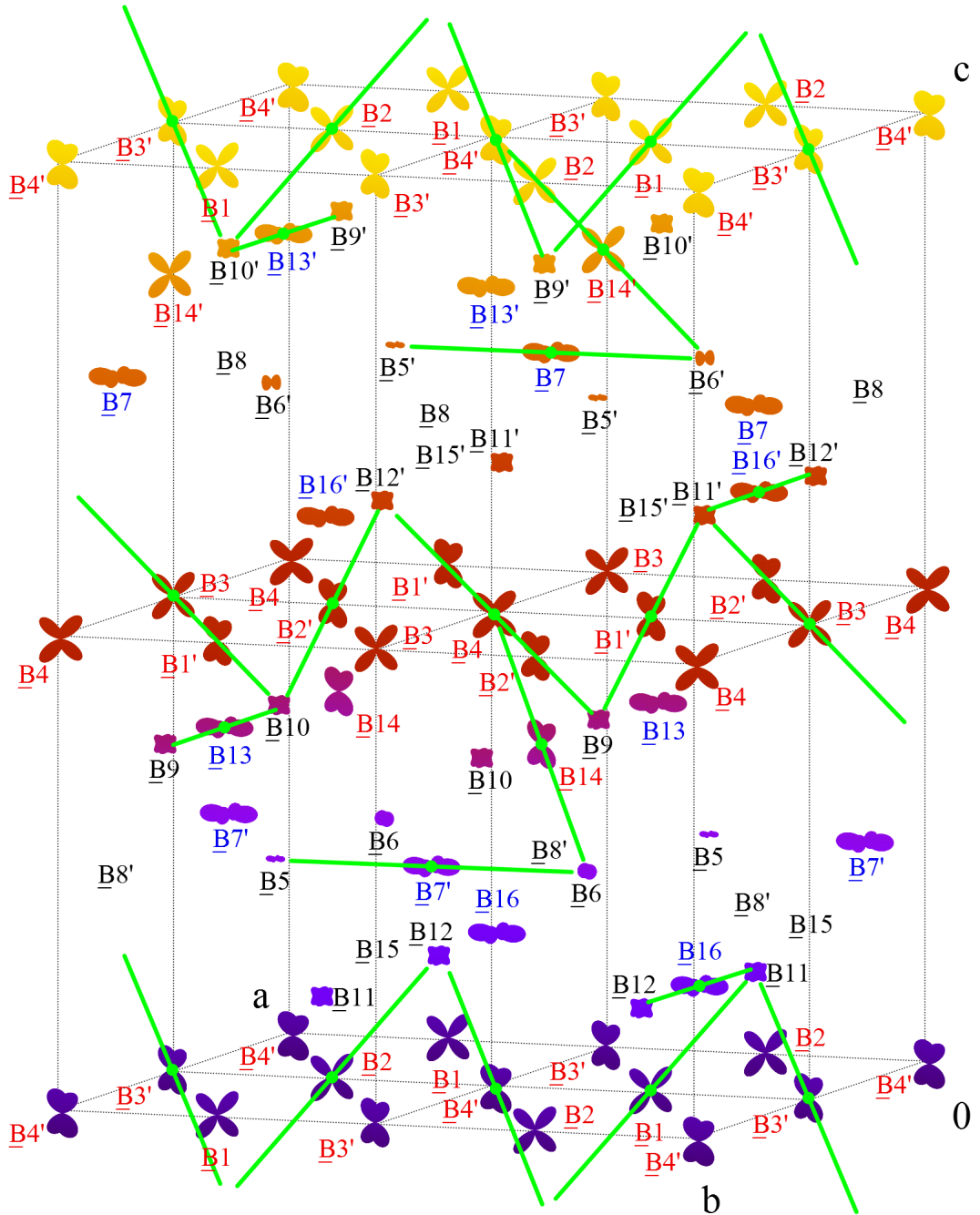
Figure A.3: Populations of minority spin t_{2g} electrons of the B site iron ions derived from Ref. [1] visualized as an angular variation of the electron density, i.e. the distance of the surface from a given site denotes the density at the corresponding angle scaled by $3\,\text{Å}\cdot\text{e}^{-1}$ coefficient. Green lines highlight trimerons [1]. Site numbering and label colours follow the convention introduced in part 7.1; primes indicate the ac-glide symmetry generated sites. (Surface colour indicating z-coordinate is intended just to improve clarity.)
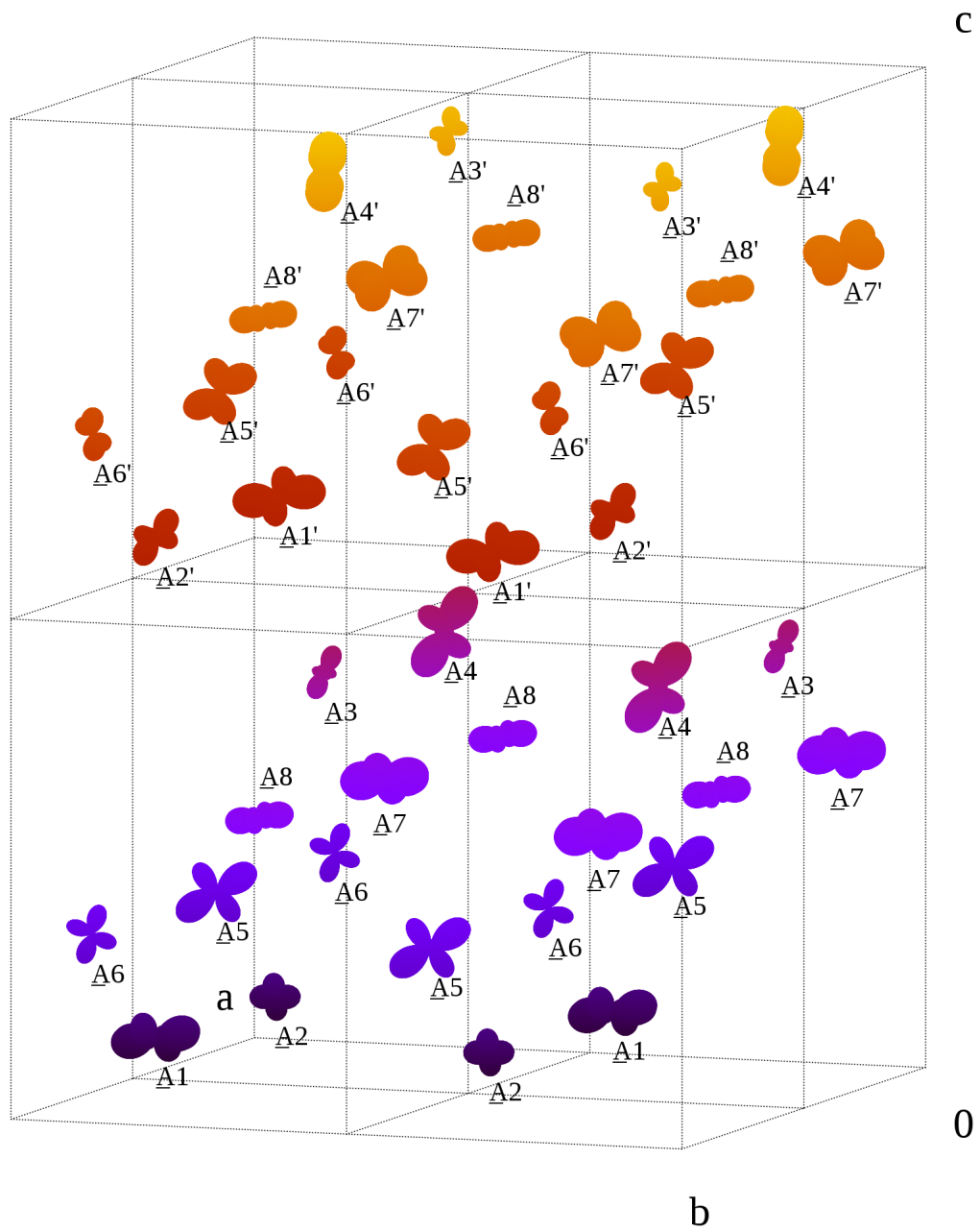
Figure A.4: EFG tensors at iron A sites obtained from the DFT calculations visualized in the elementary cell (scaling coefficient $C = 0.5$ Å $\cdot 10^{-21}$ V$^{-1} \cdot$ m^2). Site numbering follows the convention introduced in part 7.1; primes indicate the *ac*-glide symmetry generated sites. (Surface colour indicating *z*-coordinate is intended just to improve clarity.)
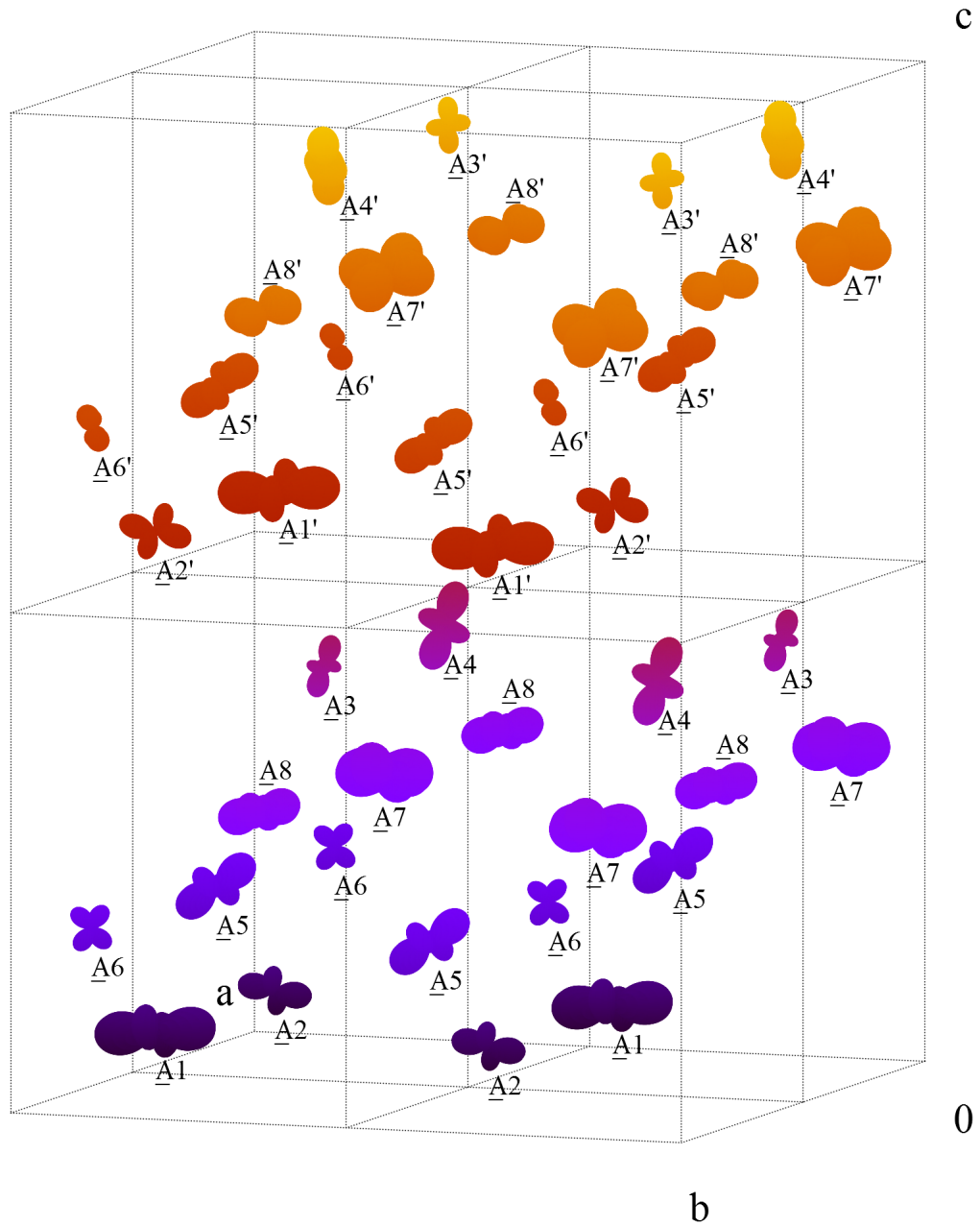
A.1.2 Hyperfine Field Anisotropy

Figure A.5: Hyperfine field anisotropy tensors of iron A sites extracted from the DFT calculations visualized in the elementary cell (scaling coefficient $C = 1.25$ Å·MHz^{-1}). Site numbering follows the convention introduced in part 7.1; primes indicate the ac-glide symmetry generated sites. (Surface colour indicating z-coordinate is intended just to improve clarity.)
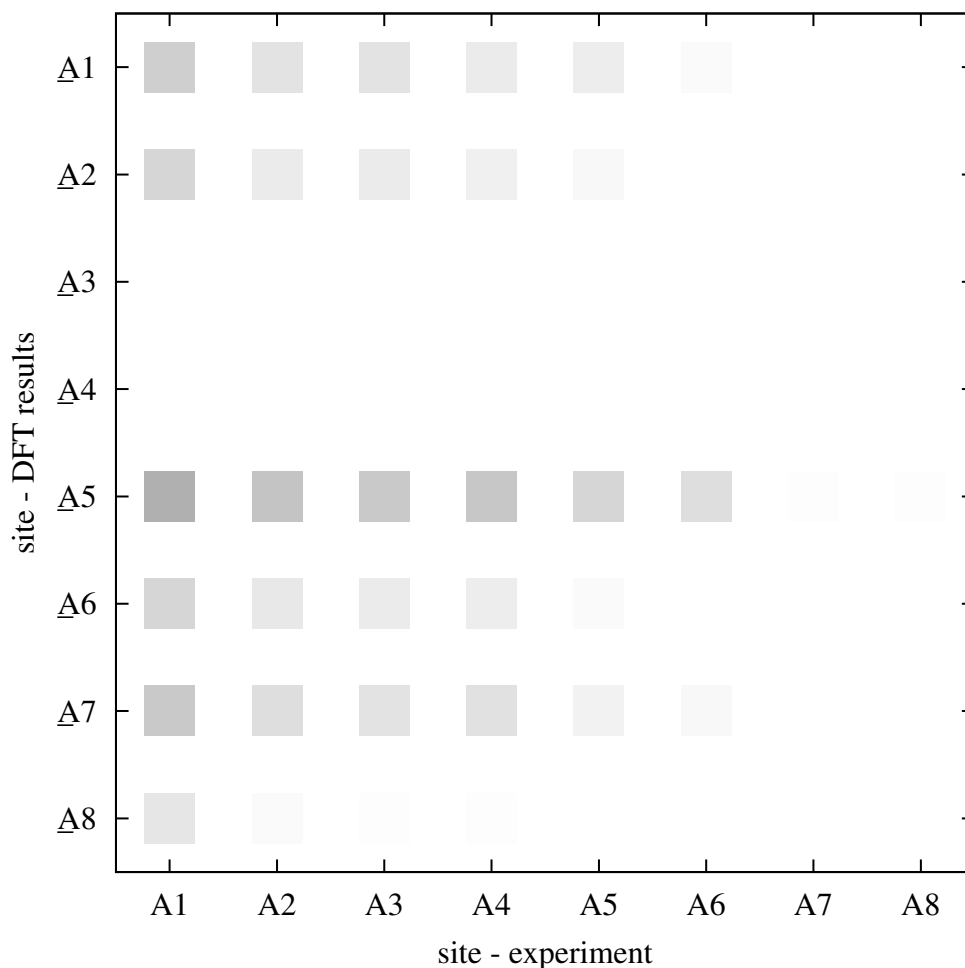
Figure A.6: Visualization of mean square deviation $\sigma(i,j)$ calculated using equation (7.11) for all combinations of the A site data extracted from the DFT results and from the experiment. Brightness of each mark is proportional to $\sigma(i,j)$ magnitude (black for $\sigma(i,j) = 0$ MHz; white for $\sigma(i,j) \geq 5$ MHz) – darker field means better match. Site numbering follows the convention introduced in part 7.1.
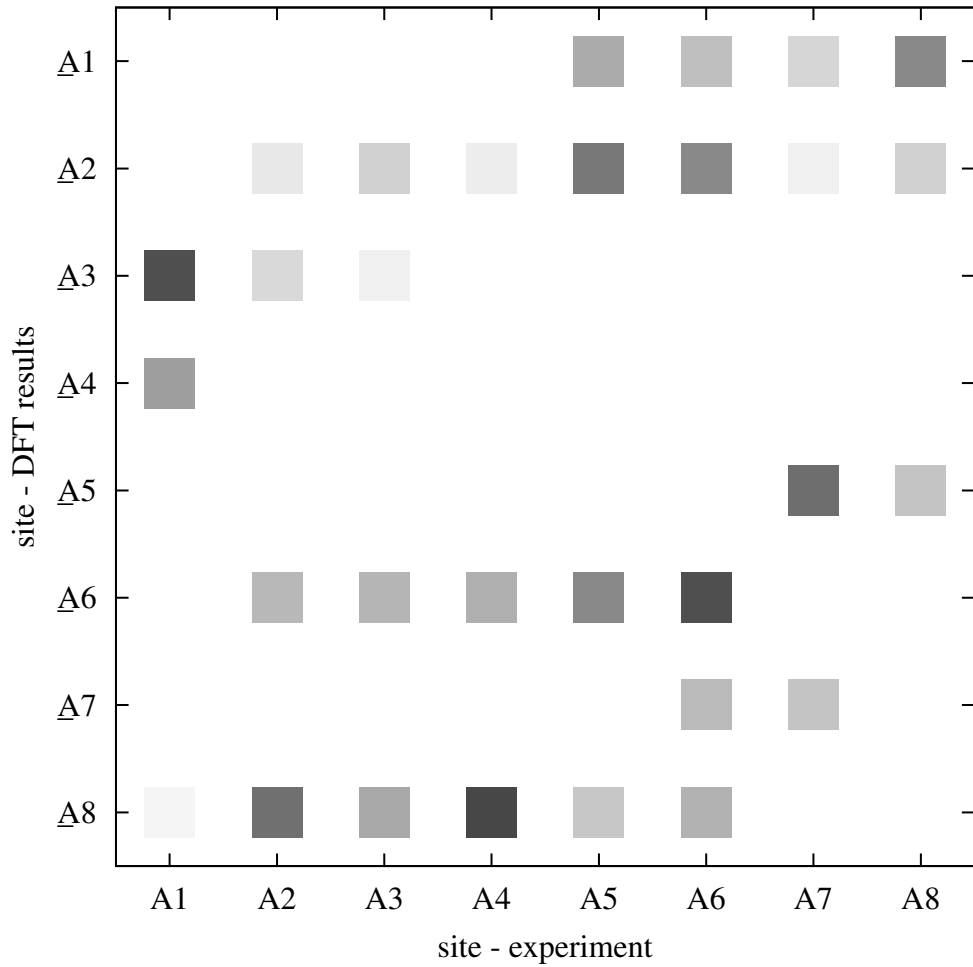
Figure A.7: Visualization of mean square deviation $\sigma'(i,j)$ calculated using equation (7.13) for all combinations of the A site data extracted from the DFT results and from the experiment. Brightness of each mark is proportional to $\sigma'(i,j)$ magnitude (black for $\sigma'(i,j) = 0$ MHz; white for $\sigma'(i,j) \geq 0.7$ MHz) – darker field means better match. Site numbering follows the convention introduced in part 7.1.

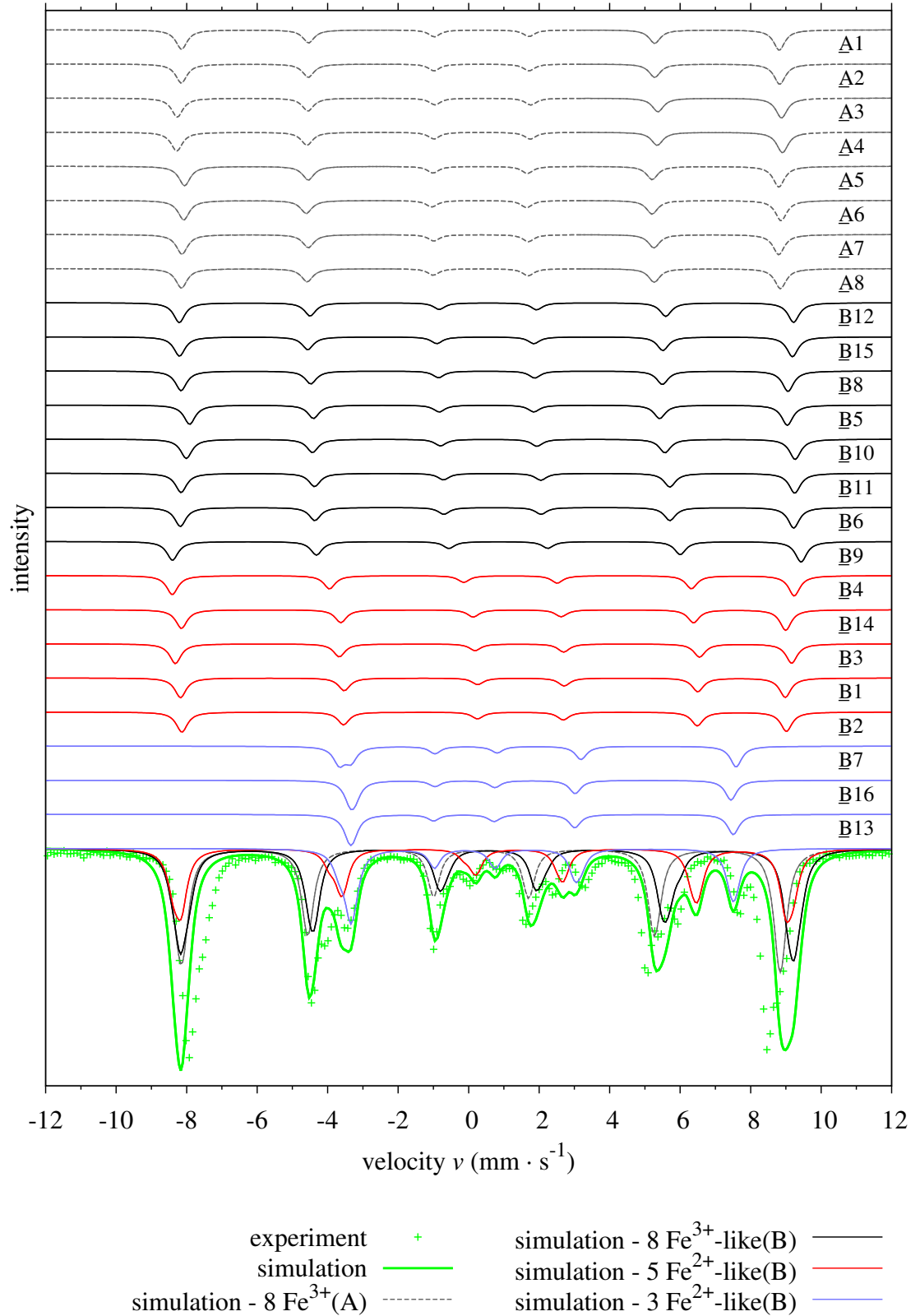### A.1.3   Mössbauer Spectra Simulation

Figure A.8: Simulated zero-field ^{57}Fe Mössbauer spectrum of a single-domain single crystal of (Cc phase) magnetite oriented in [201] direction towards the γ-ray in comparison with experimental data [94]. Contributions of individual iron sites are included; Fe(B) contributions are plotted in the same order as in Fig. 7.12. The three groups of Fe(B) components correspond to the three groups of Fe(B) ions in Fig. 7.12.
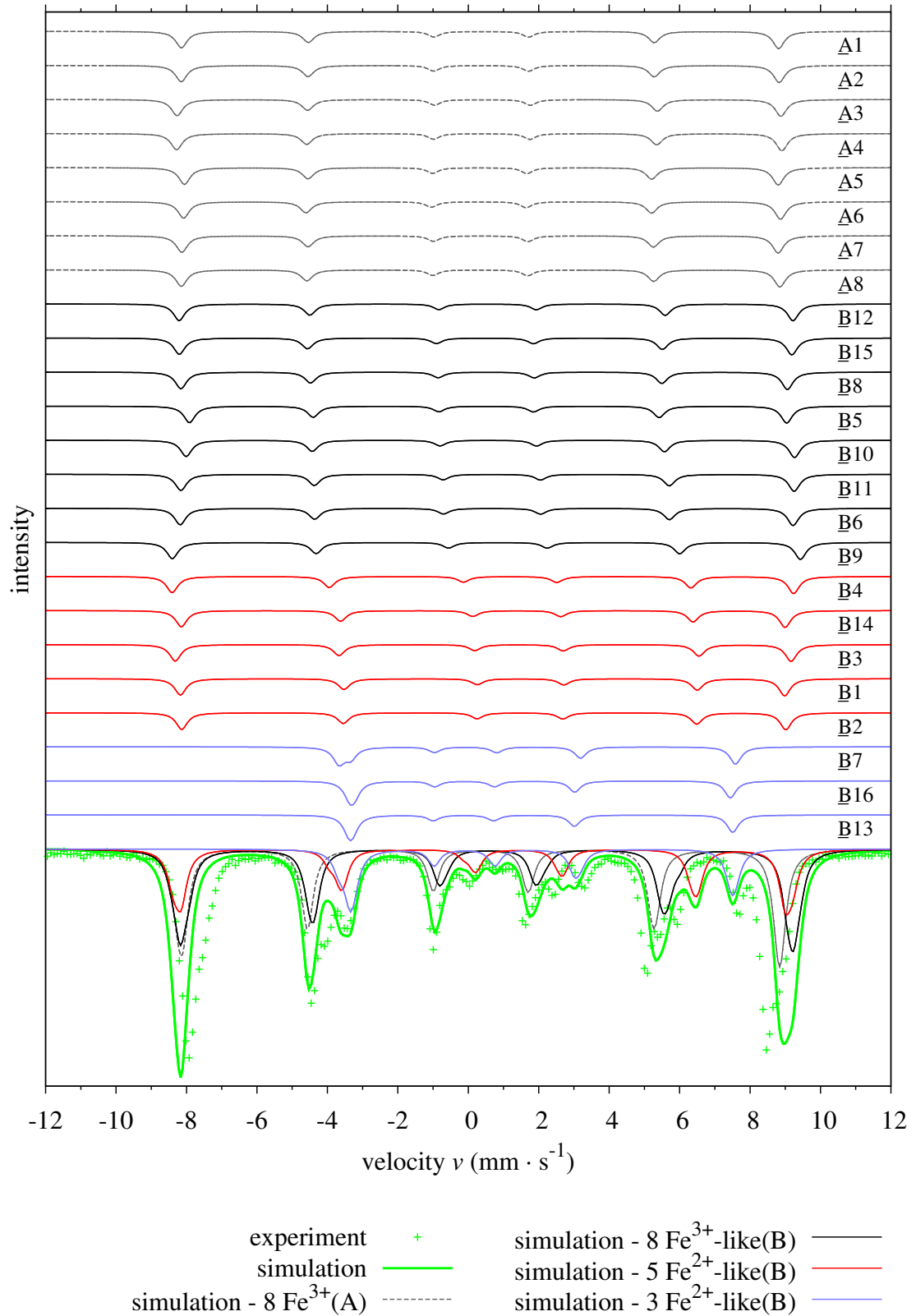
Figure A.9: Simulated zero-field ^{57}Fe Mössbauer spectrum of a powder sample of (Cc phase) magnetite in comparison with experimental data [94]. Contributions of individual iron sites are included; Fe(B) contributions are plotted in the same order as in Fig. 7.12. The three groups of Fe(B) components correspond to the three groups of Fe(B) ions in Fig. 7.12.
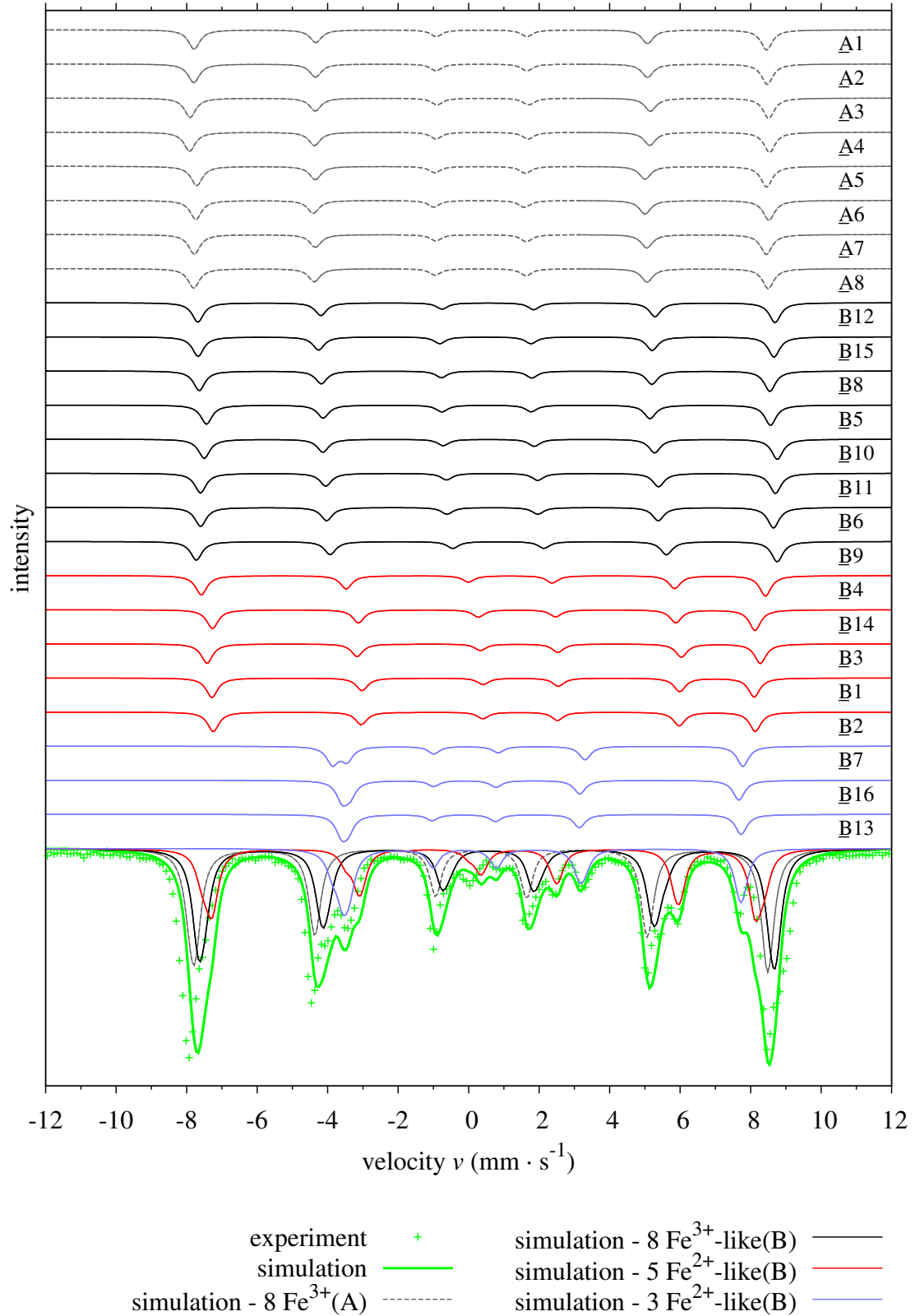
Figure A.10: Simulated zero-field ^{57}Fe Mössbauer spectrum of a single-domain single crystal of (Cc phase) magnetite oriented in [201] direction towards the γ-ray in comparison with experimental data [94]. This simulation is based on renormalized hyperfine fields (see text). Contributions of individual iron sites are included; Fe(B) contributions are plotted in the same order as in Fig. 7.12. The three groups of Fe(B) components correspond to the three groups of Fe(B) ions in Fig. 7.12.
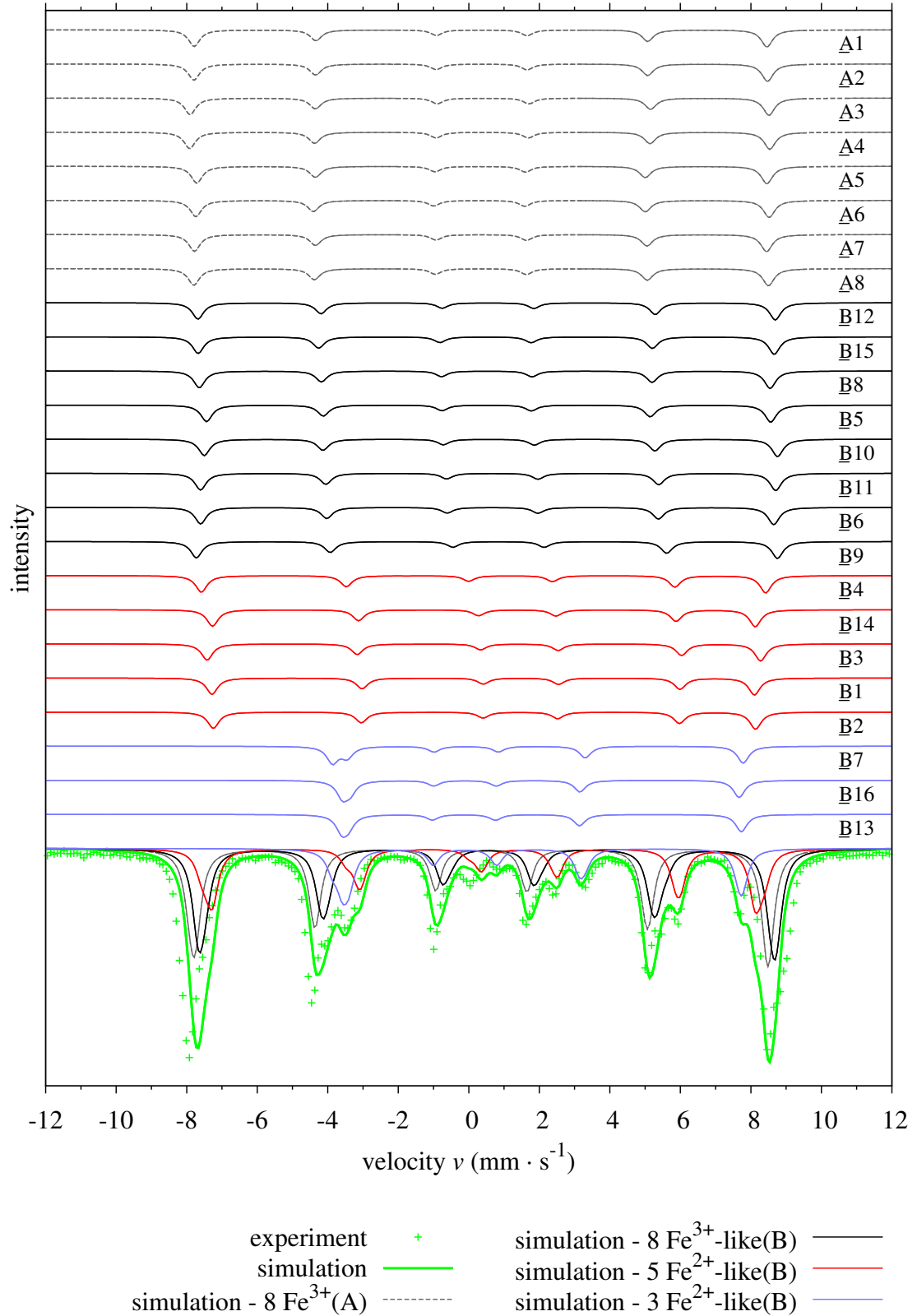
Figure A.11: Simulated zero-field ^{57}Fe Mössbauer spectrum of a powder sample of (Cc phase) magnetite in comparison with experimental data [94]. This simulation is based on renormalized hyperfine fields (see text). Contributions of individual iron sites are included; Fe(B) contributions are plotted in the same order as in Fig. 7.12. The three groups of Fe(B) components correspond to the three groups of Fe(B) ions in Fig. 7.12.
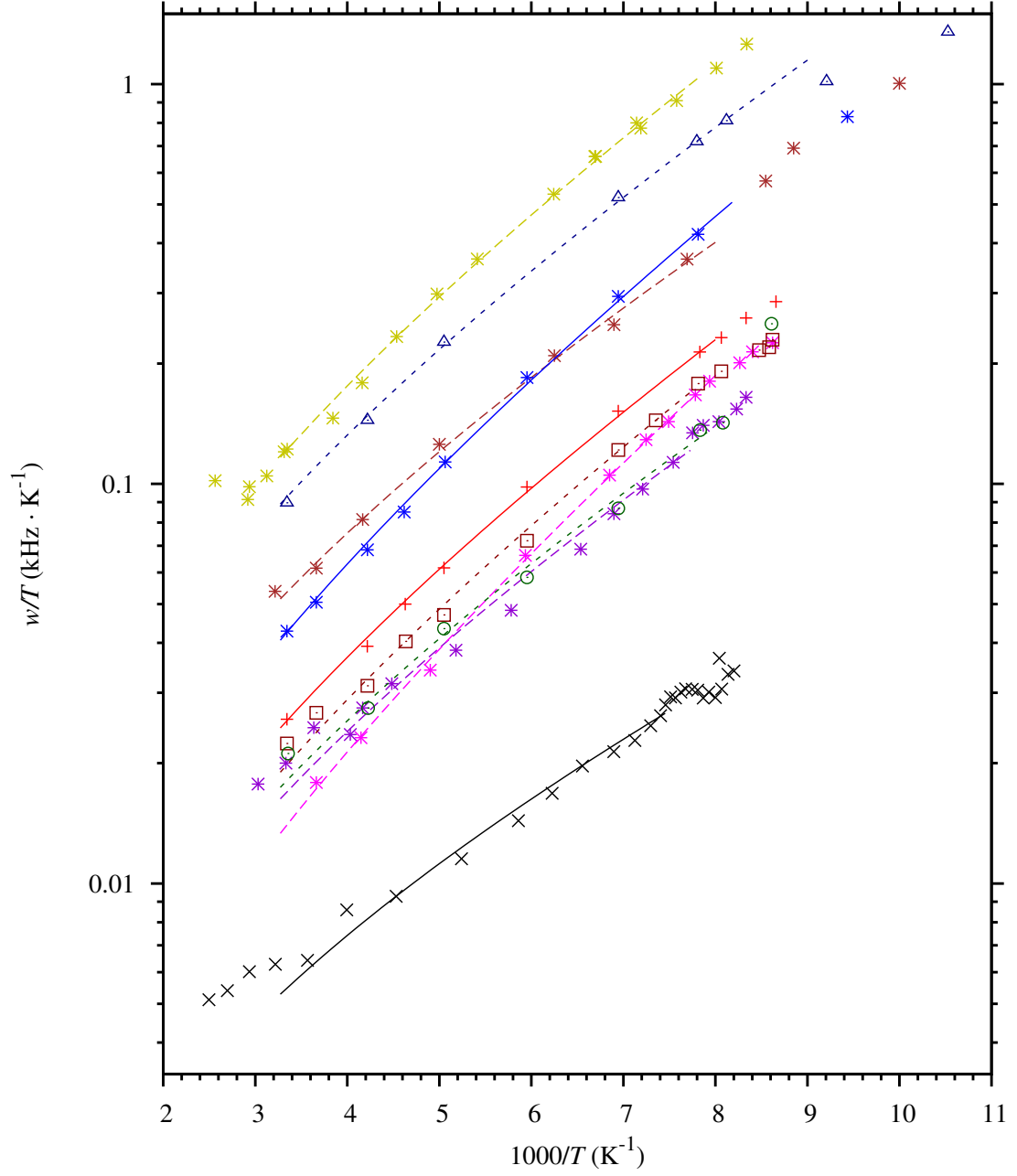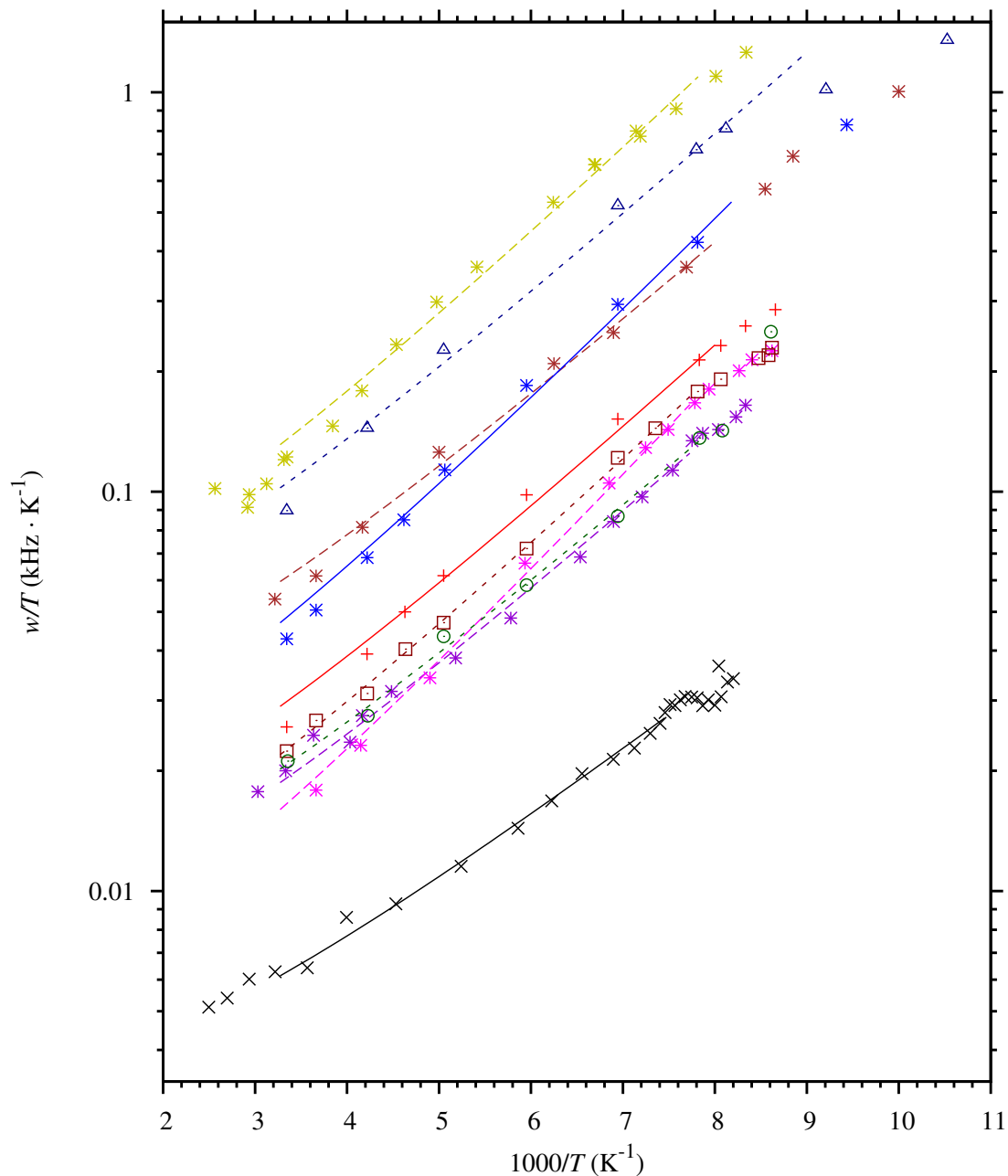
A.2 Electronic Structure and Hyperfine Interactions in Magnetite Above the Verwey Transition

A.2.1 Temperature Dependence of Linewidth of Main NMR Signals

Figure A.12: Temperature dependences of HWHM of the A lines in the spectra of pure and substituted magnetite (pure magnetite [70], [72], aluminium substituted magnetite [70], zinc and titanium substituted magnetite [118]) fitted in the range between T_{sr} and 310 K with (8.11) expression.

Figure A.13: Temperature dependences of HWHM of the B lines in the spectra of pure and substituted magnetite (pure magnetite [70], [72], aluminium substituted magnetite [70]) fitted in the range between T_{sr} and 310 K with (8.11) expression.

Figure A.14: Temperature dependences of HWHM of the A lines in the spectra of pure and substituted magnetite (pure magnetite [70], [72], aluminium substituted magnetite [70], zinc and titanium substituted magnetite [118]) fitted in the range between T_{sr} and 310 K with (8.13) expression.

Figure A.15: Temperature dependences of HWHM of the B lines in the spectra of pure and substituted magnetite (pure magnetite [70], [72], aluminium substituted magnetite [70]) fitted in the range between T_{sr} and 310 K with (8.13) expression.

Figure A.16: Visualization of the parameters of temperature dependences of NMR line width (8.11) with respect to the nominal Fe(B) valence v_B. Substitution types are distinguished by different symbols.
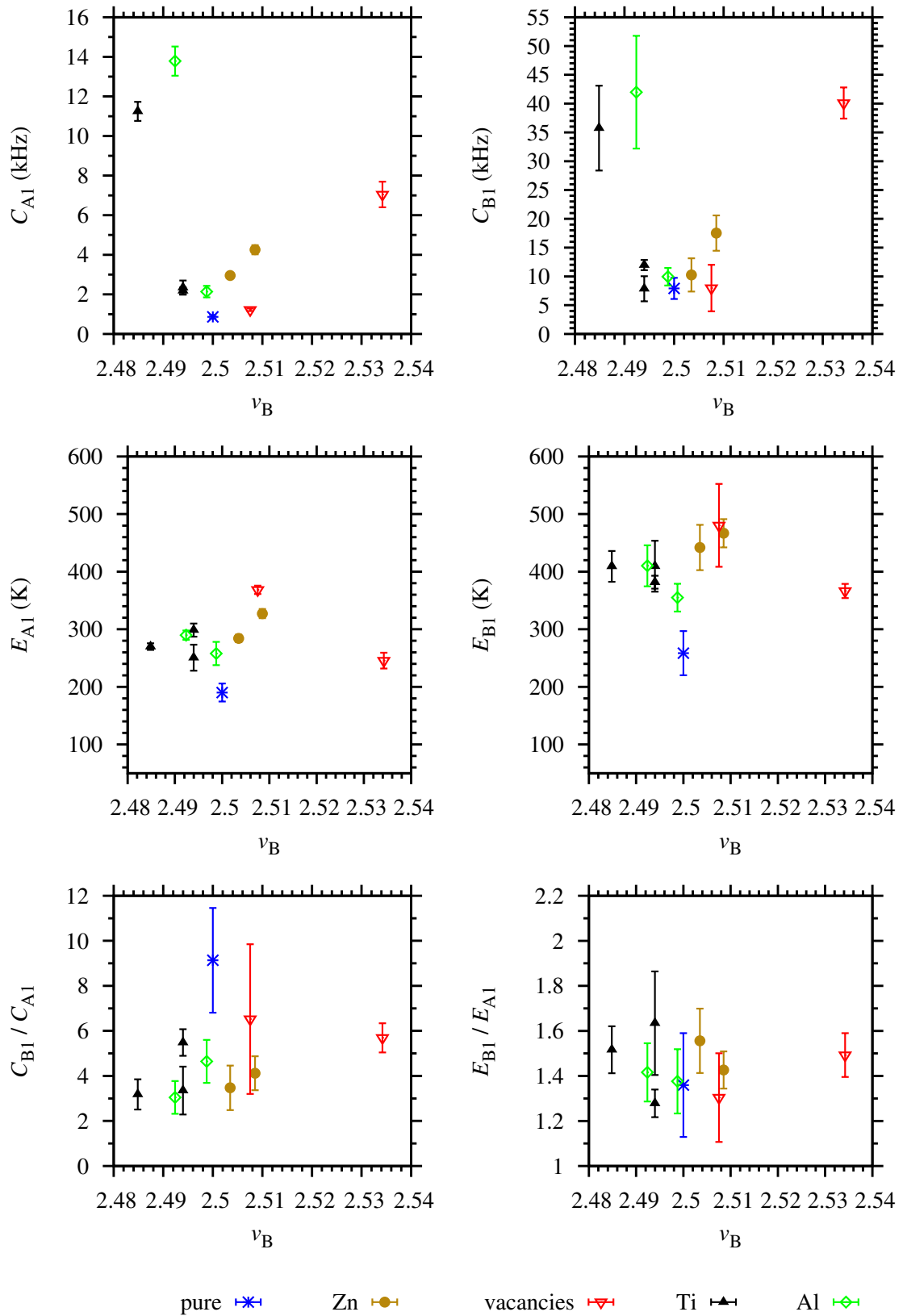
Figure A.17: Visualization of the parameters of temperature dependences of NMR line width (8.13) with respect to the nominal Fe(B) valence v_B. Substitution types are distinguished by different symbols.
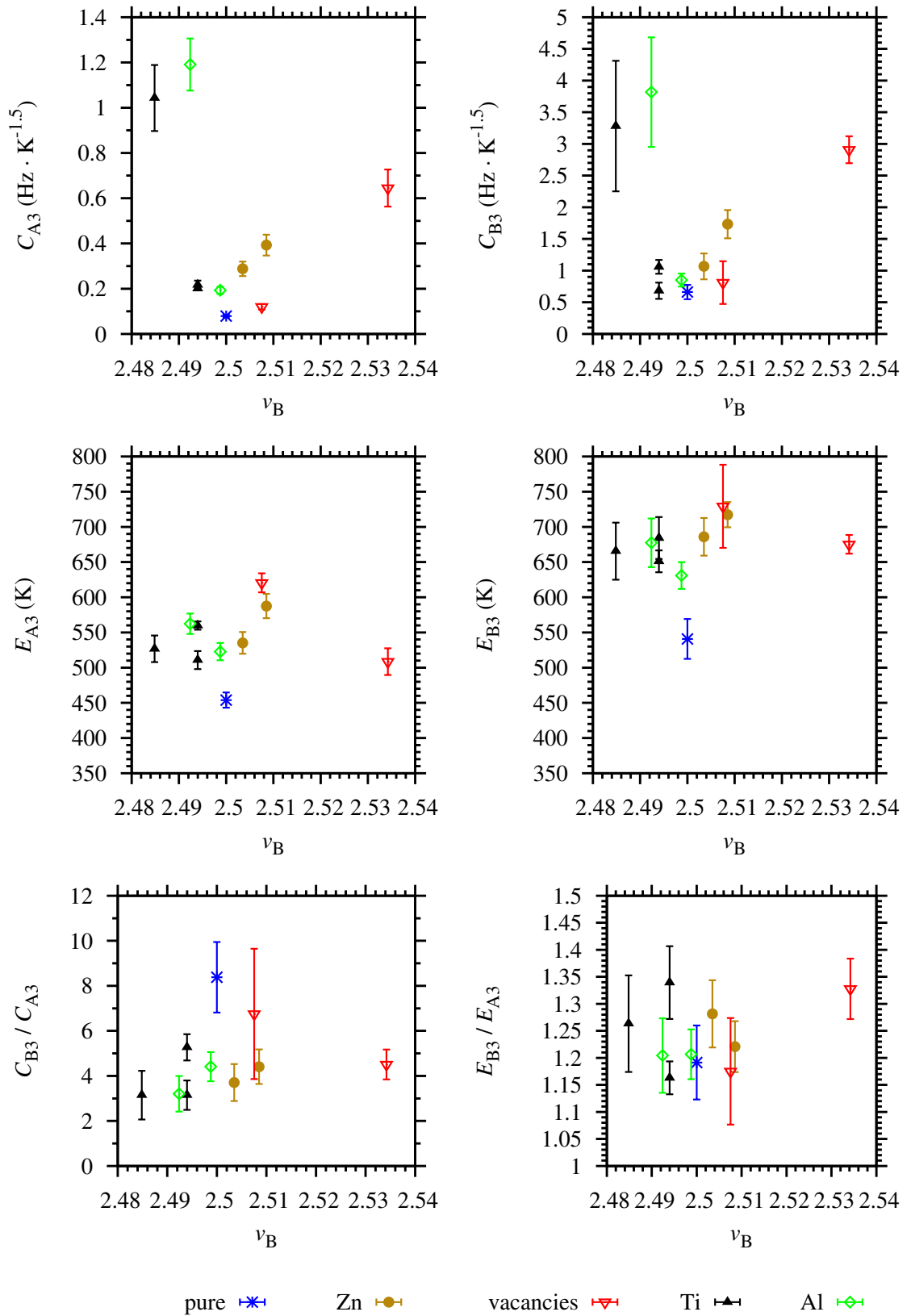
Appendix B

Supplementary Tables

B.1 Electronic Structure and Hyperfine Interactions in Magnetite Below the Verwey Transition

B.1.1 Electronic Structure

Table B.1: The EFG tensors obtained from the DFT calculations (see relations (4.31), (4.32), (4.33) for symbol definitions). Site numbering follows the convention introduced in part 7.1.

site	V_{aa} (10^{21} V·m^{-2})	V_{bb} (10^{21} V·m^{-2})	V_{cc} (10^{21} V·m^{-2})	V_{ab} (10^{21} V·m^{-2})	V_{ac} (10^{21} V·m^{-2})	V_{bc} (10^{21} V·m^{-2})	V_{zz} (10^{21} V·m^{-2})	V_{yy} (10^{21} V·m^{-2})	V_{xx} (10^{21} V·m^{-2})	η	principal axis $\vec{v}_{zz}$	principal axis $\vec{v}_{yy}$	principal axis $\vec{v}_{xx}$
A1	1.522	-1.294	-0.228	-0.298	-0.395	-0.439	1.621	-1.509	-0.112	0.862	(0.979, -0.071, -0.192)	(-0.137, -0.923, -0.359)	(0.152, -0.378, 0.913)
A2	0.739	-0.573	-0.166	0.404	0.211	-0.752	-1.250	0.853	0.397	0.365	(-0.221, 0.781, 0.585)	(0.962, 0.274, -0.004)	(0.163, -0.561, 0.811)
A3	0.286	0.344	-0.630	-0.367	0.256	0.508	-0.965	0.724	0.242	0.499	(0.298, 0.417, -0.859)	(0.561, -0.804, -0.196)	(-0.772, -0.423, -0.473)
A4	0.289	0.166	-0.455	-0.235	0.603	1.415	-1.778	1.344	0.433	0.512	(0.287, 0.586, -0.758)	(0.205, 0.735, 0.646)	(0.936, -0.341, 0.091)
A5	-0.839	0.568	0.272	-0.096	1.038	0.662	-1.550	1.298	0.252	0.675	(0.816, 0.206, -0.540)	(0.323, 0.612, 0.722)	(0.479, -0.764, 0.433)
A6	-0.472	-0.127	0.599	-0.259	-0.363	-0.711	1.055	-0.937	-0.118	0.776	(-0.122, -0.492, 0.862)	(0.673, 0.598, 0.436)	(0.729, -0.633, -0.258)
A7	-1.434	1.572	-0.138	-0.426	0.050	0.651	1.838	-1.509	-0.329	0.642	(0.118, -0.944, -0.308)	(0.981, 0.159, -0.111)	(0.154, -0.289, 0.945)
A8	-1.162	1.104	0.059	-0.035	0.237	-0.035	-1.207	1.106	0.101	0.832	(0.983, 0.012, -0.184)	(-0.019, 0.999, -0.038)	(0.183, 0.041, 0.982)
B1	0.223	6.949	-7.171	-9.551	-0.314	-0.832	13.723	-7.666	-6.058	0.117	(-0.577, 0.816, -0.024)	(0.436, 0.332, 0.836)	(0.691, 0.472, -0.548)
B2	0.622	6.221	-6.843	-10.170	-0.330	-0.857	13.980	-7.784	-6.196	0.114	(-0.605, 0.796, -0.023)	(-0.600, -0.475, -0.643)	(0.523, 0.375, -0.765)
B3	-0.485	7.224	-6.738	-9.466	0.389	0.849	13.601	-7.598	-6.003	0.117	(-0.557, 0.830, 0.024)	(0.596, 0.420, -0.684)	(0.578, 0.367, 0.729)
B4	0.841	4.201	-5.042	-7.589	0.845	0.953	10.297	-6.408	-3.889	0.245	(-0.625, 0.780, 0.014)	(0.568, 0.467, -0.677)	(0.535, 0.415, 0.735)
B5	0.897	-1.249	0.352	0.036	0.277	0.133	-1.260	1.016	0.243	0.614	(0.006, -0.997, 0.081)	(0.919, 0.038, 0.391)	(0.393, -0.072, -0.917)
B6	1.079	-0.092	-0.987	1.629	0.700	-1.053	-2.383	2.224	0.158	0.867	(0.422, -0.609, -0.671)	(-0.815, -0.579, 0.012)	(0.396, -0.542, 0.741)
B7	-4.473	-8.621	13.095	0.393	0.297	0.061	13.100	-8.658	-4.441	0.322	(0.017, 0.003, 1.000)	(0.093, -0.996, 0.002)	(0.995, 0.093, -0.017)
B8	-0.123	0.501	-0.379	0.279	-0.023	-0.191	0.642	-0.424	-0.219	0.319	(0.342, 0.922, -0.180)	(-0.155, 0.244, 0.957)	(0.927, -0.300, 0.226)
B9	1.936	0.174	-2.110	-3.495	0.892	1.376	4.662	-3.979	-0.683	0.707	(0.786, -0.618, -0.022)	(0.454, 0.600, -0.659)	(0.421, 0.507, 0.752)
B10	-1.012	0.640	0.372	-0.313	0.039	0.953	1.486	-1.113	-0.373	0.497	(-0.085, 0.759, 0.646)	(0.939, 0.278, -0.203)	(0.334, -0.589, 0.736)
B11	0.023	0.746	-0.769	-0.764	-0.130	-1.024	1.533	-1.445	-0.088	0.885	(0.398, -0.847, 0.354)	(-0.327, -0.491, -0.807)	(0.857, 0.205, -0.472)
B12	-0.571	0.839	-0.268	0.100	-0.312	-0.889	1.363	-0.918	-0.444	0.348	(0.124, 0.861, -0.493)	(0.571, 0.344, 0.745)	(0.812, -0.374, -0.449)
B13	-8.337	-5.836	14.173	-0.328	0.034	0.401	14.181	-8.380	-5.801	0.182	(0.001, 0.020, 1.000)	(0.992, 0.129, -0.004)	(0.129, -0.991, 0.020)
B14	5.018	1.274	-6.291	9.161	0.845	-0.507	12.502	-7.179	-5.323	0.148	(0.775, 0.632, 0.018)	(0.445, -0.526, -0.725)	(-0.448, 0.570, -0.689)
B15	0.160	-0.283	0.124	-0.179	-0.192	-0.139	-0.421	0.338	0.083	0.606	(-0.381, -0.855, -0.353)	(-0.766, 0.078, 0.638)	(0.518, -0.513, 0.685)
B16	-8.531	-5.295	13.826	-0.040	0.025	-0.397	13.835	-8.531	-5.303	0.233	(0.001, -0.021, 1.000)	(1.000, 0.012, -0.001)	(0.012, -1.000, -0.021)

B.1.2   Hyperfine Field Anisotropy

Table B.2: Fitted parameters of relations (7.3), (7.4), (7.5) based on the DFT calculation results. The "error" column lists the typical error of the fitted parameters. Site numbering follows the convention introduced in part 7.1.

site	f_{iso} (MHz)	f_{ani} (MHz)	f_{aa} (MHz)	f_{bb} (MHz)	f_{cc} (MHz)	f_{ab} (MHz)	f_{ac} (MHz)	f_{bc} (MHz)	error (MHz)	f'_a (MHz)	f'_b (MHz)	f'_c (MHz)	principal axis $\vec{p}_a$	principal axis $\vec{p}_b$	principal axis $\vec{p}_c$
A1	72.506	1.088	-0.843	0.601	0.242	0.028	0.117	0.109	0.023	-0.856	0.634	0.222	(0.994,-0.011,-0.105)	(-0.041,-0.959,-0.279)	(-0.098,0.282,-0.954)
A2	72.631	0.689	-0.490	0.278	0.213	-0.060	-0.133	0.185	0.016	-0.516	0.452	0.064	(0.985,0.035,0.172)	(0.140,-0.744,-0.654)	(-0.105,-0.668,0.737)
A3	73.280	0.553	-0.230	-0.062	0.292	0.119	-0.051	-0.255	0.031	0.441	-0.305	-0.136	(-0.151,-0.475,0.867)	(-0.796,0.578,0.178)	(0.586,0.663,0.466)
A4	73.408	0.808	-0.285	-0.009	0.294	0.013	-0.124	-0.476	0.017	0.654	-0.397	-0.258	(0.115,0.580,-0.806)	(0.530,0.650,0.544)	(0.840,-0.490,-0.233)
A5	72.207	0.840	0.374	-0.493	0.120	-0.005	-0.363	-0.148	0.016	0.637	-0.537	-0.100	(0.806,0.073,-0.587)	(-0.116,-0.953,-0.279)	(-0.580,0.293,-0.760)
A6	72.650	0.557	0.128	-0.195	0.067	0.012	0.162	0.315	0.013	-0.418	0.365	0.053	(-0.152,-0.805,0.574)	(0.526,0.426,0.736)	(0.837,-0.414,-0.358)
A7	72.460	1.181	0.677	-0.847	0.170	0.054	-0.001	-0.303	0.021	-0.932	0.679	0.253	(0.032,-0.964,-0.265)	(0.999,0.041,-0.026)	(0.036,-0.264,0.964)
A8	72.811	0.890	0.531	-0.646	0.115	0.112	-0.106	-0.129	0.031	-0.674	0.573	0.102	(-0.078,0.986,0.150)	(0.960,0.115,-0.255)	(0.269,-0.124,0.955)
B1	61.01	24.69	-0.92	-10.67	11.59	13.39	0.72	0.51	0.44	-20.05	11.83	8.22	(-0.57,0.82,-0.00)	(0.21,0.15,0.97)	(0.79,0.55,-0.25)
B2	60.81	24.90	-2.29	-9.40	11.69	13.92	1.01	0.53	0.44	-20.21	12.05	8.16	(0.61,-0.79,-0.01)	(0.24,0.18,0.95)	(-0.75,-0.59,0.30)
B3	62.52	24.23	-0.71	-10.79	11.50	12.99	-0.01	-0.45	0.42	-19.69	11.52	8.17	(-0.56,0.83,0.01)	(-0.06,-0.05,1.00)	(0.82,0.56,0.08)
B4	66.21	18.55	-2.58	-6.33	8.91	10.36	-1.04	-0.87	0.32	-14.98	9.45	5.52	(0.64,-0.77,-0.00)	(-0.29,-0.24,0.93)	(-0.71,-0.60,-0.37)
B5	73.676	3.796	-1.806	2.715	-0.909	-0.036	-1.205	-0.150	0.087	2.721	-2.646	-0.075	(-0.003,-0.999,0.042)	(0.821,0.022,0.571)	(0.572,-0.037,-0.820)
B6	73.063	5.235	-2.297	0.735	1.562	-2.599	-1.193	1.181	0.088	-3.830	3.558	0.272	(-0.875,-0.475,-0.090)	(-0.418,0.650,0.635)	(0.243,-0.593,0.768)
B7	63.93	19.57	5.56	10.14	-15.70	-0.11	1.09	0.02	0.56	-15.76	10.14	5.62	(0.05,0.00,-1.00)	(-0.02,1.00,-0.00)	(1.00,0.02,0.05)
B8	73.934	1.629	-0.549	0.581	-0.032	-0.011	1.003	-0.018	0.058	-1.326	0.748	0.578	(0.790,-0.001,-0.612)	(0.608,-0.123,0.785)	(0.076,0.992,0.097)
B9	72.11	9.50	-3.51	-0.74	4.25	5.01	-1.05	-1.86	0.17	-7.33	5.86	1.47	(0.79,-0.61,-0.03)	(-0.35,-0.49,0.80)	(-0.50,-0.62,-0.60)
B10	74.422	1.409	0.766	-0.447	-0.319	-0.352	-0.118	-0.641	0.032	-1.090	0.864	0.227	(0.182,0.742,0.645)	(0.956,-0.286,0.060)	(-0.229,-0.606,0.762)
B11	73.897	1.825	-0.405	-0.393	0.798	0.739	0.047	0.800	0.038	1.292	-1.289	-0.004	(0.241,0.500,0.832)	(0.609,-0.745,0.272)	(-0.756,-0.441,0.484)
B12	74.608	3.383	1.236	-1.415	0.178	0.755	-0.008	1.837	0.055	-2.723	1.765	0.958	(-0.160,0.834,-0.528)	(-0.680,-0.481,-0.554)	(-0.716,0.270,0.644)
B13	62.86	20.09	10.29	5.91	-16.20	0.33	0.27	0.38	0.61	-16.21	10.31	5.89	(-0.01,-0.02,1.00)	(1.00,0.08,0.01)	(0.08,-1.00,-0.02)
B14	61.54	22.79	-8.27	-2.88	11.15	-12.59	-0.47	0.76	0.40	-18.45	11.34	7.10	(0.78,0.63,-0.00)	(-0.13,0.17,0.98)	(0.61,-0.76,0.21)
B15	74.498	1.849	0.730	-0.867	0.137	-0.322	-0.188	-0.958	0.031	-1.509	0.793	0.716	(0.164,0.844,0.510)	(0.983,-0.180,-0.018)	(-0.077,-0.505,0.860)
B16	62.46	20.32	11.19	4.99	-16.18	-0.24	0.22	-0.50	0.61	-16.20	11.20	5.00	(-0.01,0.02,1.00)	(1.00,-0.04,0.01)	(-0.04,-1.00,0.02)

Table B.3: Fitted parameters of relations (7.3), (7.4), (7.5) based on the experimental data [14]. The "error" column lists the typical error of the fitted parameters. Site numbering follows the convention introduced in part 7.1. The signs of f_{ab}, f_{bc} and of b-component of principal axes are arbitrary (but the sign of $f_{ab} \cdot f_{bc}$ is known) since the iron positions connected by the ac-glide symmetry cannot be distinguished by the experiment.

site	f_{iso} (MHz)	f_{ani} (MHz)	f_{aa} (MHz)	f_{bb} (MHz)	f_{cc} (MHz)	f_{ab} (MHz)	f_{ac} (MHz)	f_{bc} (MHz)	error (MHz)	f'_a (MHz)	f'_b (MHz)	f'_c (MHz)	principal axis $\vec{p}_a$	principal axis $\vec{p}_b$	principal axis $\vec{p}_c$
A1	70.253	0.092	0.021	-0.062	0.041	0.019	-0.030	-0.000	0.003	-0.067	0.064	0.003	(-0.236,0.970,-0.065)	(0.601,0.093,-0.794)	(0.763,0.226,0.605)
A2	70.020	0.188	0.087	-0.104	0.016	0.027	0.057	0.066	0.005	0.133	-0.133	-0.000	(0.810,0.242,0.534)	(0.009,-0.916,0.401)	(0.586,-0.320,-0.744)
A3	69.994	0.236	-0.039	0.042	-0.004	0.018	0.151	0.056	0.003	-0.176	0.157	0.019	(-0.728,-0.114,0.676)	(0.576,0.432,0.694)	(0.371,-0.895,0.249)
A4	69.968	0.325	0.217	-0.191	-0.026	0.026	-0.036	0.095	0.004	-0.237	0.222	0.015	(0.086,-0.904,0.419)	(0.991,0.034,-0.130)	(0.104,0.427,0.898)
A5	69.848	0.280	-0.149	0.182	-0.033	0.027	0.085	0.055	0.010	0.202	-0.194	-0.008	(-0.139,-0.952,-0.273)	(0.883,0.006,-0.470)	(-0.449,0.307,-0.839)
A6	69.731	0.362	0.012	-0.016	0.005	0.041	0.094	-0.234	0.003	-0.272	0.236	0.036	(0.319,-0.667,-0.673)	(0.191,-0.651,0.735)	(-0.928,-0.363,-0.080)
A7	69.366	0.305	-0.020	0.023	-0.003	0.001	-0.141	-0.161	0.004	0.217	-0.214	-0.003	(-0.419,-0.582,0.697)	(0.513,0.482,0.710)	(0.749,-0.656,-0.097)
A8	69.400	0.308	-0.188	0.230	-0.041	0.023	-0.031	0.033	0.003	0.234	-0.197	-0.038	(0.045,0.992,0.115)	(0.975,-0.069,0.212)	(-0.218,-0.103,0.970)
B1	71.113	1.499	-0.407	0.628	-0.221	0.067	0.901	-0.052	0.019	-1.224	0.633	0.591	(0.742,-0.046,-0.669)	(-0.146,-0.985,-0.095)	(-0.654,0.168,-0.737)
B2	70.576	1.889	0.854	-0.959	0.106	0.077	0.238	0.944	0.034	-1.512	1.020	0.492	(-0.023,-0.862,0.506)	(0.829,0.266,0.491)	(0.559,-0.431,-0.709)
B3	69.933	2.957	0.833	-0.825	-0.008	1.049	0.066	1.607	0.069	-2.283	1.823	0.459	(-0.255,0.793,-0.553)	(-0.636,-0.568,-0.522)	(-0.728,0.219,0.650)
B4	65.900	7.994	-1.846	-1.274	3.120	4.729	1.036	-1.060	0.098	-6.526	3.367	3.159	(0.719,-0.678,-0.152)	(-0.104,-0.320,0.942)	(-0.687,-0.661,-0.301)
B5	63.55	11.39	-0.93	-3.59	4.52	6.70	0.62	-1.56	0.22	-9.28	5.15	4.13	(-0.63,0.77,0.12)	(0.46,0.48,-0.75)	(-0.63,-0.42,-0.66)
B6	67.19	6.19	0.01	-0.39	0.38	4.10	-0.36	-1.45	0.15	-4.43	4.32	0.11	(0.66,-0.73,-0.17)	(-0.67,-0.68,0.31)	(0.34,0.09,0.94)
B7	61.856	13.580	1.792	-6.964	5.172	6.261	2.684	2.566	0.095	-10.299	8.708	1.590	(-0.446,0.892,-0.071)	(-0.601,-0.357,-0.715)	(-0.663,-0.277,0.695)
B8	69.323	4.813	0.356	2.672	-3.028	0.333	-1.776	-0.316	0.068	-3.793	2.787	1.005	(0.392,0.025,0.920)	(0.220,0.968,-0.120)	(-0.893,0.249,0.374)
B9	66.221	1.453	-0.103	-0.002	0.105	0.637	0.120	-0.790	0.026	-1.071	0.977	0.094	(0.515,-0.686,-0.513)	(-0.356,-0.716,0.600)	(-0.780,-0.126,-0.613)
B10	61.96	9.90	-1.53	-1.80	3.33	6.10	-1.85	-0.14	0.22	-7.90	5.44	2.45	(-0.70,0.70,-0.11)	(0.62,0.53,-0.58)	(0.35,0.47,0.81)
B11	66.661	2.515	0.650	0.988	-1.638	0.027	-0.029	-1.058	0.082	-2.011	1.363	0.648	(0.007,0.333,0.943)	(-0.049,-0.942,0.333)	(0.999,-0.048,0.010)
B12	59.873	13.490	0.978	-5.437	4.459	6.742	-3.263	3.111	0.091	-10.943	6.552	4.392	(-0.529,0.803,-0.274)	(0.639,0.164,-0.752)	(0.559,0.573,0.600)
B13	58.83	13.51	-0.50	-3.96	4.46	8.43	0.94	-1.16	0.10	-10.99	6.38	4.61	(-0.63,0.77,0.10)	(0.77,0.63,-0.00)	(0.06,-0.07,1.00)
B14	59.97	14.33	4.77	6.80	-11.57	0.20	1.02	-0.37	0.26	-11.64	6.82	4.82	(-0.06,0.02,1.00)	(-0.09,-1.00,0.02)	(0.99,-0.09,0.06)
B15	57.34	13.60	6.80	4.09	-10.89	0.53	0.03	-1.16	0.14	-10.98	6.90	4.08	(-0.00,0.08,1.00)	(0.98,0.19,-0.01)	(0.19,-0.98,0.08)
B16	55.29	13.12	5.72	4.97	-10.68	0.16	-0.44	-0.39	0.70	-10.70	5.76	4.94	(-0.03,-0.02,-1.00)	(0.98,0.21,-0.03)	(-0.21,0.98,-0.02)

Table B.4: Values of mean square deviation $\sigma(i,j)$ (in MHz; in bold font for $\sigma(i,j) < 18$ MHz) calculated using equation (7.11) for all combinations of the B site data extracted from the DFT results and from the experiment. Lower value means better match. Site numbering follows the convention introduced in part 7.1. The sites are arranged to make their grouping (see text) apparent.

site	B3	B2	B1	B8	B11	B9	B6	B4	B5	B10	B12	B7	B13	B14	B15	B16
B12	**8.15**	**7.20**	**7.28**	**11.17**	**14.19**	**14.86**	**14.56**	**17.21**	22.13	23.87	27.97	24.90	30.21	29.47	32.90	36.12
B15	**8.04**	**6.83**	**6.51**	**10.48**	**13.83**	**14.46**	**14.17**	**16.96**	22.01	23.72	28.14	25.21	30.16	29.14	32.68	35.84
B8	**7.80**	**6.41**	**4.89**	**9.68**	**12.93**	**13.51**	**13.39**	**15.99**	21.37	23.21	28.25	24.98	29.50	28.02	31.87	34.92
B5	**8.48**	**7.47**	**5.95**	**8.18**	**12.71**	**13.54**	**13.41**	**16.45**	21.88	22.91	28.12	26.12	29.84	27.33	31.34	34.25
B10	**7.98**	**6.74**	**6.21**	**10.09**	**13.61**	**14.32**	**13.96**	**16.85**	21.96	23.66	28.22	25.30	30.10	28.72	32.35	35.51
B11	**7.14**	**6.04**	**5.40**	**9.84**	**12.94**	**13.47**	**12.98**	**15.52**	20.70	22.45	27.12	24.15	28.90	28.59	32.17	35.21
B6	**8.22**	**7.21**	**6.50**	**9.29**	**12.57**	**12.62**	**10.84**	**13.40**	18.47	20.19	25.67	23.47	26.81	28.21	31.66	34.56
B9	**10.44**	**10.00**	**9.87**	**12.34**	**14.04**	**13.29**	**10.16**	**11.41**	**15.69**	18.02	23.59	21.29	24.11	29.61	32.51	35.24
B4	18.74	19.91	20.72	21.54	19.78	**17.76**	**14.06**	**11.48**	**9.16**	**12.07**	**14.88**	**13.24**	**14.44**	31.27	31.94	33.88
B14	26.47	27.81	28.22	28.14	25.55	23.43	20.77	**17.13**	**13.54**	**14.03**	**16.10**	**16.62**	**12.93**	33.15	33.26	34.07
B3	26.32	27.59	28.73	29.31	26.49	24.36	21.41	18.32	**13.64**	**15.85**	**15.06**	**13.62**	**13.47**	34.93	34.22	35.61
B1	27.95	29.31	30.49	30.91	27.77	25.64	23.02	19.70	**14.75**	**16.44**	**14.81**	**13.51**	**12.85**	35.04	34.08	35.19
B2	28.37	29.76	30.80	31.19	28.08	25.94	23.26	19.78	**14.92**	**16.48**	**15.30**	**14.12**	**12.75**	35.12	34.30	35.32
B7	22.50	23.05	22.82	18.64	18.24	20.11	21.73	24.41	27.06	25.61	29.41	29.15	29.35	**8.72**	**14.02**	**16.77**
B16	23.96	24.61	25.19	21.12	19.81	21.50	23.10	25.77	27.30	25.84	27.96	27.96	28.70	**9.27**	**11.35**	**14.69**
B13	23.48	24.11	24.56	20.43	19.33	21.09	22.63	25.37	27.12	25.67	28.12	28.09	28.74	**8.90**	**11.74**	**15.02**

Table B.5: Values of mean square deviation $\sigma(i,j)$ (in MHz; in bold font for $\sigma(i,j) < 5$ MHz) calculated using equation (7.11) for all combinations of the A site data extracted from the DFT results and from the experiment. Lower value means better match. Site numbering follows the convention introduced in part 7.1.

site	A1	A2	A3	A4	A5	A6	A7	A8
A1	**4.06**	**4.47**	**4.47**	**4.60**	**4.68**	**4.93**	5.55	5.44
A2	**4.18**	**4.59**	**4.62**	**4.70**	**4.86**	5.07	5.69	5.62
A3	5.27	5.67	5.72	5.77	5.97	6.16	6.79	6.74
A4	5.52	5.92	5.97	6.02	6.22	6.40	7.03	6.98
A5	**3.47**	**3.87**	**3.96**	**3.92**	**4.23**	**4.38**	**4.98**	**4.97**
A6	**4.19**	**4.57**	**4.62**	**4.67**	**4.89**	5.06	5.72	5.67
A7	**3.98**	**4.35**	**4.44**	**4.41**	**4.73**	**4.85**	5.48	5.49
A8	**4.51**	**4.90**	**4.98**	**4.96**	5.26	5.41	6.03	6.02

Table B.6: Values of mean square deviation $\sigma'(i,j)$ (in MHz; in bold font for $\sigma'(i,j) < 15$ MHz) calculated using equation (7.13) for all combinations of the B site data extracted from the DFT results and from the experiment. Lower value means better match. Site numbering follows the convention introduced in part 7.1. The sites are arranged to make their grouping (see text) apparent.

site	B3	B2	B1	B8	B11	B9	B6	B4	B5	B10	B12	B7	B13	B14	B15	B16
B12	**1.04**	**1.13**	**3.45**	**5.83**	**6.54**	**7.05**	**8.16**	**10.83**	15.85	16.99	21.44	18.76	23.45	22.89	25.94	28.92
B15	**1.91**	**1.35**	**2.99**	**5.27**	**6.27**	**6.71**	**7.91**	**10.71**	15.82	16.93	21.63	19.08	23.45	22.65	25.78	28.70
B8	**3.39**	**3.01**	**2.90**	**5.20**	**5.54**	**5.87**	**7.50**	**10.01**	15.37	16.53	21.73	18.94	22.88	21.72	25.07	27.88
B5	**4.55**	**4.58**	**4.29**	**3.39**	**5.26**	**5.94**	**7.57**	**10.49**	15.81	16.21	21.56	19.87	23.10	21.09	24.55	27.25
B10	**2.16**	**1.66**	**2.87**	**4.93**	**6.05**	**6.60**	**7.75**	**10.65**	15.80	16.89	21.71	19.18	23.40	22.30	25.50	28.43
B11	**2.36**	**2.57**	**3.51**	**5.43**	**5.58**	**5.82**	**7.03**	**9.53**	**14.77**	15.83	20.77	18.23	22.37	22.19	25.31	28.11
B6	**5.16**	**5.28**	**5.73**	**5.66**	**5.52**	**4.94**	**4.76**	**7.45**	**12.75**	**13.67**	19.43	17.60	20.47	21.78	24.73	27.38
B9	**7.64**	**8.06**	**8.69**	**8.88**	**7.44**	**5.86**	**3.69**	**4.64**	**9.75**	**11.16**	17.30	15.42	17.78	22.70	25.11	27.59
B4	17.45	18.79	19.80	19.07	15.39	**13.24**	**11.65**	**8.38**	**3.63**	**3.93**	**8.21**	**7.97**	**7.02**	23.82	23.80	25.26
B14	25.34	26.72	27.40	26.12	22.15	20.19	19.39	15.91	**11.69**	**9.73**	**10.99**	**13.20**	**6.55**	26.00	25.11	25.27
B3	24.24	25.60	26.80	26.03	21.87	19.83	18.68	15.43	**9.99**	**9.69**	**8.21**	**8.93**	**4.64**	26.87	25.39	26.15
B1	26.33	27.73	28.93	28.05	23.73	21.75	20.88	17.59	**12.31**	**11.56**	**9.19**	**10.22**	**5.47**	27.36	25.56	25.95
B2	26.71	28.13	29.23	28.33	24.04	22.06	21.15	17.75	**12.55**	**11.68**	**9.76**	**10.85**	**5.40**	27.46	25.77	26.06
B7	21.60	22.45	22.74	18.63	15.71	16.71	19.08	20.41	21.67	19.39	22.50	23.02	22.14	**1.95**	**6.56**	**8.87**
B16	23.51	24.42	25.23	21.25	17.88	18.69	20.95	22.19	22.45	20.13	21.64	22.53	21.88	**5.17**	**2.97**	**6.39**
B13	22.94	23.84	24.57	20.53	17.26	18.15	20.38	21.69	22.15	19.84	21.67	22.50	21.84	**4.22**	**3.45**	**6.78**

Table B.7: Values of mean square deviation $\sigma'(i,j)$ (in MHz; in bold font for $\sigma'(i,j) < 0.7$ MHz) calculated using equation (7.13) for all combinations of the A site data extracted from the DFT results and from the experiment. Lower value means better match. Site numbering follows the convention introduced in part 7.1.

site	A1	A2	A3	A4	A5	A6	A7	A8
A1	1.21	0.87	0.77	0.91	**0.47**	**0.52**	**0.59**	**0.38**
A2	0.97	**0.63**	**0.58**	**0.65**	**0.33**	**0.38**	**0.66**	**0.58**
A3	**0.22**	**0.60**	**0.66**	0.74	0.90	1.09	1.70	1.65
A4	**0.44**	0.81	0.87	0.94	1.11	1.29	1.90	1.86
A5	1.65	1.26	1.27	1.16	1.07	0.86	**0.30**	**0.54**
A6	0.92	**0.51**	**0.50**	**0.48**	**0.38**	**0.22**	0.70	0.70
A7	1.26	0.85	0.90	0.74	0.79	**0.51**	**0.54**	0.71
A8	**0.67**	**0.31**	**0.46**	**0.20**	**0.54**	**0.49**	0.98	1.02

B.2 Electronic Structure and Hyperfine Interactions in Magnetite Above the Verwey Transition

B.2.1 Temperature Dependence of Linewidth of Main NMR Signals

Table B.8: Parameters of temperature dependences of NMR line width (8.11) obtained from experimental data by a fit. The uncertainties correspond to the errors from the fit.

sample composition	nominal Fe(B) valence v_B	C_{A1} (kHz)	E_{A1} (K)	C_{B1} (kHz)	E_{B1} (K)
$[Fe]_A[Fe_2]_BO_4$	2.500	0.87 ± 0.09	190 ± 16	7.9 ± 1.8	258 ± 38
$[Fe_{0.993}Zn^{2+}_{0.007}]_A[Fe_2]_BO_4$	2.504	2.95 ± 0.14	284 ± 6	10.3 ± 2.9	442 ± 39
$[Fe_{0.983}Zn^{2+}_{0.017}]_A[Fe_2]_BO_4$	2.509	4.25 ± 0.23	327 ± 8	17.5 ± 3.1	467 ± 24
$[Fe]_A[Fe_{1.994}...^0_{0.006}]_BO_4$	2.508	1.22 ± 0.06	368 ± 7	8.0 ± 4.0	480 ± 72
$[Fe]_A[Fe_{1.973}...^0_{0.027}]_BO_4$	2.534	7.05 ± 0.64	246 ± 14	40.1 ± 2.7	367 ± 12
$[Fe]_A[Fe_{1.992}Ti^{4+}_{0.008}]_BO_4$	2.494	2.18 ± 0.17	299 ± 11	12.0 ± 0.9	382 ± 11
$[Fe]_A[Fe_{1.992}Ti^{4+}_{0.008}]_BO_4$	2.494	2.34 ± 0.36	251 ± 23	7.8 ± 2.2	409 ± 44
$[Fe]_A[Fe_{1.98}Ti^{4+}_{0.02}]_BO_4$	2.485	11.25 ± 0.48	270 ± 6	35.7 ± 7.4	409 ± 27
$[Fe]_A[Fe_{1.995}Al^{3+}_{0.005}]_BO_4$	2.499	2.14 ± 0.29	258 ± 20	9.9 ± 1.5	355 ± 24
$[Fe]_A[Fe_{1.97}Al^{3+}_{0.03}]_BO_4$	2.492	13.78 ± 0.74	290 ± 8	42.0 ± 9.8	410 ± 36

Table B.9: Parameters of temperature dependences of NMR line width (8.13) obtained from experimental data by a fit. The uncertainties correspond to the errors from the fit.

sample composition	nominal Fe(B) valence v_B	C_{A3} (Hz $\cdot$ K$^{-3/2}$)	E_{A3} (K)	C_{B3} (Hz $\cdot$ K$^{-3/2}$)	E_{B3} (K)
$[Fe]_A[Fe_2]_BO_4$	2.500	0.079 ± 0.006	454 ± 11	0.66 ± 0.11	541 ± 28
$[Fe_{0.993}Zn^{2+}_{0.007}]_A[Fe_2]_BO_4$	2.504	0.288 ± 0.032	535 ± 15	1.07 ± 0.20	686 ± 27
$[Fe_{0.983}Zn^{2+}_{0.017}]_A[Fe_2]_BO_4$	2.509	0.393 ± 0.046	588 ± 17	1.73 ± 0.22	717 ± 18
$[Fe]_A[Fe_{1.994}...^0_{0.006}]_BO_4$	2.508	0.120 ± 0.012	621 ± 14	0.81 ± 0.34	729 ± 59
$[Fe]_A[Fe_{1.973}...^0_{0.027}]_BO_4$	2.534	0.645 ± 0.082	509 ± 19	2.91 ± 0.21	675 ± 13
$[Fe]_A[Fe_{1.992}Ti^{4+}_{0.008}]_BO_4$	2.494	0.201 ± 0.008	560 ± 6	1.06 ± 0.11	651 ± 16
$[Fe]_A[Fe_{1.992}Ti^{4+}_{0.008}]_BO_4$	2.494	0.217 ± 0.019	511 ± 13	0.68 ± 0.13	684 ± 30
$[Fe]_A[Fe_{1.98}Ti^{4+}_{0.02}]_BO_4$	2.485	1.04 ± 0.15	527 ± 19	3.3 ± 1.0	666 ± 41
$[Fe]_A[Fe_{1.995}Al^{3+}_{0.005}]_BO_4$	2.499	0.193 ± 0.016	523 ± 12	0.85 ± 0.10	631 ± 19
$[Fe]_A[Fe_{1.97}Al^{3+}_{0.03}]_BO_4$	2.492	1.19 ± 0.11	562 ± 15	3.82 ± 0.87	677 ± 35

Bibliography

[1] Senn M. S., Wright J. P. and Attfield J. P. Charge order and three-site distortions in the Verwey structure of magnetite. *Nature.* 2012, **481**, 173-176.

[2] Brabers V. A. M. Progress in spinel ferrite research. In: Buschow K. H. J. *Handbook of Magnetic Materials.* Amsterdam: Elsevier, 1995.

[3] Honig J. M. Analysis of the Verwey transition in magnetite. *J. Alloys Compd.* 1995, **229**, 24–39.

[4] Walz F. The Verwey transition–a topical review, *J. Phys.: Condens. Matter.* 2002, **14**, R285–R340.

[5] García J. and Subías G. The Verwey transition–a new perspective. *J. Phys.: Condens. Matter.* 2004, **16**, R145–R178.

[6] Krupička S. *Fyzika feritů a příbuzných magnetických kysličníků.* Praha: Academia, 1969.

[7] Loos J. and Novák P. Double exchange and superexchange in a ferrimagnetic half-metal. *Phys. Rev. B.* 2002, **66**, 132403.

[8] De Grave E., Persoons R. M., Vandenberghe R. E. and de Bakker P. M. A. Mössbauer study of the high-temperature phase of Co-substituted magnetites, $Co_xFe_{3-x}O_4$. I. x≤0.04. *Phys. Rev. B.* 1993, **47**, 5881–5893.

[9] Kubo K. and Ohata N. A Quantum Theory of Double Exchange. I. *J. Phys. Soc. Jpn.* 1972, **33**, 21.

[10] Wright J. P., Attfield J. P. and Radaelli P. G. Charge ordered structure of magnetite Fe_3O_4 below the Verwey transition. *Phys. Rev. B.* 2002, **66**, 214422.

[11] Kakol Z. *Effect of Titanium and Zinc Doping and Influence of Stoichiometry Changes on Physical Properties of Magnetite.* Kraków, 1994. AGH University. Faculty of Physics and Nuclear Techniques.

[12] Aroyo M. I., Perez-Mato J. M., Capillas C., Kroumova E., Ivantchev S., Madariaga G., Kirov A. and Wondratschek H. Bilbao Crystallographic Server: I. Databases and crystallographic computing programs. *Z. Kristallogr.* 2006, **221**(1), 15–27.

[13] Mizoguchi M. NMR Study of the Low Temperature Phase of Fe_3O_4. I. Experiments. *J. Phys. Soc. Jpn.* 1978, **44**, 1501-1511.

[14] Mizoguchi M. Charge and Orbital Ordering Structure of Fe_3O_4 in the Low-Temperature Phase as Deduced from NMR Study. *J. Phys. Soc. Jpn.* 2001, **70**, 2333–2344.

[15] Abe K. and Chikazumi S. Computer Controlled Torque Magnetometer for Automatic Determination of Crystal Orientation. *Japan. J. Appl. Phys.* 1976, **15**, 619.

[16] Abe K., Miyamoto Y. and Chikazumi S. Magnetocrystalline anisotropy of low-temperature phase of magnetite. *J. Phys. Soc. Jpn.* 1976, **41**, 1894-1902.

[17] Miles P. A., Westphal W. B. and von Hippel A. Dielectric Spectroscopy of Ferromagnetic Semiconductors. *Rev. Mod. Phys.* 1957, **29**, 279.

[18] Verwey E. J. W. Electronic Conduction of Magnetite (Fe_3O_4) and its Transition Point at Low Temperatures, *Nature.* 1939, **144**, 327-328.

[19] Kita E., Siratori K., Kohn K., Tasaki A., Kimura S. and Shindo I. Magneto-electric Effect of Fe_3O_4 at 77 K. II. Electric Field Dependence of Magnetic Anisotropy. *J. Phys. Soc. Jpn.* 1979, **47**, 1788.

[20] Iida S., Mizushima K., Mizoguchi M., Mada J., Umemura S., Nakao K. and Yoshida J. Mössbauer, NMR, and X-ray studies and a new ordering model of Fe_3O_4. *AIP Conf. Proc.* 1976, **29**, 388.

[21] Kakol Z. and Honig J. M. Influence of deviations from ideal stoichiometry on the anisotropy parameters of magnetite $Fe_{3(1-\delta)}O_4$. *Phys. Rev. B.* 1989, **40**, 9090.

[22] Anderson P. W. Ordering and Antiferromagnetism in Ferrites. *Phys. Rev.* 1956, **102**, 1008.

[23] Lorenz B. and Ihle D. Calculation of the electrical conductivity above and below the Verwey transition in magnetite. *Phys. Status Solidi (b).* 1975, **69**, 451.

[24] Ihle D. and Lorenz B. Small-polaron conduction and short-range order in Fe_3O_4. *J. Phys. C: Solid State Phys.* 1986, **19** 5239-5251.

[25] Degiorgi L., Wachter P. and Ihle D. Small-polaron conductivity in magnetite, *Phys. Rev. B.* 1987, **35**(17), 9259-9264.

[26] Belov K. P. Electronic processes in magnetite (or, "Enigmas of magnetite"). *Phys.-Usp.* 1993, **36**, 380–391.

[27] Iida S., Mizushima K., Mada J., Umemura S., Yoshida J. and Nakao K. Physical aspects of magnetite. *Journal de Physique Colloques.* 1977, **38**(C1), C1-73–C1-77.

[28] Mizoguchi M. NMR Study of the Low Temperature Phase of Fe_3O_4. II. Electron Ordering Analysis. *J. Phys. Soc. Jpn.* 1978, **44**, 1512-1520.

[29] Zuo J. M., Spence J. C. H. and Petuskey W. Charge ordering in magnetite at low temperatures. *Phys. Rev. B.* 1990, **42**(13), 8451.

[30] Jeng H.-T. Guo G. Y. and Huang D. J. Charge-Orbital Ordering and Verwey Transition in Magnetite. *Phys. Rev. Lett.* 2004, **93**, 156403.

[31] Jeng H.-T., Guo G. Y. and Huang D. J. Charge-orbital ordering in low-temperature structures of magnetite: GGA+U investigations. *Phys. Rev. B.* 2006, **74**, 195115.

[32] Madsen G. K. H. and Novák P. Charge order in magnetite. An LDA+U study. *Europhys. Lett.* 2005, **69**(5), 777-783.

[33] Rowan A. D. and Patterson C. H. Hybrid density functional theory applied to magnetite: Crystal structure, charge order, and phonons. *Phys. Rev. B.* 2009, **79**, 205103.

[34] Yamauchi K., Fukushima T. and Picozzi S. Ferroelectricity inmultiferroic magnetite Fe_3O_4 driven by noncentrosymmetric Fe^{2+}/Fe^{3+} charge-ordering: first-principles study. *Phys. Rev. B* 2009, **79**, 212404.

[35] Zhou F. and Gerbrand C. First-principles determination of charge and orbital interactions in Fe_3O_4. *Phys. Rev. B.* 2010, **81**, 205113.

[36] Fukushima T., Yamauchi K. and Picozzi S. Ab initio investigations of Fe^{2+}/Fe^{3+} bond dimerization and ferroelectricity induced by intermediate site/bondcentered charge ordering in magnetite. *J. Phys. Soc. Jpn.* 2011, **80**, 014709.

[37] Novák P., Štěpánková H., Englich J., Kohout J. and Brabers V. A. M. NMR in magnetite below and around the Verwey transition. *Phys. Rev. B.* 2000, **61**, 1256-1260.

[38] Senn M. S., Loa I., Wright J. P. and Attfield J. P. Electronic orders in the Verwey structure of magnetite. *Phys. Rev. B.* 2012, **85**, 125119.

[39] Patterson C. H. Hybrid DFT calculation of ^{57}Fe NMR resonances and orbital order in magnetite. *Phys. Rev. B.* 2014, **90**, 075134.

[40] de Jong S., Kukreja R. et al. Speed limit of the insulator-metal transition in magnetite. *Nature Mater.* 2013, **12**, 882–886.

[41] Chainani A., Yokoya T., Morimoto T., Takahashi T. and Todo S. High-resolution photoemission spectroscopy of the Verwey transition in Fe_3O_4. *Phys. Rev. B.* 1995, **51**, 17976.

[42] Park J. H., Tjeng L. H., Allen J. W., Metcalf P. and Chen C. T. Single-particle gap above the Verwey transition in Fe_3O_4. *Phys. Rev. B.* 1997, **55**, 12813.

[43] Schrupp D., Sing M., Tsunekawa M., Fujiwara H., Kasai S., Sekiyama A., Suga S., Muro T., Brabers V. A. M. and Claessen R., High-Energy Photoemission on Fe_3O_4: Small Polaron Physics and the Verwey Transition. *Europhys. Lett.* 2005, **70**, 789.

[44] Kimura M. et al. Polaronic Behavior of Photoelectron Spectra of Fe_3O_4 Revealed by Both Hard X-ray and Extremely Low Energy Photons. *J. Phys. Soc. Jpn.* 2010, **79**(6), 064710.

[45] Fujii Y., Shirane G. and Yamada Y. Study of the 123 K Phase Transition of Magnetite by Critical Neutron Scattering. *Phys. Rev. B.* 1975, **11** 2036.

[46] Chiba K., Suzuki K. and Chikazumi S. Diffuse Electron Scattering from Magnetite above the Verwey Transition Temperature. *J. Phys. Soc. Jpn.* 1975, **39**, 839.

[47] Shapiro S. M., Iizumi M. and Shirane G. Neutron Scattering Study of the Diffuse Critical Scattering Associated with the Verwey Transition in Magnetite (Fe_3O_4). *Phys. Rev. B.* 1976, **14**, 200.

[48] Yamada Y., Wakabayashi N. and Nicklow R. M. Neutron Diffuse Scattering in Magnetite due to Molecular Polarons, *Phys. Rev. B.* 1980, **21**, 4642.

[49] Seikh M. M., Narayana C., Metcalf P. A., Honig J. M. and Sood A. K., Brillouin Scattering Studies in Fe_3O_4 across the Verwey Transition. *Phys. Rev. B.* 2005, **71**, 174106.

[50] Subías G., García J. and Blasco J. EXAFS Spectroscopic Analysis of the Verwey Transition in Fe_3O_4. *Phys. Rev. B.* 2005, **71**, 155103.

[51] Park S. K., Ishikawa T. and Tokura Y. Charge-Gap Formation upon the Verwey Transition in Fe_3O_4. *Phys. Rev. B.* 1998, **58**, 3717.

[52] Moran T. J. and Lüthi B. Elastic and Magnetoelastic Effects in Magnetite. *Phys. Rev.* 1969, **187**, 710.

[53] Schwenk H., Bareiter S., Hinkel C., Lüthi B., Kakol Z., Kozłowski A. and Honig J. M. Charge Ordering and Elastic Constants in $Fe_{3-x}Zn_xO_4$. *Eur. Phys. J. B.* 2000, **13**, 491.

[54] Bosak A. et al. Short-Range Correlations in Magnetite above the Verwey Temperature. *Phys. Rev. X.* 2014, **4**, 011040.

[55] Miyahara Y. Impurity Effects on the Transition Temperature of Magnetite. *J. Phys. Soc. Jpn.* 1972, **32**, 629-634.

[56] Aragón R., Buttrey D., Shepherd J. P. and Honig J. M. Influence of non-stoichiometry on the Verwey transition. *Phys. Rev. B.* 1985, **31**, 430.

[57] Brabers V. A. M., Walz F. and Kronmüller H. Impurity effects upon the Verwey transition in magnetite. *Phys. Rev. B.* 1998, **58**(21), 14163.

[58] Kakol Z., Sabol J., Stickler J. and Honig J. M. Effect of low-level titanium(IV) doping on the resistivity of magnetite near the Verwey transition. *Phys. Rev. B.* 1992, **46**, 1975–1978.

[59] Kozłowski A., Metcalf P., Kakol Z. and Honig J. M. Electrical and magnetic properties of $Fe_{3-z}Al_zO_4$ (z¡0.06). *Phys. Rev. B.* 1996, **53**(22), 15113.

[60] Dehe G., Seidel B., Melzer K. and Michalk C. Determination of a cation distribution model of the spinel system $Fe_{3-x}Al_xO_4$. *Phys. Status Solidi (a).* 1975, **31**, 439.

[61] Sorescu M., Diamandescu L., Brand R. A. and Tarabasanu-Mihaila D. Mössbauer study of manganese-doped magnetite below the Verwey transition. *Materials Letters.* 2004, **58**, 885– 888.

[62] Lelis M. F. F., Porto A. O., Gonçalves C. M. and Fabris J. D. Cation occupancy sites in synthetic Co-doped magnetites as determined with X-ray absorption (XAS) and Mössbauer spectroscopies, *J. Magn. Magn. Mater.* 2004, **278**, 263–269.

[63] Shirley D. A. Application and Interpretation of Isomer Shifts. *Rev. Mod. Phys.* 1964, **36**, 339.

[64] Bodmer A. R. Isotope shift calculations for non-uniform charge distributions. *Nuclear Physics* 1960, **21**, 347–352.

[65] Filatov M. First principles calculation of Mössbauer isomer shift. *Coordin. Chem. Rev.* 2009, **253**, 594–605.

[66] Häggström L. *Determination of hyperfine parameters from 1/2 → 3/2 transitions in Mössbauer spectroscopy.* Report UUIP-851. Uppsala, 1974. Institute of Physics. University of Uppsala.

[67] Sedlák B. and Kuz'min R. N. *Jaderné resonanční metody ve fyzice pevných látek.* Praha: Státní pedagogické nakladatelství, 1978.

[68] Meiboom S. and Gill D. Modified Spin-Echo Method for Measuring Nuclear Relaxation Times. *Rev. Sci. Instrum.* 1958, **29**, 688–691.

[69] Štěpánková H. *Anizotropie hyperjemného pole ve ferimagnetických oxidech.* Habilitation thesis. Praha, 1999. Charles University in Prague. Faculty of Mathematics and Physics.

[70] Gamaliy E., Štěpánková H., Englich J., Kohout J., Snezhko A., Novák P. and Brabers V. A. M. NMR of ^{57}Fe above the Verwey transition in Al-substituted magnetite, *J. Magn. Magn. Mater.* 2002, **242–245**, 732–734.

[71] Chlan V., Novák P., Štěpánková H., Řezníček R., Kouřil K. and Kozłowski A. Electronic structure and hyperfine fields in non-stoichiometric magnetite above the Verwey transition. *J. Magn. Magn. Mater.* 2010, **322**, 1079–1081.

[72] Novák P., Štěpánková H., Englich J., Kohout J. and Brabers V. A. M. Temperature Dependence of NMR in Magnetite. In: *Ferrites: Proc. ICF 8, Kyoto and Tokyo.* Kyoto and Tokyo: Japan Society of Powder and Powder Metallurgy, 2000, p. 131.

[73] Řezníček R. *Spektra jaderné magnetické rezonance magnetitu se substitucí zinku.* Bachelor thesis. Prague, 2008. Charles University in Prague. Faculty of Mathematics and Physics.

[74] Cadogan J. M. and Ryan D. H. Mössbauer Spectroscopy. In: Vij D. R. *Handbook of Applied Solid State Spectroscopy.* New York: Springer, 2006.

[75] Mössbauer R. L. Kernresonanzfluoreszenz von Gammastrahlung in Ir^{191}. *Z. Physik.* 1958, **151**, 124-143.

[76] Shvyd'ko Y. et al. γ-Ray Wavelength Standard for Atomic Scales. *Phys. Rev. Lett.* 2000, **85**, 495-498.

[77] Phillips W. R., Ahmad I., Banes D. W., Glagola B. G., Henning W., Kutschera W., Rehm K. E., Schiffer J. P. and Wang T. F. Charge-state dependence of nuclear lifetimes. *Phys. Rev. Lett.* 1989, **62**, 1025.

[78] Sahm W. and Schwenk A. Precision Measurements of Magnetic Moments of Nuclei with Weak NMR Signals. *Z. Naturforsch.* 1974, **29a**, 1763.

[79] Perlow G. J., Johnson C. E. and Marshall W. Mössbauer Effect of Fe^{37} in a Cobalt Single Crystal. *Phys. Rev.* 1965, **140**, A875.

[80] Martínez-Pinedo G., Schwerdtfeger P., Caurier E., Langanke K., Nazarewicz W. and Söhnelm T. Nuclear Quadrupole Moment of ^{57}Fe from Microscopic Nuclear and Atomic Calculations. *Phys. Rev. Lett.* 2001, **87**, 062701.

[81] Hohenberg P. and Kohn W.. Inhomogeneous Electron Gas. *Phys. Rev.* 1964, **136**, B864-B871.

[82] Anisimov V. I., Solovyev I. V., Korotin M. A., Czyżyk M. T. and Sawatzky G. A. Density-functional theory and NiO photoemission spectra. *Phys. Rev. B.* 1993, **48**, 16929-16934.

[83] Hubbard J. Generalized Wigner lattices in one dimension and some applications to tetracyanoquinodimethane (TCNQ) salts. *Phys. Rev. B.* 1978, **17**, 494-505.

[84] Kohn W. and Sham L. J. Self-Consistent Equations Including Exchange and Correlation Effects. *Phys. Rev.* 1965, **140**, A1133-A1138.

[85] Singh D. J. *Planewaves, Pseudopotentials and the LAPW Method.* Boston: Kluwer Academic, 1994.

[86] Sjøstedt E., Nordström L., and Singh D. J. An alternative way of linearizing the augmented plane-wave method. *Solid State Commun.* 2000, **114**, 15.

[87] Bałanda M., Wiecheć A., Kim D., Kakol Z., Kozłowski A., Niedziela P., Sabol J., Tarnawski Z. and Honig J. M. Magnetic AC susceptibility of stoichiometric and low zinc doped magnetite single crystals. *Eur. Phys. J. B.* 2005, **43**, 201–212.

[88] Brabers V. A. M., Whall T. E. and Knapen P. S. A. Preparation of polycrystalline and monocrystalline $Fe_{3-x}Ti_xO_4$ spinels. *J. Cryst. Growth.* 1984, **69**, 101-107.

[89] Blaha P., Schwarz K., Madsen G. K. H., Kvasnicka D. and Luitz J. *WIEN2k, An Augmented Plane Wave + Local Orbitals Program for Calculating Crystal Properties.* Ed. Schwarz K. Wien: Technische Universität, 2001.

[90] Novák P. and Chlan V. Contact hyperfine field at Fe nuclei from density functional calculations. *Phys. Rev. B.* 2010, **81**, 174412.

[91] Blügel S., Akai H., Zeller R. and Dederichs P. H. Hyperfine fields of 3d and 4d impurities in nickel. *Phys. Rev. B.* 1987, **35**, 3271.

[92] Bader R. F. W. *Atoms in Molecules. A Quantum Theory.* Oxford: Oxford University Press, 1990.

[93] Řezníček R., Chlan V., Štěpánková H. and Novák P. Hyperfine field and electronic structure of magnetite below the Verwey transition. *Phys. Rev. B.* 2015, **91**, 125134.

[94] Żukrowski J. et al., unpublished results

[95] Wdowik U. D. and Ruebenbauer K. Calibration of the isomer shift for the 14.4-keV transition in ^{57}Fe using the full-potential linearized augmented plane-wave method, *Phys. Rev. B.* 2007, **76**, 155118.

[96] Sinnecker S., Slep L. D., Bill E. and Neese F. Performance of Nonrelativistic and Quasi-Relativistic Hybrid DFT for the Prediction of Electric and Magnetic Hyperfine Parameters in ^{57}Fe Mössbauer Spectra. *Inorg. Chem.* 2005, **44**(7), 2245–2254.

[97] Duff K. J. Calibration of the isomer shift for ^{57}Fe, *Phys. Rev. B.* 1974, **9**(1), 66.

[98] Zhang Y., Mao J. and Oldfield E. ^{57}Fe Mössbauer Isomer Shifts of Heme Protein Model Systems: Electronic Structure Calculations. *J. Am. Chem. Soc.* 2002, **124**, 7829-7839.

[99] Mielczarek E. V. and Winfree W. P. Isomer shift in TiFe and a calibration of the ^{57}Fe isomer shift. *Phys. Rev. B.* 1975, **11**(3), 1026.

[100] Mielczarek E. V., Papaconstantopoulos D. A. Isomer shift and charge density in FeAl and the ^{57}Fe isomer shift. *Phys. Rev. B.* 1978, **17**(11), 4223.

[101] Kistner O. C. and Sunyar A. W. Evidence for Quadrupole Interaction of Fe_{57m}, and Influence of Chemical Binding on Nuclear Gamma-Ray Energy. *Phys. Rev. Lett.* 1960, **4**, 412.

[102] Wertheim G. K., Guggenheim H. J. and Buchanan D. N. E., Sublattice Magnetization in FeF_3 near the Critical Point. *Phys. Rev.* 1968, **169**, 465.

[103] Walker L. R., Wertheim G. K. and Jaccarino V. Interpretation of the Fe^{57} Isomer Shift. *Phys. Rev. Lett.* 1961, **6**(3), 98.

[104] Żukrowski J., Wiecheć A., Zach R., Tabiś W., Tarnawski Z., Kim-Ngan N. –T. H., Kakol Z. and Kozłowski A. AC magnetic susceptibility under pressure and Mössbauer effect studies of the isotropy point T_{IP} in magnetite. *J. Alloys and Compounds.* 2007, **442**, 219–221.

[105] Pasternak M. P., Xu W. M., Rozenberg G. Kh., Taylor R. D., Jeanloz R. Pressure-induced coordination crossover in magnetite; the breakdown of the Verwey–Mott localization hypothesis. *J. Magn. Magn. Mater.* 2003, **265**, L107–L112.

[106] Evans B. J. and Hafner S. S., ^{57}Fe Hyperfine Fields in Magnetite (Fe_3O_4). *J. Appl. Phys.* 1969, **40**(3), 1411.

[107] Wertheim G. K. and Buchanan D. N. E. Temperature Dependence of the Fe^{57} hfs in FeF_2 below the Néel Temperature. *Phys. Rev.* 1967, **161**, 478.

[108] Kurian R. and Filatov M. Calibration of ^{57}Fe isomer shift from ab initio calculations: can theory and experiment reach an agreement? *Phys. Chem. Chem. Phys.* 2010, **12**, 2758–2762.

[109] Neese F. Prediction and interpretation of the ^{57}Fe isomer shift in Mössbauer spectra by density functional theory. *Inorganica Chimica Acta.* 2002, **337** 181–192.

[110] Berger S. and Braun S. *200 and More NMR Experiments.* Weinheim: Wiley-VCH, 2004.

[111] Sajti Sz., Deák L. and Bottyán L. FitSuite a general program for simultaneous fitting (and simulation) of experimental data. *eprint arXiv:0907.2805* 2009. Available at http://arxiv.org/abs/0907.2805v1

[112] Hargrove R. S. and Kündig W. Mössbauer measurements of magnetite below the Verwey transition. *Solid State Commun.* 1970, **8**(5), 303-308.

[113] Berry F. J., Skinner S. and Thomas M. F. ^{57}Fe Mössbauer spectroscopic examination of a single crystal of Fe_3O_4. *J. Phys.: Condens. Matter.* 1998, **10**, 215-220.

[114] Harrison H. R. and Aragón R. Skull melter growth of magnetite (Fe_3O_4). *Mater. Res. Bull.* 1978, **13**(11), 1097.

[115] Aragón R., Harrison H. R., McCallister R. H. and Sandberg C. J. Skull melter single crystal growth of magnetite (Fe_3O_4) - ulvospinel (Fe_2TiO_4) solid solution members. *J. Cryst. Growth.* 1983, **61**(2), 221-228.

[116] Flood H. and Hill D. G. The redox equilibrium in iron oxide spinels and related systems. *Z. Elektrochem.* 1957, **61**, 18–24.

[117] Chlan V. *Hyperfine Interactions in Ferrites with Spinel Structure.* Doctoral thesis. Prague, 2010. Charles University in Prague. Faculty of Mathematics and Physics.

[118] Řezníček R. *Influence of cationic substitution on hyperfine interactions in magnetite.* Diploma thesis. Prague, 2010. Charles University in Prague. Faculty of Mathematics and Physics.

[119] Gamaliy O. *Hyperfine interactions in magnetic iron oxides with nonmagnetic substitutions.* Doctoral thesis. Prague, 2006. Charles University in Prague. Faculty of Mathematics and Physics.

[120] Kohout J., Gamaliy E., Štěpánková H., Englich J., Novák P. and Brabers V. A. M. NMR of ^{57}Fe below and around the Verwey transition in Al-substituted magnetite, *J. Magn. Magn. Mater.* 2004, **272–276**, e1687–e1688.

[121] Kohout J., Gamaliy E., Štěpánková H., Englich J., Procházka V., Chlan V. and Brabers V. A. M. NMR of ^{57}Fe, ^{69}Ga and ^{71}Ga in Ga substituted magnetite. *J. Magn. Magn. Mater.* 2005, **290–291**, 1018–1020.

[122] Dehe G., Suwalski J., Wiener E. and Kabisch R. The cation distribution in the spinel system $Fe_{3-x}Ga_zO_4$. *Phys. Status Solidi (a).* 1981, **65,** 669.

[123] Chlan V., Gamaliy E., Štěpánková H., Kouřil K., Englich J., Kohout J. and Brabers V. A. M. Nuclear magnetic resonance of ^{57}Fe in Al-, Ga- and Ti-substituted magnetite above Verwey temperature, *J. Magn. Magn. Mater.* 2007, **310**, 2555–2557.

[124] Řezníček R., Chlan V., Štěpánková H., Novák P. and Maryško M., Magnetocrystalline anisotropy of magnetite. *J. Phys.: Condens. Matter.* 2012, **24**, 055501.

[125] Arras R., Warot-Fonrose B. and Calmels L. Electronic structure near cationic defects in magnetite. *J. Phys.: Condens. Matter.* 2013, **25**, 256002.

[126] Štěpánková H., J. Kohout, Novák P., Englich J., e. g. Caspary, and H. Lutgemeier. Dependence of hyperfine field in yttrium iron garnet on ionic radius of diamagnetic defects: NMR study. *Aust. J. Phys.* 1998, **51**, 437–452.

[127] Novák P., Englich J., Štěpánková H., Kohout J., Lütgemeier H., Wagner K. and Tolksdorf W. Antisite defects in yttrium iron garnet. *J. Phys. IV France.* 1997, **7**, C1-283 – C1-287.

[128] Kozłowski A., Rasmussen R. J., Sabol J. E., Metcalf P. and Honig J. M. Electrical conduction in single-crystal $Fe_{3-y}Ti_yO_4$ (0 ¡ y ¡ 0.9). *Phys. Rev. B.* 1993, **48**(4), 2057.

[129] Lenge N., Kronmüller H., Walz F. The Relation between Electrical Conductivity Mechanisms and Magnetic After-Effects in Single Crystal Magnetite. *J. Phys. Soc. Jpn.* 1984, **53**, 1406-1414.

[130] Honig J. M. Electrical Properties of Metal Oxides Which Have "Hopping" Charge Carriers. *J. Chem. Educ.* 1966, **43**(2), 76-82.

[131] Ihle D. and Lorenz B. Small-polaron band versus hopping conduction in Fe_3O_4. *J. Phys. C: Solid State Phys.* 1985, **18** L647-L650.

[132] Ciuchi S. and Fratini S. Signatures of polaronic charge ordering in optical and dc conductivity using dynamical mean field theory. *Phys. Rev. B.* 2008, **77**, 205127.

[133] Tannhauser D. S. Conductivity in iron oxides. *J. Phys. Chem. Solids.* 1962, **23**, 25-34.

Articles Related to the Thesis

1. Řezníček R., Chlan V., Štěpánková H. and Novák P. Hyperfine field and electronic structure of magnetite below the Verwey transition. *Phys. Rev. B.* 2015, **91**, 125134.

2. Řezníček R., Štěpánková H., Chlan V., Novák P. and Kozłowski A. Analysis of Cationic Impurity Impact on Hyperfine Interactions in Magnetite. *IEEE Trans. Magn.* 2012, **48**, 3039-3042.

3. Řezníček R., Chlan V., Štěpánková H., Novák P. and Maryško M. Magnetocrystalline anisotropy of magnetite. *J. Phys.: Condens. Matter.* 2012, **24**, 055501.

4. Pfeffer M., Řezníček R., Křišťan P. and Štěpánková H. Device for measurement of power and shape of radio frequency pulses in nuclear magnetic resonance. *Meas. Sci. Technol.* 2012, **23**, 057001.

5. Chlan V., Štěpánková H., Řezníček R. and Novák P. Anisotropy of hyperfine interactions as a tool for interpretation of NMR spectra in magnetic materials. *Solid State Nuclear Magnetic Resonance.* 2011, **40**, 27-30.

6. Chlan V., Novák P., Štěpánková H., Řezníček R., Kouřil K. and Kozłowski A. Electronic structure and hyperfine fields in nonstoichiometric magnetite above the Verwey transition. *J. Magn. Magn. Mater.* 2010, **322**, 1079-1081.

Other Articles

1. Křišťan P., Hondlík O., Štepánková H., Chlan V., Kouřil K., Řezníček R., Pollert E. and Veverka P. Nuclear Magnetic Resonance in Hexaferrite/Maghemite Composite Nanoparticles. *Acta Physica Polonica A.* 2015, **127**, 514.

2. Kouřil K., Chlan V., Štěpánková H., Řezníček R., Laguta V. V. and Raevski I. P. NMR Study of Multiferroic Iron Niobate Perovskites. *Acta Physica Polonica A.* 2015, **127**, 234.

3. Chlan V., Kouřil K., Štěpánková H., Řezníček R. and Englich J. Study of Y-type Hexaferrite by Means of ^{57}Fe NMR and Electronic Structure Calculations. *Acta Physica Polonica A.* 2014, **126**, 42-43.

4. Křišťan P., Chlan V., Štěpánková H., Řezníček R., Görnert P. and Payer P. Structure of Iron Oxide Nanoparticles Studied by ^{57}Fe NMR. *Acta Physica Polonica A.* 2014, **126**, 138-139.

5. Křišťan P., Chlan V., Štěpánková H., Řezníček R., Kouřil K., Štěpánek J., Poláková K., Procházka V., Čuda J. and Medřík I. Bentonite/Iron Oxide Composites: Preparation and Characterization by Hyperfine Methods. *Journal of Nanomaterials.* 2013, Article ID 179794.

6. Sedlák B., Kouřil K., Chlan V., Řezníček R., Křišťan P., Pfeffer M., Englich J. and Štěpánková H. Tuned Probehead for NMR Spectroscopy in Magnetically Ordered Materials. *Acta Physica Polonica A.* 2010, **118**, 924-925.

7. Chlan V., Štěpánková H., Englich J., Řezníček R., Kouřil K., Kučera M. and Nitsch K. Antisite Defects in Epitaxial Films of Lutetium Doped Yttrium Iron Garnets Studied by Nuclear Magnetic Resonance. *Acta Physica Polonica A.* 2010, **118**, 846-847.

8. Chlan V., Kouřil K., Štěpánková H., Řezníček R., Štěpánek J., Tabiś W., Król G., Tarnawski Z., Kakol Z. and Kozłowski A. Magnetically induced structural reorientation in magnetite studied by nuclear magnetic resonance. *J. Appl. Phys.* 2010, **108**, 083914.

9. Procházka V., Sedlák B., Štěpánková H., Pfeffer M., Řezníček R. and Chlan V. New experimental procedure for broad NMR spectra measurement. *Proceedings of the 16th Conference of Czech and Slovac Physicists (Hradec Králové 2008)*, ed. Jan Kříž, pp 212-221, MAFY Hradec Králové 2009.

10. Procházka V., Štěpánková H., Sedlák B., Kapusta Cz., Knížek K., Jirák Z., Englich J. and Řezníček R. NMR study of $LaMn_{1-x}Co_xO_3$ perovskites. *J. Magn. Magn. Mater.* 2008, **320**, e12-e15.

List of Tables

List of Abbreviations

NMR   nuclear magnetic resonance

DC   direct current

LRO   long range ordered

SRO   short range ordered

B3LYP   Becke, three-parameter, Lee-Yang-Parr

EFG   electric field gradient

FID   free induction decay

CPMG   Carr-Purcell-Meiboom-Gill

SNR   signal-to-noise ratio

HWHM   half-width at half-maximum

RX/TX   receive/transmit

LC   inductor and capacitor

IF   intermediate frequency

I/Q   in-phase/quadrature

A/D   analog-to-digital

DFT   density functional theory

LSDA   local spin density approximation

GGA   generalized gradient approximation

SIC   self-interaction corrected

LAPW   linearized augmented plane wave

LO   local orbitals

APW   augmented plane wave

lo   local orbital

AIM   atoms in molecules approach

BVS   bond valence sum

YIG   yttrium iron garnet